THE UNIVERSITY
of EDINBURGH

‘Investigating the anti-tumour effects of macrophages in the zebrafish brain.’

Lloyd Liang Ming Hamilton

Doctor of Philosophy

The University of Edinburgh

2019

Statement of Originality

This is to certify that unless otherwise stated, the content of this thesis is my own work. I, Lloyd Liang Ming Hamilton, declare that the content presented in this document is original and that all sources and references mentioned in the text have been acknowledged.

This thesis has not been submitted for any degree or academic merit at another educational institution. Data within this thesis has been submitted for the following publication:

PEREZ-LOPEZ, A. M., RUBIO-RUIZ, B., SEBASTIAN, V., HAMILTON, L., ADAM, C., BRAY, T. L., IRUSTA, S., BRENNAN, P. M., LLOYD-JONES, G. C., SIEGER, D., SANTAMARIA, J. & UNCITI-BROCETA, A. 2017. Gold-Triggered Uncaging Chemistry in Living Systems. *Angew Chem Int Ed Engl,* 56**,** 12548-12552.

Lloyd Liang Ming Hamilton

29th August 2019

Acknowledgements

First, I would like to thank Dr. Dirk Sieger for being the best supervisor anyone could have asked for. You have been a great source of guidance and inspiration. You have led me though some tough times and guided me through my failures. You have given me the freedom to explore my interests and made this PhD an incredible learning experience. I am a better man thanks to you.

I would like also thank family for their unrelenting support though my studies. Mom and Dad, you have always been there for me. Thank you Sarah for always being there for me too.

To all my lab members, thank you for your guidance over the years. I would like to especially thank Dr. Katy Astell for making the last 4 years possible. Your day to day help and advice on everything science and life has taught me a great deal. I would like to also thank Dr. Julie Mazzolini for proofreading this thesis and to all the staff at the fish facility.

Finally, I would like to thank Cancer Research UK for funding and making this research opportunity possible.

Thank you

Abstract

Glioblastoma (GBM) remains an incurable tumour fraught with a high probability of death. One of the key characteristic of GBM is the development of local immunosuppression that promotes immune evasion and lays a solid foundation for the tumour to progress. Breakthroughs in our understanding in cancer biology have shown that GBM have evolved unique mechanisms that influence infiltrating macrophages, a key immune cell type, to facilitate tumour progression. Macrophages have been identified in many studies to promote angiogenesis, extra cellular matrix reorganisation, establishment of local immunosuppression and tumour growth. Thus, there is great need to improve the clinical development of immunotherapeutics that can address tumour-specific immune responses. Herein, we tested the capability of solidly supported Gold and Palladium nanoparticles as biorthogonal catalytic converters of prodrugs in a zebrafish U87 glioblastoma xenograft model. Intriguingly, we report that the implantation of Palladium and Gold bead into the zebrafish brain causes a potent anti-tumour responses that leads to U87 cell clearance, fragmentation and increased macrophage number. Further investigation revealed that Gold and Palladium beads did not cause aberrant necrosis when implanted in the zebrafish brain and that macrophages played a key role in mediating the associated anti-tumour response of Palladium and Gold bead implantation. The role of macrophages was investigated further using Next Generation RNA sequencing of macrophages isolated from Palladium bead implanted zebrafish. RNA sequencing results revealed differentially expressed genes in Palladium bead implanted zebrafish with 389 genes upregulated and 361 genes downregulated. Enrichment analysis of these genes showed significant enrichment of oxidation-reduction processes as a result of Palladium bead implantation. In addition, confirmatory RT-qPCR highlighted two key TLR signalling inflammatory genes, Cxcl8b.1 and TNF-a , to be overexpressed in macrophages of Palladium and Gold bead implanted zebrafish. Since Cxcl8b.1 is a potent attractant of neutrophils, we studied the dynamics of macrophages and neutrophil number in the zebrafish brain. Indeed, we detected an accumulation of neutrophils upon gold bead transplantation. Thus, we analysed the role of Cxcl8b.1 and TNF-a in the initiation of the anti-tumour effect. This was achieved by combining CRISPR-Cas9 knock out and genetic overexpression transgenesis techniques of Cxcl8b.1 and TNF-a. The results here conclude that TNF-a were not key genetic mediators of the associated bead induced anti-tumour phenotype. Finally, this study opens new avenues for the development of novel cancer immunotherapeutics. RNA sequencing results showed high number of other candidate genes that exploit the intrinsic capabilities of transitions metals to initiate an anti-tumour response.

Lay Abstract

Glioblastoma is an incurable brain tumour fraught with a high probability of death. One of the key properties of glioblastoma is the ability to avoid the immune system and thus allowing it to grow. Breakthroughs in our understanding in cancer biology have shown that glioblastoma have evolved unique traits that interact with the immune system. These interactions influence macrophages, a key immune cell type, to help the tumour growth. Macrophages have been identified in many studies to enter the site of the tumour to promote blood vessel development, reorganisation of surrounding tissue and immune system avoidance. Therefore, there is great need to improve the clinical development of treatments that can address these interactions between the tumour and the immune system. We do so by using a widely use animal model, the zebrafish. The zebrafish has many advantages and one of them is its optical transparency. This allows us to look into the brain of the zebrafish with a microscope to directly observe the interaction of immune cells and tumour cells. We have previously used this model to study immune interactions between macrophages and human brain tumours that were transplanted into zebrafish brains. To extend our previous study, we investigate the ability of solidly supported Palladium and Gold nanoparticles to stimulate macrophages to kill brain tumours. To do so, Gold and Palladium beads were carefully implanted into the zebrafish brain and any anti-tumour responses were studied closely. The implantation of Gold and Palladium beads led to the clearance and break down of tumour cells. In addition, Gold and Palladium stimulated increased macrophage number in the zebrafish brain. Gold and Palladium did not cause direct cell death of these tumour cells, but induced an anti-tumour response in macrophages. Genetic studies of these macrophages showed changes in the expression of many genes related to the oxidation-reduction processes. In addition, two key immune system activating genes, Cxcl8b.1 and TNF-α , were confirmed to be over-expressed in Palladium and Gold bead implanted zebrafish. Cxcl8b.1 and TNF-α are important genes that can influence how the immune system respond; Cxcl8b.1 is an important activator of neutrophil number, another key immune cell type. Therefore, we investigated the dynamics of how these genes can affect macrophages and neutrophil number to regulate anti-tumour effects in the zebrafish brain. In order to do so, we altered genetic expression of Cxcl8b.1 and TNF-α in the zebrafish brain, either by increasing or decreasing the expression of each gene. Our results conclude that TNF-α and Cxcl8b.1 were not key genetic effectors of the associated bead induced anti-tumour responses. Finally, this study here opens new avenues for the development of new anti-cancer drugs that exploit the innate properties of transitions metals to interact with the immune system.

Table of Contents

1. Introduction

1.1. The role of tumour associated macrophages and their impact on the tumour microenvironment in Glioblastomas

1.1.1. Glioblastomas and its origins

The advent of genomics within the last decade has accelerated the integration of phenotypic and genomic parameters to classify tumours of the central nervous system (CNS) (Louis et al., 2014 , Louis et al., 2016). Molecular insights into CNS tumours have led to the refinement of diagnostic categories that expanded the 2007 World Health Organisation (WHO) classification of tumours of the CNS (Louis et al., 2014, Louis et al., 2016). Gliomas are the most common malignant primary brain tumours (Gusyatiner and Hegi, 2018). Accurate classification of gliomas has significant implication for the patient in addition to having important ramifications in the interpretation of clinical and scientific experiments encompassing tumours of the CNS (Louis et al., 2016). Today, the combination of diagnostic molecular testing

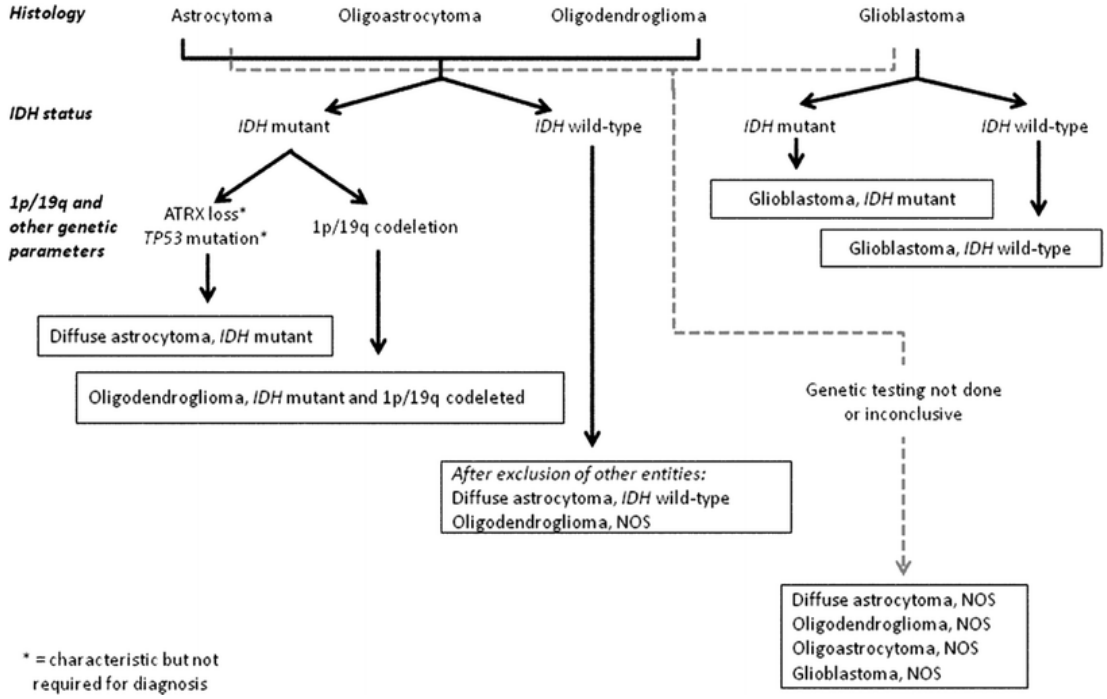

Figure 1.Gliomas are classified based on histological and genetic features.

Gliomas are classified based on morphology genotype such as IDH status, presence or absence of 1p/19q co-deletion, ATRX loss and TP53 mutations. Glioma diagnosis consist of a histopathological name followed by a genetic feature (Diffuse astrocytoma, IDH-mutant). Tumour lacking a molecular diagnosis is termed NOS.

Image taken from Louis et al., 2016

and histological analysis is fundamental in the clinical classification of CNS tumour and guides the use of therapies (Summarised in Figure 1) (Louis et al., 2016).

Glioma defines a heterogenous group of CNS cancers that are anatomically similar to each other but are diverse in the context of morphology and molecular biology (Crocetti et al., 2012, Ho et al., 2014). Glioma is a complex disease that presents a multitude of histopathological features and resembles various neural cell types (Lu et al., 2019). High grade gliomas can display a high degree of heterogeneity between tumours and within cells of the same tumour (Alcantara Llaguno and Parada, 2016, Jiang and Uhrbom, 2012). Gliomas were thought to originate from glial cells due to the high proportion of expression of glial specific GFAP protein (Jones et al., 1981). However, histopathological classification have identified morphological resemblance of gliomas, such as astrocytomas, oligodendrogliomas, oligoastrocytomas and glioblastomas, to glial tissue. Gliomas can show morphological characteristics similar to astrocytes and express astrocytic lineage markers such as GFAP and APO-E (Rousseau et al., 2006). Gliomas of astrocytic lineage are termed Astrocytomas (Rousseau et al., 2006). In contrast, Oligodendroglioma have morphological characteristics that resemble oligodendrocyte progenitor cells (OPC) and often express OPC markers that include Olig2, NG2 and PDGFRα (Rousseau et al., 2006, Zong et al., 2012). Gliomas with mixed cellular or anaplastic features have also been identified and these tumours are classified as oligoastrocytomas and glioblastomas (Zong et al., 2012).

The cellular origins of gliomas are widely debated, however, studies have shown that glioma can originate from multiple cells. Neural stem cells and glial progenitors have been early contender as the cell origins of gliomas (Zong et al., 2012, Pollard et al., 2009). The inactivation of tumour suppressor (*Nf1*, *p53* and *Pten*) in nestin expressing neural progenitor niches have been shown to induce high grade astrocytoma formation and premature death in mice (Alcantara Llaguno et al., 2009, Zhu et al., 2005). Likewise, the inactivation or deletion of tumour suppressors in oligodendrocyte precursor cells promotes the transformation from a quiescent to a malignant state (Galvao et al., 2014). Furthermore, astrocytes have been

shown to dedifferentiate into multipotent progenitors that malignantly transformation into Astrocytomas (Bachoo et al., 2002). There is a growing body of evidence to show that gliomas are maintained by a subpopulation of cancer cells displaying stem cell like characteristics; long term self-renewal and differentiation capabilities (Pollard et al., 2009, Hemmati et al., 2003, Fleurence et al., 2019). These glioma cancer stem-like cells are generally not completely removed during surgery and are resistant to chemotherapy and radiotherapy; leading to the regeneration and recurrence of the GBMs (Fleurence et al., 2019). Altogether, gliomas can develop from many difference cell types and thus contributes to the complexity of glioma biology.

Gliomas are clinically classified under the 2016 World's Health Organisation classification of tumour of the central nervous system from grade I to IV. It classifies gliomas based on morphology, histology grade, genotype such as IDH status and the presence or absence of 1p/19q co-deletion (Back et al., 2018). The less aggressive diffuse astrocytomas and oligodendrogliomas are designated as Grade II (Louis et al., 2016). Glioblastomas multiforme (GBM), the most aggressive form of gliomas, are classed under grade IV, the highest in severity (Back et al., 2018, Louis et al., 2016). The most effective treatment includes maximal tumour resection followed by radiotherapy and temozolomide chemotherapy (Weller et al., 2014). GBM remains an incurable tumour with a low survival rate of 14.4% at 3 years (Gramatzki et al., 2016). GBMs are histologically and genetically heterogenous (Pollard et al., 2009). Transcriptomic and genomic analysis of GBM have identified distinct molecular subtypes of GBMs and can be classified further. Four expression subtypes of GBMs have been reported, proneural, neural, classical and mesenchymal, each with unique genetic markers that indicate the cell of origin and distinct clinical outcomes (Verhaak et al., 2010). Oligodendrocytic signatures have been identified in the proneural subtype. The proneural subtype of GBM are predominantly secondary gliomas and occur at a younger age (Verhaak et al., 2010). Hallmark characteristics include PDGFRA abnormalities and IDH1 mutations (Verhaak et al., 2010). IDH1 mutations have been inversely correlated with GBM grading affecting 71% in grade II, 64% in grade III and 6% in primary glioblastomas (Labussiere et al., 2010, Back et

al., 2018). The Increase of *PDGFRA* expression in proneural subtypes are due to increased P*DGFRA* mutation and *PDGFRA* gene amplification (Verhaak et al., 2010). The *PDGFRA* gene is selectively expressed in OPC and is critical in stimulating the proliferation and migration of OPCs (Zong et al., 2012). The classical subtype is characterised by astrocytic gene signatures and epidermal growth factor receptor (*EGFR)* amplification, mutations and *EGFRvIII* intragenic deletions. *EGFRvIII* intragenic deletions of the epidermal growth factor (EGF) receptor leads to an in frame deletion and consequently results in the constitutively active kinase domain of the receptor (Zadeh et al., 2013, Li et al., 2009). EGFRvIII enhances cell proliferation, tumour growth and invasiveness in GBMs (Li et al., 2009). In contrast, neural subtypes are associated with gene of both astrocytes and oligodendrocytes but the strongest association are of gene associated with neurones (Verhaak et al., 2010). Neural markers such as NEFL and GABAA1 are identifiers of the neural subtype of GBMs (Verhaak et al., 2010). Finally, macrophage markers such as *CD68* and *TNF* are identified to be highly expressed in the mesenchymal subtype (Verhaak et al., 2010). In addition, the mesenchymal subtype had been correlated with genes associated with inflammation and has been linked to increased overall fraction of necrosis in tumours (Verhaak et al., 2010). The mesenchymal subtype of GBMs have been associated with high immune cell infiltration (microglia and macrophages) which has been shown to contribute to tumour progression (Prionisti et al., 2019, Gajewski et al., 2013, Noy and Pollard, 2014). Therefore, the tumour microenvironment constitutes malignant and non-malignant cells, including immune and stromal cells, that provides tumour promoting functions (Noy and Pollard, 2014, Balkwill et al., 2012). The complex network of signals between immune cells and GBMs establishes a tumour supporting environment that facilitates the transition to malignancy (Hambardzumyan et al., 2016, Noy and Pollard, 2014).

1.1.2. The innate and adaptive immune system, a brief overview

Vertebrates have evolved a highly complex immune system to recognise many components of foreign organism and elicit an immediate defence. The immune system consists of two distinct levels, the adaptive and innate immune system. The cells of the innate and adaptive immune systems are distinct (macrophages, dendritic cells, neutrophils and natural killer (NK) cells are considered innate immune cells, and lymphocytes are considered adaptive immune cells) but are not isolated from each other (Renshaw and Trede, 2012, Janeway and Medzhitov, 2002, Riera Romo et al., 2016). Significant crosstalk exists between the innate and adaptive immune system and is vital for the proper recognition and the proper immune response to an invading pathogen, bacterial or cancerous cell (Renshaw and Trede, 2012, Janeway and Medzhitov, 2002, Riera Romo et al., 2016).

The innate immune system is the first line of defence against invading pathogens or tissue injury. The mechanism of pathogen recognition by the innate immune system is extensively studied. The recognition of conserved features of microbial pathogens by the innate immune system are mediated through pattern recognition receptors, such as toll like receptors (TLRs), C-type lectin receptors (CLRs) and nucleotide-binding oligomerization domain (NOD) (Li et al., 2017, Iwasaki and Medzhitov, 2015). These receptors recognise pathogen-associated molecular patterns (PAMPs) such as bacterial (LPS, flagellin), fungal cell-wall component and viral nucleic acids (Beutler, 2009, Iwasaki and Medzhitov, 2015). In addition to recognising structural features, the innate immune system is also capable of detecting pathogens through changes in tissue homeostasis (Iwasaki and Medzhitov, 2015, Chovatiya and Medzhitov, 2014). Alterations in tissue homeostasis such as protein folding, level of reactive oxygen species (ROS) and nutrient availability are sensed by sensors such as ATF4, NRF2, and CHREBP respectively, which engages a stress response to restore homeostasis (Chovatiya and Medzhitov, 2014). Macrophages have been defined as key sensory cells that monitor and control tissue homeostasis under stress, infection and also during tissue development and normal tissue states (Chovatiya and Medzhitov, 2014, Casano and Peri, 2015, Mosser

and Edwards, 2008). The advantages of this recognition system negates the requirement of a whole host of specific receptors against a diverse range of toxins, allergens, bacterial structures or virulent factors. The recognition of multicellular parasitic infections are detected by changes in tissue homeostasis as parasites lack structurally invariant targets that are detectable by pathogen recognition receptors (Iwasaki and Medzhitov, 2015). The innate immune system is also capable of discriminating self from non-self through inhibitory receptors. NK cells contain an immunoreceptor tyrosine-based inhibitory motif that detects major histocompatibility complex class I (MHC class I) molecules in order to avoid targeting healthy cells (Raulet, 2006). Indeed, normal cells from mice deficient in MHC class I were susceptible to NK cells (Raulet, 2006). Viral infection and cellular stress reduces the surface expression of MHC class I which rapidly flags these cells to be killed by NK cells (Iwasaki and Medzhitov, 2015).

The detection of a pathogen by the innate immune system initiates a signalling cascade that generates a phagocytic inflammatory responses. Neutrophils are one of the first responders of the immune system and migrate into tissue in response to injury or infection (Kim and Luster, 2015). Neutrophils are an important cell type of the innate immune system. Neutrophils develop in the bone marrow and form the majority, 50% – 75%, of circulating peripheral blood leukocytes (Kienle and Lammermann, 2016, Kim and Luster, 2015). They patrol the body and migrate into the brain or any tissue in response to an insult (Kienle and Lammermann, 2016, Kim and Luster, 2015). Neutrophils are potent innate immune cells that contain cytotoxic granules enriched with antimicrobial molecules such as cationic peptides, proteases and myeloperoxidase (MPO) (Rosales et al., 2016). One unique aspect that separates neutrophils from other innate immune cells is their ability to release neutrophil extracellular traps (NETs) (Brinkmann and Zychlinsky, 2012, Rosales et al., 2016). NETs are composed of decondensed chromatin material as well as cytoplasmic protein released into the extracellular space (Garley et al., 2016, Brinkmann and Zychlinsky, 2012). These NETs binds microorganism to prevent their spread and releases a high local concentration of cytotoxic factors such as MPO and neutrophil elastase (Rosales et al., 2016, Garley et al., 2016, Berger-Achituv

et al., 2013). MPO has been shown to kill melanoma cells and inhibit tumour progression (Odajima et al., 1996). Patients deficient in MPO have increased predisposition to cancer (Lanza et al., 1988). In addition, the uptake of neutrophil elastase, a serine protease expressed in neutrophil primary granules by breast cancer cells, promotes specific lysis by cytotoxic T-lymphocytes (Mittendorf et al., 2012). Neutrophil release of NETs activates dendritic cells and primes T cells and marks a key step towards the activation of the adaptive immune system (Berger-Achituv et al., 2013, Brinkmann and Zychlinsky, 2012).

Microglia, the resident macrophage of the brain, are derived from primitive macrophages that invade and differentiate in the brain during development (Ginhoux et al., 2010). Microglia and macrophages, are cells of the mononuclear phagocytic system derived from the bone marrow and are myeloid in origin (Simard and Rivest, 2004, Nayak et al., 2014, Pollard, 2009). Microglia and macrophages are phagocytic cells of the innate immune system and have key roles in the development and immune related functions against pathogens and injuries in the brain (Casano and Peri, 2015, Nayak et al., 2014, Greter and Merad, 2013, Pollard, 2009). The differentiation of microglia from primitive macrophages is regulated by various transcription factors such as PU.1, Irf8, TGF-β and colony stimulating factor (CSF)-1R in the brain (Walton et al., 2000, Shiau et al., 2015, Lavin et al., 2014, Butovsky et al., 2014, Elmore et al., 2014). PU.1 is an essential transcription factor that regulates adult myelopoiesis and is expressed in macrophages, neutrophils, B cell, T cells and microglia (Olson et al., 1995, Walton et al., 2000, Nayak et al., 2014, McKercher et al., 1996, Pang et al., 2018). PU.1 has been identified as a key regulator of myeloid differentiation that promote lineage specific gene expression (Pang et al., 2018). Consequently, mice deficient in PU.1 expression are devoid of macrophage and microglia (Anderson et al., 1998). Likewise, the genetic knockout of TGF-β and pharmacological inhibition CSF-1R expression in mice abolishes microglia expression in the CNS (Butovsky et al., 2014, Elmore et al., 2014). In contrast, Interferon regulatory factor 8 (irf8) is a key factor in early stage myelopoiesis of the immature zebrafish immune system during development (Shiau et al., 2015). Knock out of irf8 in the zebrafish leads to the char-

acteristic development of a macrophage null background up to around seven days post fertilization (Shiau et al., 2015). In addition, irf8-/- mutant mice have a reduction in the number of parenchymal microglia in the midbrain (Kierdorf et al., 2013).

Although microglia and macrophages share a common lineage, these cell types can be functional distinct from one another. Studies have shown that infiltrating macrophages are capable of performing indispensable roles not provided by resident macrophages (Shechter et al., 2009, London et al., 2011). In one study, infiltrating monocyte derived macrophages was responsible for the neuroprotective secretion of anti-inflammatory cytokine, il-10, in a spinal cord injury mice model (Shechter et al., 2009). Therefore, the distinction between resident microglia and peripheral macrophages in the CNS will allow investigators to further investigate the differential role of microglia and macrophages functional contribution CNS diseases. However, the shared lineage between differentiated microglia and macrophages of monocyte lineage means that these two cell types share many genetic markers such as Iba1, CD68, F4/80, PU.1 and mpeg1 (Brochhausen et al., 2017, Hendrickx et al., 2017, Ohsawa et al., 2004, Hsu et al., 2004, Ellett et al., 2011). In efforts to discriminate between microglia and macrophages researchers have identified key genetic markers that allowed separate identification of these two closely related cell type in the CNS. Traditional approaches to differentiate microglia from invading macrophages relied on the use of CD45 antibody where resident microglia were CD45Lo and macrophages CD45Hi (Badie and Schartner, 2000). However new markers have been recently identified, the microglia specific protein 199 (TMEM119) was discovered through comparative transcriptomic studies (Satoh et al., 2016) and was recently demonstrated to selectively label microglia (Kaiser and Feng, 2019). In addition, the P2 purinergic receptor (P2Y12) was also demonstrated to be a microglia specific marker in mice and zebrafish (Zhu et al., 2017, Butovsky et al., 2014, Sieger et al., 2012). Together these markers expanded the repertoire of biological tools to allow effective identification of microglia from infiltrating macrophages in order to study CNS diseases.

The maturation of dendritic cells and macrophages into antigen presenting cells recruits the adaptive immune system and provides an important link between the innate and

adaptive immunity (Li et al., 2017, Renshaw and Trede, 2012). Antigen presenting cells are important modulators of immunity that are capable of phagocytosis (Mantegazza et al., 2013, Broeke et al., 2013). Peptides derived from phagocytosis and subsequent cytosolic proteolysis of pathogens associate intracellularly with either MHC class I or MHC class II molecules and are translocated to the plasma membrane (Mantegazza et al., 2013, Broeke et al., 2013). Peptide antigens are unique to each pathogen and the presentation of these peptides associated with MHC molecules activate the adaptive immune system (Mantegazza et al., 2013, Broeke et al., 2013). These MHC-peptide complexes are recognise by T and B lymphocytes from the adaptive immune system (Hato and Dagher, 2015, Gajewski et al., 2013). The activation of T and B lymphocytes initiate cytotoxic activity and antibody production respectively, which specifically target the pathogen (Hato and Dagher, 2015, Gajewski et al., 2013). Unlike pattern recognition receptors of the innate immune system, antigen receptors on the adaptive immune system recognize individual classes of pathogens based on specific protein antigen presentation (Broeke et al., 2013). Therefore, the adaptive immune system is more versed in pathogen recognition than the innate immune system. The adaptive immune system is estimated to recognise 107 or more antigens versus the 103 molecular patterns in the innate immune system (Janeway and Medzhitov, 2002, Hato and Dagher, 2015). Together, the innate and adaptive immune systems trigger an immune response that adapts to acquire long term immune memory against the pathogen for future rapid response.

Tumours have evolved mechanisms that circumvent immune surveillance. These mechanisms exploit the ability of the innate immune system to influence the adaptive immune system in order to promote tumour progression. Substantial evidence has been provided in support of the view that the defence and immune functions are suppressed in gliomas (Biswas et al., 2013, Li and Graeber, 2012, Markovic et al., 2009). In particular, microglia and macrophages have been identified to play a key role in establishing an immunosuppressive milieu in cancer and will be the focus for this study.

1.1.3. The environment regulates the functional plasticity of microglia and macrophages

The functions of microglia are highly plastic and are stimulus dependent (Casano and Peri, 2015). A myriad of microglia functions have been identified in the brain that include phagocytosis of apoptotic neurons, synaptic refinement of neurones, vesicle patterning, inflammation and wound healing (For review see (Casano and Peri, 2015). Microglia are highly motile and are actively scanning their environment by extending and retracting their ramified processes without translocating the main cell body (Nimmerjahn et al., 2005). Microglia baseline surveillance of the parenchyma is regulated by a two pore domain potassium channel called THIK-1 (Madry et al., 2018) while the convergence of microglia processes toward a damaged area are regulated by purinoreceptors of the P2Y12 receptor highly expressed on microglia (Haynes et al., 2006). Microglia transition from the surveillance state to the activated state in response to stimuli such as inflammation or disease. The activation of microglia initiates a phenotypic change in addition to a change in its morphology (Nimmerjahn et al., 2005). Under the activated state, microglia attain an ameboid shape, are highly motile in their entirety and become morphologically indistinguishable from other macrophages (Prionisti et al., 2019). The functional plasticity and rapid response to external stimuli make microglia a highly versatile cell type that has the ability to adapt to its environment.

Microglia and macrophages are dynamic cell types that respond to cytokines released in their environment. The local microenvironment has an instructive role in directing the differentiation pathway primitive macrophages take, which ultimately shapes their function (Casano and Peri, 2015). Lavin et al. demonstrated that the transplantation of adult bone marrow derived macrophages into the lung, spleen and liver modified the chromatin landscape towards that of tissue-resident macrophages (Lavin et al., 2014). In addition, TGF-β was shown to regulate microglia differentiation and was required for the in vitro development of the microglia molecular signature characteristic of adult microglia. (Lavin et al., 2014, Butovsky et al., 2014). This plasticity is maintained in tissue macrophages to a certain extent, as differentiated resident macrophages can be influenced by the tissue microenvironment to

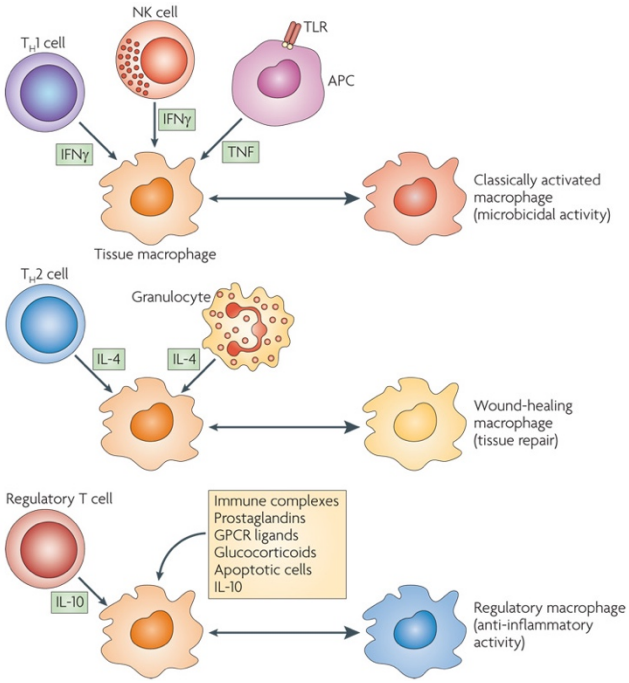

Moser and Edwards, 2008

Figure 2. Endogenous cytokines produced by cells of the innate and adaptive immune system can shape macrophage phenotype.

Interferon (IFN)-γ and tumour-necrosis factor (TNF) produced by T helper 1 (T_H1) cells, Natural Killer (NK) cells and antigen presenting cells (APC) polarises macrophages to secretes pro-inflammatory cytokine that enhances microbicidal and tumoricidal capacity. The expression Interleukin (IL)-4 by TH2 or by granulocyte promotes the development of the wound healing macrophage require for tissue repair. While IL-10 release by regulatory T-cells from the adaptive immunity promotes polarisation towards regulatory macrophages to suppress immune response. Regulatory macrophages can also be expressed by other stimuli including immune complexes, prostaglandins, GPCR ligands, gluococorticoids and apototic cells.

adapt their functions. The cytokines produced in the macrophage local environment can give rise to macrophages of distinct physiologies. Macrophages can respond to endogenous stimuli produced by immune cells of both the innate and adaptive immune system by altering their phenotype to facilitate anti-microbial activity, tissue repair or anti-inflammatory activities (Mosser and Edwards, 2008, Qian and Pollard, 2010, Rougeot et al., 2019). Figure 2 summarises how different endogenous cytokines produced by cells of the innate and adaptive immune system can shape macrophage phenotype. Interferon (IFN)-γ and tumour-necrosis factor (TNF) produced by T helper 1 (TH1) cells, NK cells and antigen presenting cells (APC) polarises macrophages to secrete pro-inflammatory cytokines (Mosser and Edwards, 2008). The expression of Interleukin (IL)-4 by TH2 cells or by granulocyte promotes the development

of the wound healing macrophage involved in tissue repair (Loke et al., 2007, Gordon and Martinez, 2010). While IL-10 release by regulatory T-cells from the adaptive immunity promotes polarisation towards regulatory macrophages to suppress immune response (Mosser and Edwards, 2008). The interaction between antigen specific T lymphocytes and microglia promotes wound healing functions of resident microglia following insult. The activation of microglia by IFN gamma facilitates glutamate clearance and contributes to a neuroprotective effect (Shaked et al., 2005). In addition, neurones have also be shown to secrete factors that regulated microglia activation. The secretion of CD22 and CD200 by neurones acted as an inhibitor of microglia proinflammatory cytokine TNF-a production and facilitate the maintenance of an anti-inflammatory expression profile in microglia (Mott et al., 2004, Lyons et al., 2009).

These studies suggest that the local environment is critical in influencing the functional identity of macrophages and result in a diverse range of macrophage subpopulation. Therefore, the microenvironment has a significant impact in modulating microglia and macrophage function that can drive the polarisation of microglia/macrophage towards a pro or anti-tumoural phenotype.

1.1.4. The tumour promoting functions of Tumour Associated Macrophages (TAMs)

GBMs have evolved mechanisms that exploit the intrinsic functional plasticity of macrophages to facilitate tumour growth (Hambardzumyan et al., 2016, Prionisti et al., 2019). The link between inflammation and GBM is well established. GBMs, like many other tumours, have evolved complex ecological mechanisms that promote the malignancy of tumours. The tumour microenvironment is a convoluted web of interacting biological signals between different cell populations that serves to enhance and promote the survival of tumours (Markovic et al., 2009, Wu et al., 2010, Li and Graeber, 2012). Innate immune cells are highly represented in the tumour microenvironment and macrophages are the most abundant cell type (Coniglio et al., 2012, Zhai et al., 2011, Markovic et al., 2009).. In particular, microglia and macrophages,

have been identified to contribute to GBM progression leading to tumour growth, tissue invasion and chemotherapeutic resistance (Prionisti et al., 2019, Hambardzumyan et al., 2016, Jacobs et al., 2012, Coniglio et al., 2012, Zhai et al., 2011, Hamilton et al., 2016). In the diseased CNS the compromised blood brain barrier leads to the infiltration of peripheral macrophages. Microglia and macrophages can contribute up to 50% of non-neoplastic cells (Hambardzumyan et al., 2016). In agreement, a further study using genetical modified mice showed that infiltrating monocytes/macrophages constitutes 85% total TAM while microglia accounted for the remaining 15% (Chen et al., 2017). The authors revealed that the genetic expression patterns between infiltrating monocytes/macrophages and resident microglia were unique when compared with each other thus highlighting a difference in functions (Chen et al., 2017). Furthermore, the authors concluded that there was a continuous transformation of infiltrating monocytes to mature macrophages and microglia-like cells in the tumour microenvironment (Chen et al., 2017). The level of infiltration by macrophages and microglia in GBMs have been positively correlated with poorer prognosis (Bingle et al., 2002, Li and Graeber, 2012). Under the influence cytokines such as CSF1, IL-4, IL-13 and IL-10, infiltrating monocytes can differentiated into tropic/developmental macrophages that downregulate tumoricidal activity (Noy and Pollard, 2014, Quail and Joyce, 2017, van Dalen et al., 2018). Therefore, microglia and macrophages in glioma have been described to resemble regulatory macrophages and wound healing macrophages possessing both anti-inflammatory activity and tissue repair capabilities (Mosser and Edwards, 2008).

The infiltration of macrophages and microglia in tumours, known as tumour associated macrophages (TAMs), modifies the tumour microenvironment to facilitate immune system avoidance and promote tumour progression. TAMs are capable of remodelling the tumour microenvironment to release inhibitory mechanisms that otherwise would lead to an anti-tumour phenotype (Noy and Pollard, 2014). TAMs have been shown to regulate tumour angiogenesis, invasion, metastasis, extracellular matrix reorganisation and suppression of inflammatory responses (Qian and Pollard, 2010, Zhang et al., 2016). The transition from benign growth towards a malignant cancer are marked by a plethora of cytokines that hijack the

intrinsic capabilities of macrophages to influence the local tumour microenvironment (Li and Graeber, 2012, Reichel et al., 2019, Qian and Pollard, 2010). Therefore the tumour promoting role of macrophages and microglia are supported by crosstalk with the oncogenic microenvironment. Substantial evidence has been provided in support of the view that the defence and immune functions of macrophages and microglia are suppressed in gliomas (Li and Graeber, 2012). The recruitment of macrophages and microglia into the tumour microenvironment are mediated by chemoattractant such as CC chemokine ligand 2 (CCL2) and soluble colony-stimulating factor (sCSF-1) (Conti and Rollins, 2004, Noy and Pollard, 2014). These chemoattracts are identified to be highly expressed in tumours including GBMs (Conti and Rollins, 2004, Noy and Pollard, 2014). In addition, TGF-β, an immunosuppressive cytokine, is overexpressed in tumours and plays an important role in the maintenance of an immunosuppressive milieu in the tumour microenvironment (Zhang et al., 2016). The expression of TGF-β exploits capabilities of the innate immune system to influence the adaptive immune response by inhibiting antigen presentation thereby inhibiting the activation and differentiation of cytotoxic T-cells. (Flavell et al., 2010, Li and Graeber, 2012). Once in the local tumour microenvironment, TAMs secrete proangiogenic factor such as matrix metalloproteinase (MMP)-9 and vascular endothelial growth factor (VEGF) that promotes angiogenesis, tumour progression and metastasis (Chen et al., 2014, Kim et al., 2018). In addition, TAMs produce immunosuppressive factors like interleukin (IL)-10 and IL-13 that inhibit macrophage activation, T-cell proliferation and reduces the production of proinflammatory cytokine IL-12 (Zhang et al., 2016). TAMs also produce epidermal growth factor (EGF) that increases tumour invasion by activating receptors on GBM (Coniglio et al., 2012). These TAMs are maintained by the gliomas through the secretion of glioma derived CSF-1 and IFN-γ a well-known chemoattractant of microglia and promoter of microglia proliferation (Coniglio et al., 2012, Pyonteck et al., 2013). Indeed, it was shown that the depletion of microglia by CSF-1 inhibition altered macrophage polarisation and increased the survival of a mouse proneural GBM model (Pyonteck et al., 2013). In addition, we also previously showed that microglia and macrophages form intimate interactions with GBM cells and these interactions are critical for GBM cell survival

in the zebrafish brain in vivo (Hamilton et al., 2016). The interactions between microglia/macrophages and glioma cells can alter microglia phenotype. In vitro co-cultures of microglia and glioma cells showed that microglia lose their phagocytic activity when in contact with C6 glioma cells (Voisin et al., 2010). Therefore, the close association of microglia and tumour cells suggests a symbiotic relationship that promotes tumour progression.

While many studies support for the tumour promoting role of macrophage in tumours, studies have shown that macrophages retain tumoricidal capabilities and that repolarisation of TAMs can be achieved towards an anti-tumour phenotype. The delivery of IL-12 containing microspheres into the tumour microenvironment led to proinflammatory cytokine production of Tnf-α, IL-15 and IL-18 and reduction in tumour promoting cytokines IL-10, MCP-1 and TGF-β (Watkins et al., 2007). Furthermore, toll like receptor (TLR) activation have been extensively documented to polarise TAMs towards pro-inflammatory tumoural phenotype through the upregulation of IL-6, IL-12, Tnf-α and iNOS secretion and enhancement of antigen uptake and T-cell priming (van Dalen et al., 2018, Vidyarthi et al., 2018, Banerjee et al., 2015, Yang et al., 2015, Rodell et al., 2018b). These studies highlights the potential of immunotherapeutics to repolarise TAM as a strategy to cancer treatment.

1.2. Nanoparticles in the treatment of Glioblastomas

The current standard treatment for GBM is surgery followed by adjuvant radiotherapy or chemotherapy. Even with multimodal treatment, modern medicine is still ineffective in increasing the median survival of 15 months in GBMs (Stupp et al., 2017). The anti-tumour properties of radiotherapy are still widely debated (Reviewed in Vatner and Formenti, 2015). Radiotherapy of tumours have been shown to actively recruit myeloid derived cells, especially TAMs, into the tumour microenvironment through CSF-1R activation (Vatner and Formenti, 2015). The recruitment of TAMs persists for years after radiotherapy and are detrimental to the patient (Vatner and Formenti, 2015). The anti-tumour effects of recruited macrophages are subverted and are polarised towards a tumour promoting phenotype (Vatner and For-

menti, 2015). In addition, radiotherapy can repolarise existing macrophages towards the tumour promoting, anti-inflammatory, phenotype (Vatner and Formenti, 2015). Chemotherapeutic resistance to Temozolomide (TMZ), the first line of treatment against GBM, is commonly reported due to intrinsic or acquired resistance of the tumour to the drug (Yi et al., 2019). Thus a more effective treatment option is long overdue.

One of the major challenge facing cancer therapy is the difficulty of homogeneous delivery of intravenous chemotherapeutics throughout the solid tumour mass. The high interstitial pressures contribute to the suboptimal diffusion of drugs from blood circulation which prevents intratumor penetration (Stohrer et al., 2000). The problem is exacerbated by the clearance of intravenous drugs by the liver and kidneys which can lead to fatal organ toxicity (Hoop et al., 2018). Inadequate intratumoural delivery of chemotherapeutic agents cannot be solved by increasing systemic dose. In addition, conventional chemotherapy lacks target specificity and nontarget tissue distribution. Thus the use of nanoparticles as carriers of chemotherapeutic drugs have been explored as a more effective drug delivery system. The medical applications of nanoparticles as a therapeutic agent in the treatment of cancer is not a novel approach. Nanoparticles are defined as small particles (1000<nm diameter) comprised of metals or polymers or any other materials that usually contain a hydrophobic region that can trap a hydrophobic drug (Reichel et al., 2019). Nanoparticles have been tested as combination therapies to induce cellular death through thermal ablation or oxidative stress (Phillips et al., 2014). Nanoparticles have been used to improve the efficiency of thermal ablation methods that includes radiofrequency, microwave, cryoablation and high intensity focused ultrasound (Manthe et al., 2010). In addition, nanoparticle-based drugs can be multifunctional, possessing both therapeutic and theranostic (diagnostic imaging probe) properties (Phillips et al., 2014). A wide range of radiotherapeutic nanoparticles have been studied to deliver ionising radiotherapy to the tumour in combination with imaging platforms like magnetic resonance imaging (MRI), positron emission tomography (PET) and X-ray computed tomography (CT) (Phillips et al., 2014).

Nanoparticles have also found new applications in the emerging field of bioorthogonal catalytic reactions in cancer therapy (Adam et al., 2018). By design, bioorthogonal reactions occur in a living organism without interfering with biological functions (Adam et al., 2018). Solidly supported Palladium and Gold nanoparticles have been recently demonstrated to catalyse bioorthogonal reactions that generate active agents from inactivated precursors (Adam et al., 2018, Perez-Lopez et al., 2017). The chemical inactivation of compounds can dramatically reduce the bioactivity of the resulting derivative while maintaining catalytic chemistry with Palladium (Weiss et al., 2014b, Adam et al., 2018), Gold (Perez-Lopez et al., 2017, Tonga et al., 2015), Copper (Clavadetscher et al., 2016) or Ruthenium (Tonga et al., 2015). Chemotherapeutic agents such as Fluorouracil (5-FU), Vorinostat, doxorubicin and SN-38 (active metabolite of irinotecan) can be synthesised from inactive precursors through bioorthogonal organometallic catalysis with Gold and Palladium nanoparticles (Adam et al., 2018, Perez-Lopez et al., 2017). The highly selective reactions of these implantable devices confer spatiotemporal control of chemotherapeutic drug delivery, in addition to increasing the potency of drugs at the tumour site. It also has the potential to reduce side effects, since systemic circulating inactivated precursor, when chemically inactivated, would have dramatically reduced bioactivity. A 44 fold reduction in cytotoxicity was achieved with SN-38 precursors on human colon rectal cancer cell line HCT116 and human glioblastoma cell lines U87 and U251 in vitro (Adam et al., 2018). Adam et al., demonstrated that Palladium mediated bioorthogonal catalytic release of SN-38 result in a dose dependent inhibition on HCT116, U87 and U251, cell viability (Adam et al., 2018). One study combined the magnetic properties of iron and bioorthogonal properties of Palladium to deliver chemotherapeutic 5-FU to a predefined area in tumour xenografts using magnetism (Hoop et al., 2018). Nanorobotic Palladium mediated bioorthogonal organometallic (BOOM) reactions result in a significant reduction in breast cancer cell growth in vitro and in vivo (Hoop et al., 2018). This technology presents a novel therapeutic approach combining nanorobotics and BOOM activation of prodrugs as a minimally invasive alternative to conventional chemotherapy.

1.2.1. Nanoparticle uptake polarises macrophages

Recent evidence suggests that the uptake of nanoparticles is capable of polarising macrophages towards an anti-tumour phenotype. Nanoparticles, either implanted or systemically administered, readily accumulated within both TAMs and macrophages (Bastus et al., 2009a, Reichel et al., 2019). The accumulation of nanoparticles in macrophages present the opportunity to enhance drug delivery to macrophages. Nanoparticles have also been used to enhance cancer immunotherapy (Rodell et al., 2018a, Huang et al., 2016, Wang et al., 2019). Drug loaded nanoparticles have been demonstrated to mediate synchronous biodistribution of drugs. The separate cell targeted delivery of chemotherapeutic agent and TAM repolarising agent was achieved using twin-like core-shell nanoparticles to cancer cells and TAMs respectively (Wang et al., 2019). The co-delivery strategy exhibited anti-tumour efficacy on TAMs and tumours leading to decreased tumour size in vivo (Wang et al., 2019). A recent study demonstrated the utility of drug loaded nanoparticles. R848, a TLR7/8 agonist, was loaded onto β-cyclodextrin nanoparticles which accumulated in macrophages and consequently led to the biodistribution of R848 in macrophages (Rodell et al., 2018a). Nanoparticles have extensive clinical application in immunotherapeutic drug delivery that targets TAMs (Rodell et al., 2018a, Huang et al., 2016, Penn et al., 2018, Binnemars-Postma et al., 2017)

The response of macrophage to nanoparticles is dependent on particle size, composition, dose, route of entry and surface properties (Reviewed in Reichel et al., 2019). These variables can modulate the efficacy of nanoparticle delivery and activity in macrophages. However, material composition and surface properties of nanoparticles are the most significant determinant of macrophage polarisation. The exposure of nanoparticles to endogenous serum in an in vivo system results in the formation of what is known as a protein ‘corona’ on the surface (Kharazian et al., 2016). Endogenous proteins compete with one another to bind the surface of the nanoparticle leading to opsonization and subsequent endocytosis or phagocytosis by macrophages (Ge et al., 2015). The most common method of blocking nonspecific binding of proteins to nanoparticles surfaces is to graft nanomaterials with linear chains

of poly(ethyleneglycol) (PEG) in a process known as PEGylation (Walkey et al., 2012). PEGylation of Gold nanoparticles blocks macrophage uptake and macrophage polarisation (Walkey et al., 2012). Thus the protein corona has significant implications in altering the bio-identity of nanoparticles (Cedervall et al., 2007, Ge et al., 2015, Kharazian et al., 2016, Walkey et al., 2012). The surface composition of nanoparticles can be artificially manipulated to modulate macrophage uptake of nanoparticles. One study showed that by changing the surface stabilizer of nanoparticles to either citrate or polyethylene imine from PEG, an increase in macrophage internalisation of nanoparticles was achieved (Zazo et al., 2017). As these nanoparticles are not recognised as inert by macrophages, the uptake of these nanoparticle can initiate intracellular responses that lead to macrophage polarisation (Reichel et al., 2019).

1.2.2. Harnessing the therapeutic potential of nanoparticle polarised macrophages and microglia in glioblastoma

Silica, Gold, Palladium and Iron oxide nanoparticles have all been described to polarise macrophages towards the pro-inflammatory phenotype (Reichel et al., 2019, Leso and Iavicoli, 2018). The inhibition of macrophage uptake of nanoparticles by either PEGylation, increasing surface ionization, adding inert polymers on the surface or blocking macrophage endocytosis has a significant effect in reducing macrophage polarisation capabilities (Cedervall et al., 2007, Reichel et al., 2019, Walkey et al., 2012). Thus the intracellular transport of nanoparticles by macrophages is essential in initiating macrophage polarisation pathways. The uptake of nanoparticles by macrophages is mediated by cytoskeleton dependent pathways (Kusaka et al., 2014). The treatment of bone marrow derived macrophages (BMDM) with Cyto D, an inhibitor of actin polymerization, dramatically inhibited the internalization of Silica nanoparticles (Kusaka et al., 2014).

The biological effects of nanoparticles on macrophage cytokine expression have been extensively investigated (Mukherjee et al., 2005, Hutter et al., 2010, Walkey et al., 2012, Niikura et al., 2013, Kusaka et al., 2014, Zanganeh et al., 2016, Alarifi et al., 2017, Leso and Iavicoli, 2018). Silica nanoparticles have been shown to activate capase-1 activity which

cleaves immature pro-IL-1β into mature IL-1β and leading to increased IL-1β secretion (Kusaka et al., 2014). In addition, increased ROS generation and increased IL-6, TNF-a and iNOS expression have been described in silica internalised macrophages. Likewise, Palladium nanoparticles polarise macrophages and lead to increased TNF-a, IL-6 and IL-8 expression (Schmidt and Goebeler, 2015, Leso and Iavicoli, 2018). However, significant ROS generation is considered as one of the key mechanisms responsible for the cytotoxic effect of metallic nanoparticles like Palladium (Leso and Iavicoli, 2018). Metallic nanoparticles such as Cobalt, Titanium and Palladium increase ROS generation in macrophages (Reichel et al., 2019, Alarifi et al., 2017). In addition, in one study, the treatment of Palladium nanoparticles on human skin malignant melanoma (A375) cells led to excessive production of ROS resulting in oxidative stress induced apoptosis, DNA damage and cell cycle arrest (Alarifi et al., 2017). Therefore, metallic nanoparticles like Palladium may have the potential to be used as a combination therapy that targets both TAMs and cancer cells. The effects of Gold nanoparticles on TAMs have also been previously investigated. Increased IL-1β, TNF-a, IL-6, iNOS secretion have all been described in macrophages treated with gold nanoparticles, driving a shift in macrophage polarisation towards the anti-tumorigenic phenotype (Bastus et al., 2009a, Reichel et al., 2019). Gold nanoparticles have been shown to be effective vaccine adjuvants that enhance macrophage inflammatory cytokine production including IL-12 and granulocyte macrophage colony stimulating factor (GM-CSF) (Hutter et al., 2010). In addition, Gold nanoparticles have been reported to possess anti-angiogenic properties by selectively inhibiting VEGF induced proliferation of endothelial cells which can have major implications in inhibiting tumour growth (Mukherjee et al., 2005). In contrast to Silica, Gold and Palladium, Iron oxide nanoparticles are currently used clinically as iron replacement therapies in the form of Ferumoxytol (Reichel et al., 2019, Toth et al., 2017). They also have imaging applications in contrast-enhanced magnetic resonance imaging and have been used as drug carriers in preclinical and clinical setting (Zanganeh et al., 2016, Toth et al., 2017). Ferumoxytol nanoparticles have been shown to attract macrophages and enhance ROS production leading to adenocarcinoma cells cytotoxicity in vitro (Zanganeh et al., 2016). Iron oxide nanoparticles polarise

macrophages towards the pro-inflammatory phenotype, causing an increase in TNF-α and a decrease in IL-10 expression (Zanganeh et al., 2016, Kodali et al., 2013). The treatment with Ferumoxytol polarises infiltrating and existing TAMs towards the pro inflammatory phenotype (Zanganeh et al., 2016). In vivo, proinflammatory polarisation of macrophages by iron oxide nanoparticles inhibits mammary tumour growth (Zanganeh et al., 2016). The effects were conserved to nanoparticle material composition, as alteration of surface chemistry had no effect on the inhibitory effect of macrophage on mammary tumour growth (Zanganeh et al., 2016). In addition, Iron oxide nanoparticles have a much greater impact on basal transcription in macrophages than silica nanoparticles (Kodali et al., 2013). Kodali et al. compared the effects of silica and iron oxide nanoparticles on macrophage polarisation. A total of 1029 genes and 67 genes were differentially expressed in macrophages treated with iron oxide nanoparticles and silica nanoparticles respectively (Kodali et al., 2013). Kodali et al also report that iron oxide treated macrophages elicit a greater inhibition on IL-10 secretion than in silica nanoparticle treated macrophages (Kodali et al., 2013). Altogether, nanoparticles have significant benefits in improving existing cancer treatment by inducing tumour-suppressive macrophage polarisation within tumours. In particular, Gold and Palladium have been identified to polarise macrophages through activation of toll like receptor (tlr)-4 signalling (Bastus et al., 2009a, Rachmawati et al., 2013). However, the effects of Gold and Palladium repolarisation of TAMs in GBMs remain to be investigated. Significant knowledge gaps exist in regards to Gold and Palladium nanoparticle effects on TAM in GBMs.

1.3. Toll Like Receptor Family

1.3.1. Toll Like Receptor family signaling and its effects on macrophage polarisation

Toll Like Receptors (TLRs) are pattern recognition receptors that recognize pathogen associated molecular patterns derived from microbial pathogens, including viruses, bacteria, fungi and damage associated molecular patterns such as ATP and double stranded DNA (dsDNA) (Brajer-Luftmann et al., 2019). TLR activation is the consequence of pathogenic infection or cellular stress that leads to a cascade of signalling events that promote inflammation, macrophage polarization and priming of the adaptive immune system (Brajer-Luftmann et al., 2019, Barton and Kagan, 2009). The expression of TLRs on macrophages plays a central role in host immunity against pathogens (Barton and Kagan, 2009). To date, eleven members of the TLR family have been identified. tlr1, tlr2, tlr4, tlr5, tlr6, and tlr11 are expressed on the cell surface and tlr3, tlr7 tlr8 and tlr9 are localised to the endosomal and lysosomal compartments (Figure 3) (Barton and Kagan, 2009, Mandreka, 2009). Each member of the TLR family recognises a specific ligand that triggers TLR signalling cascades leading to TNF-a, IL-8 and IL-1β secretion in macrophages (Bastus et al., 2009a). In mammals, TLR are responsible for recognising lipopolysaccharide (LPS) from gram-negative bacteria (tlr4) and flagellin protein (tlr5) (Kawai and Akira, 2010). While tlr3,tl7 and tlr9 recognise dsRNA, pharmacological compounds (Imiquimod and Resiquimod) and unmethylated CpG DNA motifs, respectively (Kawai and Akira, 2010). Ligand binding to TLR on the extracellular domain leads to the dimerization of TLRs which recruit and activate cytosolic adaptor proteins such as MyD88, TRIF, TRAM. MyD88 is a key protein in the TLR signal transduction pathways that recruits IL-1 receptor associated kinase 4 (IRAK-4) to activate MAP kinases and nuclear factor (NF)-κB. Additional modes of activation include the activation of TRAF6 by RIP1 and MyD88 independent TRIF and TRAF3 mediated activation of NF-κB (Mandreka, 2009). Individual TLRs selectively recruit distinct adaptor proteins that mediate signal transduction to tailor the response to the infecting pathogen (Summarised in Figure 3).

Although TLRs are important for their protective properties against infection, inappropriate TLR activation contributes to acute and chronic inflammation that promote the development of systemic autoimmune disease. Mutations in genes encoding for negative regulators of TLR signalling have been linked to the development of autoimmune diseases such as autoimmune glomerular nephritis and Crohn's disease (Cario, 2010). Mice deficient in TANK protein, an inhibitor of TBK1 and IKKE kinases, develop fatal glomerulonephritist as a result of excess inflammatory response (Kawagoe et al., 2009). Macrophages isolated from TANK-/- mutant mice have elevated NF-κB activation, IL-6 and TNF production as a result of TLR overactivation (Kawagoe et al., 2009). In addition, genetic polymorphism of genes encoding TLRs or downstream signalling, have been identified as increasing the predisposition to sepsis in humans as a result of impaired inflammatory response to bacterial infections (Cook et al., 2004). The best characterized TLR polymorphism is an amino acid substitution from aspartic acid to glycine at position 299 (D299G) in TLR4 which has been linked to increased Gram-negative infections (Cook et al., 2004). Polymorphism have also been identified in the TLR2 and IRAK4 that enhances the susceptibility to tuberculosis and infection from gram positive bacteria streptococcus pneumoniae (Cook et al., 2004). These studies demonstrate that the TLR signalling cascade plays a key role in the induction of inflammatory genes that has significant systemic consequence on the inflammatory response of immune cells.

The TLR family is conserved from mammals to insects, however, TLR signal transduction in fish exhibit notable differences than those in mammals (Li et al., 2017, Jault et al., 2004). A total of 20 putative TLR variants have been identified in fish of which ten are orthologs of human TLR family and two are fish specific TLRs (tlr21 and tlr22) (Jault et al., 2004). Gene duplication events during evolution led to the development of isoforms of tlr-4 (tlr4ba/tlr4bb), tlr5 (tlr5a/tlr5b) and tlr8 (tlr8a/tlr8b) (Li et al., 2017). Both isoforms of tlr5a and tlr5b have been shown to respond to mycobacterial infection similarly in mammals but zebrafish tlr4 does not respond to LPS stimulation unlike its mammalian counterpart (Li et al., 2017). The knockdown of tlr4a, tlr4b and MyD88 did not alter the zebrafish response to LPS which suggests a differential mechanism of LPS activation in zebrafish and an unidentified role of tlr4 in zebrafish

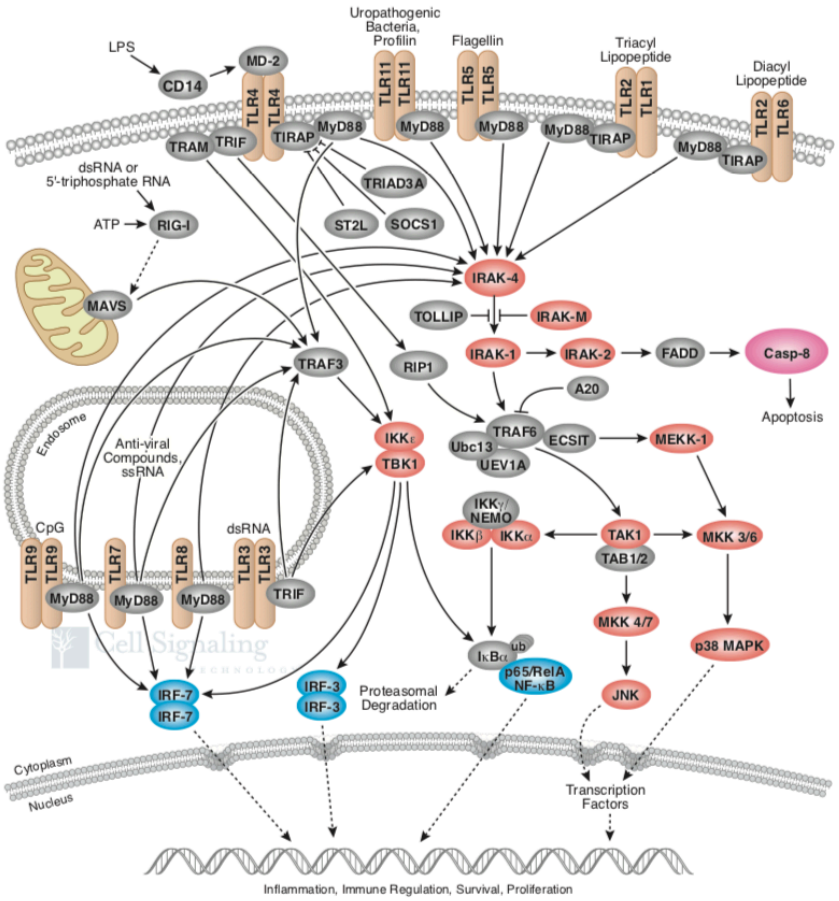

Figure 3. Toll Like Receptor (TLR) Signalling

To date, eleven members of the TLR family have been identified. *tlr1, tlr2, tlr4, tlr5, tlr6*, and *tlr11* are expressed on the cell surface and *tlr3, tlr7 tlr8* and *tlr9* are localised to the endosomal and lysosomal compartments. TLR are responsible for recognising lipopolysaccharide (LPS) from gram-negative bacteria (tlr4) and flagellin protein (tlr5). While tlr3,tl7 and tlr9 recognise dsRNA, pharmacological compounds (Imiquimod and Resiquimod) and unmethylated CpG DNA motifs respectively. Ligand binding to TLR on the extracellular domain leads to the dimerization of TLRs which recruits and activate cytosolic adaptor proteins such as MyD88, TRIF, TRAM. MyD88 is a key protein in the TLR signal transduction pathways that recruits IL-1 receptor associated kinase 4 (IRAK-4) to activate MAP kinases and nuclear factor (NF)-κB. Additional modes of activation include the activation of TRAF6 by RIP1 and MyD88 independent TRIF and TRAF3 mediated activation of NF-κB. Individual TLRs selectively recruit distinct adaptor proteins that mediates signal transduction to tailor the response to the infecting pathogen.

Image adapted from (Mandreka, 2009)

(Jault et al., 2004, Li et al., 2017). Although homologs of tlr6 are absent from fish, it was reported that tlr14 in fish may be a functional substitute for tlr6 in mammals (Hwang et al., 2011). In addition, tlr18 in zebrafish is the homolog of human tlr1 (Meijer et al., 2004). These studies highlight the interspecies diversification of TLR family proteins but also indicate a high

conservation of TLR function between mammals and teleost. Nearly all TLRs described in mammals have been identified as orthologs or as TLRs with similar functions in fish.

1.3.2. Toll Like Receptors family signaling; a target for Gold and Palladium nanoparticles?

The internalization of Gold and Palladium nanoparticles induced a pro-inflammatory response in macrophages which was reminiscent of the typical pattern of TLR mediated mechanisms; increased tnf-α. il-6, il1-β and il-8 secretion. This strongly suggests that Gold and Palladium nanoparticles activate TLR signaling. Indeed, in one study, peptide conjugated Gold nanoparticles were identified to mediate its effects through tlr4 signaling *in vivo* (Bastus et al., 2009a). The knockout of tlr4 activity in mice abolished peptide conjugated gold nanoparticle mediated activation of macrophages (Bastus et al., 2009a). Studies have shown that metallic compounds like nickel and cobalt ions activate tlr4 by directly interacting with conserved histidine residue exposed at the dimerization interface of opposing tlr4 monomers (Schmidt and Goebeler, 2015). These interactions trigger the formation of tetrameric tlr4 and md2 complexes that initiate downstream NF-κB activation and *tnf-α*, *il-8* and *il-6* secretion in macrophages (Schmidt and Goebeler, 2015). Monoclonal anti-tlr4 antibody inhibition of tlr4 activity impaired cobalt mediate increase in pro-inflammatory il-8 expression (Lawrence et al., 2016). Since Palladium metal is a close neighbor of cobalt and nickel in the periodic table, it also has been demonstrated to interact with tlr4. The stimulatory capacity of Palladium to activate tlr4 was confirmed *in vitro* in one study (Rachmawati et al., 2013). Palladium induced the secretion of il-8 in tlr4/md2 transfected HEK293 cell line and not in wild type, non-transfected HEK293 cells (Rachmawati et al., 2013). Overall, there is strong evidence in support of the view that Gold and Palladium induce macrophage polarization via tlr4 activation.

1.4. Zebrafish model system

1.4.1. Advantages of the zebrafish model system.

The zebrafish represents a powerful model system for investigating cellular and molecular events in vivo. The utility of the zebrafish model for live imaging innate immune cells and investigating intimate interactions between host and pathogens has been extensively reviewed (Meijer et al., 2014, Harvie and Huttenlocher, 2015). The zebrafish model represents a viable alternative to mammalian models as they are easier and less expensive to house and care for. The genetic amenability and large sample size of the zebrafish model system makes it advantageous to study cancer through forward and reverse genetic approaches (Mione and Trede, 2010, White et al., 2013). The zebrafish larvae are optically transparent and develop externally which allows the use of in vivo live image techniques to track the consequences of genetic manipulation or chemical treatment (Garcia et al., 2016). By combining the advantages of optical transparency and the large availability of genetic tools, the zebrafish model system has the potential to significantly extend our understanding of the inflammatory response associated with infectious diseases.

A key issue with any translational model, such as zebrafish, is identifying which biological interactions are conserved when compared to humans. Humans and zebrafish share many anatomical and physiological features due to a shared evolutionary ancestor (Garcia et al., 2016). In the brain, the neurotransmitter structure and systems such as GABA, serotonin, noradrenaline, histamine and acetylcholine in the zebrafish brain are well conserved and share many features with humans (Schmidt et al., 2013). In addition, many of the broad structures of the human brain have homologous structures identified in the zebrafish brain; cerebellum, telencephalon, diencephalon and spinal cord (Schmidt et al., 2013, Garcia et al., 2016). At the biochemical and genetic level, the zebrafish share 70% of human genes and at least one zebrafish orthologue has been identified in 82% of human disease related genes (Howe et al., 2013). However, due to a genome duplication event during the evolution of the zebrafish, 15% of the human genes have several additional orthologs (Howe et al., 2013).

1.4.2. Development of zebrafish immune system

Temporal-spatial resolved fate mapping analysis revealed that the development of zebrafish immune system occurred in successive waves originating from anatomically distinct locations (Xu et al., 2012, Bertrand et al., 2007). During zebrafish development, the first wave of haematopoiesis initiates at 11 hours post fertilisation (hpf) from the posterior lateral mesoderm and the rostral blood island (Gore et al., 2018). Cells from the posterior lateral mesoderm contribute to embryonic erythrocytes vital for the survival of the embryo (Xu et al., 2012). In contrast, cells from the rostral blood island give rise to myeloid cells that differentiates into early innate immune cells such as macrophages and neutrophils (Xu et al., 2015). The second definitive wave originating from the ventral wall of dorsal aorta at 26-28 hpf produces hematopoietic stem cells capable of differentiating into all mature erythroid and myeloid lineage cells in the larvae and adult zebrafish (Xu et al., 2015, Xu et al., 2012). Finally a third or intermediate wave at 30 hpf originating from the posterior blood island give rise to hematopoietic stem and progenitor cells responsible for myeloid and erythroid cells (Xu et al., 2015, Bertrand et al., 2007). In line with zebrafish haematopoiesis, the development of embryonic microglia was observed to originate from the rostral blood island whereas mature adult microglia originated from the ventral dorsal wall of aorta (Xu et al., 2015, Ferrero et al., 2018). Xu et al., showed that primitive microglia formation was PU.1 dependent and runx1 independent while mature adult microglia were runx1 dependent. The maturation of hematopoietic stem and progenitor cells seeds the caudal hematopoietic tissue (CHT), thymus and kidney marrow (Gore et al., 2018). The CHT serves as a source of embryonic macrophages, neutrophils and monocytes while the kidney, as in mammalian counterparts, provides a niche for hematopoietic stem and progenitor cells (Gore et al., 2018). Finally, the thymus serve to generate mature lymphoid T cells during adulthood (Langenau et al., 2004, Gore et al., 2018). The development of zebrafish immunity is unique in the sense that the innate and adaptive immune system are temporally separated. The zebrafish larvae only survives with the innate immune system up to 4 to 6 weeks post fertilisation (Novoa and Figueras, 2012). At 4 to 6 weeks post fertilisation,

the adaptive immune system becomes mature where lymphocytes become functional (Novoa and Figueras, 2012, Lieschke and Currie, 2007, Davidson and Zon, 2004). Intriguingly, a recent study challenged the biphasic nature of the innate and adaptive immune system. Tian et al., indicated that the first wave of haematopoiesis may also give rise to a larval population of T cells (Tian et al., 2017). The function of these early T cell population was unknown but was speculated to play an immune-repressive function (Tian et al., 2017). Nonetheless, it is still widely accepted that the adaptive immune system does not become functional until approximate 4 weeks post fertilisation (Novoa and Figueras, 2012, Lieschke and Currie, 2007, Davidson and Zon, 2004). Therefore, the temporal separation makes it advantageous to study vertebrate innate immune responses in vivo independently from the adaptive immune response (Hamilton et al., 2016, Tsarouchas et al., 2018, Li et al., 2017, Novoa and Figueras, 2012, Renshaw et al., 2007).

1.4.3. The zebrafish as an established model system to study cancer biology

The zebrafish has been proven to be an excellent tool in advancing our understanding of cancer biology. Zebrafish have been used in many studies to recapitulate tumours to investigate cellular and molecular signals governing tumorigenesis (Jung et al., 2013, Chia et al., 2018, Mayrhofer et al., 2017, Ju et al., 2014). The earliest application of zebrafish as tumour models were developed using a range of carcinogenic compounds. Fish treated with N-methyl-N'-nitro-M-nitrosoguanidine (MNNG) develop a variety of mesenchymal neoplasms (Spitsbergen et al., 2000b). While other studies have also used 7,12-dimethylbenz(a)anthracene (DMBA) and ethylnitrosourea (ENU) to induce tumour formation in zebrafish (Spitsbergen et al., 2000a, Beckwith et al., 2000). Many of the oncogenes and tumour suppressor genes found in mice and humans are conserved in fish, these include myc, ras, notch family members, p53, mdm2, pten and bcl-2 (Gutierrez et al., 2011, Langenau et al., 2003, den Hertog, 2016, Langheinrich et al., 2002, Schreiber-Agus et al., 1993, Berghmans et al., 2005). Conservation of these genes are crucial for the translational application of key findings from zebrafish to humans.

The genetic amenability of zebrafish allows the generation of transgenic tumour-bearing fish that serves as a platform for drug and genetic screens. Earlier transgenic models of T cell acute lymphoblastic leukaemia were generated by expressing mouse c-myc under the control of zebrafish Rag2 promoter and have been extensively used to model lymphoblastic leukemia (Langenau et al., 2003, Langenau et al., 2005, Gutierrez et al., 2011, Borga et al., 2019). Transgene overexpression of Akt1 and $HRAS^{V12}$ signalling have also been used to induced glioma formation in zebrafish (Jung et al., 2013, Mayrhofer et al., 2017). Moreover, the overexpression of these oncogenes led to the development of brain tumours resembling gliomas (Jung et al., 2013, Mayrhofer et al., 2017).

The zebrafish is also frequently used in xenotransplantation assays (Eden et al., 2015, Welker et al., 2016). The combination of xenotransplantation, *in vivo* imaging and ability of the fish to absorb chemical compound from the water make the zebrafish model an ideal platform to conduct drug screens (Eden et al., 2015, Welker et al., 2016). We have previously shown

in an orthotopic transplantation GBM zebrafish model that microglia and macrophages performed pro-tumoural activities (Hamilton et al., 2016). The ablation of tumour promoting microglia/macrophage by genetic and pharmacological means inhibited tumour growth (Hamilton et al., 2016). Other studies have shown that implanted mouse brain tumours cells were viable in zebrafish and that transplanted cells developed into tumours that recapitulate the histology of parent tumour (Eden et al., 2015). Eden et al., demonstrated the utility of the zebrafish model for pre-clinical drug testing as tumours in zebrafish responded to chemotherapeutic agents (Eden et al., 2015). Furthermore, zebrafish larvae xenotransplantation assays were observed to constitute highly sensitive differential therapy responses to different chemotherapeutic agents (Fior et al., 2017). This highlighted the significance of cancer xenotransplantation zebrafish models as a pre-clinical chemosensitive profiler to access drug toxicity for precision medicine (Fior et al., 2017). More recent advancement in xenotransplantation methodology included the utility of genetically immunocompromised zebrafish (Yan et al., 2019). The generation of *prkdc* (protein kinase DNA-activated catalytic polypeptide and *il2rga* (interleukin-2 receptor gamma a) mutant zebrafish, lacking T, B and NK cells, extended the capabilities of zebrafish xenotransplantation models into adult zebrafish without the need of dexamethasone treatment (Yan et al., 2019). Taken together, the zebrafish model system have significant advantages as a model organism to investigate cancer biology *in vivo*.

1.4.4. Inducible transgenic expression of transgenes in zebrafish

The Tol2 transgenesis method has been applied in many studies to generate transgenic zebrafish that express fluorescent proteins in specific tissue and organs (Ellett et al., 2011, Ballim et al., 2019). In addition, the Tol2 system has been shown to mediate reliable genetic expression of transgenes under a variety of regulatory elements. Heat shock promoters (hsp70l) have been used to temporally and spatially control gene expression (Venero Galanternik et al., 2016, Shoji and Sato-Maeda, 2008). One of the advantages of the zebrafish model is the zebrafish's ability to readily absorb compounds through the water (Garcia et al., 2016). This allows the utility of chemical-inducible techniques to temporally control gene expression. Unlike conventional promoters, chemical inducible expression allows temporal control of genes, where early expression during development causes fatal or severely dysmorphic effects and, as a result, precludes the possible role of the gene of interest at later stages (Watanabe et al., 2007). The mifepristone inducible LexPR system is a hormone-response transcriptional activator that confers accurate spatiotemporal control of transgene expression (Emelyanov and Parinov, 2008). This system utilises a hybrid transcription factor (LexPR) engineered by fusion of the DNA binding domain of the bacterial LexA repressor, a truncated ligand-binding domain of the human progesterone receptor, and the activation domain of the human NF- κB/p65 protein (Emelyanov and Parinov, 2008). The hybrid transcription factor (LexPR) is activated when bound to mifepristone and induces genetic expression of a gene of interest placed under the control of a synthetic operator-promoter sequence (LexOP) (Emelyanov and Parinov, 2008). This system has been shown to conditionally control the expression of oncogenic kras(V12) in zebrafish (Nguyen et al., 2016, Emelyanov and Parinov, 2008). The versatility in inducible transgene expression systems extends the available transgenic tool kit to allow the study of gene function at various stages of development.

1.4.5. CRISPR/Cas9 mediated mutagenesis

The advent of clustered regularly interspaced short palindromic repeats (CRISPR) and CRISPR associated protein (Cas)9 genome modification has now made it easy to routinely and efficiently generate stable mutant organisms. The precise modification of specific genetic sites is a standard approach to study gene function and generate stable mutants (Wu et al., 2019, Ma et al., 2014). The ability to precisely alter gene function has significant therapeutic applications in nanomedicines to control cancers and treat genetic diseases such as cystic fibrosis (Jiang et al., 2019, Wu et al., 2015).

The CRISPR/Cas9 system originates from the immune system of prokaryotes under infection. A fragment of the infecting phage is taken up and integrated into the CRISPR motif that is transcribed into CRISPR RNA (crRNA) and trans-activating crRNA (tracRNA) (Wu et al., 2019, Ma et al., 2014). crRNA and tracRNA interact to form a crRNA/tracRNA duplex that directs the Cas9 protein to the matching sequence of the invading phage to introduce double strand breaks (Wu et al., 2019, Ma et al., 2014). Researchers exploit this system by introducing custom crRNA and tracrRNA and fusing them into a single guide RNA (sgRNA) in order to direct the Cas9 to a specific sequence in the genome (Wu et al., 2019, Ma et al., 2014). The custom sgRNA should contain a 20 nucleotide long sequence that is homologous to the target site followed by a protospacer adjacent motif (PAM) sequence (Wu et al., 2019). The PAM site is required for target site recognition. These engineered nucleases direct double strand breaks at the targeted genome locus which activates error prone nonhomologous end joining (NHEJ) or homology directed repair (HDR) (Ma et al., 2014, Wu et al., 2019). Error prone NHEJ induces frame shift mutations due to insertions-deletions (Indel) at the target site (Wu et al., 2019). These short frame shift indels in the exonic sequences introduce premature stop codons that are recognised and degraded by the nonsense mediated mRNA decay mechanisms or are translated into truncated non-functional proteins (Hu and Ng, 2012). In contrast, precise

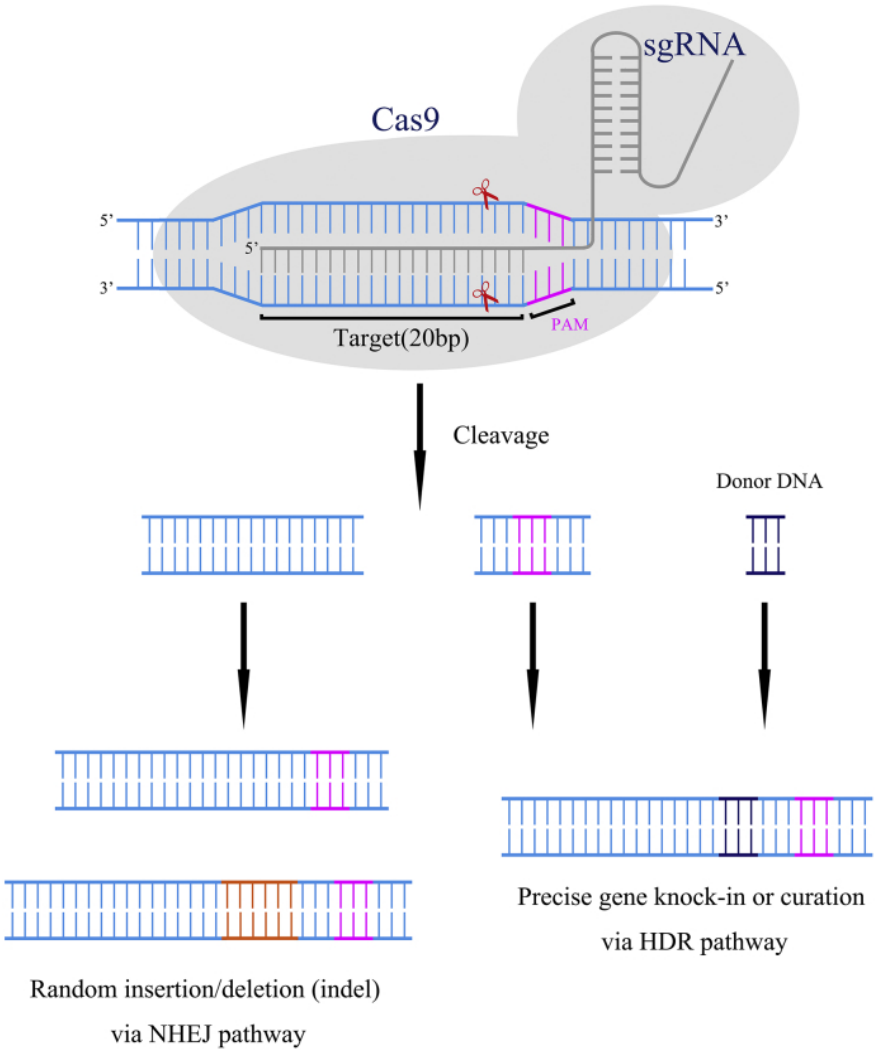

Figure 4. Mechanisms of the CRISPR-Cas9 targeting system.

The fusion of crRNA and tracrRNA into a single guide RNA (sgRNA) directs the Cas9 to a specific target sequence in the genome. These engineered nucleases direct double strand breaks three base pairs from protospacer adjacent motif (PAM) sequence. Double strand breaks at the targeted genome locus activates DNA repair machinery that facilitates error prone nonhomologous end joining (NHEJ) or homology directed repair (HDR). Error prone NHEJ induces frame shift mutations due to insertions or deletions (indel) at the target site. While on the other hand, precise gene knock-in can be achieved by co-injecting with single-strand oligodeoxynucleotides or double strand DNA (Wu et al. 2019)

Image adapted from (Wu et al. 2019)

gene knock-in can be achieved by co-injecting with single-strand oligodeoxynucleotides or double strand DNA as a donor for HDR (Wu et al., 2019) (Figure 4).

The CRISPR/Cas9 system is versatile as multiple modifications can be introduced by providing multiple sgRNA, making it possible to simultaneous modify multiple genes in the

organism. Up to five genes have been modified simultaneously using the CRISPR/Cas9 system in mice with an efficiency of 75% (Zhou et al., 2014). The high efficiency of CRISPR/Cas9 system represents a rapid genome editing technique that allowed for the rapid establishment of clinical relevant disease model in zebrafish through the generation of transient loss of function animals (Crispants) (Naert and Vleminckx, 2018, Trubiroha et al., 2018). The generation of crispants forgoes the requirement of time-consuming genetic screening methodologies in order to generate stable transgenic mutant lines. However, one major limitation that limits CRISPR/Cas9 clinical application is off target effects. Mismatches in the sgRNA sequences may guide the Cas9 complex to sites of similar sequences and introduce off target mutations (Fu et al., 2013). Off target sites were identified to harbour up to five base pair mismatches that induced mutations comparable to those of intended target (Fu et al., 2013). Nonetheless, due to its simplicity, low cost, and high efficiency, the CRISPR/Cas9 system is widely used in many organisms to create loss of function alleles to study gene function in bacteria, rodents, zebrafish and human cells (Wu et al., 2015, Ma et al., 2014, Zhou et al., 2014, Tsarouchas et al., 2018).

1.5. Statement of Aims

The aim of my PhD was to test the capability of Pd and Au for targeted drug delivery in a GBM model in the zebrafish using Gold and Palladium nanoparticles solidly supported on a polystyrene matrix (beads). We used a human glioblastoma (U87) xenotransplantation zebrafish model, previously established (Hamilton et al., 2016), as a platform to develop bioorthogonal chemotherapeutic drug screening assay.

Over the course to the experiment, the aim of my PhD shifted to investigate the anti-tumour properties initiated by Palladium and Gold bead implantation. This included investigating the mechanisms involved in anti-tumour effects of Palladium and Gold and identifying genetic candidates that induced macrophage polarisation. To achieve these goals, the following aims were addressed:

1. To develop a bioorthogonal chemotherapeutic drug screen platform in the zebrafish brain using Palladium and Gold nanoparticles solidly supported on a polystyrene matrix (beads).
    - To achieve this aim, the catalytic activity of Palladium and Gold bead will be evaluated in the zebrafish brain.

2. To investigate the associated anti-tumour effects of Palladium and Gold bead implantation.

    - To achieve this aim, the effects of Palladium and Gold bead implantation on U87 cell survival, U87 cell fragmentation and macrophage number were evaluated. In order to investigate if macrophage function contributed to the anti-tumour effects, bead induced anti-tumour activity was investigated in a macrophage null zebrafish. We also investigated the effects on necrosis using propidium iodide staining in the zebrafish brain.

3. To identify the intracellular signalling mediators of Palladium and Gold bead induced anti-tumour effects in macrophages.

    - To achieve this aim, we isolated macrophages from Palladium bead implanted, U87 xenografted and Bead null zebrafish and conducted next generation RNA sequencing.

4. To investigate if TLR signalling play a key role in mediating the anti-tumour effects of Palladium and Gold bead implanted zebrafish.

    - To achieve this aim we conducted *in vivo* experiments to establish if the pharmacological inhibition of TLR signalling would promote U87 cell survival.

5. To investigate the role of tnf-α and cxcl8b.1 in mediating the anti-tumour responses of macrophages and neutrophils in the zebrafish brain.

    - The role of tnf-α and cxcl8b.1 in mediating anti-tumour responses of macrophages will be investigate using CRISPR/Cas9 crispants and Tol2 mediated overexpression transgenesis assays.

2. Material and Methods

2.1. U87-nls-mKate2 cell culture

2.1.1. Cell Culture Reagents

Reagent Name	Composition and Final Concentration
DMEM (ThermoFisher Scientific, Loughborough, UK)	Dulbecco's modified Eagle's medium (DMEM) containing 1% L-glutamine 10% (v/v) fetal calf serum.
Penicillin/Streptomycin (ThermoFisher Scientific, Loughborough, UK)	100 mg/ml penicillin and 100 mg/ml streptomycin
Fetal Calf Serum (ThermoFisher Scientific, Loughborough, UK)	Fetal Calf Serum
1X Phosphate Buffer Saline (Sigma Aldrich, Dorset, UK)	137 mM NaCl, 2.7 mM KCl, 10 mM Na_2HPO_4, 1.8 mM KH_2PO_4, pH 7.4.
EDTA (ThermoFisher Scientific, Loughborough, UK)	0.5 M EDTA (ThermoFisher Scientific, Loughborough, UK) suspended in 1X PBS
Accutase (ThermoFisher Scientific, Loughborough, UK)	1X Accutase in Dulbecco's PBS containing 0.5 mM EDTA and 3 mg/L Phenol Red
Polybrene (ThermoFisher Scientific, Loughborough, UK)	10 mg/ml polybrene

2.1.2. U87 cell culture

Human U87MG glioblastoma cells were kindly provided by Prof Tobias Pukrop (University Hospital Regensburg, Germany). U87 cells originated from the American Type Culture Collection (Manassas ,VA, USA) and were cultured in DMEM containing 1% L-glutamine, 1% (v/v) Penicillin/Streptomycin supplemented with 10% (v/v) fetal calf serum (FCS). U87 cells were incubated at the standard conditions of 100% humidity, 95% air and 5% CO_2.

2.1.3. Thawing of cells from liquid nitrogen storage

U87 cells were thawed at 37°C using a water bath after being removed from liquid nitrogen. The cells were mixed with 8 ml DMEM containing 1% L-glutamine, 1% (v/v) Penicillin/Streptomycin supplemented with 10% (v/v) FCS and centrifuged at 200 g for 3 minutes. The supernatant was removed and cells resuspended in 10 ml DMEM medium and seeded into 25 cm^2 cell culture flasks.

2.1.4. Freezing of U87 cells into liquid nitrogen

U87 cells cultured on cell culture flasks were lifted using 2 ml 1X Accutase solution and incubated at 37°C for 5 minutes. Cells were dissociated by agitation and 8 ml DMEM medium was added. The cell suspension was centrifuged at 200 g for 3 minutes. The supernatant was removed and U87 cells were resuspended in 3 ml FCS containing 10% dimethyl sulfoxide (DMSO). Cell suspension with FCS was aliquoted in 1 ml volumes into screw top 1.8 ml Nunc CryoTube™ vials (Sigma Aldrich, Dorset, UK). The tubes were frozen in polystyrene boxes at -80°C and then transferred to liquid nitrogen storage at -150°C.

2.1.5. Lentiviral transduction of human glioblastoma cell lines

U87MG glioblastoma cells (4.5×10^5) cell were seeded into a 60 mm dish in a final volume of 5 ml DMEM for four hours at standard conditions of 100% humidity and 5% CO_2 at 37°C in DMEM containing 1% L-glutamine, 1% (v/v) Penicillin/Steptomycin supplemented with 10% (v/v) fetal calf serum. In order to increase transduction efficiency, the cells were incubated in 5 mM polybrene for 10 minutes. The Lv-cppt-IRES-NLS-mKate2-opre viral vector was generated by Pam Brown (shared university research facilities (SuRF), the University of Edinburgh, UK). A SV40 nuclear localizing signal sequence coding for Pro-Lys-Lys-Lys-Arg-Lys-Val was cloned into the N-terminus of the protein leading to the nuclear transport of the fused nls-mKate2 fluorescent protein monomer (Kalderon et al., 1984). A multiplicity of infection (MOI) of ten viral vectors to infection targets was added to the existing media for a period of 48 hours. The transformed cells were then washed with 5 ml 1X PBS and lifted using 1 ml 2.5 mM EDTA-PBS at 37°C and washed twice in 10 ml DMEM; cells were centrifuged

for 3 minutes at 200 g between washes. The resulting cell pellet was re-suspended in 10 ml DMEM and a 1:5 split of the transduced U87 cell population (U87-nls-mKate2) was plated into a T75 cell culture flask.

2.1.6. Routine culture of U87-nls-mKate2 human glioblastoma cell line for xenografts

U87-nls-mKate2 cells were initially cultured at standard conditions of 100% humidity and 5% CO_2 at 37°C in DMEM. The cultured U87-nls-mKate2 were then incubated at 34°C for a 2 week equilibration period. One of the limiting factor in xenotransplantation was the temperature. Zebrafish were routinely maintained at 28°C which differed by nine degrees from that of standard cell culture temperature for U87 cells (37°C). As a compromise solution, to optimize the temperature for U87 cell proliferation and zebrafish survival, an incubation temperature of 34°C was chosen. Thus all cell culture procedures following the 2 weeks equilibration period was conducted at 34°C to allow habituation of the cells at the same temperature as the zebrafish (34°C). The cells were passaged when approximately 80% confluent. First, the cells were washed once with 10 ml 1X PBS and incubated in 2 ml 1X Accutase. Cells were dissociated by agitation and the Accutase inactivated by adding 8 ml DMEM medium. Cells were pelleted at 200 g for 3 minutes and passaged into a 75 cm^2 cell cultured flask at a 1:10 ratio with 20 ml DMEM medium.

2.1.7. U87-nls-mKate cell preparation for xenografts

Cells were harvested on the same day as xenograft experiments. U87-nls-mKate2 cells were washed with 10 ml 1X PBS followed by an 8 minute incubation in 2 ml 2.5 mM EDTA-PBS. DMEM (8 ml) was added to the cell suspension and centrifuged for 3 minutes at 200 g. Cell pellet was washed in 10 ml DMEM and centrifuged for 3 minutes at 200 g. The resulting cellular pellet was supplemented with 1:10 (v/v) phenol red and immediately used for xenografting experiments.

2.1.8. U87-nls-mKate2 cell preparation for fluorescent activated cell sorting (FACS)

U87-nls-mKate2 cells cultured in T75 flasks were dissociated from the surface of the flask using 2 ml Accutase after a 10 ml 1X PBS wash. The cell suspension was spun down at 200 g for 3 minutes then resuspended in 2% FCS/DMEM medium at a density of 7.5 million cells/ml. All procedures were conducted at room temp.

2.2. Zebrafish Husbandry and In-vivo experiments

2.2.1. Zebrafish Husbandry

Zebrafish were housed in a purposed built zebrafish facility in the Queen's Medical Research Institute (QMRI, the University of Edinburgh, UK) maintained by the University of Edinburgh Biological Resources. All adult zebrafish were kept at 28°C on a 14 hours light/10 hours dark photoperiod. All zebrafish embryos were obtained through pair mating conducted in the facility. Animal experimentation was approved by the home office (PPL P5042DEFB) in accordance with the Animals (Scientific Procedure) Act 1986. Zebrafish embryos were treated with 140 μM 1-phenyl 2-thiourea (PTU) in E3 embryo media (6.4 mM KCl, 0.22 mM NaCl, 0.33 mM $CaCl_2$ $2H_2O$, 0.33 mM $MgSO_4$ $7H_2O$) continuously to inhibit pigmentation. Zebrafish embryo were house in no more than 50 embryos in 50 ml E3 in 9 cm^2 petri dishes. During experimentation, zebrafish embryos were housed individually in 12 well plates in 1 ml E3 containing 140 μM PTU.

2.2.2. Transgenic Zebrafish Lines

Tg(mpeg1:EGFP) zebrafish were generated by cloning the 1.86 kb mpeg upstream sequence in front of EGFP. Tol2 mRNA and the tol2-flanked *Tg(mpeg1:EGFP)* construct were co-injected into the AB wildtype zebrafish embryos at the single cell stage. Germ line transmission of the transgene was screened for by outcrossing to the AB strain. The mpeg1 promoter, a macrophage lineage promoter sequence, expressed EGFP fluorescent protein in macrophages and microglia. *Tg(mpeg1:eGFP)* zebrafish were used to visualise macrophages

in vivo and have been used to study a diverse range of macrophage related processes (Ellett et al., 2011, Rougeot et al., 2019).

Tg(mpeg1:EGFP:mpeg1:Kal4/UAS:nls-E2-Crimson) were generated by co injecting Tol2 mRNA and the tol2-flanked *Tg(*mpeg1:Kal4/UAS:nls-E2-Crimson*)* construct into mpeg1:eGFP embryo at the single cell stage. mpeg1:Kal4/UAS:nls-E2-Crimson construct contained the mpeg1 promoter in addition to Kal4/UAS transcriptional activator system and a zebrafish nuclear localisation signal fused to the N-terminal of E2-Crimson. Double transgene germ line transmission was confirmed by outcrossing to the AB strain. The mpeg1 promoter drove the expression of cytoplasmic EGFP and nuclear E2-Crimson in macrophages.

Tg(mpo:EGFP), may also be known as Tg(mpx:GFP) was generated by BAC transgenesis (Renshaw et al., 2006). EGFP with an SV40 polyadenylation site (Clontexh, Palo Alto, CA) was inserted at the *mpo* ATG start site. The myeloperoxidase (MPO) enzyme is a neutrophil specific granule protein. Thus the *mpo* promoter was used to drive EGFP in neutrophils.

2.2.3. Zebrafish screening of fluorescent proteins

All zebrafish larvae between 3 to 5 days post fertilization (dpf) used for the experiments were first screened for the expression of transgene using a Leica MZ16FA optical fluorescence microscope (Leica, Houston, USA). Zebrafish larvae were anaesthetised in 2.5mM tricaine in E3 medium and screened for the highest level of expression of the fluorescent protein of interest. Zebrafish expressing the highest level of fluorescence intensity in the brain were selected for further experimentation.

2.2.4. Zebrafish Larvae imaging

Time lapse and still images were acquired using an Andor spinning disk confocal microscope (Oxford Instruments, Belfast) with a 20X/NA 0.75 Olympus air objective lens . The zebrafish were anaesthetised with 2.5 mM tricaine in E3 medium, immobilized in 1.5% low

melting point agarose in E3 medium on a 35 mm glass bottom MatTex petri dish (MatTek, Ashland, USA), and submerged in E3 medium containing 2.5 mM tricaine. Green (GFP), mCherry and E2-Crimson fluorescent proteins were excited using 488 nm, 561 nm and 561 nm wavelength lasers respectively . The emission spectrums were reflected through a Semrock quad multi-band filter (IDEX Health and Science, LLC, Rochester, USA) depending on the excitation wavelength. Laser exposure and intensity was calibrated for each experiment to obtain best possible image resolution at the same time minimising exposure of the samples to the laser. The filtered emitted spectrum was detected using a TuCam multi wavelength imaging camera (Oxford Instruments, Belfast, UK) with image gain set at 50 for all acquisitions. Acquired Z stacks were set accordingly to encompass all regions of interest within the zebrafish brain.

2.2.5. Palladium, Gold and Naked bead preparation

Palladium, Gold and Naked beads were kindly provided by collaborators (Unciti-Broceta's Lab, Edinburgh Cancer Research Centre, IGMM). Solidly supported Gold (Perez-Lopez et al., 2017) and Palladium (Weiss et al., 2014a) nanoparticles were prepared within a polystyrene matrix of 75 microns in diameter. Palladium (5 nm) and Gold (30nm) nanoparticles were uniformly distributed across the polystyrene matrix. Non-functionalised resin (Naked bead) were untreated and represented the precursors used for Palladium and Gold bead synthesis.

2.2.6. Zebrafish xenografts and bead implantation

mpeg1:EGFP and mpo:EGFP zebrafish (3 days post fertilised (dpf)) were anaesthetised with 2.5 mM tricaine and immobilised in 1.5% low melting point agarose in E3 medium. The frontal-dorsal section of the zebrafish head was carefully exposed from the agarose (Figure 5, A1-A2). Cell suspension (10 µl) were loaded into borosilicate glass capillary needles (1 mm O.D x 0.78 mm I.D.; Harvard Aparatus) using a microloader tip and the ends broken using a micro

forceps to expose a sharp tip. The left optic tectum of the zebrafish larvae (3 dpf) were xenografted with U87-nls-mKate2 cells (n = 40-100) using a Femtojet micro-injector (Eppendorf, Hamburg, Germany) (Figure 5, B1 - B4). After cell transplantation, the zebrafish larvae were liberated from the agarose and maintained in E3 medium containing 140 µM PTU at 34 °C for a period of 24 hours before bead implantation.

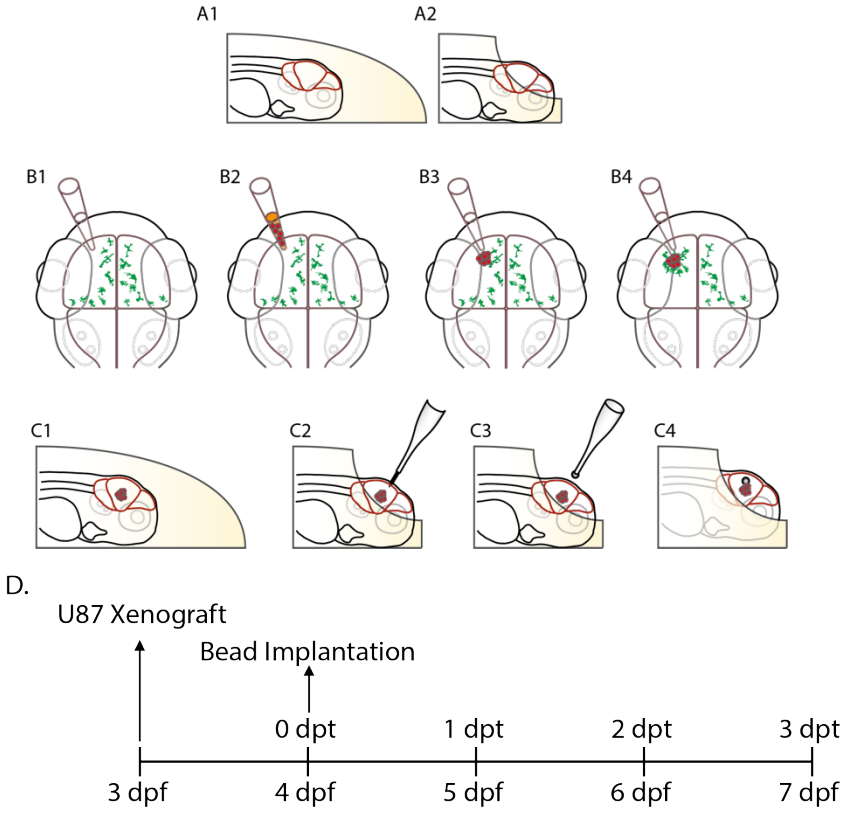

Figure 5. Schematic diagram of zebrafish U87-nls-mKate2 xenograft and bead implantation.

(A1) Zebrafish larvae (3-4 dpf) anaesthetised in 2.5 mM tricaine were immobilised in 1.5% low melting point agarose in E3 medium and submerged in E3 medium.

(A2) The frontal dorsal section of the zebrafish brain was exposed from the agarose allowing access to the brain.

(B1-B4) U87-nls-mKate2 human glioblastoma cell lines were loaded into borosilicate glass capillaries and the ends broken to expose a sharp tip. The needle was inserted into the left optic tectum of the zebrafish brain (3 dpf) and U87-nls-mKate2 cells were xenografted into the brain using a Femtojet micro-injector. A 24 hour recovery period followed xenografting prior to bead implantation.

(C1) Zebrafish larvae (4 dpf) were remounted in 1.5% low melting point agarose in E3 and submerged in E3 medium .

(C2) The dorsal frontal section of the head was exposed. A small incision was then made on the medial dorsal frontal section of the zebrafish head, between both optic tectums, using an ophthalmic scalpel mounted on a micro-manipulator.

(C3 and C4) Using a borosilicate glass capillary with negative pressure palladium/gold/naked beads were manipulated into position above the incision and were inserted into the zebrafish brain (4 dpf). The negative pressure was released and the glass capillary was extracted.

(D) Zebrafish larvae were xenografted with U87-nls-mKate2 cells at 3 dpf. Bead implantation procedure occurred at 4 dpf. At 0 days post bead transplantation (dpt), U87 xenografted zebrafish were utilised for experiments.

On the day of bead implantation, 4 dpf mpeg1:EGFP or mpo:EGFP zebrafish larvae were anaesthetised in 2.5 mM tricaine in E3 medium and immobilised in 1.5% low melting point agarose in E3 medium. The frontal dorsal section of the zebrafish head was exposed from the agarose to facilitate bead implantation (Figure 5, C1-C4). A small incision was made on the medial dorsal frontal section of the zebrafish head, between both optic tectums, using an ophthalmic scalpel (PFM medical, Germany) mounted on a micro-manipulator as shown in Figure 5, C2. Following incision, the gold/naked/palladium bead was carefully moved into position above the incision site and the bead was surgically placed between both hemispheres of the optic tectum (Figure 5, C3 - C4). To replicate an implantation injury, a Naked bead was implanted and immediately removed. A negative pressure was created between the bead and the needle using tubing connected to 10 ml Eccentric luer slip tip syringe (BD Plastipak, Franklin Lakes, USA) to allow for careful manipulation of bead. After bead implantation, the zebrafish larvae (4 dpf/0 dpt) were liberated from the agarose and remounted in 1.5% low melting point agarose in E3 for imaging.

2.2.7. Zebrafish Gold bead in-vivo catalytic assays

To investigate the chemical capabilities of gold as a catalyst to mediate prodrug activation, we studied gold bead's catalytic properties to convert nonfluorescent precursor into fluorescent Rhodamine *in-vivo*. The lipophilic properties of prodye precursor allowed diffusion of the reagent in the media via ingestion or absorption via the skin and distributed systemically (Perez-Lopez et al., 2017). Under physiological conditions the prodye precursor is catalytically

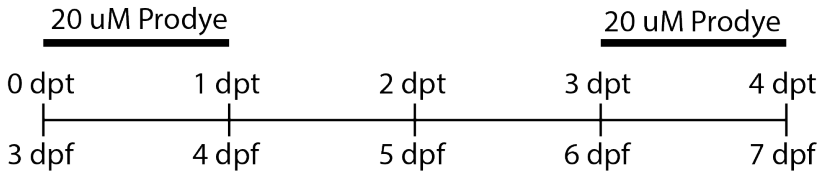

Figure 6. Pulse treatment of Au bead implanted zebrafish with 20 µM Pro-dye

Pulse treatment of Au bead implanted zebrafish occurred from 0 days post transplantation (dpt) to 1 dpt at an age of 3 days post fertilisation (dpf) to 4 dpf. Prodye (20 µM) was added to the E3 medium with 1% DMSO. In between pulse treatment, the zebrafish was washed in E3 and incubated in fresh E3 containing 140 µM PTU without prodye or DMSO. Pulse treatment of the zebrafish with 20 µM prodye resumed from 3 dpt to 4 dpt or 6 dpf to 7 dpf.

converted by the gold bead into fluorescent Rhodamine which was visible under excitation by 488 nm wavelength laser (Perez-Lopez et al., 2017). This study was the first time that biorthogonal organometallic reaction was tested locally in an *in-vivo* system in the zebrafish brain. Nonfluorescent prodye (10 mM) suspended in DMSO was kindly provided by Unciti-Broceta lab (Cancer Research UK Edinburgh Center, Edinburgh, UK). Wild type (WIK) zebrafish embryos (3 dpf) were each implanted with a Gold coated resin bead (Au beads). The experiment comprised four groups: (1) Wild type zebrafish implanted with Au beads and continuously treated with 20 µM prodye in 1% DMSO (3 dpf – 7 dpf) (2) Zebrafish implanted with Au beads pulsed with 20 µM prodye in 1% DMSO. Pulse treatment of Au bead implanted zebrafish occurred from 0 days post transplantation (dpt) to 1 dpt and at 3 dpt to 4 dpt (Figure 6). Zebrafish embryos were wash with E3 containing 140 µM PTU in between pulse treatments. (3) A negative control where zebrafish without gold beads were pulsed with 20 µM prodye in 1% DMSO from 0 days post transplantation (dpt) to 1 dpt and at 3 dpt to 4 dpt (Figure 6). (4) A background control where zebrafish transplanted with Au beads and were not treated with prodye. Zebrafish were imaged at 1 day post transplant (dpt), 3 dpt and 4 dpt and analysed using Imaris (Bitplane, Zurich, Switzerland) and p values calculated using two tailed unpaired student t-test.

2.2.8. Zebrafish Propidium Iodide assays

Wild type (WIK) zebrafish (3 dpf) were incubated with 1 mg/ml Propidium iodide (BD Biosciences, Wokingham Berkshire, UK) and 1% DMSO in E3 medium containing 140 uM PTU at 34°C 20 minutes before imaging. There were three conditions for this assay: (1) WIK zebrafish without bead (2) WIK zebrafish implanted with Naked bead (3) WIK zebrafish with Gold bead. Zebrafish were imaged at 0 dpt, 1 dpt and 3 dpt using the spinning disk confocal microscope excited using the 488 nm laser. Zebrafish larvae were incubated in 1 mg/ml Propidium iodide for the duration of the experiment.

2.2.9. IRAK-4-IN-1 inhibitor treatment

For qPCR studies, a total of 200 mpeg1:EGFP embryos (4 dpf) were treated with 10 µM IRAK4-IN-1 inhibitor (MedChemExpress LLC, New Jersey, USA) and 1% DMSO in E3 medium containing 140 uM PTU for a period of 24 hours in a 9 cm^2 petri dish incubated at 34°C. At 5 dpf, the zebrafish were anesthetised with 2.5 mM tricaine in E3 medium and washed in 50 ml 4°C E3 media containing 140 uM PTU and 2.5 mM tricaine. Anesthetised embryos were then incubated in 50 ml 4°C E3 media containing 140 uM PTU and 2.5 mM tricaine on ice in preparation for macrophage isolation protocol (See section 2.3.1 for details)

mpeg1:EGFP zebrafish (4 dpf) were treated with 1 ml 10 µM IRAK4-IN-1 inhibitor and 1% DMSO in E3 medium containing 140 uM PTU individually house in 12 well plates for the duration of the experiment. On the day of imaging, mpeg1:EGFP embryos were anesthetised with 2.5 mM tricaine and immobilised in low melting point agarose onto a Matek glass bottom petri dish. Post imaging, zebrafish embryos were liberated from agarose and incubated in 1 ml 10 µM IRAK4-IN-1 inhibitor and 1% DMSO in E3 medium containing 140 uM PTU individually house in 12 well plates until required.

2.3. Isolation of zebrafish macrophage for RNA sequencing

2.3.1. Zebrafish macrophage isolation

The zebrafish macrophage was isolated using protocols previously developed in the Sieger laboratory (Mazzolini et al., 2018). Briefly, mpeg1:EGFP zebrafish larvae (5 dpf) were anaesthetised in 2.5mM tricaine in E3 medium prior to being transferred into cold E3 medium and maintained at 4°C. For each macrophage isolation protocol, about 200 zebrafish larval heads were isolated. The larvae heads were transected above the yolk-sac using surgical micro-scissors and transferred into a glass homogeniser filled with 1 ml Media A (15 mM Hepes, 25 mM D-Glucose in 1X HBSS). The larvae heads were homogenised and strained through a 40 µM cell strainer. The homogenized tissue were distributed into two 1.5 ml microtubes and centrifuged at 300 g for 10 minutes at 4°C. The supernatant was removed and the cells were resuspended in 1 ml ice chilled 22% density gradient medium gently overlaid

by 0.5 mL of ice chilled 1X DPBS. The tubes were spun at 950 g, with slow acceleration and without brake, for 30 min at 4°C. After the spin the supernatant was removed and the cells were resuspended in 1 ml 2% normal goat serum (NGS) in media A. The cell suspension was spun again at 300 g for 10 minutes at 4°C. The final cell pellet was resuspended in 1 ml 2% NGS in Media A and the macrophage were isolated by flow cytometry (Section 2.3.2).

2.3.2. Flow cytometry sample acquisition

Fluorescent Activated Cell Sorting (FACS) was facilitated by in-house service provided by Shared University Resource Facility (SURF, QMRI). Macrophage samples were acquired using FACS AriaII (BD Biosciences, Oxford, UK) with the temperature maintained at 4°C throughout the sort. U87-nls-mKate2 glioblastoma cells were acquired using FACS Fusion at room temperature (BD Biosciences, Oxford, UK). Robust and replicable cell sort was first achieved by calibrating and setting gating parameters using unstained wild type (WIK)

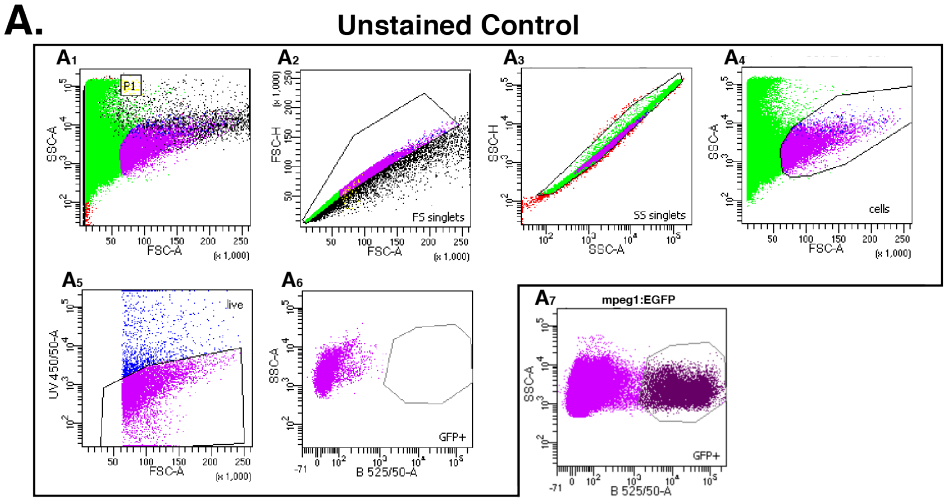

Figure 7. Fluorescence Activated Cell Sorting (FACS) of mpeg1:EGFP positive macrophages

(A_1-A_6) FACS calibration of FACS AriaII (BD Biosciences, Oxford, UK) using homogenized wild type unlabeled zebrafish brain tissue. (A_2) Cell doublets were first gated against by plotting the height of the forward scatter (FSC-H) against the area of the forward scatter (FSC-A). (A_3) Further refinement of cell singlets was achieved by gating for proportionate cells along the axis of height of the side scatter (SSC-H) vs the area of the side scatter (SSC-A).(A_4) Cell debris were gated against and macrophage cell population gate for. (A_5) Live and dead cells were identified by adding 3 µM DAPI (Thermofisher Scientific, Loughborough) counter stain into the cell suspension. (A_6) Final gating parameter denoting boundary of GFP positive cells. Note unstained cell population is outside this boundary.

(A_7) mpeg1:GFP expressing macrophages are sorted for using calibrated FACS parameter based on wild type unlabeled zebrafish brain tissue.

zebrafish brain tissue (Figure 7A) and unstained U87 glioblastomas cell. The following method being described follows the workflow of a typical fluorescent activate cell sort for mpeg1:EGFP positive zebrafish. However, FACS for U87 glioblastomas cells followed identical gating strategies with the difference in the final gate which gated using the excitation/emission spectrum of 588/633 nm for mKate2 fluorophore. Two strategies was employed to gate against cell doublets. First, cell doublets were first gated against by plotting the height of the forward scatter (FSC-H) against the area of the forward scatter (FSC-A). Cell doublets will double the FSC-A values thus FSC-H/FSC-A values would be disproportionate (Figure $7A_2$). Further refinement of cell singlets were achieved by plotting the height of the side scatter (SSC-H) against the area of the side scatter (SSC-A) (Figure $7A_3$). Again, cell doublets will double the area of SSC-A and will have greater SSC-A values than SSC-H. Generally, cellular debris is considered to be forward scatter (FSC) low thus gate was drawn around cells with higher FSC (Figure $7A_4$). Live and dead cells were identified by adding 3 μM DAPI (Thermofisher Scientific, Loughborough) counter stain into the cell suspension (Figure 7_5). Using the gated unstained sample as a guide (Figure $7A_6$), final gating parameters were defined to specifically select for GFP expressing macrophages (Figure $7A_7$).

2.3.3. RNA Extraction of fluorescent activated cell sorted macrophage

RNA extraction was achieved using a commercially available RNeasy Mini Kit (Qiagen, Manchester, UK). The protocol was performed following the manufacture's instructions with optimization for the processing of less than 100,000 cells. Briefly, sorted macrophage cells were lysed by adding 75 μl buffer RLT and the resulting lysate was pipetted directly into a QIAshredder spin column and centrifuged for 2 minutes at 9000 g. The flowthrough was transferred to a gDNA Eliminator spin column and centrifuged for 30 seconds at 9000 g. Next, 70% ethanol was added to the flowthrough and the sample was transferred to an RNeasy MinElute spin column. Several wash steps followed using supplied buffer RW1 and RPE and freshly made 80% ethanol; the samples were centrifuged at 9000 g for 1 minute between

each wash. RNA content was finally eluted by adding 14 µl RNase free water to the centre of the spin column membrane. The resulting total RNA content was stored at -80 °C in preparation for RNA amplification for sequencing or First Strand cDNA synthesis.

2.4. RNA preparation and quantitative reverse transcription PCR

2.4.1. First Strand cDNA Synthesis of RNA Isolated from Macrophage

The SuperScript III First-Strand Synthesis system (ThermoFisher Scientific, Waltham) was used to synthesis first strand cDNA from isolated total RNA before RT-qPCR. In order to ensure replicability in all RT-qPCR reactions, the amount of starting total RNA material in first strand synthesis reactions was set at 0.5 µg. cDNA synthesis was performed in the first step using total RNA primed with 1 µl Oligo(dT) mixed with 1 µl 10 mM dNTP at 65°C for five minutes. cDNA synthesis mix containing 1 µl 10X RT buffer, 4 µl 25 mM MgCl2, 2 µl 0.1 M DTT, 1 µl 40 U/µl RNaseOUT and 1 µl 200 U/µl SuperScript III reverse transcriptase was added to each reaction and incubated for 50 minutes at 50°C. The reaction was terminated after the 50 minutes period by incubating at 85°C for five minutes. RNA template from the cDNA:RNA hybrid molecule was digested with RNase H after first strand synthesis by adding 1 µl of RNase H to each reaction and incubated at 37°C for 20 minutes. The resulting cDNA product was stored at -20°C ready for use in qRT-PCR analysis.

Table 1 quantitative RT-PCR Primers Table

	Primer name	Primer Sequence 5’ - 3’
1	Arg-1 Forward	TCCGTTCTCCAAAGGACAGC
2	Arg1-Reverse	GACTCGTCGTTGGGAAGGTT
3	IFN-y Forward	CACATGATGGGCTTTGCCTG
4	IFN-y Reverse	GATTCGCAGGAAGATGGGGT
5	il4/13b Forward	CTGTTGGTACTTACATTGGTCCCC
6	il4/13b-Reverse	AGTGTCCTGTCTCATATATGTCAGGT
7	il4/13a Forward	GCACTGTATTCGTCTCGGGTTTTA
8	il4/13a Reverse	TTTTCCCCAGATCTACAAGGAAGA
9	Beta Actin Forward	CACTGAGGCTCCCCTGAATCCC

10	Beta Actin Reverse	CGTACAGAGAGAGCACAGCCTGG
11	Cxcl8b.1 Forward	GCCAATGAGGGTGAAGCTCTA
12	Cxcl8b.1 Reverse	AATCACCCACGTCTCGGTAG
13	TNF-a Forward	ACCCAGGGCAATCAACAAGA
14	TNF-a Reverse	CAAGCCACCTGAAGAAAAGGC
15	IL1-b Forward	GGCATGCGGGCAATATGAAG
16	IL1-b Reverse	TGTAGCTCATTGCAAGCGGA

2.4.2. Quantitative RT- PCR

Quantitative RT-PCR was achieved using SsoAdvanced universal SYBR Green supermix (Biorad, Watford) and quantified using Roche Lightcycler 96 system Roche Diagnostics, West Sussex, UK). Each 20 µl reaction contained 10 µl SsoAdvance universal SYBR Green supermix, 250 nM of each forward and reverse primers (Table 1) and 1 µl of cDNA template from the first strand synthesis reactions of the RNA product. Due to the nature high sensitivity of qPCR kit, variations in cycle threshold (CT) values can arise from differences in loading, extraction, mRNA-quality and reverse transcriptase efficiency. To control for such variations two technical replicates were loaded onto the plate for each gene of interest and the resulting pair of CT values averaged. A total of three biological replicates were used to analyse each gene on interest. Samples loaded on qPCR plates were analysed using a Roche Lightcycler 96 system (Roche Diagnostics, West Sussex, UK) running the thermal cycling protocol described in Table 2. Melting curve analysis followed the amplification phase and was important in assessing if the qPCR assay had produced single specific product. Melt-Curve analysis was conducted by increasing the temperature from 65-95°C at 0.5°C increments every 2 seconds in between steps. Assays producing multiple or non specific products were excluded in analysis.

Table 2 qPCR Thermal cycling protocol

Step	Thermal cycler settings	Description
1	Polymerase Activation and DNA Denaturation	95°C - 3 mins

Step	Thermal cycler settings	Description
2	3 Step Amplification for 45 cycles	95°C - 10 secs 56°C - 20 secs 72°C - 20 secs
3	Melting-Curve Analysis	65-95°C at 0.5°C increments every 2 seconds
4	Cooling	40°C - 10 secs

In order to quantify fold change in gene expression the delta-delta CT method was used. This delta-delta CT formula, 2-ΔΔCT, is well describe and widely used in qPCR analysis (Livak and Schmittgen, 2001). Of note, the delta-delta CT method normalises each gene of interest to a housekeeping gene, beta actin (*bactin1*), to calculate relative fold change. Bactin1 gene was chosen as the house keeping gene as it was shown to be stably expressed in zebrafish development and most stably expressed following chemical treatment (McCurley and Callard, 2008). ΔCT is equal to the cycle threshold of the gene of interest minus the cycle threshold of the housekeeping gene, and ΔΔCT is equal to the difference between the ΔCT values of treated sample and untreated sample.

2.5. RNA Preparation for RNA Sequencing

2.5.1. RNA quality assessment and RNA amplification

RNA Quality assessment was performed by Dr. Pamela Brown (shared university research facility SuRF, The University of Edinburgh) using a LabChip GX24 Nucleic Acid Analyzer (PerkinElmer, Seer Green, UK). LabChip GX24 Nuclei Acid Analyzer utilized a combination of microfluidic chips, voltage induced size separation in gel filled channels and laser induced fluorescence detection of RNA of different molecular weight to determine RNA integrity number (RIN) of RNA samples (Schroeder et al., 2006). In addition, LabChip GX24 was also capable of quantifying separated RNA product by laser induced fluorescence where the amount of measured fluorescence correlated with the amount of RNA of a give size. LabChip

GX24 allowed reproducible RNA quality and quantity analysis using a small volume (2 µl) of final RNA product. A RIN score of 7 or greater is considered high quality. A RIN score of less than 7 indicated poor RNA quality and RNA degradation thus any RNA product with a RIN score of less than 7 were discarded from all experiments.

RNA amplification was conducted using the commercially available Ovation® RNA-seq System V2 (Nugen, California). A dedicated sterilised pre-amplification and amplification area was assigned prior to starting the protocol to minimise risk of cross contamination. RNA amplification was performed following manufacture protocol (Ovation® RNA-seq System V2, Nugen). The seven key steps are as follows:

Pre amplification : A. First Strand cDNA synthesis

B. Second Strand cDNA synthesis

C. Purification of cDNA

Amplification: D. Single Primer Isothermal Amplification

E. Purification of SPIA cDNA (QIAGEN MinElute Reaction Cleanup Kit)

F. Nano Drop cDNA Yield

Table 3 Thermal cycler programs for RNA amplification

Program	Thermal cycler settings	
1	Primer Annealing	65°C - 2 mins, hold at 4°C
2	First Strand Synthesis	4°C - 1 min, 25°C - 10 mins, 42°C - 10 mins, 70°C - 15 mins, hold at 4°C
3	Second Strand synthesis	4°C - 1 min, 25°C - 10 mins, 50°C - 30 mins, 80°C - 10 mins, hold at 4°C
4	SPIA Amplification	4°C - 1 min, 47°C - 60 mins, 80 °C - 20 mins, hold at 4°C

During the first strand cDNA synthesis, 5 µl of RNA sample was added to 2 µl of first strand primer mix to allow annealing of primers in a thermal cycler programmed to run program 1 (Table 3). Once primer annealing was complete first strand cDNA synthesis was initiated by mixing 2.5 µl first strand buffer mix with 0.5 µl first strand enzyme mix in each reaction. Samples were then placed in a thermal cycler programmed to run program 2 (Table 3). After which the samples were removed from the thermal cycler, spun to collect condensation and placed on ice before proceeding with second strand cDNA synthesis.

Second strand cDNA synthesis was initiated by adding 9.7 µl second strand buffer mix and 0.3 µl second strand enzyme mix into each reaction tube. The tubes were placed back into the thermal cycler programmed to run Program 3 (Table 3).

Purification of cDNA was achieved using paramagnetic bead based chemistry to removed contaminants. At room temperature, 32 µl of the Agencourt purification bead (Beckman Coulter, CA, USA) suspension, supplied with the Ovation RNA-Seq System V2, was added to each reaction and mixed well by pipetting. The tubes were then transferred to a magnetic stand and left to stand for 5 minutes to completely clear the solution of the beads. The exposure of the DNA to polyethylene glycol in the solution causes the negatively charged DNA to bind with the carboxyl groups on the surface of the paramagnetic beads (DeAngelis et al., 1995). These beads were immobilised by the magnetic field of the magnetic stand allowing purification of cDNA product (DeAngelis et al., 1995). Keeping the tubes on the magnet, 45 µl of the binding buffer was removed and discarded. 70% Ethanol (200 µl) was added and allowed to stand for 30 seconds. The wash was repeated two more times before air drying the beads on the magnet for 15 to 20 minutes to allow all ethanol to evaporate. When all ethanol has been removed, cDNA was amplified by single primer isothermal amplification (SPIA) protocols.

The amplification of double strand cDNA bound to the dried beads began by the addition of SPIA master mix consisting of 20 µl SPIA buffer mix, 10 µl SPIA primer mix and

10 µl SPIA enzyme mix. The samples were then placed in tubes in a thermal cycler programmed to run program 4 (Table 3). The tubes were then transferred to the post-amplification workspace back onto the magnet and left to stand for 5 minutes to completely clear the solution of the beads. The clear supernatant containing the SPIA cDNA was transferred to a fresh tube and purified using QIAGEN MinElute Reaction Cleanup Kit (Qiagen). Briefly, the entire volume (40 µl) of the SPIA reaction was added to 300 µl of buffer ERC and mixed by pipetting. The sample/buffer mix was added into a MiniElute spin column and centrifuged for 1 minute at maximum speed in a microcentrifuge. The flow through was discarded and 750 µl Buffer PE was added and centrifuge at 10,000 g Care was taken to ensure all residual Buffer PE was completely removed. The DNA was eluted with 22 µl room temperature Buffer EB and centrifuged for 1 minute at 10,000 g. The concentration of the purified SPIA cDNA sample was measured using a Nanodrop (NanoDrop One, ThermoFisher Scientific) and stored at -20°C until required.

2.5.2. RNA sequencing and analysis of amplified cDNA product

RNA sequencing and differential analysis was performed by Edinburgh Genomics (Edinburgh, UK). Nine samples were sent for analysis and are shown in Table 4. Quality control of cDNA samples was performed prior to cDNA library generation.

Table 4 Table of samples and associated conditions

Number	Sample Name	Condition
1	Pdbead1D0305	Pd bead + U87
2	PdBead3D1705	Pd bead + U87
3	PdBead4D2405	Pd bead + U87
4	Control2D0305	No Bead
5	Control5D2405	No Bead
6	Control6D1005	No Bead
7	Control9D2806	No Bead

Number	Sample Name	Condition
8	U877D0706	No bead + U87
9	U878D2806	No bead + U87

DNA library of each cDNA samples were prepared using TruSeq DNA Nano gel free library before sequencing. Sequencing reads data generation was performed using HiSeq 4000 75PE system (Illumina). All reads were trimmed using Cutadapt (Martin, 2011) based on a quality threshold of 30 and for TruSeq adaptor sequences (AGATCGGAAGAGC). The reads were aligned to the *Danio Rerio* reference genome (GRCz10, annotation version 84) from Ensmble using STAR (Spliced Transcripts Alignment to a Reference) (Dobin et al., 2013). Read counts were mapped to exon features that were grouped by gene_id in the zebrafish reference genome using featureCounts (Liao et al., 2014) program. The number of read counts were preprocessed by removing genes with near zero counts. The data was then normalised to the library depth to avoid artefacts of RNA sequencing to give the counts per million value (CPM) for each gene. A principal component analysis was performed to identify patterns as a result of experimental factors before differential analysis. Differential analysis was performed using edgeR package comparing the three conditions with each other to give log fold changes. Once a list of differentially expressed genes for each condition were collated, an enrichment analysis was performed to highlight differentially regulated biological process associated with each condition.

2.6. Nucleic acid techniques

2.6.1. REDTaq ReadyMix PCR

Each 20 µl PCR reaction contained 10 µl REDTaq ReadyMix PCR mix (Sigma, Germany), 200 nM forward, 200 nM reverse primers, 0.4 µl of template DNA and PCR grade water up to a final volume of 20 µl. The PCR reactions were transferred to a BioRad T100 thermal cycler running a three step protocol (Table 5).

Table 5 PCR program conditions for routine PCR

	Temperature	Duration
Initial Denaturation	94 °C	2 minutes
Denaturation	94 °C	30 seconds
Annealing	Primer dependant	30 seconds
Extension	72 °C	1 minute/kb
Number of cycles		35
Final Extension	72 °C	7 minutes
Hold	4 °C	∞

2.6.2. Agarose gel electrophoresis

PCR products were loaded into horizontal 2% w/v agarose 1X TAE gels containing 1X SYBR™ Safe. Samples were electrophoresed in 1X TAE at 130 V for 25 minutes. DNA fragment sizes were determined using either a 100 bp ladder (Invitrogen, Paisley UK) or a 1 kb ladder (Invitrogen, Paisley UK) and visualised using a UV transiluminator (UVITECH, Cambridge).

2.7. Multisite Gateway® Cloning system

2.7.1. Generation of pDONR™ clones by BP recombination

pDONR™ entry clones for Cxcl8b.1 (ENSDART00000166280.4) and Tnf-α (ENSDART00000025847.9) were created by generating PCR products of the gene of interests with flanking attB1 and attB2 sequences using primers listed in Table 6. attB1/attB2 flanked PCR products were purified using the QIAquick PCR Purification Kit following manufacturers guidelines (Qiagen, Manchester UK) and confirmed by gel electrophoresis .

Table 6 Primer list for Gateway® cloning system

	Primer	Primer Sequence 5' - 3'
1	Cxcl8b.1 attB1 Forward	GGGGACAAGTTTGTACAAAAAA-GCAGGCTTCATGATGAAGTTGAGCGTTTCAGC
2	Cxcl8b.1 attB2 Reverse	GGGGACCACTTTGTACAAGAAA-GCTGGGTTTTAATTCGTGGTCATTATTGTT-GAAAATGTTGTTGT
3	Tnf-α attB1 Forward	GGGGACAAGTTTGTACAAAAAA-GCAGGCTTCATGAAGCTTGAGAGTCGGG
4	Tnf-a attB2 Reverse	GGGGACCACTTTGTACAAGAAAGCTGGGTTTCAG-CAATGTACAGATGTGTTGG

The attB flanked PCR products were cloned into the pDONR™ 221 vector, by BP reaction, to generate TNF-a and Cxcl8b.1 entry clones for Multisite Gateway® Cloning. In each 10 µl BP recombination reaction, 50 femtomoles (fmoles) of each attB flanked PCR product and pDONR™ 221 vector, 1 µl BP Clonase™ II enzyme and TE buffer, pH 8.0 to a total volume of 10 µl was incubated at 25°C for 1 hour. The reaction was terminated by addition of 0.5 µl proteinase K solution and incubated for 10 minutes at 37°C. Final BP reaction product was used immediately and transformed into One Shot® TOP10 Competent E. coli cells.

2.7.2. Generation of pDEST™ expression clones by LR recombination

The Multisite Gateway® Cloning system was used to generate the final pDEST™ expression vector required for over-expression assays. LR recombination reactions were performed according to the manufacturer's instructions. For each reaction, 10 fmoles of five prime entry, middle entry and three prime entry vectors was mixed with 20 fmoles of pDEST™ Cry:ECFP destination vector with TE buffer (pH 8.0) to a final volume of 8 µl, LR Clonase™ (2 ul) was added to the reaction, mixed by vortex and incubated overnight at 25°C. The reaction was terminated by adding 1 µl of Proteinase K solution and incubated at 37°C for 10 minutes. LR reaction product was used immediately and transformed into DH5α Competent E.coli cells.

2.7.3. Transformation of One Shot® TOP10 and DH5α Competent E. coli cells

pDONR™ entry clones and pDest™ expression clones were amplified by transforming BP reaction products into One Shot® TOP10 (ThermoFisher Scientific, Loughbrough UK) and DH5α Competent E. coli cells (ThermoFisher Scientific, Loughbrough UK) respectively. The whole reaction volume (10 µl) from previous BP reaction was incubated with 50 µl One Shot® TOP10 Competent cells on ice for 30 minutes. While on the other hand, 1 µl LR reaction product was incubated with DH5α competent E. coli cells for 30 minutes on ice. Cells were then transformed by heatshock at 42°C for 45 seconds and returned to ice for 1 minute. Lysogeny broth (LB) broth, 250 µl, was added to each vial of cells and placed in a shaking incubator at 37°C for 1 hour. The transformed cells were plated and evenly spread on LB-agarose plates containing 50 µg/ml Kanamycin for BP reactions and 50 µg/ml Ampicillin for LR reactions. Two volume of transformed cells were plated, 200 µl and 50 µl, in order to ensure even distribution of bacterial colonies. Agarose plates were incubated overnight at 37°C.

2.7.4. Isolation of plasmid DNA using QIAprep Spin Miniprep Kit

A single bacterial colony was used to inoculate 5 ml of LB-broth containing 50 µg/ml Kanamycin or Ampicillin; the choice of antibiotic was dependent on the selection marker of the plasmid DNA target being isolated. The inoculated LB-broth medium was incubated overnight at 37°C with orbital shaking at 250 rpm. The plasmid DNA from the bacterial cultureswere isolated using the QIAprep Spin Miniprep Kit (Qiagen, Manchester, UK) according to the manufacturers instructions. Plasmid DNA was eluted in 50 µl of elution buffer and quantified by nanodrop. Isolated plasmid DNA was sent for sequencing and stored at -20°C until required.

2.7.5. Plasmid DNA Sequencing

DNA sequencing was conducted using a Sanger Sequencing service provided by the commercial company Source Bioscience (Source BioScience, Nottingham UK). Plasmid DNA was aliquoted into 5 µl volume at a concentration of 100 ng/µl. M13 forward (5' GTAAAAC-GACGGCCAG 3') and reverse (5' CAGGAAACAGCTATGAC 3') primers included in the service were used in all sequencing reactions. Sequence reads were analysed using Snapgene software (GSL Biotech LLC, Chicago USA).

2.8. Image Analysis

2.8.1. U87-nls-mKate2 automated cell counting

Automated U87-nls-mKate2 cells counts were analysed using custom integration of MatLab (MathsWorks, Cambridge, version 2018b) scripts into Imaris (Bitplane, Oxford, version 9.2.1). Cell counting scripts used Imaris Bitplane's proprietary automated cell counting packages that exports data into MatLab for processing. The integration of custom MatLab scripts allows for batch processing of image data thus speeding up image processing, eliminating unconscious biases and facilitates reproducibility. A custom 'quality' threshold was set for each experimental group to control for variability in image acquisition parameters and fluorophore expression patterns. This same 'quality' threshold was applied on all imaged samples from the same experimental group for batch processing in cell counting.

2.8.2. Macrophage sum of intensity

The macrophage sum of intensity is defined as the sum of all pixel intensity values defined in a specific region of interest. Macrophage sum of intensity was used as a read out for the level of macrophage responses to a specific experimental stimuli. Custom MatLab scripts were coded to evaluate macrophage sum of intensity. The script integrates MatLab's proprietary surfacing tool to define a region of interest based on mpeg1 promoter driven fluorophore expression (Ellett et al., 2011). The mpeg1 promoter is a macrophage lineage specific marker that labels macrophages and macrophage in the zebrafish (Ellett et al., 2011). The tool

incorporates surface detail smoothing and background subtraction in order to achieve a region of interests that best reflects the borders of macrophage labelling. Custom upper intensity threshold was set for each experimental group to control for variability in image acquisition parameters and fluorophore expression patterns. The upper intensity threshold was set to achieve maximum surfacing of fluorophore signal. The surfaced images were filtered by the 'number of triangles' to remove surface noise. This same upper intensity threshold and 'number of triangle' filter was applied to all imaged samples from the same experimental group for batch processing to evaluate macrophage sum of intensity.

2.9. CRISPR-mediated genome editing of TNF-α and Cxcl8b.1 in zebrafish

2.9.1. CRISPR-mediated genome mutagenesis

All CRISPR guide RNA (gRNA) were designed using Snapgene (GSL Biotech LLC, Chicago USA), a commercially available software. Trans-activating CRISPR RNA (tracrRNA) and CrRNA for Tnf-α BSL1 (target sequence: 5' ACAAAATAAATGCCATCATC 3'), Tnf-α MWO1 (target sequence: 5' GCTCCTGCGTGCAGATTGAG 3'), Cxcl8b.1 Alu1 (target sequence: 5' GACCATTCACCGAGCAGCTG 3'), Cxcl8b.1 Rsa1 (target sequence: 5' ATTCCTAAACGACAAGTACT 3'), Cxcl8b.1 Bsl1 (target sequence: 5' GTCTCAATCCTACCGAGACG 3') and scrambled (target sequence: 5′-CCTCTTACCTCAGTTACAATTTATA-3′) were obtained from Merck KGaA (Darmstadt, Germany,). Knock out of TNF-α expression was achieved using an injection mix containing a mixture of 1 µl tracrRNA, 1 µl phenol red, 1 µl Cas9 protein ,1 µl Tnf-α MWO1 gRNA and 1 µl Tnf-α BSL1 gRNA (Table 7). The partial knockout of Cxcl8b.1 and knock out of Tnf-α expression was achieved by injecting a mix containing a 1ul tracrRNA, 1 µl phenol red, 1 µl Cas9 protein ,1 µl Cxcl8b.1 Alu1 gRNA, 1 µl Tnf-α MWO1 gRNA and1 µl Tnf-α BSL1 gRNA (Table 7).

Table 7 General Reagents for Crispr-Cas9 injections

Reagent	Composition/Final Concentration
tracrRNA	SygRNA Cas9 Synthetic tracrRNA 250 ng/µl
Phenol Red	phenolsulfonphthalein 5.6 µM
Cas9	Cas9 Nuclease, *S.pyrogenes* 6.66 µM
Tnf-α Bsl1 gRNA	SpCas9 crRNA HPLC 20 µM gRNA
Tnf-α Mwo1 gRNA	SpCas9 crRNA HPLC 20 µM gRNA
Cxcl8b.1 Alu1 gRNA	SpCas9 crRNA HPLC 20 µM gRNA
Cxcl8b.1 Rsa1 gRNA	SpCas9 crRNA HPLC 20 µM gRNA
Cxcl8b.1 Bsl1 gRNA	SpCas9 crRNA HPLC 20 µM gRNA
Scrambled gRNA	SpCas9 crRNA HPLC 20 µM gRNA

2.9.2. Isolation of genomic DNA from zebrafish tissue

Genomic DNA from zebrafish tissue was isolated using the NaOH method. This protocol was modified from the HotSHOT method used previously in murine models (D Meeker et al., 2007). Live zebrafish were euthanised by 15.3 mM Tricaine overdose post imaging at the end of each experiment. The genomic DNA of zebrafish tissue was isolated from the U87 human glioblastoma cells by transecting above the yolk-sac using surgical micro-scissors. Zebrafish heads containing U87 human glioblastoma cells were removed and genomic DNA was isolated from the remaining zebrafish tissue. Individual zebrafish main body tissue were heated to 95°C in 100 µl of 50 mM NaOH for ten minutes. A volume of 10 µl of 1 M TRIS pH 8.0 was added to each tissue digest, vortexed to mix and cooled to 4°C. The resulting genomic DNA extract was used immediately for PCR reaction.

2.9.3. Restriction fragment length polymorphism (RFLP) analysis

The efficiency of CRISPR induced mutagenesis was accessed by restriction fragment length polymorphism analysis (Tsarouchas et al., 2018). To accomplish this, CRISPR gRNAs were specifically designed to introduce mutations to a restriction site in the exon. Introduction of a mutation at the restriction site abolishes restriction enzyme activity and thus causes fragment length polymorphism identified as a band shift in horizontal gel electrophoresis. Each

CRISPR gRNA is paired with a specific pair of primers to amplify a region of the genome with a restriction enzyme site of interest (Table 8).

Table 8 Crispant Verification Primer Pairs

	Primer Pair	Exon Target	Primer Sequence 5' - 3'	Enzyme
1	Tnf-α Bsl1 Forward	Exon 4	ACCAGGCCTTTTCTTCAGGT	Bsl1
2	Tnf-α Bsl1 Reverse	Exon 4	AGCGGATTGCACTGAAAAGT	Bsl1
3	Tnf-α Mwo1 Forward	Exon 4	CATCAGCTGCACGTCTGAAC	Mwo1
4	Tnf-α Mwo1 Reverse	Exon 4	TGCCCAGTCTGTCTCCTTCT	Mwo1
5	Cxcl8b.1 Alu1 Forward	Exon 4	ACCAGCACAGACAACAACAACA	Alu1
6	Cxcl8b.1 Alu1 Forward	Exon 4	AGGTCAGGTAAAGTCACAGTGA	Alu1
7	Cxcl8b.1 Bsl1 Forward	Exon 3	TTTTCAACAGCGCCACACTT	Bsl1
8	Cxcl8b.1 Bsl1 Reverse	Exon 3	TGTTGTGAGGAGGGAAGTGT	Bsl1
9	Cxcl8b.1 Rsa1 Forward	Exon 2	TGCTTCTGATCTGCACGACTG	Rsa1
10	Cxcl8b.1 Rsa1 Reverse	Exon 2	TTCTGCAGTGTGATCCAGCA	Rsa1

Each PCR reaction contained 10 µl REDTaq ReadyMix PCR mix (Sigma, Dorset, UK), 200 nM final concentration of each forward and reverse primers, 0.4 µl of template DNA isolated for tissue digest and PCR grade water up to a final volume of 20 µl. The PCR mix was transferred to a thermal cycler running a three step protocol previous described in Table 5.

The resulting PCR product was digested by the respective paired restriction enzyme (Table 8). Restriction enzyme, 3.3 units, was directly added to the PCR product and was incubated at the enzyme's incubation temperature for a period of two hours; Rsa1 (37°C), Bsl1 (55°C) and Mwo1 (60°C) Horizontal gel electrophoresis was conducted on digested PCR product on 2% agarose-1X TAE gel visualized using 1X SYBR safe (Thermo Fisher, UK) DNA gel stain

2.10. Genetic overexpression of TNF-α and Cxcl8b.1 in zebrafish

2.10.1. Zebrafish Genetic Transgenesis

Zebrafish embryo microinjections were conducted at the one cell stage in order to maximise transgenesis efficiency. The overexpression of Cxcl8b.1 was achieved by injecting a solution containing a final concentration of 40 ng/µl pDest_mpeg:Cxcl8b.1 plasmid, 100 mM KCl, 200 ng/µl Tol2 transposase and 2.5 µM Fast Green FCF Dye in a final volume of 10 µl. Similarly, the overexpression of TNF-a was achieved by injecting a solution containing a final concentration of 40 ng/µl pDest_mpeg:TNF-a plasmid, 100 mM KCl, 200 ng/µl Tol2 transposase and 2.5 µM Fast Green FCF Dye in a final volume of 10 µl. The co-expression of both mpeg:TNF-a and mpeg-Cxcl8b.1 was achieved by injecting a solution containing 40 ng/µl pDest_mpeg:TNF-a plasmid, 40 ng/µl pDest_mpeg:Cxcl8b.1 plasmid, 100 mM KCl, 200 ng/µl Tol2 transposase and 2.5 µM Fast Green FCF Dye in a final volume of 10 µl. All overexpression assays were conducted in GFP labelled macrophages in the transgenic mpeg1:EGFP zebrafish.

2.10.1. Zebrafish tissue homogenisation and RNA extraction

The zebrafish tissue was isolated using adapted protocols developed in the lab previously described (Mazzolini et al., 2018). Zebrafish larvae were euthanised with 15.3 mM Tricaine prior to being transferred into cold embryo medium at 4°C. For each sample group of transgenic zebrafish, 100 zebrafish larvae were used. Whole larvae were transferred into a glass homogeniser filled with 1 ml Media A (15 mM Hepes, 25 mM D-Glucose in 1X HBSS). The larvae were homogenised using a glass homogeniser and distributed into two 1.5ml microtubes and centrifuged at 300 g for 10 minutes at 4°C. The supernatant was removed and the cell pellet from both tubes were pooled into a single 1.5 ml microtube with 1 ml media A. Homogenized tissue was centrifuged at 300 g for 10 minutes at 4°C and the resulting pellet was used for RNA extraction. RNA extraction was achieved using the RNeasy Mini Kit (Qiagen, Manchester UK) following the manufacturer's instructions. Zebrafish tissue was lysed

by adding 350 µl buffer RLT and homogenised by pipetting directly into a QIAshredder spin column (Qiagen, Manchester UK. Genomic DNA was removed from the lysate by passing through a gDNA Eliminator spin column, leaving only total RNA content. Next, 350µl 70% ethanol was added to the flowthrough and the sample was transferred to an RNeasy MinElute spin column. The sample was washed with 700 µl buffer RW1 followed by 500 µl buffer RPE and finally 500 µl 80% ethanol. Samples were centrifuged at 9000 g for 1 minute in between each wash steps. RNA content was finally eluted by adding 14 µl RNase free water to the centre of the spin column membrane, allowed to sit for 1 minute and centrifuged at 9000 g for 1 minute. Isolated total RNA content was quantified using nanodrop and 1 µg RNA for each sample was used immediately for First Strand cDNA synthesis, described in section 2.4.1, in preparation for Reverse Transcription PCR (RT PCR).

2.10.2. Reverse transcription polymerase chain reaction (RT-PCR)

RT PCR of DNA fragments is a powerful yet straight forward technique to qualitatively evaluate mRNA expression levels in genetic overexpression assays. Total RNA content was isolated from whole embryos using method described in section 2.10.1. RNA was extracted from mpeg1:EGFP zebrafish injected with pDest™_mpeg1:tnf-a, mpeg1:EGFP zebrafish injected with pDest™_mpeg1:cxcl8b.1 and from wild type (WIK) zebrafish. First strand cDNA synthesis was performed on extracted RNA and RedTaq PCR method (Section 2.6.1) was performed with an amended number of PCR cycles set at 28 cycles. RedTaq PCR was performed using forward and reverse primers for tnf-a, cxcl8b.1, β-actin and GFP listed in Table 9 on each RNA sample. RT-PCR was visualized by agarose gel electrophoresis (Section 2.6.2).

Table 9. RT-PCR Primer list

Primer name	Primer Sequence 5' - 3'
Beta Actin Forward	CACTGAGGCTCCCCTGAATCCC
Beta Actin Reverse	CGTACAGAGAGAGCACAGCCTGG
Cxcl8b.1 Forward	GCCAATGAGGGTGAAGCTCTA

Primer name	Primer Sequence 5’ - 3’
Cxcl8b.1 Reverse	AATCACCCACGTCTCGGTAG
TNF-a Forward	ACCCAGGGCAATCAACAAGA
TNF-a Reverse	CAAGCCACCTGAAGAAAAGGC
GFP Forward	ACGTAAACGGCCACAAGTTC
GFP Reverse	ACCATGTGATCGCGCTTCTC

3. Results

3.1. Biorthogonal catalytic uncaging of inactive caged compounds in the zebrafish brain

3.1.1. Caged drug, POB-Vorinostat, trials reveal palladium mediated anti tumour effects in zebrafish

One of the major challenge facing cancer therapy is the difficulty of homogeneous delivery of intravenous chemotherapeutics throughout the solid tumour mass. The high interstitial pressures contribute to the suboptimal diffusion of drugs from blood circulation which prevents intratumor penetration (Stohrer et al., 2000). This problem is exacerbated by the clearance of intravenous drugs by the liver and kidneys which can lead to fatal organ toxicity (Hoop et al., 2018). Thus a more effective drug delivery system is required. Herein, we explored the capabilities of solidly supported Gold (Perez-Lopez et al., 2017) and Palladium (Adam et al., 2018) nanoparticles to mediate local delivery of chemotherapeutic agent, Vorinostat, in zebrafish. In conjunction with *in-vivo* live imaging technologies, the efficacy of a newly designed drug delivery system to deliver chemotherapeutic Vorinostat into the zebrafish brain was studied. Vorinostat has been previously shown to be a potent chemotherapeutic *in-vitro* and was released upon biorthogonal catalytic reaction with Palladium beads leading to uncaging of inactive caged drug POB-Vorinostat (Figure S1) into its active form. The benefits of a biorthogonal catalytic drug delivery system allowed for site specific drug delivery that has the potential to significantly increase drug potency. Thus, in order to investigate the viability of biorthogonal catalytic drug delivery system in an *in vivo* setting, we utilised the zebrafish animal model to develop a Palladium bead *in vivo* assay. *mpeg1:EGFP*, macrophage labelled*,* zebrafish were xenografted with U87-mCherry cells at 3 days post fertilisation (dpf) and Palladium beads implanted into the brain at 4 dpf. These zebrafish were subsequently treated with either 100 μM inactive caged drug POB-Vorinostat in 1% DMSO or 1% DMSO for control.

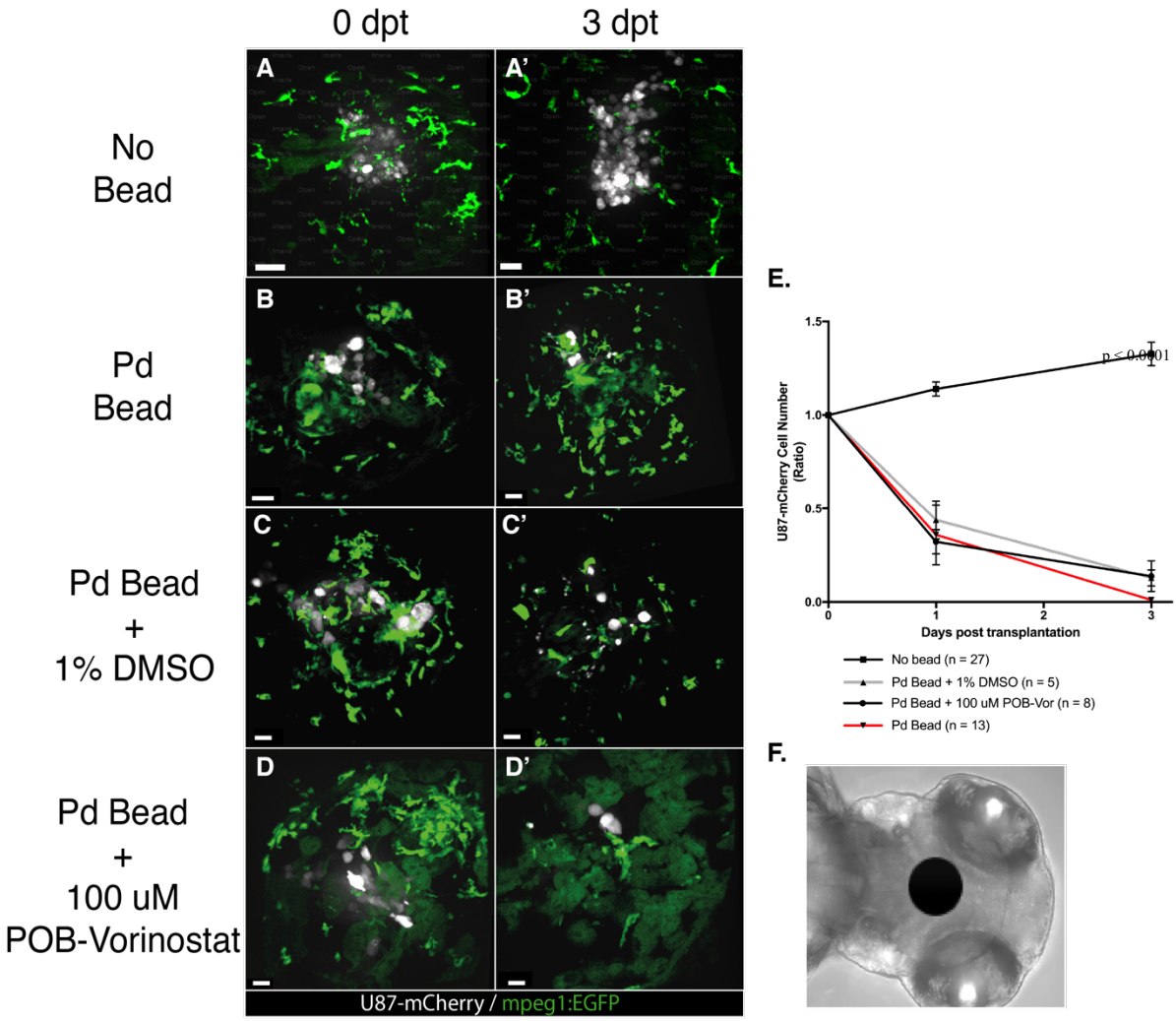

Figure 8. Palladium mediated anti-tumour effects observed in all palladium implanted zebrafish samples

(A-D) Human derived U87-mCherry (White) were xenografted into macrophage labelled (Green), 3 days post fertilized (dpf), mpeg1:EGFP zebrafish. Xenografted zebrafish were implanted with Palladium bead at 4 dpf (0 dpt). Palladium bead implanted zebrafish were treated with 1% DMSO in E3 medium or 100 μM POB-Vorinostat in E3 containing 1% DMSO. Images from left to right are in chronological order showing 0 and 3 day post bead transplantation (dpt). (A) U87-mCherry cells engrafted in the brain of the zebrafish. An increase in glioma cell mass was observed when comparing 0 dpt and 3 dpt. (B-D) The implantation of Palladium bead elicits a potent anti-tumour effect leading to a strong inhibition of U87-mCherry cell proliferation in all zebrafish samples. The implantation of Palladium bead in all zebrafish samples lead to a decrease in glioma cell mass in the zebrafish brain. All Images were captured using an Andor spinning disk confocal microscope with a 20X/NA 0.75 objective. Scale bars are set at 20 um

(E) U87-mCherry cell numbers are expressed as a ratio calculated by the number of cells at 1 or 3 day post transplantation (dpt) divided by the number of cells at 0 dpt. mpeg1:EGFP zebrafish xenografted with U87-mCherry (No bead) showed an increase in U87-mCherry cell number by 1.3 fold at 3 dpt. A potent anti tumour effect was observed in all zebrafish implanted with palladium bead. A significant, $p < 0.0001$, decrease in U87 cell number by 90% was recorded by 3 dpt.

(F) Brightfield image is representative of the orientation and imaging field of the fluorescent images shown in images A-D.

One way ANOVA statistical analysis and Tukey's multiple comparisons test were conducted to calulate p values. p values were indicated where statistically significant ($p < 0.05$). Error bar indicated standard error.

In the absence of the Palladium bead we observed the engraftment and proliferation of U87-mCherry cells in the brain. Although no cellular division was directly observed, U87-mCherry cell numbers increased by 1.3 folds by 3 days post bead transplantation (dpt). In addition, an increase in glioma mass was observed when comparing 0 dpt and 3 dpt (Figure 8A,E). In contrast, the implantation of Palladium bead into the brain of U87-mCherry transplanted mpeg1:EGFP zebrafish induced a strong inhibition of U87-mCherry cell proliferation. The impairment of U87-mCherry cells ability to engraft in the zebrafish brain was observed (Figure 8). The implantation of Palladium bead alone, in the absence of Vorinostat, resulted in a significant decrease in U87-mCherry cell count by 90% ($p < 0.0001$) at 3 dpt (Figure 8B, E). In addition, a decrease in glioma cell mass was observed in the zebrafish brain (Figure 8B, E). The same anti-tumour effect was replicated in all zebrafish samples implanted with the palladium bead including zebrafish treated with 1% DMSO and 100 μM Vorinostat (Figure 8C-E).

Furthermore, the implantation of Palladium bead in the *mpeg1:EGFP* zebrafish initiated a macrophage response that made distinguishing individual macrophages from one another difficult. Thus, a robust and reliable method was required to evaluate macrophage number as a result of Palladium bead implantation. Therefore, a correlative study was conducted to correlate the sum of intensity with the number of macrophages in the zebrafish brain. The sum of intensity was defined as the sum of pixel values of EGFP signals within the define sampling area. It was hypothesised that macrophage number would correlate with the sum of *mpeg1:EGFP* signal intensity values. To do so, double transgenic *mpeg1:EGFP* and *mpeg1:nls-Crimson*, nuclear labelled macrophages, zebrafish were implanted with Palladium beads and the effect on macrophage number and mpeg1:EGFP were evaluated

A positive correlation between the number of macrophage within the zebrafish brain and *mpeg1:EGFP* sum of intensity was demonstrated. A positive correlation coefficient (r) of 0.561 with a reported p value of 0.0016 was recorded when evaluating the number of *mpeg1:nls-Crimson* nuclear labelling and sum of intensity of *mpeg1:EGFP* signals. Thus the increase in *mpeg1:EGFP* intensity values positively correlated with an increase in the number

of macrophages. Evaluating the sum of *mpeg1:EGFP* intensity facilitated rapid and reliable quantification of macrophage number in the *mpeg1:EGFP* zebrafish brain.

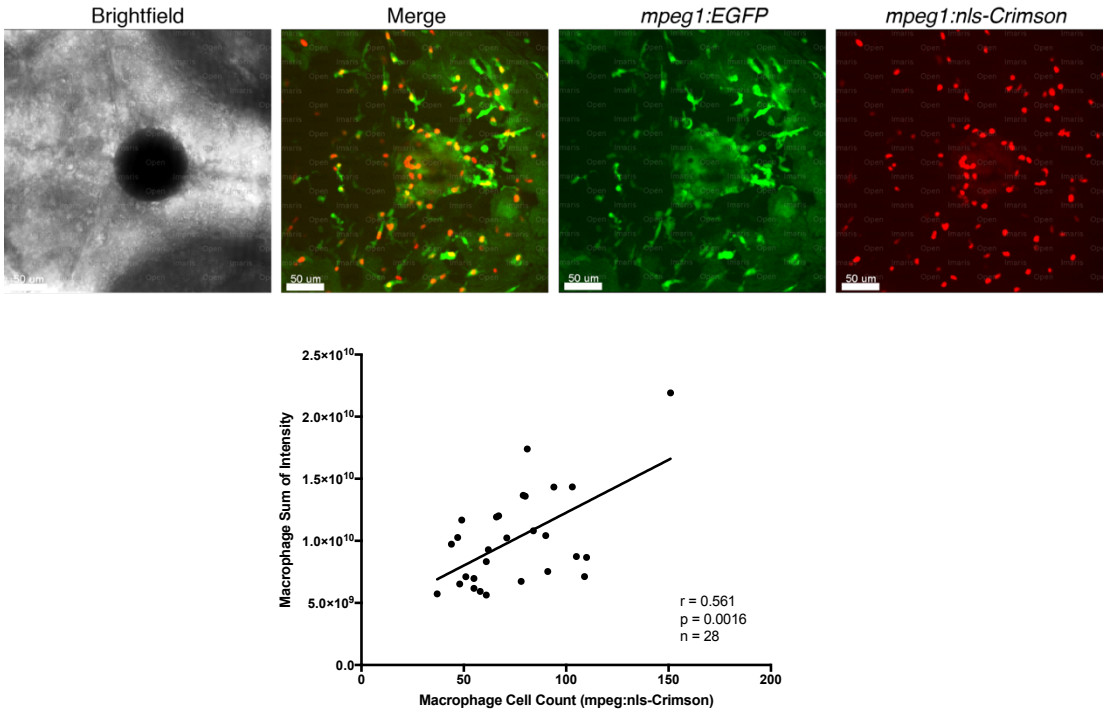

Figure 9. mpeg1:EGFP sum of intensity shows strong correlation with macrophage cell count.

Double transgenic tg(*mpeg1:EGFP:*mpeg1:Kal4/UAS:nls-Crimson), zebrafish were implanted with Palladium beads and the effect on macrophage number and *mpeg1:EGFP* signal intensities were evaluated. A positive correlation between the number of macrophage within the zebrafish brain and macrophage sum of intensity was demonstrated. A positive correlation coefficient (r) of 0.561 with a reported p value of 0.0016 was recorded when correlating the number of *mpeg1:Kal4/UAS:nls-Crimson* nuclear labelling and sum of intensity of *mpeg1:EGFP* signals. Images were captured using an Andor spinning disk confocal microscope with a 20X/NA 0.75 objective.

This initial study highlighted a novel mechanism that initiated anti-tumour responses as a result of Palladium bead exposure. The implantation of Palladium bead altered the zebrafish brain's physiological condition and led to U87-mCherry cell clearance. However, there were several questions that were raised as a result of this study. Was Palladium metal the effector of the associated anti-tumour responses or were these the effects of a reaction with the polystyrene matrix (bead) upon which the Palladium metal was bound to? How were

U87-mCherry cells being cleared? We hypothesised that Palladium bead implantation initiated an anti-tumour response in the zebrafish brain. To test this, we confirmed Palladium bead mediated anti-tumour efficacy and compared the antitumor effect to an injury model.

3.1.2. Palladium bead implantation recruits macrophages which initiates U87-mCherry cell clearance and engulfment.

To associate the anti-tumour phenotype directly to Palladium bead implantation, the anti-tumour effect of Palladium bead implantation was compared to an injury model. To replicate an implantation injury, Naked beads were implanted into the brain and immediately removed. This study aimed to test the hypothesis that *Palladium bead implantation initiated an anti-tumour response in the zebrafish brain*.

The implantation of Palladium bead initiated a potent anti-tumour phenotype in the zebrafish brain. Implantation of Palladium bead into mpeg1:EGFP zebrafish led to a significant decrease in U87-mCherry cell count by 73.4% at 3 dpt (Figure 10A-B). However, a proportion of the anti-tumour phenotype, could be attributed to the bead injury during implantation procedure. The injury model resulted in a significant decrease of 28.5%($p < 0.0001$) in U87-mCherry cell count at 3 dpt when compared to no bead controls. This indicated that the injury caused by the bead implantation procedure contributed to a proportion of the anti-tumour responses (Figure 10C-D). However, when comparing Palladium bead implanted (73.4%)and injured (28.5%) zebrafish, Palladium bead implantation led to a significantly ($p < 0.0001$) potent antitumor effect by 3 dpt (Figure 10). Intriguingly, a significant increase in macrophage number was observed in Palladium bead implanted zebrafish when compared to injured and bead null zebrafish. A four fold ($p < 0.0001$) increase in macrophage number in Palladium bead implanted zebrafish was observed by 3 dpt. In contrast, a two fold increase in macrophage number was observed in injured and bead null zebrafish. The increase in macrophage number coincided with high level of U87-mCherry cellular fragmentation in macrophages (Figure 10A, Pd Bead, Red arrows). U87-mCherry fragments were defined by pockets of mCherry fluorescent signal originating from mCherry cytoplasmic labelling encompassed by macrophage GFP signals (Figure 10A, Pd Bead, Red arrows). These fragmented signals originated from within macrophage when analysed closely in 3D using Imaris. It was highly unlikely that these fragments (4 to 10 μm) were live U87-mCherry cells as they

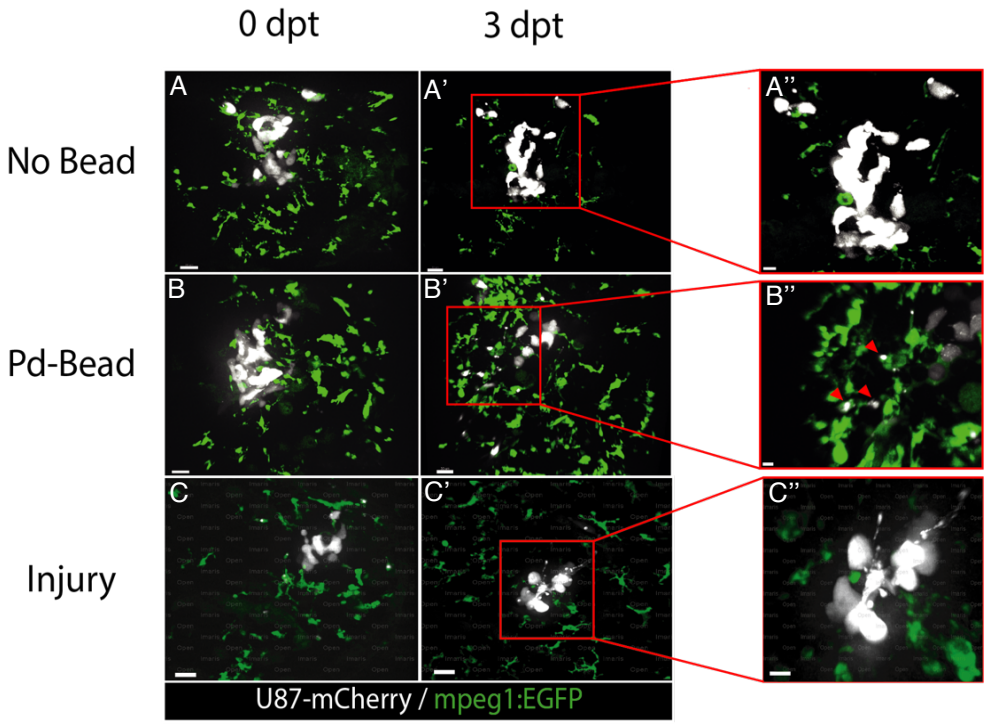
0 dpt
3 dpt
No Bead
Pd-Bead
Injury
A
A'
A''
B
B'
B''
C
C'
C''
U87-mCherry / mpeg1:EGFP

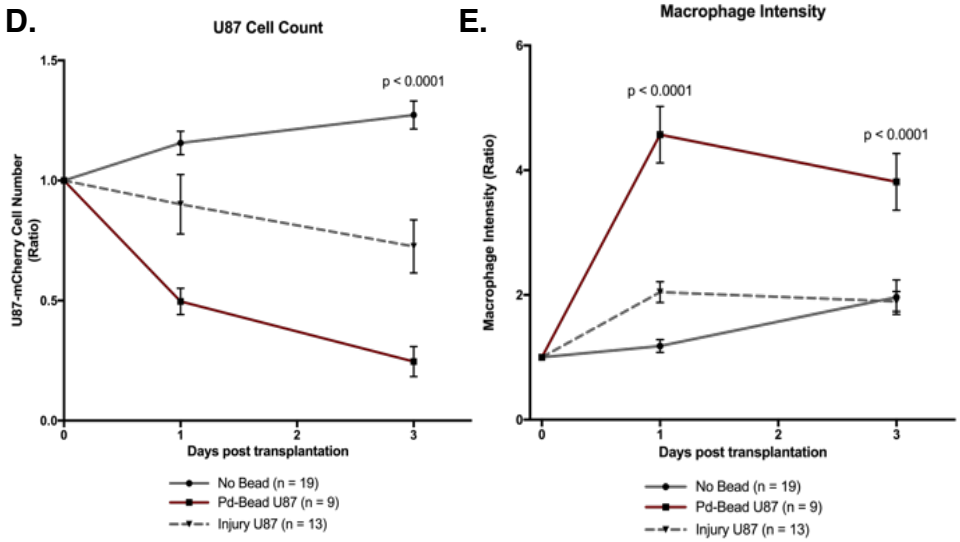
D.
U87 Cell Count
U87-mCherry Cell Number (Ratio)
p < 0.0001
Days post transplantation
No Bead (n = 19)
Pd-Bead U87 (n = 9)
Injury U87 (n = 13)
E.
Macrophage Intensity
Macrophage Intensity (Ratio)
p < 0.0001
p < 0.0001
Days post transplantation
No Bead (n = 19)
Pd-Bead U87 (n = 9)
Injury U87 (n = 13)

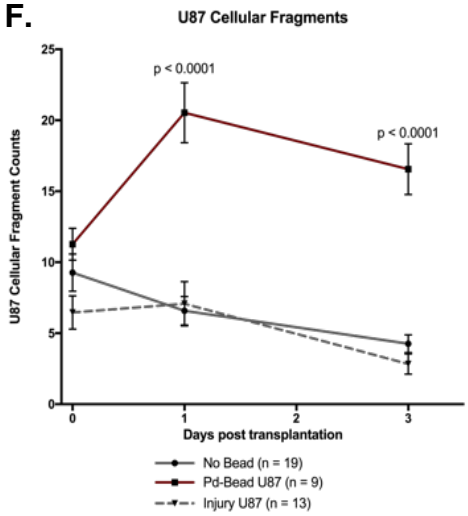
F.
U87 Cellular Fragments
U87 Cellular Fragment Counts
p < 0.0001
p < 0.0001
Days post transplantation
No Bead (n = 19)
Pd-Bead U87 (n = 9)
Injury U87 (n = 13)

Figure 10. Palladium bead implantation initiates U87-mCherry cell clearance and fragmentation.

(A-C) Human derived Lv-cppt-IRES-mCherry-opre transformed U87-mCherry cells (White) were xenografted into macrophage labelled (Green), 3 days post fertilized (dpf), mpeg1:EGFP zebrafish. Xenografted zebrafish were implanted with Palladium bead or injured with Naked beads at 4 dpf or 0 dpt. Images from left to right are in chronological order showing 0 and 3 day post bead transplantation (dpt). (A''-C'') The red box denotes the boundary for the higher magnification region of interest shown in the images on the far right column. (A) U87-mCherry cells engrafted in the brain of the zebrafish. An increase in glioma cell mass was observed when comparing 0 dpt and 3 dpt. (B) The implantation of Palladium bead recruited macrophages, initiated U87-mCherry cell clearance and fragmentation of U87-mCherry cells (B'', Red Arrows). U87-mCherry fragments were defined by pockets of mCherry fluorescent signal, originating from U87-mCherry cytoplasmic labelling, encompass by macrophage GFP signals (B'', Red Arrows). (C) The injury caused by the bead implantation procedure contributed to a proportion of the anti-tumour responses. U87-mCherry cells survived in the brain but did not proliferate. Images were captured using an Andor spinning disk confocal microscope with a 20X/NA 0.75 objective. Scale bars set at 50 μm

(D) U87-mCherry cell numbers are expressed as a ratio calculated by the number of cells at 1 or 3 day post transplantation (dpt) divided by the number of cells at 0 dpt. Injured zebrafish resulted in a significant ($p < 0.0001$) decrease of 28.5% in U87-mCherry cell count by 3 dpt when compared to no bead controls. However, implantation of Palladium bead led to the greatest decrease ($p<0.0001$) in U87-mCherry cell count of 80% by 3 dpt.

(E) A significant ($p < 0.0001$) increase by 4.2 fold in macrophage signal intensity was recorded when comparing Palladium bead implanted zebrafish to injured and bead null zebrafish conditions.

(F) High level of U87-mCherry cellular fragmentation in macrophages (Red arrows) was observed. Quantification of these fragments indicated that they were significantly ($p < 0.0001$) increased only in Palladium bead implanted zebrafish at 1 dpt

and 3 dpt.

One way ANOVA statistical analysis and Tukey's multiple comparisons test were conducted to calulate p values. p values were indicated where statistically significant ($p < 0.05$). Error bar indicated standard error.

were atypical in size when compared to live U87-mCherry cells (20 to 30 μm). Thus, these fragments were most likely products of engulfed U87-mCherry cells by macrophages. Quantification of these fragments indicated that they were significantly ($p < 0.0001$) increased only in Palladium bead implanted zebrafish at 1 dpt and 3 dpt (Figure 10D). In addition, an increase in macrophage intensity as a result of Palladium bead implantation in the brain was detected (Figure 10C). A significant ($p < 0.0001$) increase by 4.2 fold in macrophage signal intensity was recorded when comparing Palladium bead implanted zebrafish to the injured and the bead null zebrafish conditions (Figure 10C). This increase in macrophage intensity levels was sustained for the duration of the experiment and thus may indicate that Palladium bead implantation recruited macrophages.

In conclusion, this study confirmed Palladium bead mediated anti-tumour phenotype in the zebrafish. The implantation of Palladium bead led to the recruitment of macrophages

in the vicinity of the bead in addition to U87-mCherry cell clearance. The recruitment of these macrophages led to the engulfment of U87-mCherry cells, recorded in our study as an increase in U87-mCherry cellular fragmentation. This implies that macrophages played a key role in mediating the observed anti-tumour phenotype. Thus we hypothesized that *macrophages are key mediators of the Palladium bead induced anti-tumour phenotype.*

3.1.3. *irf8*$^{-/-}$ zebrafish reveals a possible role of macrophages in mediating Palladium bead induced anti-tumour phenotype.

In order to test the hypothesis that *macrophages are key mediators of the Palladium bead induced anti-tumour phenotype,* the same Palladium bead and injury experiments were repeated in the Interferon regulator factor 8 mutant (*irf8*$^{-/-}$) zebrafish. Interferon regulatory factor 8 (*irf*8) is an important regulatory factor for the development of macrophage in mammals and teleosts (Shiau et al., 2015). *irf8* is a key factor in early stage myelopoiesis of the immature zebrafish immune system during development (Shiau et al., 2015). Knock out of *irf8* in the zebrafish leads to the characteristic development of a macrophage null background up to around seven days post fertilization (Shiau et al., 2015). However, it is important to note that elevated neutrophils levels have also been reported in the *irf8*$^{-/-}$ mutant line (Shiau et al., 2015). Nonetheless, the *irf8*$^{-/-}$ zebrafish is an ideal candidate to facilitate the study of macrophage's contribution to Palladium induced anti-tumour activity.

The xenograft of U87-mCherry cells into *irf8*$^{-/-}$ zebrafish highlighted a strong impact of macrophages on tumour progression. We have previously reported that microglia, the brain's resident macrophages, and macrophages play an important role in promoting U87 cell growth and that the ablation of macrophage leads to tumour regression (Hamilton et al., 2016). Survival of U87-mCherry cells was significantly reduced in a microglia/macrophage null background *irf8*$^{-/-}$ zebrafish (Hamilton et al., 2016). Indeed, when analysing U87-mCherry cell count in *irf8*$^{-/-}$ bead null zebrafish versus mpeg1:EGFP bead null zebrafish, an impairment of 31.5% in U87-mCherry tumour progression was observed, $p < 0.001$(Figure 11E). Macrophage function was critical for U87 cell to engraft. Thus, this inherent disability of U87-mCherry cells to survive in the *irf8*$^{-/-}$ zebrafish would have affected all xenografted *irf8*$^{-/-}$ zebrafish (Figure 11D). Even so, a trend ($p = 0.109$) indicated that the Palladium mediated anti-tumour phenotype was attenuated in the *irf8*$^{-/-}$ zebrafish (Figure 11E). No significant difference was observed in U87-mCherry cell count of *irf8*$^{-/-}$ zebrafish of all three conditions, No Bead Controls, Palladium bead implanted and Injury controls (Figure 11D). In contrast the

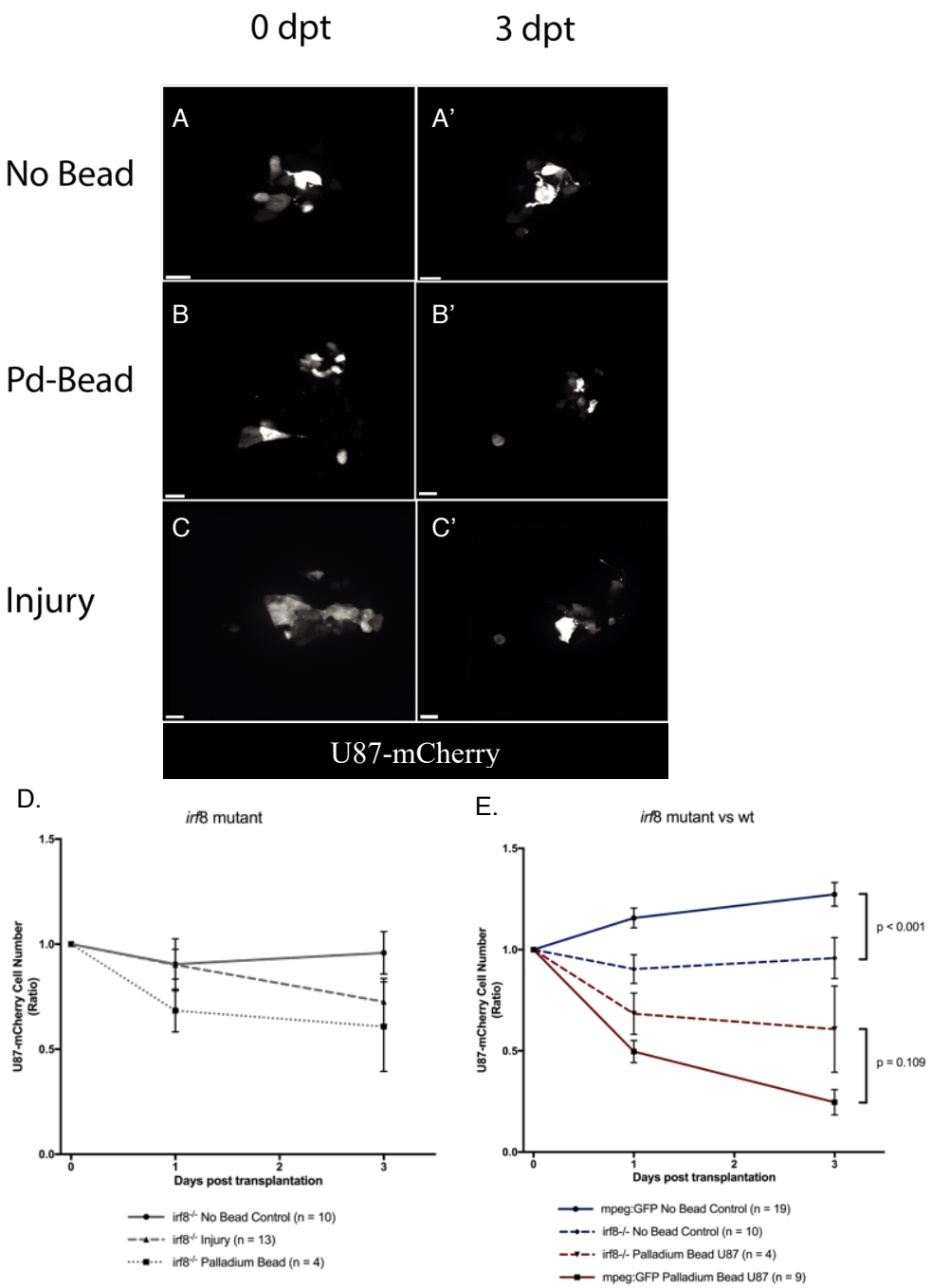

Figure 11. irf8$^{-/-}$ zebrafish reveal a possible role for macrophages in mediating Palladium bead induced anti-tumour phenotype.

Human derived U87-mCherry cells (White) were xenografted into 3 dpf *irf8*$^{-/-}$ zebrafish. At 4 dpf, *irf8*$^{-/-}$ U87-mCherry xenografted zebrafish were injured and Palladium beads were implanted. Images from *left* to *right* are in chronological order showing 0 and 3 day post bead transplantation (dpt).

(A-C) The xenograft of U87-mCherry cells in *irf8*$^{-/-}$ zebrafish highlighted a strong impact of macrophage on tumour progression. (D) No significance difference was observed in U87-mCherry cell count of *irf8*$^{-/-}$ zebrafish of all three conditions. (E) An impairment of 31.5% in U87-mCherry tumour progression was observed in *irf8*$^{-/-}$ bead null zebrafish versus mpeg1:EGFP bead null zebrafish. A trend (p = 0.109) indicated that the Palladium mediated anti-tumour phenotype was attenuated in the *irf8*$^{-/-}$ zebrafish. Images were captured using an Andor spinning disk confocal microscope with a 20X/NA 0.75 objective. Scale bars set at 20 μm. Error bars indicated standard error.

implantation of Palladium bead in wild type background (*mpeg1:EGFP* zebrafish), led to a significant decrease ($p<0.0001$) in U87-mCherry cell count by 73.4% at 3 dpt (Figure 10D, Figure 11E). A 73.4% decrease in U87-mCherry cell count was detected for Palladium bead implanted mpeg1:EGFP zebrafish versus the 35.1% in Palladium bead implanted *irf8*$^{-/-}$ zebrafish (Figure 11E). This indicated that the anti-tumour effect of Palladium bead was attenuated in the macrophage null background *irf8*$^{-/-}$ zebrafish. Thus implying that macrophage function was required in order to elicit the anti-tumour effect of Palladium bead implantation. However these results were not statically significant ($p = 0.109$). Therefore, this study only indicate a trend to support microglia/macrophage role in Palladium bead induced anti-tumour phenotype.

The aforementioned studies have shown Palladium beads as potent anti-tumour effectors. In addition, Palladium beads were seen to initiate an immune response that recruited macrophages to the brain. There was strong evidence to suggest that the recruitment of these macrophages coincided with increased U87-mCherry cell engulfment, fragmentation and clearance (Figure 10). In addition, a trend indicated that macrophage function was required in order to elicit the anti-tumour effects of Palladium bead implantation. Therefore, we speculated that Palladium bead implantation initiated an indirect effect on U87 cells mediated by macrophages to elicit an anti-tumour effect. Thus, we hypothesised that *macrophages contributed to Palladium mediated anti-tumour responses*.

3.1.4. Implantation of Palladium beads in the zebrafish brain did not cause aberrant necrosis in surrounding tissue.

To address if U87 cell death were the direct or indirect consequences of Palladium implantation, the necrotic effects of Palladium and Naked bead implantation in the surrounding tissue were investigated. Naked beads served as a 'foreign body' control to study the immune and anti-tumour response of the polystyrene bead independent of Palladium metal. Toxic consequences of Palladium bead implantation would have had significant effect on surrounding tissue necrosis detectable using *in-vivo* Propidium Iodide (PI) staining techniques (See section 2.2.8 for details). This study aimed to strengthen the argument that the anti-tumour effects mediated by Palladium bead implantation were initiated by in direct consequences mediated by macrophages. Propidium iodide is a membrane-impermeant nucleic acid stain that does not permeate live cells. The binding of propidium iodide to nucleic acids enhances fluorescence by 20 to 30 folds and thus has been widely used to stain necrotic cells (Sawai and Domae, 2011, Unal Cevik and Dalkara, 2003). Propidium iodide was applied to the zebrafish media solution of Palladium, Naked and Injured *mpo:EGFP* zebrafish (4 dpf) and imaged at 0, 1 and 3 days post bead transplantation (dpt).

The implantation of Palladium and Naked beads resulted in an increase in propidium iodide labelling when compared to injured zebrafish (Figure 12) Propidium iodide staining for bead implanted zebrafish at 0 dpt were observed to localize at the site of incision and vicinity of the beads (Figure 12A, Red Cicles). A three fold ($p = 0.0012$) increase in the number of propidium iodide labelled nuclei was recorded for Palladium bead implantation. While a two fold ($p = 0.0665$) increase in propidium iodide labelled nuclei was recorded for Naked bead implantation at 0 dpt (Figure 12C). The results here indicated that the trauma associated with the bead implantation procedure caused cellular necrosis of surrounding tissue. This was not surprising when considering a large incision was made during the procedure. It was also important to take into account the tissue damage caused by the bead implantation due to its large size, 75 μM, relative to the size of the zebrafish brain. These injury events would

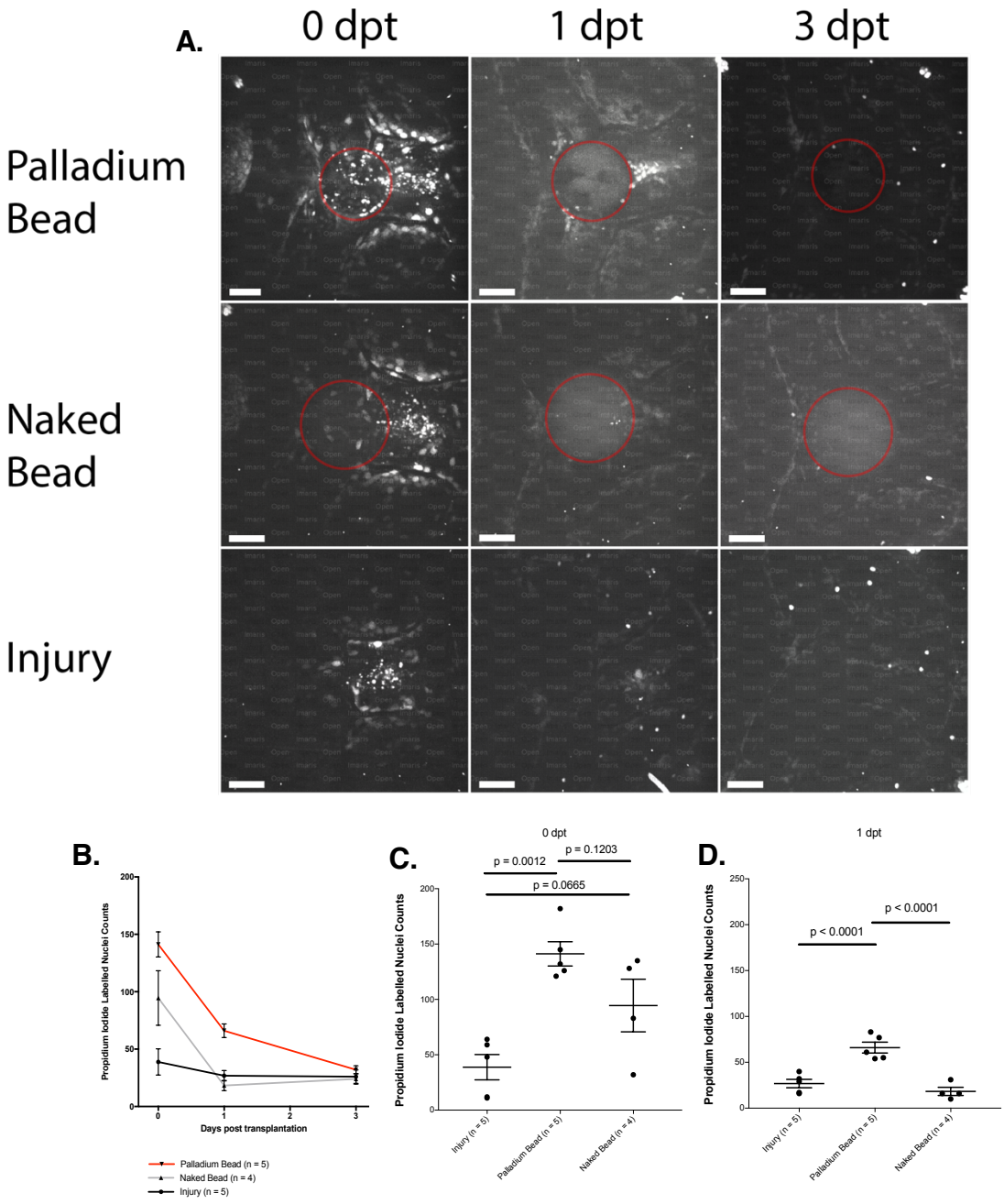

Figure 12. Implantation of Palladium and Naked beads did not initiate aberrant necrosis in the zebrafish brain.

(A) Images from rows *top* to *bottom,* mpo:EGFP zebrafish, 4 days post fertilized (dpf), were implanted with Palladium and Naked beads. Red circles in the images denote the boundary of the implanted beads. Injured zebrafish underwent the same bead implantation procedure where a naked bead was inserted but was removed immediately. Zebrafish were treated with 1 µg/ml propidium iodide in embryo media throughout the experiment. Images from *left* to *right,* time lapse imaging indicated that high level of propidium iodide necrotic cell labelling occurred during the early stages of the experiment immediately after Palladium and Naked bead implantation at

0 day post transplantation (dpt). A clearance of propidium iodide labelling was evident by 3 dpt for all bead implanted zebrafish. All Images were captured using an Andor spinning disk confocal microscope with a 20X/NA 0.75 objective. Scale bars set at 50μm.

(B) Palladium and Naked bead implantation induced an increase in the number of propidium iodide labelling at 0 dpt when compared to injured controls. Clearance of propidium iodide labelling occurred within 24 hours. Although, Palladium showed slower recovery. Propidium iodide labeling returned to injury control levels by 3 dpt indicating clearance of necrotic cells and recovery from initial bead implantation procedure.

(C) Palladium ($p = 0.0012$) showed significantly higher number of propidium iodide labelled cells at 0 dpt. Although not statically significant ($p = 0.0665$), a trend inidicates that the implatation of Naked bead increased propidium iodide cell labelling at 0 dpt.

(D) Palladium bead implanted zebrafish show significantly slower recovery from bead implantation procedure. Elevated propidium iodidie labelling was recorded at 1 dpt for Gold and Palladium implanted zebrafish when compared to both injury controls and naked bead implanted zebrafish.

One way ANOVA statistical analysis and Tukey's multiple comparisons test were conducted to calulate p values. p values were indicated where statistically significant ($p < 0.05$). Error bar indicated standard error.

cause the loss of membrane integrity and cellular necrosis which were detected through propidium iodide labelling. The recovery and clearance of propidium iodide nuclei cells was evident by 1 dpt in all bead implanted zebrafish (Figure 12A). Albeit, Palladium bead implanted zebrafish showed slower recovery to injury control levels when compared to Naked bead implanted zebrafish (Figure 12D). Nonetheless, a 60% decrease in propidium iodide labelled cells was observed by 1 dpt for Palladium bead implanted zebrafish. In addition, by 3 dpt, the decrease of propidium iodide labelling to injury control levels was recorded for all bead implanted zebrafish (Figure 12B). This indicated the clearance of necrotic cells and the recovery from the initial bead implantation procedure.

In conclusion, Palladium and Naked bead implantation did not cause aberrant cellular necrosis. Although, cellular necrosis was recorded in the surrounding tissue, these necrotic cell bodies were a direct consequence of the injury caused by the bead implantation procedure and not a reaction to the Palladium bead. Time lapse imaging indicated that the clearance of necrotic cell bodies was evident by 3 dpt for Palladium and Naked bead implanted zebrafish. In addition, despite the zebrafish being in constant incubation in 1 μg/ml Propidium iodide, no significant development of additional necrotic cell bodies was detected. Thus these results support our conclusion that bead implantation does not cause aberrant cellular necrosis. Therefore the anti-tumour effects observed were not a direct reaction to Palladium

metal on the polystyrene beads. These results in turn strengthens support for the hypothesis *that macrophages contributed to Palladium bead mediated anti-tumour phenotype in the zebrafish brain.*

3.2. RNA sequencing of macrophages isolated from palladium implanted zebrafish showed significant differentially expressed genes.

Macrophages have been well established to play a pivotal role in glioma formation in cancer biology (Graeber et al., 2002, Coniglio et al., 2012, Hamilton et al., 2016) (van Dalen et al., 2018, Prionisti et al., 2019). Macrophages infiltrate gliomas to promote tumour progression and can account for 30% of the glioma mass (Graeber et al., 2002, Coniglio et al., 2012, Li and Graeber, 2012). Infiltration of tumour associated macrophages also act to establish an immunosuppressive microenvironment that facilitates immune system avoidance of cancer cells (van Dalen et al., 2018). However, studies have shown that the polarisation of tumour associated macrophages from a pro-tumour to an anti-tumour phenotype can also occur as a result of the biological interactions with nanoparticles (Reichel et al., 2019). Consequently, tumour associated macrophages represent an attractive clinical target for immunotherapeutic strategies. Thus the discovery that Palladium bead implantation recruited macrophages and induced a potent anti-tumour phenotype may have profound contribution to our understanding of cancer biology. Therefore, to understand the genetic mechanisms underlying the associated anti-tumour responses in macrophages, RNA sequencing with next-generation sequencing was employed. It was hypothesised that *Palladium bead implantation would polarise macrophages towards an anti-tumour genetic expression profile.* The following differentially analysis was facilitated by Edinburgh Genomics.

3.2.1. Isolation of macrophages from mpeg1:EGFP zebrafish via Fluorescence Activated Cell Sorting (FACS).

Macrophages were isolated from mpeg1:EGFP transgenic zebrafish using Fluorescent Activated Cell Sorting techniques (FACS) (See section 2.3.2 for details). Macrophage were sorting for by gating for EGFP positive cells. It is important to note that the macrophages were isolated from approximately 200 individual embryonic brain tissue for each experiment. Zebrafish larvae were transected at the yolk sac and the heads isolated from the body. The heads were homogenised and macrophages isolated from the homogenised tissue. The total number of individual embryonic brain tissue used for each experimental group was 200 multiplied by the number of biological replicates, n (Figure 13A) Macrophages were isolated from three experimental groups: 1) *mpeg1:EGFP* zebrafish, 2) *mpeg1:EGFP*, U87-mCherry xenografted zebrafish, 3) *mpeg1:EGFP*, U87-mCherry xenografted, Palladium bead implanted zebrafish (Figure 13A, See also Table 4). Comparisons were made between each of the experimental groups to understand the underlying transcriptomic changes that Palladium beads induced. An average of 29,000 *mpeg1:EGFP* positive cells were sorted for each biological replicate. RNA was extracted from the sorted cells yielding a range of between 0.126 ng/µl to 0.830 ng/µl of total RNA product. RNA quality assessment was conducted for each sample with RNA Integrity Numbers (RIN) ranging between 8.3 and 10. The results here validated the macrophage isolation protocols and RNA extraction techniques used to isolate macrophage total RNA from homogenised zebrafish brain tissue. Each of the nine RNA sample was amplified using Ovation® RNA-seq System and sent to Edinburgh genomics. Further quality controls were conducted by Edinburgh Genomics to confirm high quality cDNA post amplification before DNA library preparation. DNA library preparation was conducted by Edinburgh Genomics using TruSeq DNA Nano gel free library prior to sequencing.

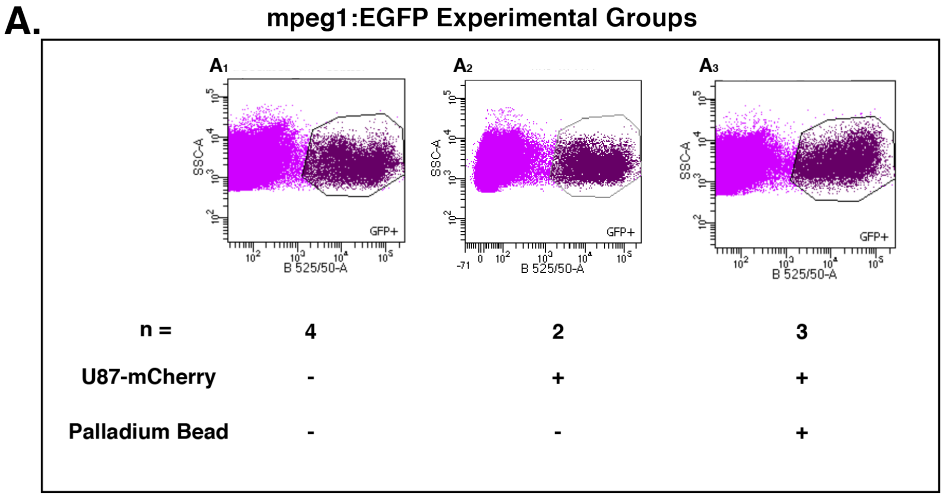

Figure 13. Fluorescence Activated Cell Sorting (FACS) of macrophages from the zebrafish brain.

(A) Macrophage, GFP positive cells, were isolated from homogenised brain tissues from three experimental groups: (A1) mpeg1:EGFP zebrafish. (A2) mpeg1:EGFP, U87-mCherry xenografted zebrafish. (A3) mpeg1:EGFP, U87-mCherry xenografted, Palladium bead implanted zebrafish. An average of 29,000 mpeg1:EGFP positive cells were sorted for each biological replicate. FACS was facilitated by in-house service provided by Shared University Resource Facility (SURF, QMRI) using FACS AriaII (BD Biosciences, Oxford, UK). The n number represents the number of biological replicates conducted for each experiment. Total number of larvae is n multipled by 200.

3.2.2. Principal component analysis of expression data reveal observable patters with respect to experimental factors.

Principal component analysis was conducted in order to study the level of structure in the data. Principal component analysis is a statistical tool that can be used to explore high-dimensional data (Ringner, 2008). Key to principal component analysis is reducing the dimensionality of the data without changing recorded variations in the data set (Ringner, 2008). This allowed visualization of complex data set, like those of large gene expression data sets, to identify clusters of highly similar data sets. PCA was applied to explore large data sets where thousands of variables had been measured. It allowed the visualization of samples to detect dominant patterns of gene expression of the expression data sets; Palladium versus Bead null versus U87 xenografted.

Initial Principal Component Analysis (PCA) revealed two distinct clusters of data sets and an outlier as shown in Figure 14A. The PCA plot of the first two principal components showed the clustering of RNA seq dataset from Palladium bead implanted zebrafish and clustering of control (mpeg1:EGFP, Palladium bead null and U87-mCherry null) with bead null U87 xenografted zebrafish. However, on further analysis of PCA plots of principal component 2 (PC2) and principal component 3 (PC3), only datasets from Palladium bead implanted zebrafish remained as a cluster (Figure 14B). Controls and bead null U87 xenografted zebrafish only clustered along the PC2 axis but were dispersed along the PC3 axis. This indicated that Palladium bead datasets were more related to one other than U87 and Control data sets were. These were early confirmatory signs that Palladium bead implantation initiated a change in genetic expression in macrophages before differential analysis was conducted. In addition, the PCA plots clearly identified an outlier that showed that the genetic expression data of Control6D1005 was far more different than any of the other samples were to each other (Figure 14A-B, Red Square). Further statistical investigation also concluded that Control6D1005 was an outlier as illustrated in a heatmap and hierarchal clustering dendrogram (Figure 14C). Outliers at this level have significant impact on differential analysis and may

mask underlying differentially expressed genes. Indeed when looking back at the experimental notes, it was discovered that a fungal infection of the zebrafish housing had taken hold. A fungal infection of the embryo media in the zebrafish housing can have significant impact on zebrafish health and consequently alterations in immune responses. Alterations in immune responses would contribute to the genetic drift of macrophages in Control6D1005 from all other samples. Therefore, the sample was removed from the analysis. Filtering and normalization was re-performed and new PCA plots was generated (Figure 15).

The revised PCA biplot (Figure 15A-B) showed the clustering of RNA seq dataset from Palladium bead implanted zebrafish in both plots (PC1 vs PC2 and PC2 vs PC3). This once again reinforces the similarity in expression data from Palladium bead implanted zebrafish and thus differential analysis could be conducted with high confidence of identifying differentially expressed genes. The removal of the outlier revealed underlying variations in expression datasets for both U87 and Control zebrafish (Figure 15A-B). PCA plots of the first two principal components showed that Control and U87 dataset no longer clustered together and were dissimilar from each other; an attribute that could be related to the date of experiment and genetic variability between clutches (Figure 15A). PCA plots of PC2 and PC3 only reinforced differences in expression datasets for Control and U87 as evident by a wide shotgun dispersal pattern of data sets (Figure 15B). Heatmap and hierarchical dendrogram supported observations from revised PCA plots showing clustering of datasets from Palladium bead implanted zebrafish (Figure 15C). Datasets from control and U87 zebrafish were shown to form a secondary cluster but similarities between Palladium bead implanted zebrafish were greater than similarities between U87 and Control datasets (Figure 15C). No discernible differences was evident to distinguish RNA expression dataset between U87 and Controls (Figure 15C) reflected by hierarchal structure of dendrogram.

The clustering of Palladium bead datasets in the principal component analysis indicated high probability of differentially expressed genes when comparing between groups. PCA analysis indicated early evidence that there may be no differences between Control and U87 dataset. The identification of outlier Control6D1005 in our dataset proved to be the most

useful application of pre-processing techniques in this study. Inclusion of Control6D1005 into differential analysis would have skewed the results and likely masked differential expressed genes. Thus, the exclusion of the dataset allows meaningful data to be extrapolated from differential analysis.

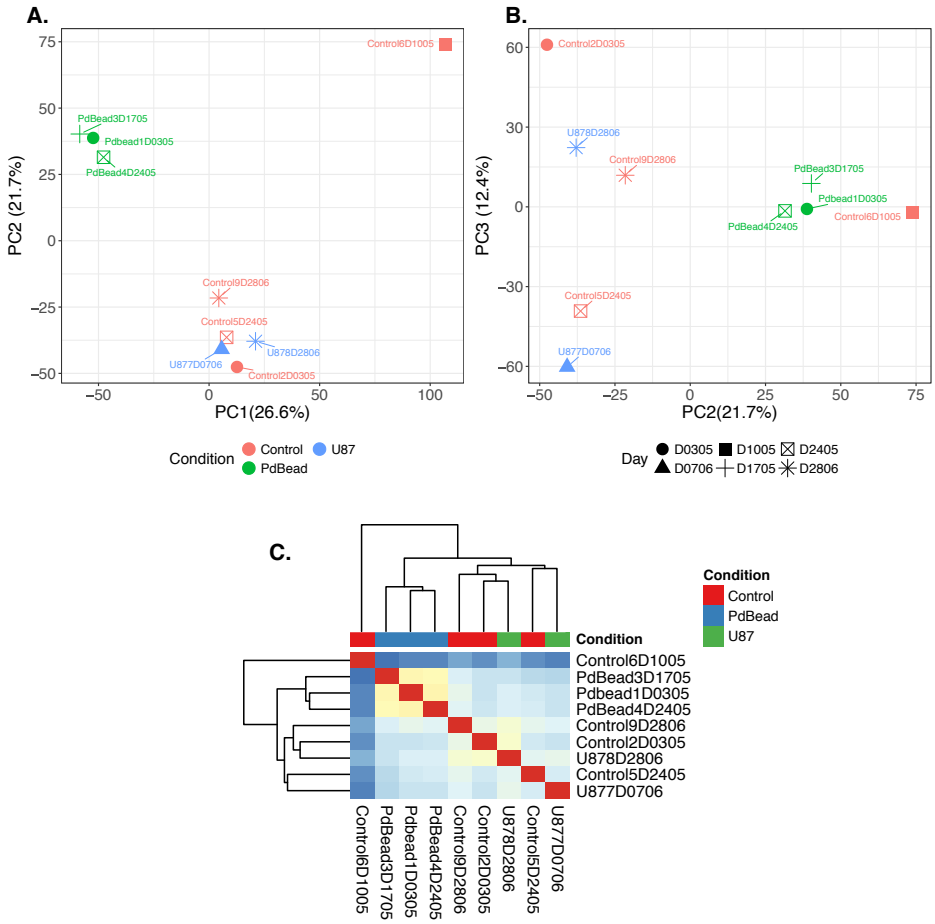

Figure 14. Principal component analysis (PCA) biplot, heatmap and hierarchical clustering dendrogram of expression data reveal outlier and patterns with respect to experimental conditions.

(A) PCA plots of the first two principal components (PC1 vs PC2) showed clustering of RNA seq dataset from Palladium bead implanted U87-mCherry xenografted *mpeg1:EGFP* zebrafish (Green, PdBead) and clustering of *mpeg1:EGFP*, Palladium bead null, U87-mCherry null controls (Red, Control) with bead null U87-mCherry xenografted *mpeg1:EGFP* zebrafish (Blue, U87). Prominent outlier, Control6D1005 (Red Square), sits outside the two clusters.

(B) PCA plots of principal component 2 and principal component 3 showed clustering of expression data sets from Palladium bead implanted samples (Green, PdBead). Datasets from Controls (Red, Control) and U87 (Red, U87) clustered along the PC2 axis but were dispersed along the PC3 axis. With one exception, Control6D1005 was plotted outside Control and U87 cluster and dispersed along the PC2 axis. Control6D1005 was an outlier when compared to dataset of Control and U87. In addition, PCA plot indicated that variations in genetic expression was as a result of experimental conditions and not due to variations in biological replicates conducted on different dates. Dates are reflected as D0305 where 0305 represents the third of May.

(C) Heat map and heirarchical clustering of dendrogram reinforces observations from PCA plots. The darker the colour the greater the difference in gene expression data. Control6D1005 showed highest variability in gene expression represented by the height of the dendrogram branch. Palladium bead implanted samples clustered together and showed strong similarities in genetic expression data. A secondary cluster formed showing similarites between Controls and U87 expression data sets.

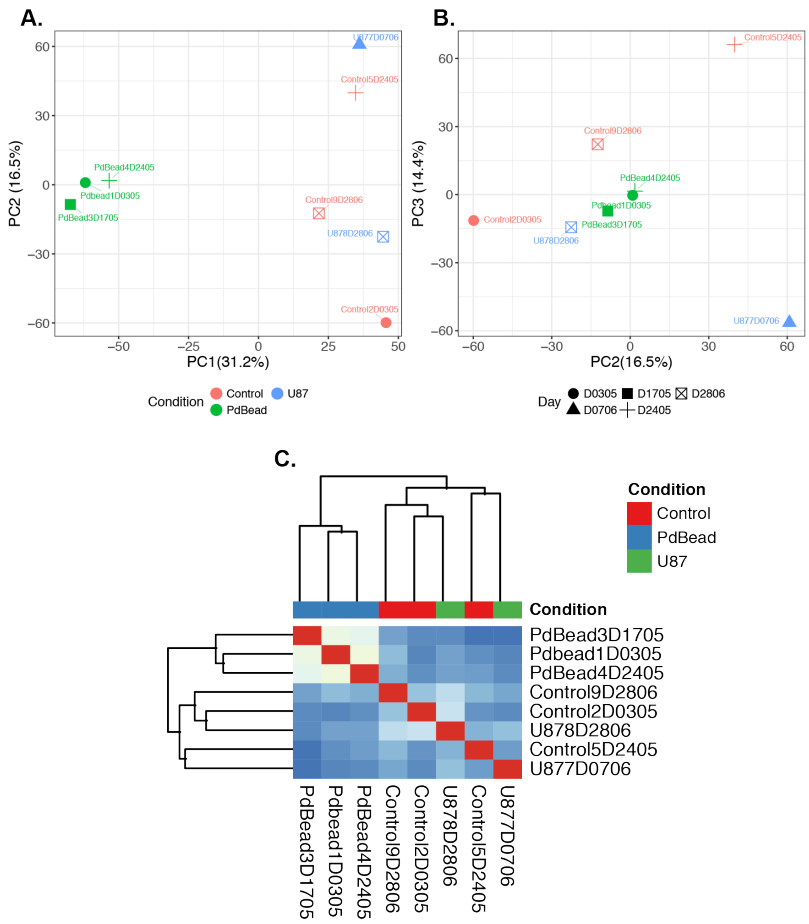

Figure 15. Revised Principal Component Analysis, heatmap and hierarchical clustering dendrogram of expression patterns with respect to experimental conditions.

(A) PCA plots of the first two principal components (PC1 vs PC2), without outlier Control6D1005, showed clustering of RNA seq datasets from Palladium bead implanted U87-mCherry xenografted *mpeg1:EGFP* zebrafish (Green, PdBead). PCA plots of dataset from Palladium bead null, U87-mCherry null controls *mpeg1:EGFP* zebrafish (Red, Control) and bead null, U87-mCherry xenografted *mpeg1:EGFP* zebrafish (Blue, U87) were dispersed along the PC2 axis showing little similarity.

(B) PCA plots of principal component 2 and principal component 3 again showing clustering of expression data from Palladium bead implanted samples (Green, PdBead). The PCA plot indicated that variations in genetic expression was as a result of experimental conditions and not due to variations in biological replicates conducted on different dates. Dates were reflected as D0305 where 0305 represents the third of May.

(C) Heat map and heirarchical clustering of dendrogram reinforced observations from PCA plots. The darker the colour the greater the difference in gene expression data. Palladium bead implanted samples clustered together and showed strong similarities in genetic expression data. A secondary cluster formed showing similarites between Controls and U87 expression data sets.

3.2.3. Differential analysis of RNA seq expression data reveal differentially expressed genes in Palladium bead implanted zebrafish.

To investigate if Palladium bead implantation induced alterations is genetic expression in macrophages, differential analysis of RNA seq expression data was conducted. Differential analysis, when filtered by a minimum fold change of 2 and a maximum False Discovery Rate of 0.05, revealed many genes to be significantly differentially expressed. The False Discover Rate (FDR) is a unit of measure used to evaluate the statistical significance (p values) of a differentially expressed gene corrected to the number of times the t-test was conducted. FDR is a better representation of significance than p values as it corrects for sample depth and decreased the probability of false positive or negatives. In total 750 genes were differentially expressed in Palladium bead implanted zebrafish when compared to controls; 389 genes upregulated vs 361 genes downregulated (Figure 16A). In contrast, 1014 genes were differentially expressed in Palladium bead implanted zebrafish when compared to U87; 524 genes upregulated vs 490 genes downregulated (Figure 16C). No significant differentially expressed genes were detected when comparing U87 and Control indicating that expression datasets of Control and U87 were very similar; an attribute previously predicted in PCA analysis (Figure 16B).

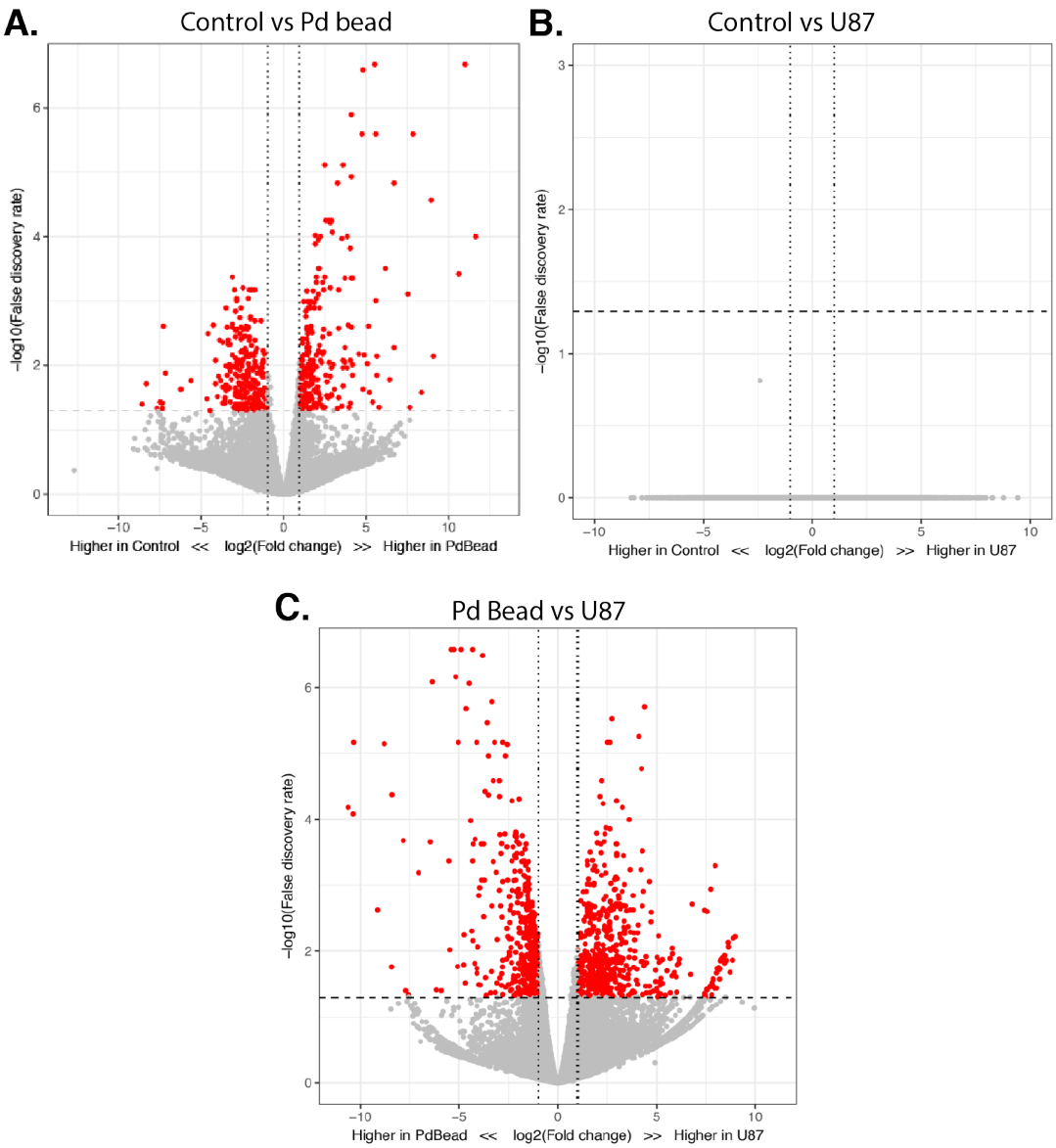

Contrast Name	Genes upregulated	Genes downregulated
A) Condition: PdBead vs Control	389	361
B) Condition: U87 vs Control	0	0
C) Condition: U87 vs PdBead	524	490

Figure 16. Differential expressed genes for each contrast according to a threshold of a minimum fold change of 2 and a maximum false discovery rate of 0.05.

Volcano Plots illustrating log(2) fold change vs -log(10) false discover rate. The horizontal dashed line represented the specified FDR thresehold significance value set at 0.05, vertical dotted lines represented the specified fold change threshold of 2 in both the positive and negative directions. Points passing through the thresholds were coloured in red. The table of statistics shows the numbers of differentially expressed genes for each contrast according to aforementioned thresholds.

3.2.4. Gene ontology enrichment analysis of differentially expressed genes in Palladium bead implanted versus Control zebrafish macrophages reveal shift in macrophage inflammatory polarisation.

To gain further insight into the functional consequences of the differentially expressed genes, gene ontology (GO) enrichment analysis was conducted. GO enrichment analysis is a genome wide statically tool that is useful to investigate if the differentially expressed genes were associated with certain biological process or molecular pathways. GO enrichment analysis compares the frequency of individually annotated differentially expressed genes against the zebrafish genome in order to identify enriched functional pathway that may explain the mechanisms leading to the anti-tumour phenotype in Palladium bead implanted zebrafish.

GO enrichment analysis of differentially expressed genes indicated greatest enrichment of pathways associated with oxidation-reduction process when comparing expression data of Palladium bead implanted zebrafish with Controls. Figure 17A illustrates a pie chart of all differentially expressed genes with a FDR of less than 0.05. The pie chart was categorised by the proportion of genes differentially expressed in each gene ontology category. As evident from Figure 17A, 42% of the genes that were differentially expressed were associated with the oxidation reduction process. Further investigation revealed differential expression in 23% of the 634 genes in the oxidation-reduction process (FDR = 0.039). In general, a greater proportion of these genes were upregulated than down regulated. Several key genes associated with cell redox homeostasis like homxa1, txn and nos1 were upregulated in Palladium bead implanted zebrafish (Figure 17B). The enrichment of oxidation-reduction processes in macrophages can alter macrophage activation profile and response to external stimuli as a result of Palladium bead implantation (Brune et al., 2013). However, redox signal regulation, despite contributing to a large proportion of the enriched pathways, would most likely be part of a larger network of signalling systems initiating the anti-tumour response. As expected, enrichment of pathways that responded to metals were up regulated (FDR = 0.0399). In particular, a three fold increase in genetic expression of the HSP70 family were recorded, hsp 70.1, hsp70.2, hsp70.3 and hsp70l. The HSP70 family of heat shock proteins are vital molecular chaperones that are critical in protein homeostasis (Evans et al., 2005, Murphy, 2013). In

addition, a 1.4 fold increase in expression of atp7a was recorded. atp7a is an important protein in the regulation of mitochondrial redox balance (Bhattacharjee et al., 2016). When combined, these proteins serve as a buffer for cells to tolerate environmental stresses, hypoxia and, most importantly, heavy metal exposure. An enrichment in protein transport pathways was also recorded in the macrophages of Palladium bead implanted zebrafish. An upregulation of 25% of 189 protein transport genes analysed was recorded. Enrichment of these genes made up 15% of the overall enrichment profile (Figure 17A). Upregulation of genes linked to protein transport described an increase in a whole host of generalised intracellular function ranging from cellular differentiation (vps11, ap2a1) to endocytosis (ap1b1,snx9b) and endosomal transport (snx1a). A large majority of the upregulated genes were genes predicted to form part of the clarthrin complex involved in vesicular transport of intracellular proteins. In addition, the upregulation of pro-inflammatory genes cxcl8b.1(4.5 fold) and tnf-α (3 fold) and downregulation of anti-inflammatory gene il-4 (1.4 fold) were recorded. tnf-α is a key cell signalling cytokine that is involved in systemic inflammation and responsible for acute phase reactions (Ciebiera et al., 2018). tnf-α had been described as an antineoplastic and antiangiogenic agent that can stimulate immune cells to kill cancer cells (Ciebiera et al., 2018). While on the other hand, *cxcl8b.1* is an orthologue of *il-8* in humans and is a potent attractant of neutrophils (Manfroi et al., 2017). Thus, the increase in *cxcl8b.1* expression may indicate the recruitment of neutrophils by macrophages. The combination of decreased *il-4* and increase *tnf-α* and *cxcl8b.1* signalling would suggest a pro-inflammatory phenotype of macrophages in Palladium bead implanted zebrafish. Altogether, these signalling molecules would initiate a potent acute phase inflammatory response of macrophages and perhaps neutrophils in the brain of the zebrafish. The evidence presented here provides early evidence that a stress induced inflammatory polarisation of macrophages occurs in Palladium bead implanted zebrafish.

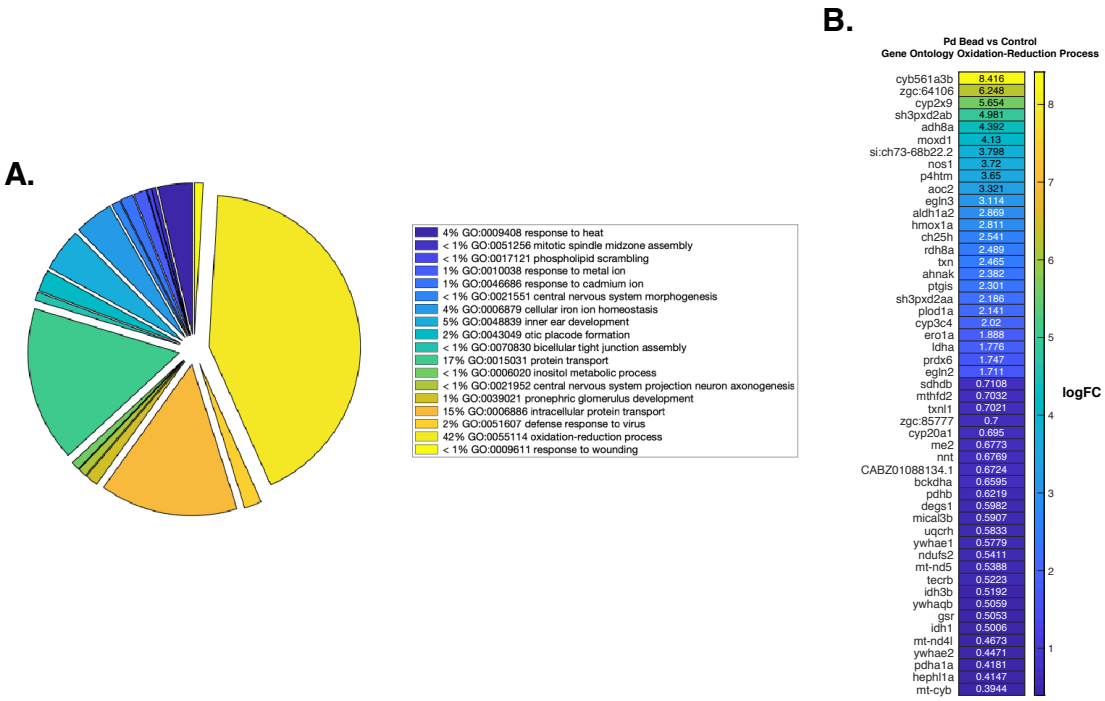

Figure 17. Gene ontology enrichment analysis of differentially expressed genes of isolated macrophages from Palladium bead implanted zebrafish versus control.

(A) Pie chart illustration of all differentially expressed genes with a FDR of less than 0.05. The pie chart is categorised by the proportion of genes differentially expressed in each gene ontology category expressed as a percentage.

(B) Heatmap of the top 20 upregulated and top 20 downregulated genes in the oxidation-reduction process. Expression values are indicatedas log(10) fold change where a logFC of 1 represents no change in genetic expression.

Heatmap and hierarchal dendrogram of the top 50 differentially expressed genes in Palladium bead versus Control illustrates clustering of genes described in oxidation-reduction process and metal ion sensing/responses (Figure 18). This again highlights a strong relationship between the two processes. In addition, hierarchal dendrogram classification of genes like *eno1a* and *txn,* genes associated in oxidative-reduction process, showed similarities with genes of unknown or predicted functions. For example, the genetic expression of *ch211–241c24.3* and *zgc:198419* were identified to be upregulated in Palladium bead zebrafish (Figure 18). Genetic functions of these genes were poorly documented. *ch211–241c24.3* had no documented function while *zgc:198419* was only predicted to sequester iron ion; Iron is a by-product of the uncoupling of oxygen atoms from iron during

oxidation processes (ZFIN, 2013). Multiple instances of significantly differentially expressed genes with undocumented functions showed strong relationship with either oxidative-reduction (Figure 18, Blue Text) or metal sensing (Figure 18, Red Text). This study, may for the first time, highlight a function for these undocumented genes in either of the described processes. Together, the genes associated with oxidative-reduction and metal response processes made up to 11 out of the top 50 differential expressed genes. This was strong evidence that these genes contributed to a significant proportion of the genetic expression profile that shaped macrophage inflammatory responses in Palladium bead implanted zebrafish.

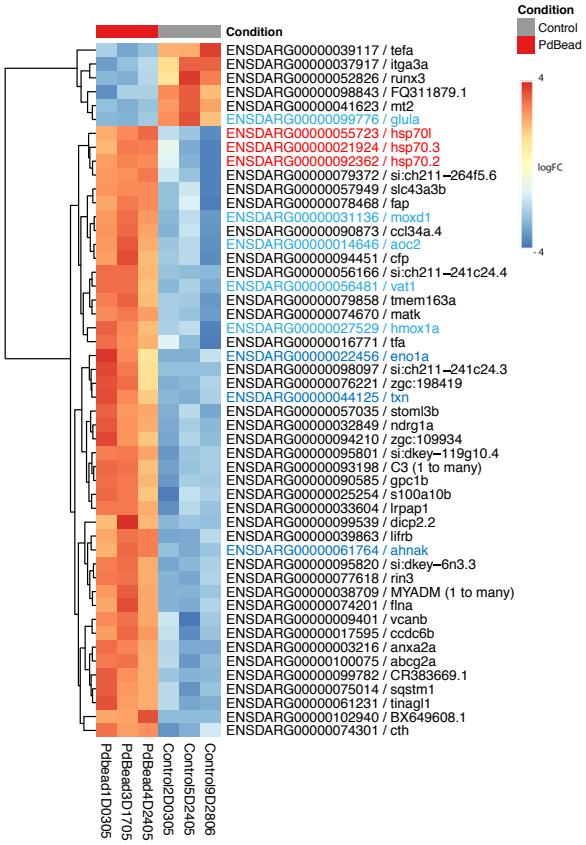

Figure 18. Heatmap and hierarchal dendrogram of top 50 differentially expressed genes in Palladium bead implanted versus Control zebrafish.

Genes described in oxidation-reduction process (blue text) and metal ion sensing/responses (red text) made up 11 out of top 50 differentially expressed genes. Values in heatmap were expressed as log fold change (logFC).

3.2.5. Differential expressed genes in macrophages isolated from Palladium bead implanted and U87 xenografted zebrafish revealed an inflammatory anti-tumour phenotype.

Further analysis of macrophage expression data comparing Palladium bead implanted zebrafish with bead null U87 xenografted zebrafish depicts an anti-tumour inflammatory profile in Palladium bead implanted zebrafish. Heatmap of the top 50 differentially expressed genes identified pro-tumoural inflammatory genes, *sema4D, sox7* and *apoc1* to be significantly expressed in U87 xenografted zebrafish and downregulated in Palladium bead implanted zebrafish (Figure 19). Both sema4D and sox7 are reported to be proangiogenic factors that promotes high-grade gliomas (Zhang et al., 2012, Sierra et al., 2008, Kim et al., 2018). A three fold increase in sema4D and four folds increase in sox7 expression was recorded in U87 xenografted zebrafish. Expression of sema4D and sox7 had both been linked to tumour associated macrophages (TAMs). TAMs were identified to be the main producers of sema4D in the tumour microenvironment and had been identified as novel immunotherapeutic target for cancer (Sierra et al., 2008, Wu et al., 2016). In addition, increased sox7 expression had been implicated to increase TAM recruitment and metastasis. Thus the down regulation of these protumoural genes in Palladium bead implanted zebrafish would have significant impact on tumour progression.

Differential analysis of Palladium bead versus U87 also indicated an increase in expression of genes associated with oxidative-reduction, stress tolerance, metal exposure and inflammation. The results here corroborate previous observations made in differential analysis of Palladium bead implanted versus Control zebrafish. The upregulation of *hsp70l*, *hsp70.2* and *hsp 70.3* proteins from HSP70 family were identified in the top 50 differentially expressed genes when comparing Palladium versus U87 zebrafish. In addition, evidence for oxidative stress was reported as *moxd1*, *porb*, *aoc2* and *ahnak*, genes in the oxidative-reduction process, were all reported to be in the top 50 differentially expressed genes. An upregulation of ten folds for cxcl8b.1 was recorded (FDR<0.0001) however, no significant differential expression of *tnf-α* (FDR = 0.305) or *il4* (FDR = 0.0950) was detected.

To gain further insight into the functional consequences of the differentially expressed genes in Palladium bead implanted versus U87 xenografted zebrafish, gene ontology enrichment analysis was conducted. Gene ontology enrichment analysis of oxidation-reduction process indicated an up regulation of the 28% of the 634 associated genes in Palladium bead implanted zebrafish. However it was not statistically significant with a reported FDR value of 0.0964. The greatest enrichment of pathways was associated with calcium ion transmembrane transport, accounting for 30% of the statistically significant enriched pathways where FDR < 0.05 (Figure 20). ARF protein signal transduction was the second most enriched pathways accounting for 11% of the significantly differential expressed genes. (Figure 20). The pie chart diagram in Figure 20 lists all the enriched pathways categorised proportionately by the number of significantly differentially expressed genes in each gene ontology category.

In conclusion, the combination of expression data from two distinct differential analysis (Palladium versus Control, Palladium versus U87) revealed different aspects of the genetic expression profile of macrophages exposed to Palladium beads. Macrophage exposure to external environmental stressors like Palladium metal stimulates an enrichment of pathways that increased its ability to tolerate stress. This was evident by the upregulation of HSP70 family proteins critical in protein homeostasis, stress tolerance and metal responses (Murphy, 2013) in addition to the enrichment of oxidative-reductive pathways that were characteristic of macrophages under cellular stress. This study also presented new evidence to indicate the possible involvement of neutrophils as increase *cxcl8b.1* was detected. This, combined with the upregulation of classical inflammatory cytokine *tnf-α*, and the downregulation of anti-inflammatory cytokine, *il-4*, depicted a pro-inflammatory profile of macrophage. Altogether, RNA sequencing data revealed a complex web of interconnected network of signalling systems that led to the polarisation of macrophage genetic profile towards a proinflammatory anti-tumour phenotype.

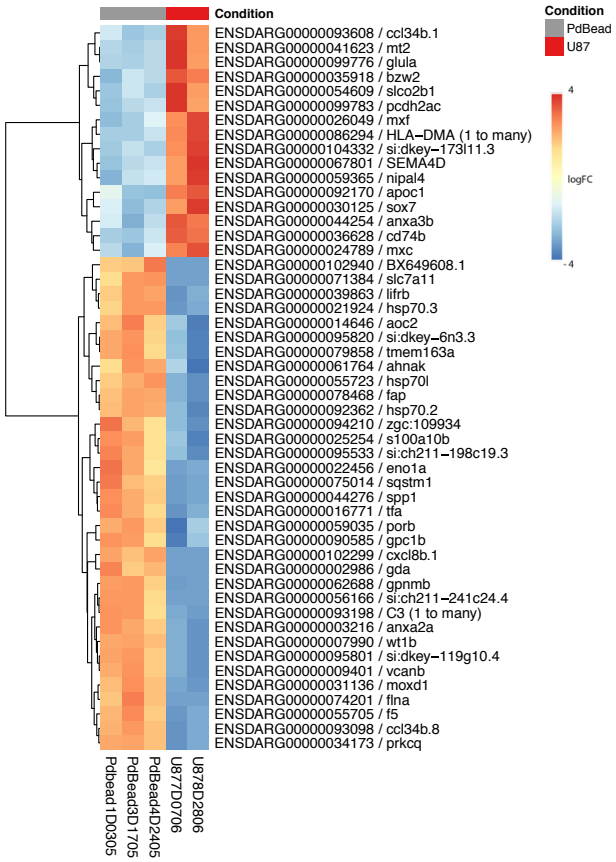

Figure 19. Heatmap and hierarchal dendrogram of top 50 differentially expressed genes in Palladium bead implanted versus U87 Xenografted zebrafish.

Expression data comparing Palladium bead implanted zebrafish with bead null U87 xenografted zebrafish depicts an anti-tumour inflammatory profile in Palladium bead implanted zebrafish. Pro-tumoural inflammatory genes, *sema4D, sox7* and *apoc1* are significantly expressed in U87 xenografted zebrafish and downregulated in Palladium bead implanted zebrafish Genes associated with oxidation-reduction process, *moxd1*, *porb*, *aoc2* and *ahnak* were all significantly expressd. The upregulation of *hsp70l*, *hsp70.2* and *hsp 70.3* proteins from HSP70 family were also identified in Palladium bead implanted zebrafish. Values in heatmap were expressed as log fold change (logFC).

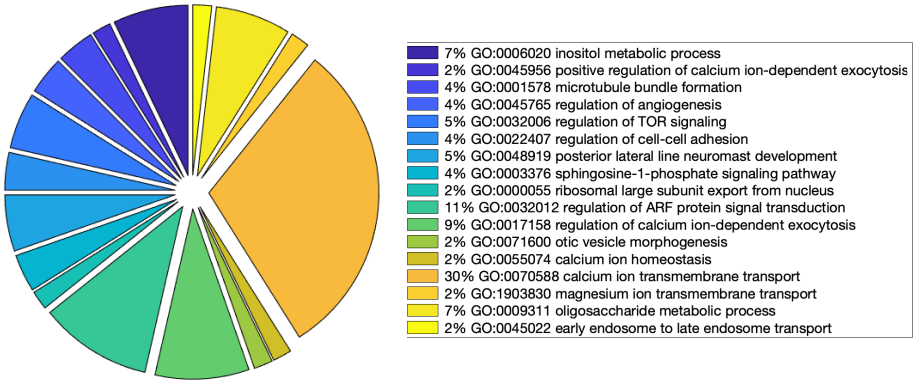

Figure 20. Gene ontology enrichment analysis of differentially expressed genes of isolated macrophages from Palladium bead implanted versus U87 xenografted zebrafish.

Pie chart diagram lists all significantly (FDR < 0.05) enriched pathways categorised proportionately by the number of significantly differentially expressed genes in each gene ontology category. Enrichment of pathways associated to calcium ion transmembrane transport accounted to 30% of the statistically significant enriched pathways. ADP-ribosylation factors (ARF) signal transduction was the second most enriched pathways accounting for 11% of the significantly differential expressed genes. Gene ontology enrichment analysis of oxidation-reduction process indicated an up regulation of the 28% of the 634 associated genes in Palladium bead implanted zebrafish. However it was not statistically significant with a reported FDR value of 0.0964.

3.3. Palladium and gold bead mediated anti-tumoral responses of macrophages

3.3.1. Gold triggered biorthogonal catalytic uncaging of fluorescent Rhodamine

The inherent anti-tumour effect of Palladium bead implantation made the Palladium bead incompatible for the development of biorthogonal catalytic chemotherapeutic assays in the zebrafish brain. Thus we explored the capability of another metal, Gold, as replacement for Palladium for the development of a robust biorthogonal catalytic drug delivery system. Gold has received enormous attention in recent years. Gold base products are safe to handle and has clinical applications in the treatment of rheumatoid arthritis (Pope et al., 2002). However, in chemistry, Gold is known for its catalytic properties and is able to mediate catalytic oxidative reactions at or below ambient temperature (Corma and Garcia, 2008, Stratakis and

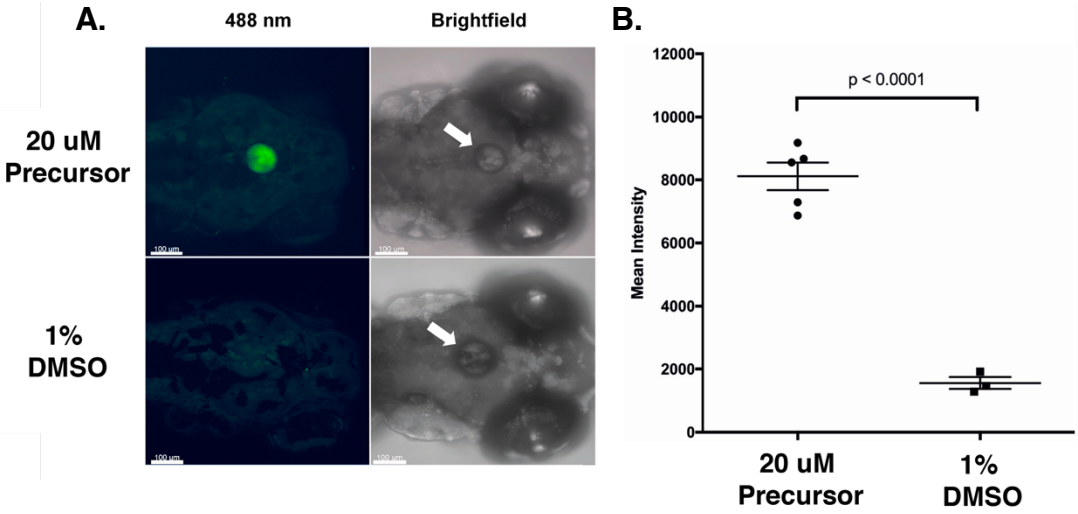

Figure 21. Gold bead catalyses prodye conversion to locally release fluorescent Rhodamine in the zebrafish brain.

(A) Image**s** from *left* to *right* showed GFP emission spectrum excited by 488 nm wavelenth laser and corresponding bright field images with white arrow indicating Gold bead. Images from *top* to *bottom* showed zebrafish embryos treated with 20 µM prodye precuror and 1% DMSO. The incubation of 20 µM prodye precursor for 24 hours resulted in a strong green fluorescent signal observable only in the gold bead implanted zebrafish larvae. All Images were captured using an Andor spinning disk confocal microscope with a 20X/NA 0.75 objective. Scale bars set at 100 µm. Error bar indicated standard error.

(B) Zebrafish treated with 20 µM Prodye precursor (n = 5) resulted in a significant increase in fluorescent intensity when compared to 1% DMSO (n = 3) treated zebrafish. Intensity values for each fish were expressed as a sum of intensity values of GFP signal.

Images adapted from Perez-Lopez et al., 2017.

Garcia, 2012). These properties has made Gold an attractive target in the development of nanotherapeutics (Takale et al., 2014, Yeo et al., 2018).

To investigate the chemical capabilities of gold as a catalyst to mediate prodrug activation, we studied Gold beads' catalytic properties to convert a nonfluorescent precursor into fluorescent Rhodamine *in-vivo*. We obtained Gold nanoparticles coated polystyrene beads and tested its catalytic properties and biocompatibility in the zebrafish. Gold beads were implanted into the brain of the wild type (WIK) zebrafish larvae and were treated with either 20 μM prodye precursor or 1% DMSO and imaged after 24 hours. The lipophilic properties of prodye precursor allows diffusion of the reagent in the media via ingestion or absorption via the skin and distribution systemically (Perez-Lopez et al., 2017). Under physiological conditions the prodye precursor is catalytically converted by the gold bead into fluorescent Rhodamine which is visible under excitation by 488 nm wavelength laser (Perez-Lopez et al., 2017). This study was the first time biorthogonal organometallic reaction was tested locally in an *in-vivo* system in the zebrafish brain with Gold beads (Figure 21) (Perez-Lopez et al., 2017).

The incubation of 20 μM prodye precursor for 24 hours resulted in a strong green fluorescent signal observable only in the Gold bead implanted zebrafish larvae (Figure 21A). An increase of approximately 4 fold in mean fluorescent intensity was observed in Gold bead implanted zebrafish (Figure 21B). The effect was statically significant, $p < 0.0001$, when compared to DMSO controls (Figure 21B). This study confirms the local generation of Rhodamine and the compatibility of Gold beads as an *in-vivo* catalyst to convert prodrugs in 24 hours. To extend this study, we further investigate the sustained functionality of the Gold beads *in vivo*. Ultimately, we tested the durability of the Gold beads to mediate the sustained release of fluorescent Rhodamine in an *in vivo* zebrafish system over three additional days.

Zebrafish larvae were implanted with Gold beads and were either persistently or pulse treated with prodye. Pulse treatment of Au bead implanted zebrafish occurred from 0 days post transplantation (dpt) to 1 dpt and 3 dpt to 4 dpt. A negative bead null control was also

included to understand if the release of fluorescent Rhodamine was mediated by Gold catalysis (Figure 6). The sustained treatment of Zebrafish larvae with precursor maintained a persistent generation of fluorescent Rhodamine in the brain localized in the vicinity of the Gold bead (Figure 22A, Group A). This was reflected by a high level of detectable fluorescence for

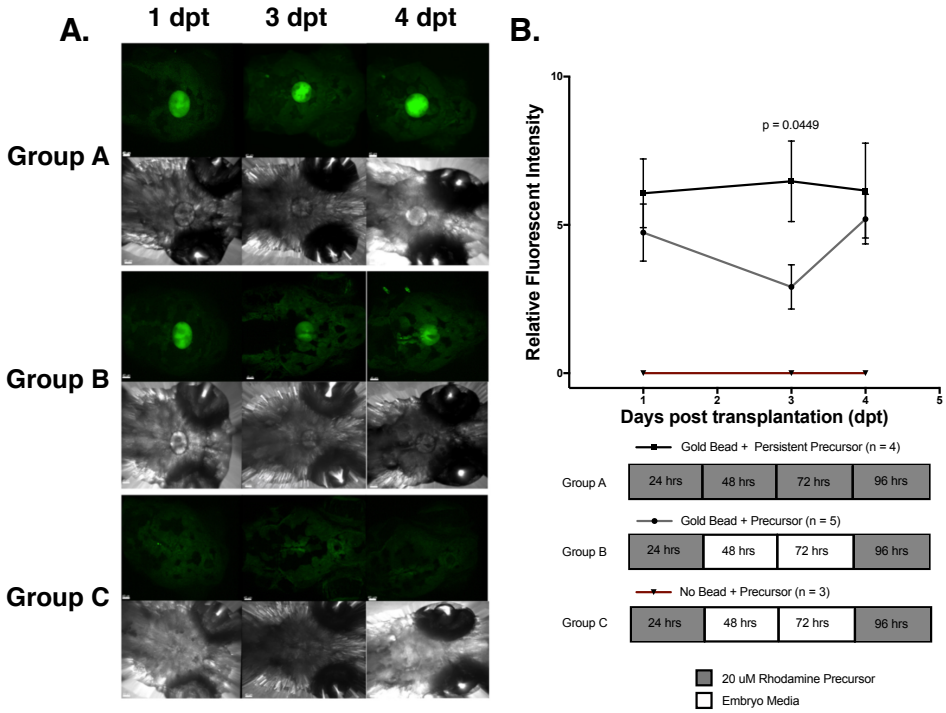

Figure 22. Gold bead mediated sustained released of fluorescent Rhodamine in the zebrafish brain.

Gold beads were implanted into wild type (WIK) zebrafish and were persistently treated with 20 µM prodye Rhodamine precursor containing 1% DMSO (Group A) or were pulse treated from 0 to 1 day post transplantation (dpt) and 3 to 4 dpt (Group B). Bead null wild type (WIK) zebrafish werepPulse treatment with 20 µM prodye Rhodamine cotaining 1% DMSO from 0 to 1 day post transplantation (dpt) and 3 to 4 dpt(Group C). The fluorescent intensity were relative to the sum of intensity of GFP signal of Gold bead implanted wild type (WIK) zebrafish treated with 1% DMSO. All Images were captured using an Andor spinning disk confocal microscope with a 20X/NA 0.75 objective. Scale bars set at 20 µm. Error bars indicated standard error. Images from *left* to *right* are in chronological order showing a time-course study of the release of fluorescent Rhodamine over 4 days post bead transplantation (dpt).

(A) Group A, sustained treatment with 20 µM prodye precursor maintained the persistent generation of fluorescent Rhodamine in the brain localized in the vicinity of the bead. Group B, pulse treatment with prodye precursor for 24 hours resulted in the generation of fluorescent Rhodamine which decayed over 48 hours. Second pulse treatment, following a 48 hour recovery phase, restored fluorescent intensity of the Gold bead. Group C, the absence of Gold bead led to no detectable fluorescence. Thus Gold beads were required for the generation of fluorescent Rhodamine.

(B) The decay in fluorescent intensity, after initial pulse treatment of 20 µM Precursor Rhodamine, led to a significant decrease ($p = 0.0449$) in fluorescent intensity from 4.73 ± 0.964 to 2.91 ± 0.745. Second pulse treatment, following a 48 hour recovery phase, restored fluorescent intensity of the Gold bead from 2.91 ± 0.745 to 5.20 ± 0.839. One way ANOVA statistical analysis and Tukey's multiple comparisons test were conducted to calulate p values. p values were indicated where statistically significant ($p < 0.05$). Error bar indicated standard error.

Images adapted from Perez-Lopez et al., 2017

the duration of the study relative to negative controls (Figure 22B). However, initial pulse treatment of prodye precursor for 24 hours resulted in the initial generation of fluorescent Rhodamine which decayed over time. The decay in fluorescent intensity led to a significant decrease ($p = 0.0449$) in fluorescent intensity from 4.73 ± 0.964 to 2.91 ± 0.745 (Figure 22A, Group B). The decrease in fluorescence intensity was most likely due to the metabolic clearance or diffusion into surrounding tissues of fluorescent Rhodamine in the zebrafish brain. More importantly, a second pulse treatment, following a 48 hour recovery phase, restored fluorescent intensity of the Gold bead to 5.19 ± 0.839 (Figure 22A, Group B). In addition, it was confirmed that the increase in fluorescent signal was dependent on the presence of the Gold bead. In the absence of the Gold bead no fluorescent signal was detected (Figure 22A, Group C).

This study highlighted the chemical capability of Gold as a biorthogonal catalyst to locally deliver caged compounds in the brain *in vivo*. In addition, Gold mediated catalytic reaction was sustainable over longer periods up to three days for this study, and may last even longer. This highlighted the Gold bead resin's durability *in vivo* and may have future applications in a chronic drug delivery systems. However, the biocompatibility of these Gold beads for *in vivo* applications remained in question. It was still unknown at this point if Gold bead implantation would elicit an immune or anti-tumour response in zebrafish previously observed in Palladium trials. The associated anti-tumour responses would make xenograft based caged drug trials, as attempted in Palladium studies, unfeasible. However, Gold had been proven to be biocompatible in humans and had wide applications in medical technologies ranging from dental implants to treatment of arthritis (Yeo et al., 2018). Thus, we hypothesised that *Gold beads did not stimulate an anti-tumour response in the zebrafish brain*. We aimed to do so by implanting Gold beads into the brains of *mpeg1:EGFP*, U87-nls-mKate2 xenografted, zebrafish and studied any associated anti-tumour and macrophage responses.

3.3.2. Palladium and Gold beads mediated anti-tumoral responses in *mpeg1:EGFP* zebrafish

To investigate the anti-tumour effects of Gold bead implantation, we compared the anti-tumour effects of Gold bead implantation to Palladium and Naked beads. These beads were implanted into U87-nls-mKate2 xenografted mpeg1:EGFP zebrafish. Naked beads serves as a 'foreign body' control to study the immune and anti-tumour response of the polystyrene bead independent of Gold or Palladium metal. These beads were implanted into the zebrafish at 4 dpf and imaged at 0 day post bead transplantation (dpt),1 dpt and 3 dpt (See section 2.2.6).

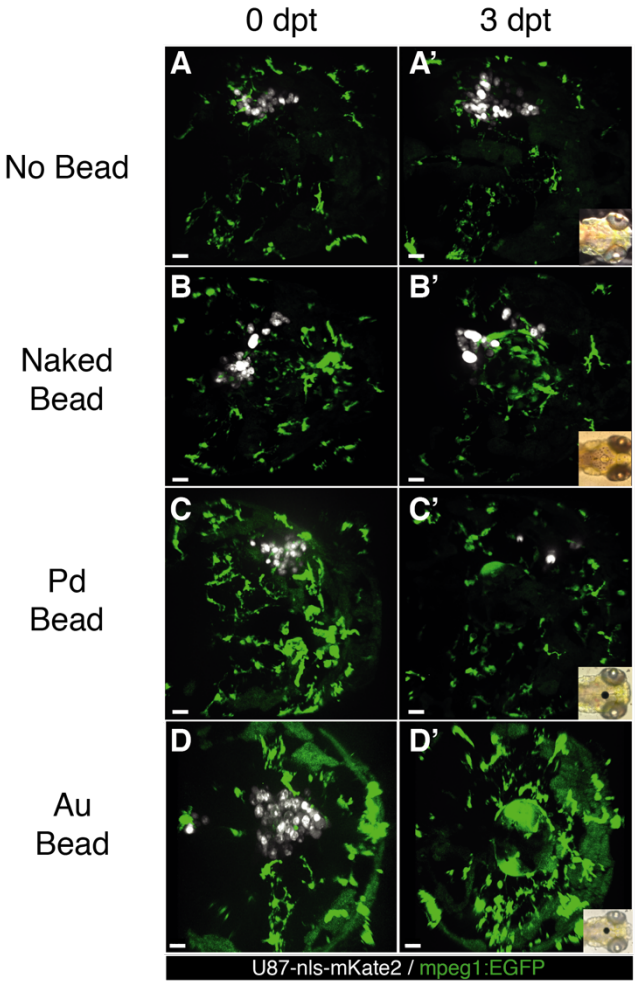

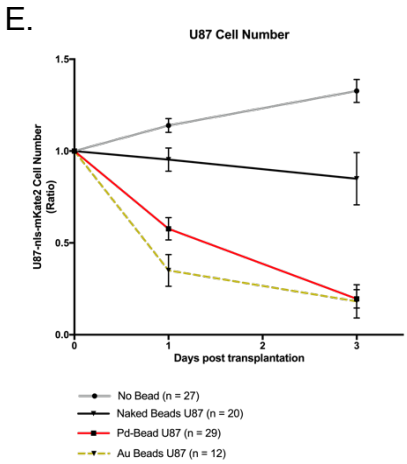

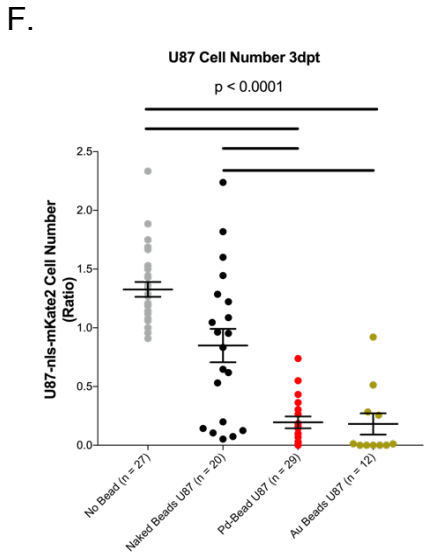

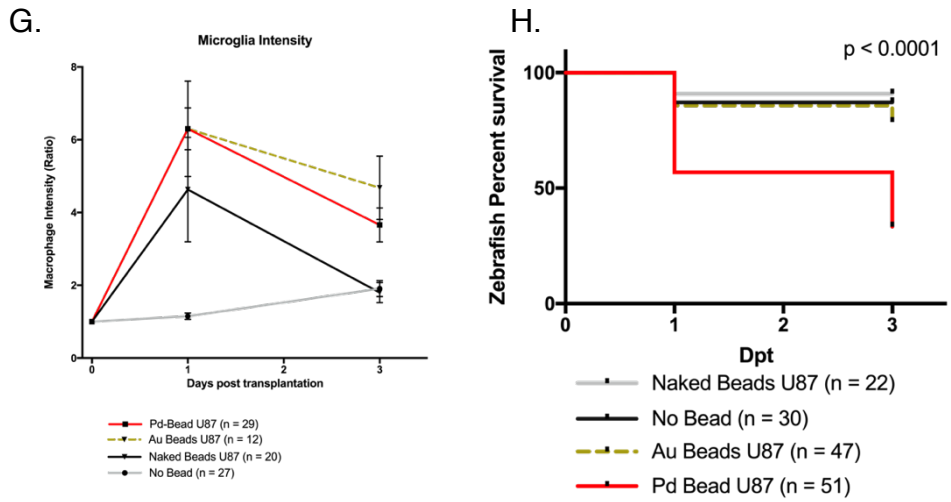

Figure 23. Macrophage anti-tumour responses is stimulated by palladium and gold bead implantation leading to decreased U87-nls-mKate2 cell counts.

(A-D) Human derived Lv-cppt-IRES-nls-mKate2-opre transformed U87-nls-mKate2 cells (White) were xenografted into macrophage labelled (Green) mpeg1:EGFP zebrafish (3 dpf). Xenografted zebrafish were implanted with Palladium bead transplantation at 4 dpf or 0 dpt. Images from *left* to *right* are in chronological order showing 0 and 3 day post bead transplantation (dpt) of palladium bead into the zebrafish brain. Images from *top* to *bottom* showing: (A-D) The implantation of naked beads inhibited the increase in U87-nls-mKate2 cell number observed in bead null control zebrafish. The implantation of Gold and Palladium beads resulted in a decrease in glioma cell mass by 3 dpt. Brightfield images on the *bottom right* corner of each A'-D' images and are representative of the orientation and imaging field of the fluorescent images. All Images were captured using an Andor spinning disk confocal microscope with a 20X/NA 0.75 objective. Scale bars set at 20 um.

(E) U87-nls-mKate2 cell numbers were expressed as a ratio calculated by the number of cells at 1 or 3 dpt divided by the number of cells at 0 dpt. Zebrafish only xenografted with U87-nls-mKate2 (No bead) showed an increase in U87-nls-mKate2 cell number by 1.3 folds. Zebrafish implanted with Naked beads showed a decrease in U87-nls-mKate2 cell count by 10%. Whereas, the implantation of Palladium or Gold bead significantly ($p = 0.0001$) decreased U87-nls-mKate2 cell count by 80% at 3 dpt.

(F) Gold and palladium bead implanted zebrafish showed an 80% decrease in U87-nls-mKate2 cell count at 3 dpt when compared to Naked bead implanted zebrafish and no bead zebrafish controls ($p<0.0001$). Zebrafish without any bead showed an increase of 1.3 fold in U87-nls-mKate cell count by 3 dpt showing engraftment and proliferation of U87-nls-mKate2 cells. Naked bead showed no significant increase in U87-nls-mKate2 cells and a trend to indicate that the U87-nls-mKate2 cells were not proliferating.

(G) Macrophage intensity are expressed as a ratio calculated by the sum of fluorescent pixel value of macrophage mpeg1:GFP labelled cells at 1 or 3 dpt divided by 0 dpt. Gold and Palladium bead implanted zebrafish showed highest levels of macrophage intensity values. A six fold increase in macrophage intensity was evident 1 dpt and the level of macrophage remains heightened for the duration of the experiment holding at a four fold increase at 3 dpt. Zebrafish implanted with naked beads showed an initial spike in macrophage levels by about four folds which recovered to bead null control levels at 3 dpt. Zebrafish without any beads showed a gradual developmental increase of macrophage levels from 0 to 3 dpt or 4 to 7 dpf.

(H) Palladium bead implantation into the zebrafish brain results in high toxicity and poor zebrafish survival. Only 33% of the zebrafish implanted with palladium bead survive the treatment. Naked bead and Gold bead showed no bead associated toxicity as the survival rates are identical to no bead control zebrafish.

One way ANOVA statistical analysis and Tukey's multiple comparisons test were conducted to calulate p values. p values were indicated where statistically significant ($p < 0.05$). Error bar indicated standard error.

As previously reported, bead null control mpeg1:EGFP zebrafish showed a 1.3 fold increase in cell number which indicated the engraftment and proliferation of U87-nls-mKate2 cells in the zebrafish brain (Figure 23A-B). In addition, a developmental increase of macrophage intensity levels by 2 fold was observed over the course of the experiment for bead null controls (Figure 23G) (Xu et al., 2015). The implantation of naked beads attenuated the increase in U87-nls-mKate2 cell number observed in bead null control zebrafish (Figure 23E-F). This coincided with an increase in macrophage intensity levels by 4.5 fold ($p < 0.0001$) at 1 dpt but recovered to control levels at 3 dpt (Figure 23G). This indicated that the injury and introduction of a foreign body in Naked bead implantations did elicit a degree of inhibitory effects on U87-nls-mKate2 cell proliferation. Nonetheless, when comparing Naked bead to Palladium and Gold bead implanted zebrafish, the inhibitory effect on U87-nls mKate2 survival and proliferative capability were only minor but was statically significant when compared to bead null controls at 3 dpt ($p < 0.0001$) (Figure 23C-C',4D-D'). Implantation of both Palladium and Gold bead implanted zebrafish resulted in a significant ($p < 0.001$) decrease of 80% in U87-nls-mKate2 cell count by 3 dpt (Figure 23E-F). In addition, a potent macrophage response to Palladium and Gold bead was observed. Both Gold and Palladium bead implantation increased macrophage intensity values six fold at 1 dpt and the effects persisted up to four fold at 3 dpt (Figure 23G). When compared to Naked beads, the implantation of Gold and Palladium bead led to significantly elevated macrophage levels in the zebrafish brain for the duration of the experiment (Figure 23G). Although, in the context of anti-tumour responses, the effects that Gold and Palladium induced were mirrored, the survival rates of Palladium bead implanted zebrafish were very different. Palladium bead implantation proved to be very toxic to the zebrafish (Figure 23F). Only one third of the zebrafish population implanted with Palladium beads survived the study by 3 dpt (Figure 23F).

In conclusion, Gold bead implantation resulted in the inhibition of U87-nls-mKate2 cell proliferation and decreased U87-nls-mKate2 cell survival; the effects were similar to Palladium bead implanted zebrafish. While on the other hand Naked bead implantation inhibited the proliferation of U87-nls-mKate2 cells in the zebrafish brain but not the cells capability to

survive in the zebrafish brain. The decrease in U87-nls-mKate2 cell proliferation and cell survival coincided with increased macrophage intensities only at 1 dpt. Macrophage intensities returned to basal level by 3 dpt. Macrophage intensities for Palladium and Gold bead implanted zebrafish remained elevated at 3 dpt when compared to Bead null and Naked bead zebrafish. This implied that Palladium and Gold bead implantation elicited an anti-tumour response that was mediated by macrophages in the zebrafish brain. In addition, it was evident that Palladium bead implantation into the zebrafish was toxic, an effect not observed in Gold bead implantation. This highlighted the biocompatibility of Gold in biological systems. Despite this, the anti-cancer phenotype rendered Gold bead incompatible for the development of an *in vivo* biorthogonal catalytic cancer drug screen system in the zebrafish brain. Nevertheless, the discovery that Palladium and Gold bead implantation initiated an anti-tumour responses in the zebrafish brain, warranted further investigation. Thus further investigation was conducted to elucidate the underlying mechanisms that dictated the anti-tumour milieu established by Gold bead implantation. We speculated that Gold bead implantation, similar to Palladium bead implantation, initiated an indirect effect on U87 cells mediated by macrophages to elicit an anti-tumour effect. Thus, we hypothesised that *macrophages contributed to Gold bead mediated anti-tumour responses*.

3.3.3. Implantation of Palladium and Gold beads in the zebrafish brain did not cause aberrant necrosis in surrounding tissue.

To address if U87 cell death were the direct or indirect consequences of Palladium and Gold bead implantation, the necrotic effects of Palladium, Gold and Naked bead implantation in the surrounding tissue were investigated. We contrasted the effects of Gold and Palladium bead implantation on Propidium iodide staining to understand if Gold bead implantation elicited similar effects as observed previously in Palladium bead implanted zebrafish. Propidium iodide was applied to the zebrafish media solution of Palladium, Gold, Naked and Injured *mpo:EGFP* zebrafish (4 dpf) and imaged at 0, 1 and 3 days post bead transplantation (dpt).

The implantation of Gold resulted in an increase in propidium iodide labelling when compared to injured zebrafish (Figure 24.) Similar to Naked and Palladium beads, the implantation of Gold bead led to Propidium iodide staining localizing at the site of incision and vicinity of the beads (Figure 24A, Red Cicles). Gold ($p = 0.0004$) and Palladium ($p = 0.0008$) bead implantation elicited similar increase (three fold) in the number of propidium iodide labelled nuclei. The recovery and clearance of propidium iodide nuclei cells was evident by 1 dpt in all bead implanted zebrafish (Figure 24A). However, Gold bead implanted zebrafish also showed slower recovery to injury control levels when compared to Naked bead implanted zebrafish (Figure 24D). The rate at which propidium iodide labelling were being cleared in Gold bead implanted zebrafish mirrored that of Palladium bead implanted zebrafish. At 1 dpt, both Gold and Palladium bead implanted zebrafish showed a 60% decrease in propidium iodide labelled cells while propidium iodide labelling in Naked bead implanted zebrafish returned to injury control levels. However, by 3 dpt, propidium iodide labelling in Gold and Palladium bead implanted zebrafish returned to injury control levels. A 60% decrease in propidium iodide labelled cells was observed by 1 dpt for Gold and Palladium bead implanted zebrafish. In addition, by 3 dpt, the decrease of propidium iodide labelling to injury control levels was recorded for all bead implanted zebrafish (Figure 24B). This indicated the clearance of necrotic cells and the recovery from the initial bead implantation procedure.

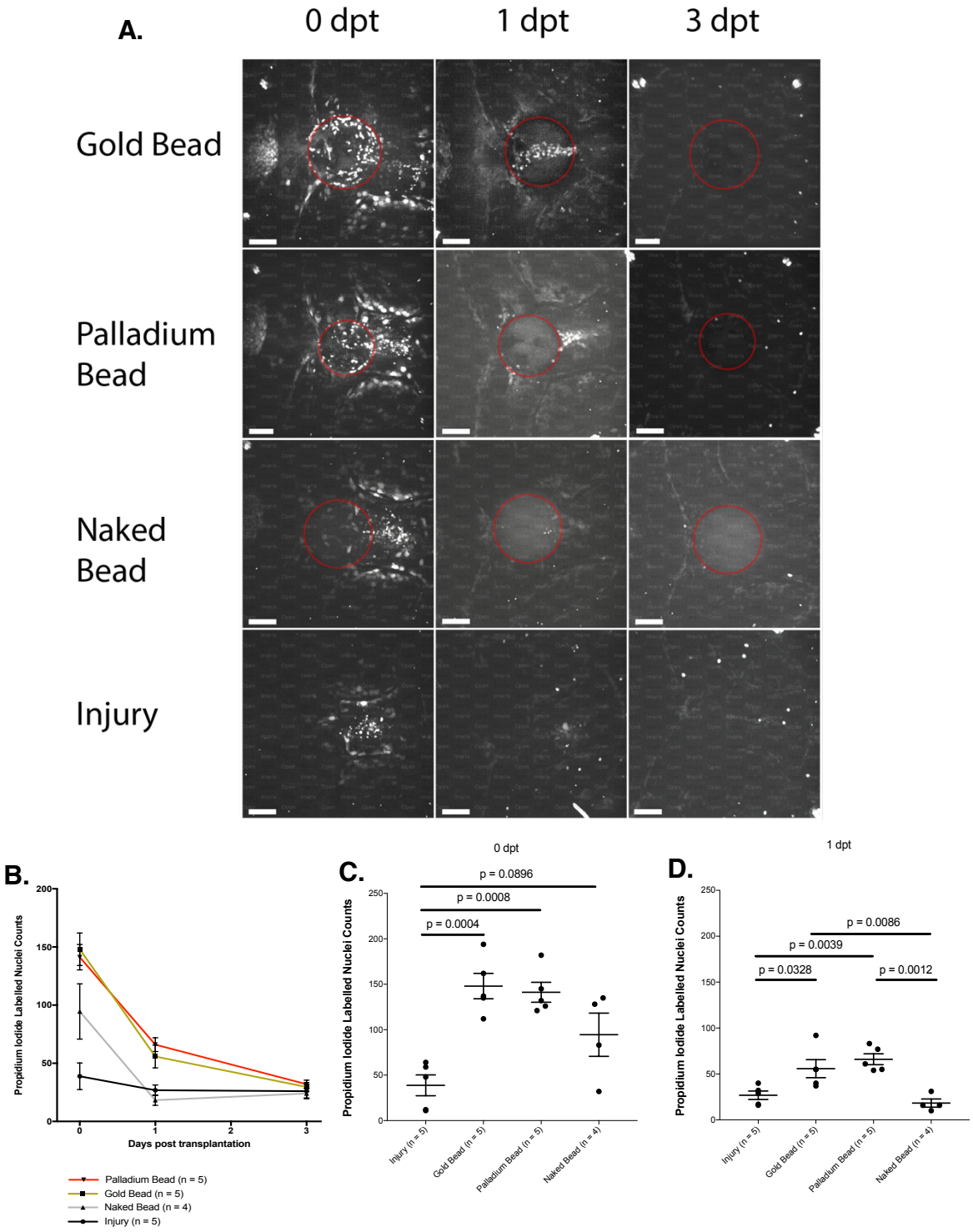

Figure 24. Implantation of Gold, Palladium and Naked beads did not initiate aberrant necrosis in the zebrafish brain.

(A) Images from rows *top* to *bottom,* mpo:EGFP zebrafish, 4 days post fertilized (dpf), were implanted with Gold, Palladium and Naked beads. Red circles in the images denote the boundary of the implanted beads. Injured zebrafish underwent the same bead implantation procedure where a naked bead was inserted but was removed immediately. Zebrafish were treated with 1 µg/ml propidium iodide in embryo media throughout the experiment. Images from *left* to *right,* time lapse imaging indicated that high level of propidium iodide necrotic cell labelling occurred during the early stages of the experiment immediately after Gold, Palladium and Naked bead

implantation at 0 day post transplantation (dpt). A clearance of propidium iodide labelling was evident by 3 dpt for all bead implanted zebrafish. All Images were captured using an Andor spinning disk confocal microscope with a 20X/NA 0.75 objective. Scale bars set at 50μm.

(B) Gold, Palladium and Naked bead implantation induced an increase in the number of propidium iodide labelling at 0 dpt when compared to injured controls. Clearance of propidium iodide labelling occurred within 24 hours. Although, Gold and Palladium showed slower recovery. Propidium iodide labeling returned to injury control levels by 3 dpt indicating clearance of necrotic cells and recovery from initial bead implantation procedure.

(C) Gold ($p = 0.0004$) and Palladium ($p = 0.0008$) showed significantly higher number of propidium iodide labelled cells at 0 dpt. Although not statically significant ($p = 0.0896$), a trend inidicates that the implatation of Naked bead increased propidium iodide cell labelling at 0 dpt.

(D) Gold and Palladium bead implanted zebrafish show significantly slower recovery from bead implantation procedure. Elevated propidium iodidie labelling was recorded at 1 dpt for Gold and Palladium implanted zebrafish when compared to both injury controls and naked bead implanted zebrafish.

One way ANOVA statistical analysis and Tukey's multiple comparisons test were conducted to calulate p values. Error bar indicated standard error.

In conclusion, Gold bead implantation did not cause aberrant cellular necrosis. Both Gold and Palladium bead implantation displayed identical levels of propidium labelling over 3 days of experimentation. We observed the clearance of necrotic cell bodies by 3 dpt for all bead implanted zebrafish and no new development of additional necrotic cell bodies were detected. Therefore, as in Palladium bead implanted zebrafish, the anti-tumour effects of Gold bead implantation were not a direct reaction to solidly supported Gold nanoparticles on the bead. These results support the hypothesis *that macrophages contributed to Gold bead mediated anti-tumour phenotype in the zebrafish brain.*

3.4. TLR receptor family mediates anti-tumour responses in Gold bead implanted zebrafish.

Macrophages can undergo significant phenotypic changes in response to molecular signals from their environment (Biswas et al., 2013). The biological effects of various disassociated nanoparticles on macrophage polarization has been reviewed recently (Reichel et al., 2019) and in some cases a strong anti-tumour immunological response was initiated (Bastus et al., 2009b, Zanganeh et al., 2016). The degree of macrophage polarization is highly dependent on the nanoparticle composition and size (Reichel et al., 2019). In this study, Palladium and Gold nanoparticles were solidly supported within a polyethylene glycol (PEG)-grafted low cross linked polystyrene matrix and not dissociated (Perez-Lopez et al., 2017). Macrophages were observed to form intimate interactions on the surface of Palladium and Gold beads (Figure 23D'). In addition, we showed macrophage numbers increased as a result of Palladium and Gold bead implantation (Figure 23G). Thus, there was strong evidence for the formation of intimate interactions of macrophages with Gold and Palladium beads. The effects of these interactions between macrophages and either Gold or Palladium have been previously reported (Bastus et al., 2009a, Reichel et al., 2019, Schmidt and Goebeler, 2015). The internalization of Gold nanoparticles by macrophages has been shown to induce a pro-inflammatory response of macrophages that increased tnf-α, and il-1β secretion (Bastus et al., 2009a). The increase in tnf-α, and il-1β secretion was mediated by a pattern recognition receptor called tlr-4 (Bastus et al., 2009a). Similarly, Palladium metal had also been shown to interact with tlr-4 receptor to initiate proinflammatory gene expression of tnf-α and il-8 in mice (Schmidt and Goebeler, 2015). Thus there was increasing evidence to support for tlr-4 function in Palladium or Gold bead induced anti-tumour effects of macrophages. In support, we recorded increased cxcl8b.1 and tnf-α expression in RNA sequencing data set of Palladium bead implanted.

Although the TLR protein family is conserved between mammals and teleost fish, it is well reported that TLR signalling pathways in the zebrafish differs in feature than those in mammals (Li et al., 2017, Jault et al., 2004). Gene duplication events during evolution led to

the development of isoforms of tlr-4 (tlr4ba/tlr4bb), tlr5 (tlr5a/tlr5b) and tlr8 (tlr8a/tlr8b) (Li et al., 2017). In addition, zebrafish tlr4 does not respond to LPS stimulation unlike it's mammalian counterpart (Li et al., 2017). Nonetheless, tlr4 signalling mediates only a part of the whole TLR family pathway which constitutes a whole host of receptors, tlr1-11 and tlr13, that are capable of upregulating tnf-α and cxcl8b.1 expression. Therefore, a more generalized approach was taken to elucidate the contribution of TLR family signalling, instead of just tlr4, in mediating Palladium/Gold bead induced anti-tumour effects of macrophages.

RNA sequencing of macrophages isolated from Palladium bead implanted zebrafish indeed was an invaluable insight into the underlying mechanisms that mediated the anti-tumour phenotype. By combining evidence from the literature and RNA sequencing data, we hypothesis that the TLR receptor family in macrophages play a key role in mediating the observed anti-tumour response in Palladium and Gold bead implanted zebrafish. This hypothesis was formed based on key evidence that indicated an increase in *tnf-α* and *cxcl8b.1* expression in macrophages of Palladium bead implanted zebrafish.

3.4.1. RT-qPCR confirms upregulation of *cxcl8b.1* and *tnf-α* expression in Palladium and Gold bead implanted zebrafish.

Reverse transcription quantitative PCR was conducted in order to confirm upregulation of *cxcl8b.1* and tnf-α in Palladium and Gold bead implanted zebrafish compared to Naked bead implanted zebrafish. In addition, we investigated the expression of other classically inflammatory genes, *il-4*, *tgfβ1*-a and *il1-β* . Macrophages were isolated from mpeg1:EGFP, U87-nls-mKate2 xenografted zebrafish implanted with Palladium, Gold or Naked beads. The relative fold change for each condition was calculated using the delta-delta CT method for each gene of interest using beta-actin as the reference gene. Final delta-delta CT fold change for each condition was normalised to the expression of each gene of interest in Naked bead implanted zebrafish. Zebrafish implanted with Naked beads served as an ideal control as any measurable genetic alterations could be attributed to Gold and Palladium nanoparticles solidly supported on the surface of the polystyrene bead.

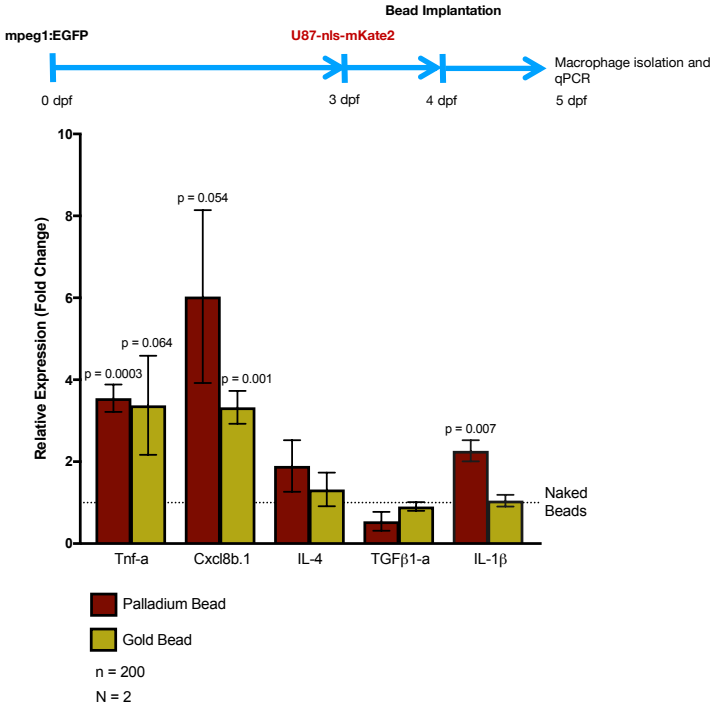

Figure 25. RT-qPCR confirms upregulation of *cxcl8b.1*, *tnf-α* and il-1*β* expression in Palladium and Gold bead implanted zebrafish.

Timeline (Blue arrows) illustrates workflow for qPCR experiment described here. RT-qPCR of each gene of interest (tnf-a, cxcl8b.1 il-4, *tgfβ1-a* and il-1*β)* were conducted on macrophages isolated from 5 day post fertilised, U87-nls-mKate xenografted, mpeg1:EGFP zebrafish implanted with either Palladium, Gold or Naked Beads. mpeg1:EGFP zebrafish were xenografted with U87-nls-mKate2 at 3 dpf. Bead implantation procedure occurred 24 hours after xenograft at 4 dpf. The relative fold change for each condition was calculated using the delta-delta CT method for each gene of interest using beta-actin as the reference gene. Final delta-delta CT fold change for Gold and Palladium bead implanted zebrafish were normalised to the expression of each gene of interest in Naked beads implanted zebrafish (Dotted horizontal line, Naked Beads). Two-tailed student t-test was conducted comparing each gene of interest to Naked bead implanted zebrafish. Macrophage were isolated from homogenised brain tissue from 200 embryo (n) for each biological replicates (N). One way ANOVA statistical analysis and Tukey's multiple comparisons test were conducted to calulate p values. p values were indicated where statistically significant ($p < 0.05$). Error bar indicated standard error.

Reverse transcription quantitative PCR confirmed the upregulation of proinflammatory cytokines *cxcl8b.1* and *tnf-α* in Palladium and Gold bead implanted zebrafish. In agreement with RNA sequencing expression data set, a 3.5 fold increase in *tnf-α* expression was recorded in Palladium ($p = 0.0003$) and Gold ($p = 0.0658$) bead implanted zebrafish (Figure 25). The upregulation of cxcl8b.1 in Palladium and Gold bead implanted zebrafish by six folds ($p = 0.050$) and three folds ($p = 0.0011$) was recorded respectively. No significant difference in expression of either *tgfβ1-a or il-4* anti-inflammatory cytokines was detected. Intriguingly, a

significant upregulation of a potent inflammatory cytokine, *il-1β*, by 2 folds was recorded only in Palladium bead implanted zebrafish. Thus altogether, the increase in *tnf-α*, *cxcl8b.1* and *il-1β* supports the hypothesis that TLR *family signaling play a key role in mediating the observed anti-tumour response in Palladium and Gold bead implanted zebrafish*.

3.4.2. IRAK-4-IN-1 Pharmacological inhibition of TLR family signalling decreases tnf-α and cxcl8b.1 expression.

In order to elucidate the level of contribution of TLR family signalling on *tnf-α* and *cxcl8b.1* expression *in vivo*, pharmacological inhibition of TLR signalling was employed using commercially available pharmacological inhibitor IRAK4-IN-1. IRAK4-IN-1 is a selective inhibitor of Interleukin-1 receptor associated kinase 4 (IRAK4) with a reported IC_{50} of 7 nM *in-vitro* and high bioavailability *in-vivo* (Smith et al., 2017). IRAK4 plays a critical role in mediating TLR signal transduction and innate immune responses (Gimenez et al., 2019). Ligand binding to TLR on the extracellular domain leads to the dimerization of TLRs which recruits and activate cytosolic adaptor proteins such as MyD88 that recruits IL-1 receptor associated kinase 4 (IRAK-4) to activate MAP kinases and nuclear factor (NF)-κB. Prior to *in vivo* experiments, we first confirmed IRAK4-IN-1 inhibitor efficacy in zebrafish by reverse transcription qPCR. Zebrafish embryos were implanted with Palladium beads and either treated with 10 μM IRAK4-IN-1 or 1% DMSO. The aim of this experiment was to confirm IRAK4-IN-1 inhibitor efficacy in zebrafish thus Palladium bead implantation was sufficient for this study. Reverse transcription qPCR of macrophages isolated from Palladium bead implanted zebrafish treated with 10 μM IRAK4-IN-1 inhibitor showed significantly downregulated expression of *tnf-α* , *cxcl8b.1* and *il-4* compared DMSO treated Palladium bead implanted zebrafish. The relative fold change for each gene of interest was normalised to Palladium bead implanted DMSO controls. A 70% decrease in *tnf-α* ($p<0.0001$) and *cxcl8b.1* ($p = 0.0017$) expression was recorded in IRAK4-IN-1 treated zebrafish. While a 50% ($p < 0.0001$) decrease in *il-4* expression was recorded. No significant difference in expression of *tgfβ1-a* or *il-1β* was rec-

orded as a result of treatment with 10 μM IRAK4-IN-1 inhibitor. Although no significant decrease in il-1β expression levels was recorded, the downregulation of *tnf-α* and *cxcl8b.1,* both key downstream genes of TLR activity, confirms the efficacy of IRAK4-IN-1 inhibitor for the first time in an *in-vivo* zebrafish model. It also validated the contribution of TLR signal transduction in Palladium bead implanted zebrafish.

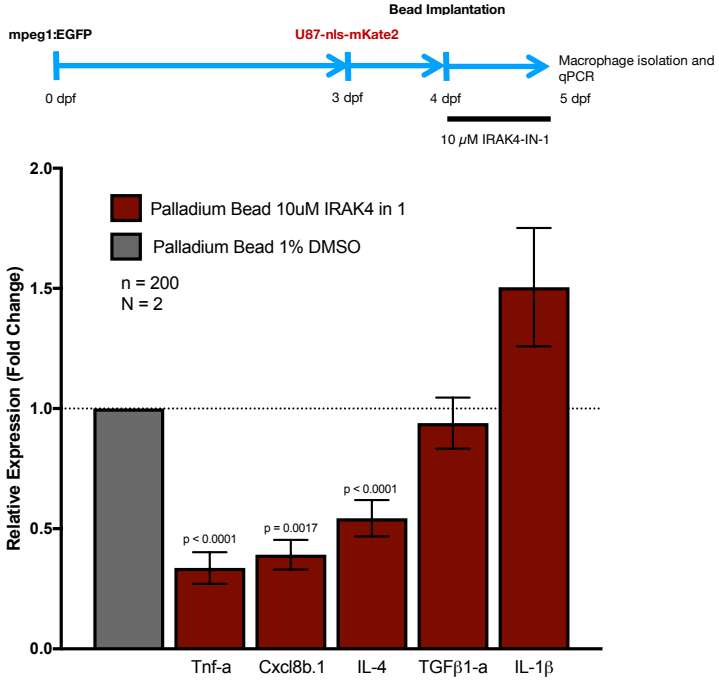

Figure 26. IRAK-4-IN-1 pharmacological inhibition of TLR family signalling decreases tnf-*a*, cxcl8b.1 and il-4 expression.

Timeline (Blue arrows) illustrates workflow for qPCR experiment described here. RT-qPCR of each gene of interest (tnf-a, cxcl8b.1 il-4, *tgfβ1-a* and il-1*β)* were conducted on macrophages isolated from 5 day post fertilised (dpf), Palladium bead implanted, U87-nls-mKate xenografted, mpeg1:EGFP zebrafish treated with either 1% DMSO or 10 µM IRAK4-IN-1 inhibitor. mpeg1:EGFP zebrafish were xenografted with U87-nls-mKate2 at 3 dpf. Bead implantation procedure occurred 24 hours after xenograft at 4 dpf. Zebrafish were treated with either 1% DMSO or 10 µM IRAK4-IN-1 for 24 hours between 4 dpf and 5 dpf. The relative fold change for each condition was calculated using the delta-delta CT method for each gene of interest using beta-actin as the reference gene. Final delta-delta CT fold change for IRAK4-IN-1 treated Palladium bead implanted zebrafish were normalised to the expression of each gene of interest in DMSO treated Palladium bead implanted zebrafish (Dotted horizontal line, Palladium bead 1% DMSA). Two-tailed student t-test was conducted comparing each gene of interest to DMSO treated zebrafish. Macrophage were isolated from homogenised brain tissue from 200 embryo (n) for each biological replicates (N). One way ANOVA statistical analysis and Tukey's multiple comparisons test were conducted to calulate p values. p values were indicated where statistically significant ($p < 0.05$). Error bar indicated standard error.

3.4.3. Pharmacological inhibition of TLR signalling promotes U87 cell survival in Gold bead implanted zebrafish.

To elucidate if TLR signalling contributed to the overall macrophage mediated anti-tumour phenotype observed in Palladium and Gold bead implanted zebrafish, the effects of TLR inhibition on U87 survival was investigated *in vivo.* mpeg1:EGFP zebrafish implanted with Gold, Palladium and Naked beads were either treated with 1% DMSO or 10 μM IRAK4-IN-1 inhibitor. The effect on U87-nls-mKate2 survival was assessed for each condition as a measure for anti-tumour efficacy. We hypothesised that the inhibition of TLR signalling in the anti-tumour phenotype would promote U87 cell survival in the zebrafish brain.

First, it was established that IRAK4-IN-1 did not directly affect U87-nls-mKate2 survival. To do so, bead null U87-nls-mKate2 xenografted zebrafish were treated with 10 μM IRAK4-IN-1. The results showed that IRAK4-IN-1(10 μM) had no direct effect on U87-nls-mKate2 cellular growth. Both DMSO and IRAK4-IN-1 treated, bead null, zebrafish conditions indicated identical growth rates up to 3 days post transplantation (dpt) (Figure 27A). An average increase of 30% in cell number was recorded for both IRAK4-IN-1 treated and DMSO bead null zebrafish conditions. Similarly, 10 μM IRAK4-IN-1 treatment of Naked Bead implanted zebrafish indicated no significant alterations in U87-nls-mKate2 cellular growth (Figure 27B) when compared to DMSO treated counterpart. Naked bead implanted led to an impairment of U87-nls-mKate2 proliferation but not its ability to survive in the zebrafish brain. No significant increase in U87-nls-mKate2 cell number was recorded for both DMSO and IRAK4-IN-1 treated Naked bead implanted zebrafish over the course of the experiment (Figure 27B). The results here highlighted the absence of TLR signalling in Naked bead implanted zebrafish.

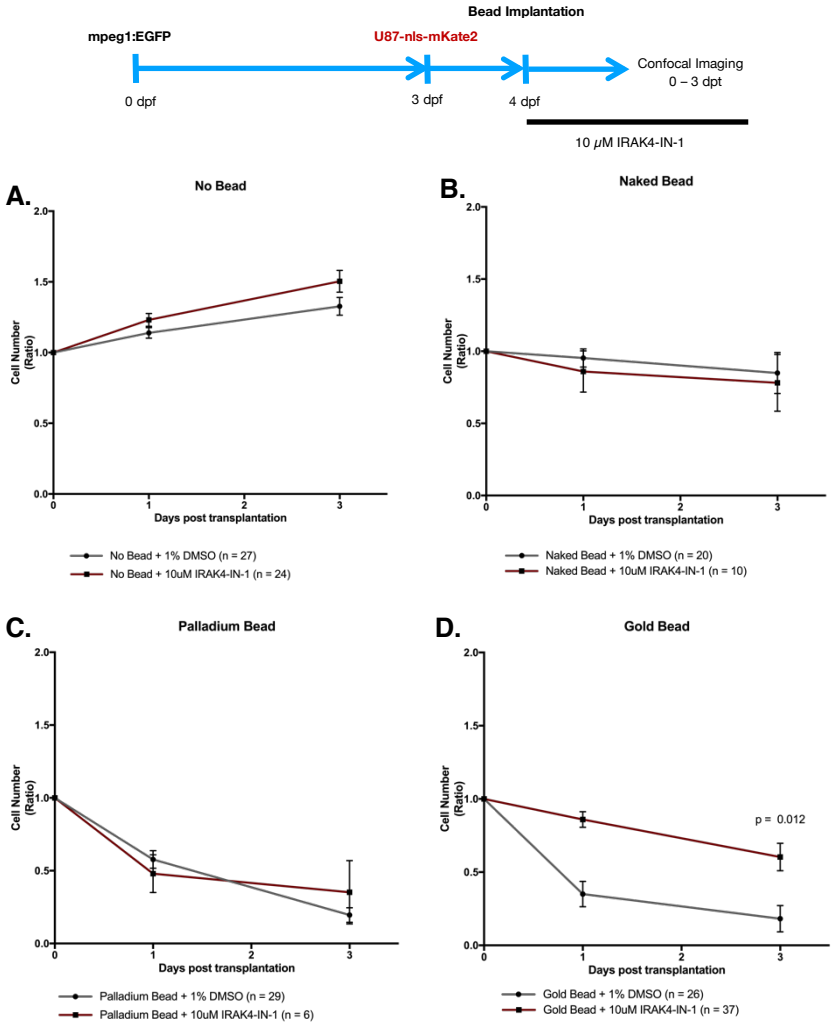

Figure 27. Pharmacological inhibition of IRAK4 promotes U87 cell survival in Gold bead implanted zebrafish.

Timeline (Blue arrows) illustrates workflow for *in vivo* IRAK4-IN-1 inhibitor experiments described here. mpeg1:EGFP zebrafish were xenografted with U87-nls-mKate2 at 3 day post fertilisation (dpf) and implanted with Gold, Palladium or Naked Bead at 4 dpf. Bead implanted and U87-nls-mKate2 xenografted zebrafish were treated with either 1% DMSO or 10 μM IRAK4-IN-1 for the duration of the experiment from 4 dpf to 7 dpf (0 dpt to 3 dpt). U87-nls-mKate2 cell numbers were expressed as a ratio calculated by the number of cells at 1 or 3 dpt divided by the number of cells at 0 dpt. Two-tailed student t-test was conducted comparing the average cell number for each condition on each day. p values were shown for significant results ($p<0.05$) Standard error was plotted for all error bars in all graphs.

(A) No effect on U87-nls-mKate2 cell survival was recorded following IRAK4-IN-1 inhibitor treatment. Both DMSO and IRAK4-IN-1 treated, bead null, zebrafish conditions indicated identical growth rates up to 3 days post transplantation (dpt)

(B) Naked bead implanted led to an impairment of U87-nls-mKate2 proliferation but not its ability to survive in the zebrafish brain. No significant increase in U87-nls-mKate2 cell number was recorded for both DMSO and IRAK4-IN-1 treated Naked bead implanted zebrafish over the course of the experiment

(C) Inhbiton of TLR signalling had no significant effect on U87-nls-mKate cell survival. A significant decrease of 60% in U87-nls-mKate2 cell count for both DMSO and IRAK4-IN-1 treated conditions was evident by 3 dpt.

(D) IRAK4-IN-1 treatment in Gold bead implanted zebrafish promoted the survival of U87-nls-mKate2 ($p = 0.012$). A 40% increase in U87-nls-mKate2 cell count was recorded in IRAK4-IN-1 treated zebrafish when compared to DMSO treated counterpart.

Intriguingly, no significant effect on U87-nls-mKate cell survival was evident in IRAK4-IN-1 treated Palladium bead implanted zebrafish. Similar to results described previously, the implantation of Palladium bead led to a significant decrease in U87-nls-Kate2 cell count (Figure 27C). A significant decrease in U87-nls-mKate2 cell count for both DMSO and IRAK4-IN-1 treated conditions was evident by 3 dpt (Figure 27C). A decrease of 60% in U87-nls-mKate2 cell count was evident by 3 dpt for both DMSO and IRAK4-IN-1 treated conditions (Figure 27C). It is important to note that the implantation of Palladium bead in addition to IRAK4-IN-1 drug treatment was extremely detrimental to zebrafish survival. The implantation of Palladium bead led to a 33% survival rate compared to 98% in Gold bead implanted zebrafish (Figure 23H). The additional treatment with IRAK4-IN-1 inhibitor led to poor survival rates (results not shown) of Palladium bead implanted zebrafish below that of 33% threshold. This was evident by the low n number (n = 6) illustrated in Figure 27C. Thus this may rationalise the results where IRAK4-IN-1 treatment in Palladium bead implanted zebrafish had no effect in promoting U87-nls-mKate2 cell survival.

In contrast, IRAK4-IN-1 treatment in Gold bead implanted zebrafish promoted the survival of U87-nls-mKate2 ($p = 0.012$). A 40% increase in U87-nls-mKate2 cell count was recorded when compared to DMSO treated Gold implanted zebrafish (Figure 27D). However, the treatment with IRAK4-IN-1 in Gold bead implanted zebrafish only elicited a partial recovery of U87-nls-mKate2 cell number. U87-nls-mKate2 cell count in IRAK4-IN-1 treated Gold bead implanted zebrafish at 3 dpt (0.603 ± 0.0938) was at a level half that of bead null implanted zebrafish (1.50 ± 0.0775). Despite this, the rescue of U87-nls-mKate2 survival in Gold bead implanted zebrafish (0.603 ± 0.0938) was comparable to cell ratios recorded in Naked Bead (0.781 ± 0.197) implanted zebrafish at 3 dpt. Thus this indicated that there may be additional signalling pathways, outside of TLR family, that form part of the anti-tumour phenotype.

In conclusion, TLR signalling did indeed contribute to macrophage mediated anti-tumour phenotype. The results here indicated that TLR signalling consisted part of the regulatory mechanisms that contributed to a proportion of the anti-tumour phenotype only in Gold

bead implanted zebrafish. A partial recovery of U87-nls-mKate2 cell number in IRAK4-IN-1 treated Gold bead implanted zebrafish was recorded. This highlighted additional unknown mechanisms, outside TLR signalling, that may have contributed to Naked bead mediated impairment of U87-nls-mKate2 cell proliferation. Nonetheless, TLR receptor family in macrophages play a key role in mediating the observed anti-tumour responses in Gold bead implanted zebrafish.

3.5. Investigating the role of *tnf-α* and *cxcl8b.1* in the anti-tumour responses of macrophages and neutrophils using CRIPSR-Cas9 and genetic transgenesis overexpression strategies.

In conjunction with the NC3Rs (National Centre for the Replacement, Refinement and Reduction of Animals in Research), further refinement of future experiments were conducted due to the innate toxicity of Palladium bead implantation. Gold bead implantation was now well established to initiate an anti-tumour response. Results from RT-qPCR studies had demonstrated that Gold bead implantation, like Palladium bead, stimulated increased tnf-α and cxcl8b.1 expression. In addition, it was confirmed that TLR signalling in Gold bead implanted zebrafish, not in Palladium bead implanted zebrafish, significantly contributed to macrophage mediated anti-tumour responses. However, one key benefit that separated Gold bead from Palladium bead was lower bead toxicity. The survival rates for Gold bead implanted zebrafish was significant higher than Palladium bead implanted zebrafish; 98% vs 33%. In fact, survival rates in Gold bead implanted zebrafish were comparable to that of Naked bead implanted and bead null zebrafish (Figure 23H). Therefore, the refinement of future experiments excluded Palladium bead implantation in order to reduce animal numbers and to refine the care of animals to keep suffering to a minimum.

The results thus far concluded that TLR family signalling was an important signal transduction pathway that mediated Gold bead induced anti-tumour phenotype in macrophages. However, the exact genetic effector of TLR family activation had not been identified. Based on key evidence from the literature and from previous RT-qPCR results, it was well established that TLR signalling regulated the expression of pro-inflammatory cytokines tnf-a and cxcl8b.1. The upregulation of cxcl8b.1 is known to be a potent chemoattract for neutrophils (Manfroi et al., 2017). It is widely accepted that macrophages regulate site specific recruitment of neutrophil to facilitate the inflammatory response (Kim and Luster, 2015). As a result, future experimental design also explored the contribution of neutrophils to Gold induced anti-tumour effects. Thus, we hypothesised that Gold bead implantation recruited neutrophils into the zebrafish brain and that the expression of tnf-a and cxcl8b.1 in macrophages stimulated an anti-tumour response in macrophages and/or neutrophils in the zebrafish brain.

In order to test this, a set of experiments combining CRISPR-cas9 knock out and genetic overexpression strategies were employed. These experiments aimed to evaluate the effects of tnf-a and cxcl8b.1 expression in macrophages on the dynamics of anti-tumour responses of both macrophages and neutrophils in the zebrafish brain.

3.5.1. Implantation of Gold beads recruit neutrophils into the zebrafish brain.

In order to test if Gold bead implantation did indeed recruit neutrophils into the brain of the zebrafish, mpo:EGFP zebrafish were xenografted with U87-nls-mKate at 3 dpf and were implanted with Naked and Gold beads at 4 dpf. Myeloperoxidase (MPO) is a neutrophil specific promoter that drives EGFP expression in mpo:EGFP zebrafish. The effects on neutrophil recruitment after bead implantation were subsequently studied at 0,1 and 3 dpt.

Neutrophils are an important cell type of the innate immune system. They rapidly migrate to tissue in response to injury or infection and are one of the first responders of the immune system (Kim and Luster, 2015). Thus it was unsurprising that the implantation of Naked and Gold bead led to the recruitment of neutrophils into the brain. When compared to bead null zebrafish, both Naked and Gold bead implanted mpo:EGFP zebrafish showed increased neutrophil infiltration into the brain at 1 and 3 dpt (Figure 28). However, the results indicated that Gold bead implanted zebrafish recruited more neutrophils into the brain of the zebrafish than Naked bead implanted. At 1 dpt, an average of 13.2 ± 1.27 neutrophils were present in Gold bead implanted zebrafish versus an average of 7.00 ± 1.43 neutrophils in Naked bead implanted zebrafish ($p = 0.0026$) (Figure 28D'). Similar to macrophages, neutrophils were observed to localized in the vicinity of the beads in Gold implanted zebrafish (Figure 28C'). However, by 3 dpt neutrophil level in Gold bead implanted zebrafish recovered to the same level as Naked bead implanted zebrafish (6.76 ± 0.633 versus 7.17 ± 1.96) (Figure 28D''). In addition, neutrophil numbers in the brain of both Gold and Naked bead implanted zebrafish remained significantly ($p < 0.05$) elevated for the duration of the experiment up to 3 dpt when compared to bead null zebrafish (Figure 28D''). This indicated that the Naked bead itself recruited neutrophils and that recruited neutrophils persisted in the brain for the duration

of the experiment. Thus this may indicate two distinct neutrophil recruitment events occurring with the first, a reaction to the foreign body (polystyrene bead) and the second, a reaction to Gold nanoparticles solidly supported on the beads. These results here conclude that Gold bead implantation recruited higher number of neutrophils than Naked bead but only at 1 dpt.

Establishing that neutrophil infiltrated the brain as a result of Gold bead implantation was an important step forward in this study. It confirmed the hypothesis that neutrophils infiltrated the brain following Gold bead implantation, hypothesis postulated based on results from previous RT-qPCR studies. The increase in Gold bead induced neutrophil recruitment, at 1 dpt, coincided with a six folds increase in cxcl8b.1 and three folds increase in tnf-α expression in macrophages of Gold bead implanted zebrafish. The timeline of experiments for both in-vivo and RT-qPCR studies were aligned as RNA extraction from macrophages of Gold bead implanted zebrafish both occurred at 1 dpt. This solidified support for the key role of *tnf-α* and *cxcl8b.1* expression in mediating the anti-tumour response of macrophages and neutrophils. The neutrophil study drove a paradigm shift that included both macrophages and neutrophils as a contributing factor in mediating Gold bead induced anti-tumour responses. Studies have shown that both macrophages and neutrophils had been identified to be important effector cells of the anti-tumour effect (Fridlender et al., 2009, Reichel et al., 2019). Thus it was important to investigate how *tnf-a* and *cxcl8b.1* expression in macrophages influenced the dynamics of intercellular interactions that regulated the anti-tumour effect of these innate immune cells. We hypothesized that *cxcl8b.1 and tnf-a expression in macrophages were important genetic mediators of Gold bead implantation that facilitated the anti-tumour effects of macrophages and neutrophils in the zebrafish brain.*

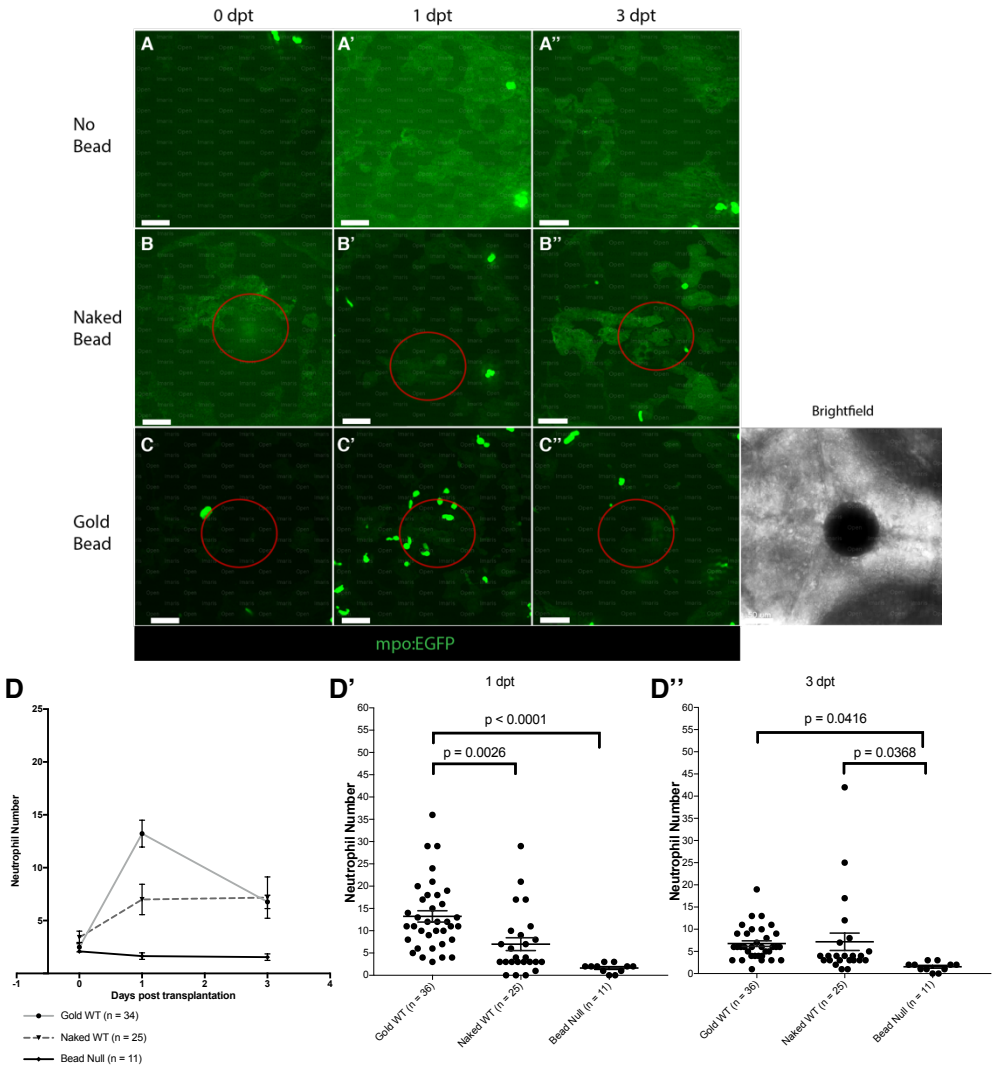

Figure 28. Gold bead implantation promoted neutrophil infiltration at 1 day post transplantation in the zebrafish brain.

(A-C) The implantation of Gold bead led to increase neutrophil infiltration into the brain at 1 dpt. Both Naked and Gold bead showed increased neutrophil recruitment when compared to bead null control zebrafish. Human derived Lv-cppt-IRES-nls-mKate2-opre transformed U87-nls-mKate2 cells (not shown) were xenografted into neutrophil labelled (Green), 3 days post fertilized (dpf), mpo:EGFP zebrafish. Following a 24 hour recovery phase, xenografted zebrafish were implanted with Gold or Naked bead. Images from *left* to *right* are in chronological order showing 0,1 and 3 day post bead transplantation (dpt). Images from *top* to *bottom* showing: (A-A'') U87-nls-mKate2 xenografted mpo:EGFP zebrafish No bead control, (B-B'') U87-nls-mKate2 xenografted mpo:EGFP zebrafish implanted with Naked bead, (C-C'') U87-nls-mKate2 xenografted mpo:EGFP zebrafish implanted with Gold bead. Red circles in images denotes boundary of Gold or Naked beads in the zebrafish brain. All Images were captured using an Andor spinning disk confocal microscope with a 20X/NA 0.75 objective. Scale bars set at 50 um. Brightfield image is representative of the orientation and imaging field of the fluorescent images shown in images A-C.

(D-D'') Gold bead implantation (13.2 ± 1.27 neutrophils) led to a statically significant ($p = 0.0026$) increase in neutrophil infiltration into the brain of the zebrafish at 1 dpt when compared to Naked bead (7.00 ± 1.43 neutrophils). By 3 dpt, both Gold (6.76 ± 0.633 neutrophils) and Naked bead (7.17 ± 1.96 neutrophils) implantation had significantly elevated number of neutrophils when compared to bead null controls (1.55 ± 0.312 neutrophils). One way ANOVA statistical analysis and Tukey's multiple comparisons test were conducted to calulate p values. p values were indicated where statistically significant ($p < 0.05$). Error bar indicated standard error.

3.5.2. CRISPR-Cas9 manipulation of *tnf-α* and *cxcl8b.1* were specific to genetic targets.

To investigate the function of *tnf-α* and *cxcl8b.1* in promoting anti-tumour effects of macrophages and neutrophils, *tnf-a* and *cxcl8b.1* were targeted using CRISPR manipulation with a gene-specific guideRNA (gRNA). Zebrafish embryo were injected with *tnf-a* and *cxcl8b.1* gRNA at the one cell stage in order to introduce mutations at specific restrictions sites in the genes. Due to the high efficiency of CRISPR-Cas9 system, transient knock out of *tnf-a* and *cxcl8b.1* function was conducted. The *tnf-α* gene was targeted using gRNA described previously and robustly reduced *tnf-α* protein levels in western blots (Tsarouchas et al., 2018). Efficient mutation of *tnf-α* gene was introduced into zebrafish larvae by co-injecting

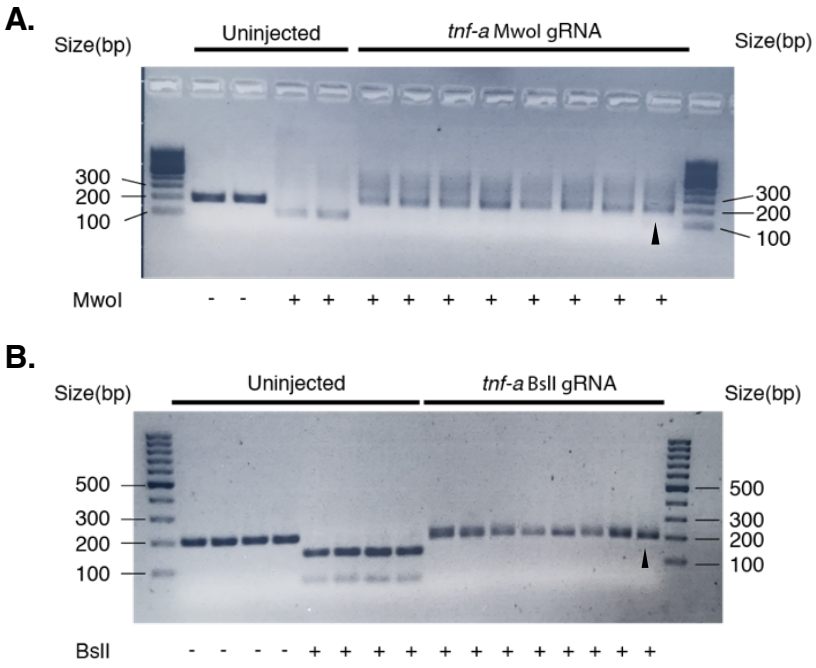

Figure 29. Restriction fragment length polymorphism (RFLP) analysis revealed that tnf-α CRISPR-Cas9 manipulation induced mutations in exon 4.

RFLP analysis of wild type (WIK) zebrafish embryos (1dpf) co-injected, 24 hours prior, with *tnf-α* MwoI gRNA and *tnf-α* BslI gRNA. gRNA injection induced site directed mutagenesis of respective restriction enzyme sites on exon 4. Each well represented PCR product from a single embryo.

(A) The mutation of MwoI restriction site on tnf-α exon 4 conferred resistance to MwoI restriction endonuclease digestion. MwoI restriction digest of PCR product from uninjected zebrafish yielded DNA fragments at 114 bp and 92 bp. The mutation of MwoI restriction site would yield an expected fragment of 206 bp for tnf-α MwoI (Black arrow) similar to uninjected and undigested control zebrafish.

(B) The inhibition of restiction endonuclease digestion by BslI on tnf-α exon 4 was also evident. BslI restriction digest of PCR product from uninjected zebrafish yielded DNA fragments of 147 and 60 bp. The mutation of BslI restriction site by tnf-α BslI gRNA resulted in the inhibition of BslI restriciton digest yielding a 207 bp long DNA fragment (Black arrow).

two gRNA directing a double mutation on exon 4 of *tnf-α*. First we confirmed efficient introduction of CRISPR-Cas9 mediated site directed mutagenesis of *tnf-α* gRNA by restriction fragment length polymorphism analysis (RFLP)(Figure 29). RFLP analysis was conducted on each embryo to confirm CRISPR-Cas9 mediated site directed mutagenesis. The co-injection of *tnf-α* MwoI gRNA and *tnf-α* BslI gRNA resulted in efficient somatic mutation at gRNA target sites 24 hours after injection. A resistance to restriction endonuclease digestion by MwoI (Figure 29A) and BslI (Figure 29B) was evident in RFLP analysis. Mutation of the MwoI restriction site inhibited restriction digest and resulted in a band shift on agarose gel producing undigested DNA fragment 206 bp long (Figure 29A). Likewise, the mutation of the BslI restriction site inhibited BslI restriction digest also reflected as a band shift during RFLP analysis. Mutation of BslI restriction site produced a single band which indicated undigested DNA product 207 bp long (Figure 29B).

cxcl8b.1 was targeted using gRNA designed specifically for this study. Several iterations of the design process were required in order to achieve knock out of *cxcl8b.1*, albeit only a partial knock out of cxcl8b.1 was finally achieved. In total, three gRNAs were designed to target *cxcl8b.1* BslI Exon 3, *cxcl8b.1* RsaI Exon 2 and *cxcl8b.1* AluI Exon 4. RFLP analysis was conducted on 1 dpf wild type (WIK) zebrafish injected 24 hours prior with each gRNA. *cxcl8b.1* BslI gRNA injection failed to introduce any mutations at BslI restrictions sites on exon 3 (Figure 30A). No band shift was detected when analysing digested PCR product of *cxcl8b.1* BslI gRNA injected and uninjected zebrafish (Figure 30A). The complete digestion of PCR product indicated an active BslI restriction site on exon 3 in all cells of the zebrafish. While on the other hand, *cxcl8b.1* RsaI gRNA induced inefficient site directed mutagenesis. Complete RsaI digestion of PCR product (197 bp and 41 bp (not visible)) was evident for most injected zebrafish except two (Figure 30B). These two zebrafish sample indicated partially digested product (Figure 30B, Black arrow) showing very a faint band (238 bp) where mutated fragments were expected. However, the inefficient nature of *cxcl8b.1* RsaI gRNA induced mutagenesis made it not viable for knock out studies. In contrast, RFLP analysis of zebrafish injected with *cxcl8b.1* AluI gRNA showed more promise. RFLP analysis indicated a band shift

towards 181 bp where DNA fragments with mutated AluI restriction sites were expected. However, faint bands indicating partially digested DNA fragments at 111 bp and 70 bp were also visible. Thus *cxcl8b.1* AluI Exon 4 mutations were not conferred efficiently into all cells of the zebrafish. Nonetheless, as neutrophils are highly sensitive to *cxcl8b.1* cytokine, a partial knock out of *cxcl8b.1* expression maybe sufficient to elicit a detectable phenotype.

Finally, in order to confirm that site directed mutagenesis by CRISPR-Cas9 was specifically mediated by each target specific gRNA sequences. Scrambled gRNA sequence and

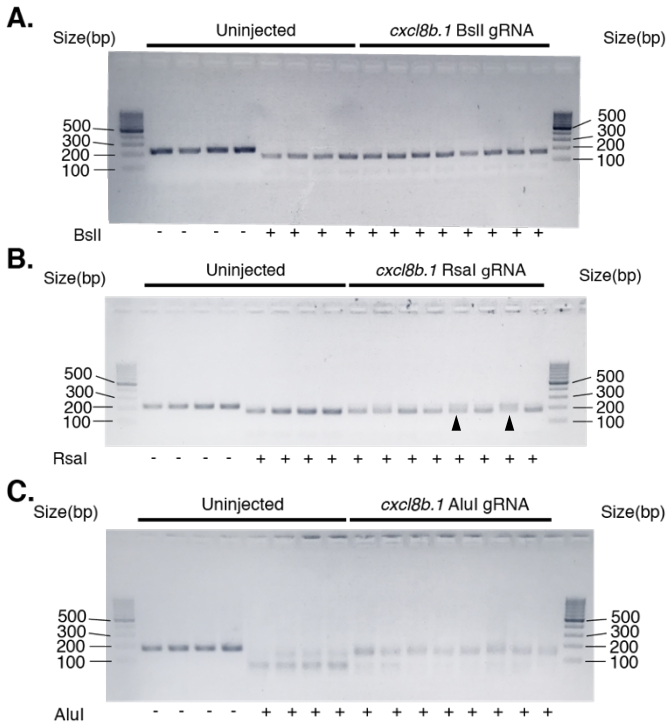

Figure 30. Restriction fragment length polymorphism (RFLP) analysis revealed partial mutation of cxcl8b.1 AluI restriction site.

RFLP analysis of 1 dpf wild type (WIK) zebrafish injected, 24 hours prior, with *cxcl8b.1* BslI gRNA, *cxcl8b.1* RsaI gRNA or cxcl8b.1 AluI gRNA. Each well represented PCR product from a single embryo.

(A) No band shift was detected when analysing digested PCR product of *cxcl8b.1* BslI gRNA injected and uninjected zebrafish. The complete digestion of PCR product indicated an active BslI restriction site on exon 3 in all cells of the zebrafish. Complete BslI digestion of PCR product was expected to yield DNA fragments 158 bp and 55 bp long.

(B) The injection of *cxcl8b.1* RsaI gRNA induced inefficient site directed mutagenesis. Complete RsaI digestion of PCR product (197 bp and 41 bp (not visible)) was evident for most injected zebrafish. Two zebrafish sample indicated partial ly digested product (Black arrow) showing very a faint band (238 bp) where mutated fragments were expected. Thus, most cells in the zebrafish contained a fully function RsaI restriction site on exon 2.

(C) *cxcl8b.1* AluI gRNA injections induced mutations of AluI restriction sites in some cells of the zebrafish. The mutation of AluI restriction sites induced a band shift towards 181 bp where DNA fragments with mutated AluI restriction sites were expected. However, faint bands indicating partially digested DNA fragments at 111 bp and 70 bp were also visible.

the components required for CRISPR-Cas9 mutagenesis (see section 2.9.1) were injected into wild type (WIK) zebrafish. RFLP analysis was conducted on each specific target restriction site in order to determine if mutations were conferred; tnf-α BslI, tnf-α MwoI and Cxcl8b.1 AluI (Figure 31). RFLP analysis indicated a complete digestion of all PCR products by each respective restriction enzyme of scrambled gRNA injected zebrafish. Mutations of restrictions sites were not conferred by scrambled gRNA or any of the components of CRISPR-Cas9 mutagenesis. The digestion of each tnf-α PCR product by respective BslI and MwoI restriction enzyme produced DNA fragments that indicated active, unmutated, restriction sites (Figure 31). Likewise, AluI Restriction endonuclease digestion of PCR product emcompassing restriction site of cxcl8b.1 AluI Exon 4 produced DNA fragments of 111 bp and 70 bp (Figure 31). This indicated an active AluI restriction site. Together, the results implied that the injection of scramble gRNA and components of CRISPR-Cas9 mutagenesis did not induce mutations at tnf-α MwoI Exon 4, tnf-α BslI Exon 4 or cxcl8b.1 AluI Exon 4 restriction sites. Therefore, gRNA directing CRISPR-Cas9 knockouts were indeed specific for each genetic target of interest. These experiment were vital in establishing that the CRIPSR-Cas9 knockout strategies employed were reproducible and specific for *tnf-α* and *cxcl8b.1*. Next we tested the hypothesis that *tnf-α and cxcl8b.1 expression in macrophages were important genetic mediator of Gold bead induced anti-tumour responses of macrophages and neutrophils in the zebrafish brain.*

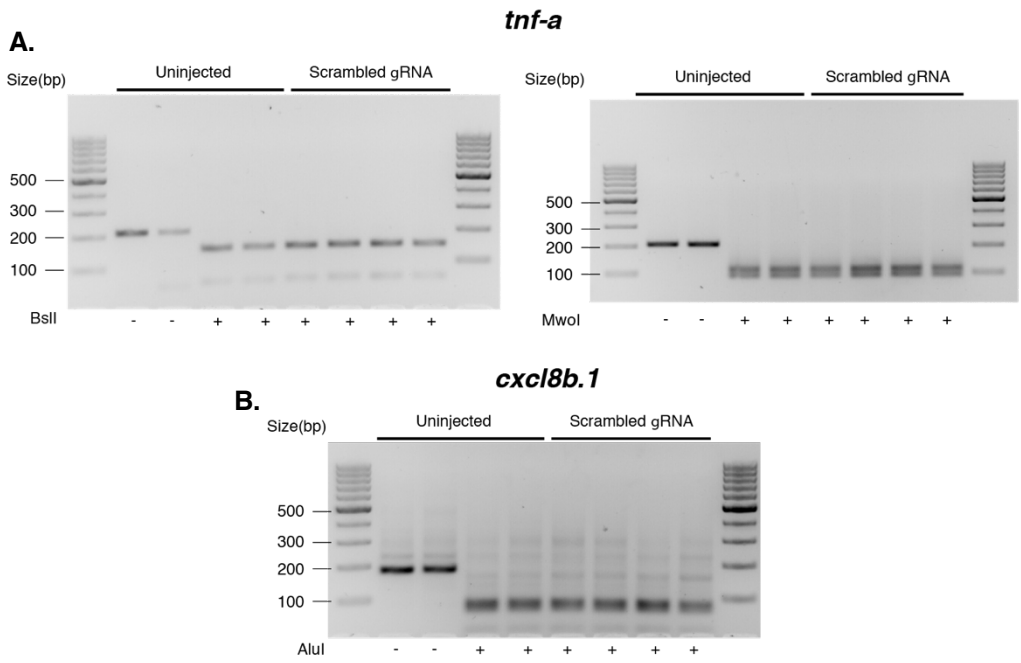

Figure 31. The injection of scramble gRNA and components of CRISPR-Cas9 mutagenesis did not induce restriction site mutations.

Restriction Fragment Length Polymorphism analysis showed complete digestion of all PCR products from specifc regions emcompassing CRISPR target restriction sites of zebrafish injected with scramble gRNA.

(A) PCR was conducted on scramble gRNA injected zebrafish emcompassing restriction sites of tnf-α BslI Exon 4 (*left*) and tnf-α MwoI Exon 4 (*right*). The digestion of each PCR product by respective BslI and MwoI restriction enzyme produced DNA fragments that indicated active, unmutated, restriction sites. BslI digestion produced DNA fragments of 147 bp and 60 bp. MwoI digestion produced DNA fragments of 114 bp and 92 bp. The injection of scramble gRNA did not induce mutations at these restriction sites.

(B) AluI Restriction endonuclease digestion of PCR product emcompassing restriction site of cxcl8b.1 AluI Exon 4 produced DNA fragments of 111 bp and 70 bp. This indicated an active AluI restriction site. Thus implied that the injection of scramble gRNA also did not induce mutations at AluI restriction sites.

3.5.3. CRISPR knockout of *tnf-α* and *cxcl8b.1* had no effect on Gold induced anti-tumour responses of macrophage and neutrophils.

The function of tnf-α and cxcl8b.1 in mediating Gold induced anti-tumour effects were investigated using CRISPR knock out solutions as described before. We tested the hypothesis that cxcl8b.1 and tnf-a expression in macrophages were important genetic mediators of Gold bead implantation that facilitated the anti-tumour effects in the zebrafish brain. In order to do so, mpeg1:EGFP or mpo:EGFP zebrafish were co-injected with tnf-α BslI, tnf-α MwoI and cxcl8b.1 AluI gRNA in order to knockout tnf-α and partially knockout cxcl8b.1 expression. Injected zebrafish were implanted with either Gold or Naked beads and the effects on U87-nls-mKate2 survival, macrophage number and neutrophil infiltration were evaluated at 0, 1 and 3 dpt. RFLP analysis was conducted on all zebrafish larvae at the end of in-vivo experiments to confirm knockout of tnf-α and cxcl8b.1.

The consequences of tnf-α and cxcl8b.1 knockout on macrophage number was analyzed to understand if tnf-α and cxcl8b.1 played a role in Gold bead induced macrophage recruitment. The implantation of Gold and Naked beads in wild type and double knockout mpeg1:EGFP zebrafish induced an initial spike in macrophage intensities at 1 dpt. The knockout of tnf-α and cxcl8b.1 in Gold bead implanted zebrafish elicited no detectable effects on macrophage intensities when compared to wild type (p= 0.943) (Figure 32H-I). A 12 and 10 fold increase in macrophage intensities were recorded in, Gold bead implanted, wild type and knockout mpeg1:EGFP zebrafish respectively (Figure 32H). Likewise, the implantation of Naked beads also induced a similar spike in macrophage intensities at 1 dpt, although to a lesser degree. A 6 folds and 8 fold increase in macrophage intensities of Naked bead implanted wild type and knockout zebrafish were recorded respectively (Figure 32H). This initial spike in macrophage intensities were attributed to a response to the foreign body and also the clearance of necrotic tissue as a result of the injury caused by the implantation procedure. Clearance of necrotic cell bodies were observed after 1 dpt (see section 3.3.3 for details). At 3 dpt,

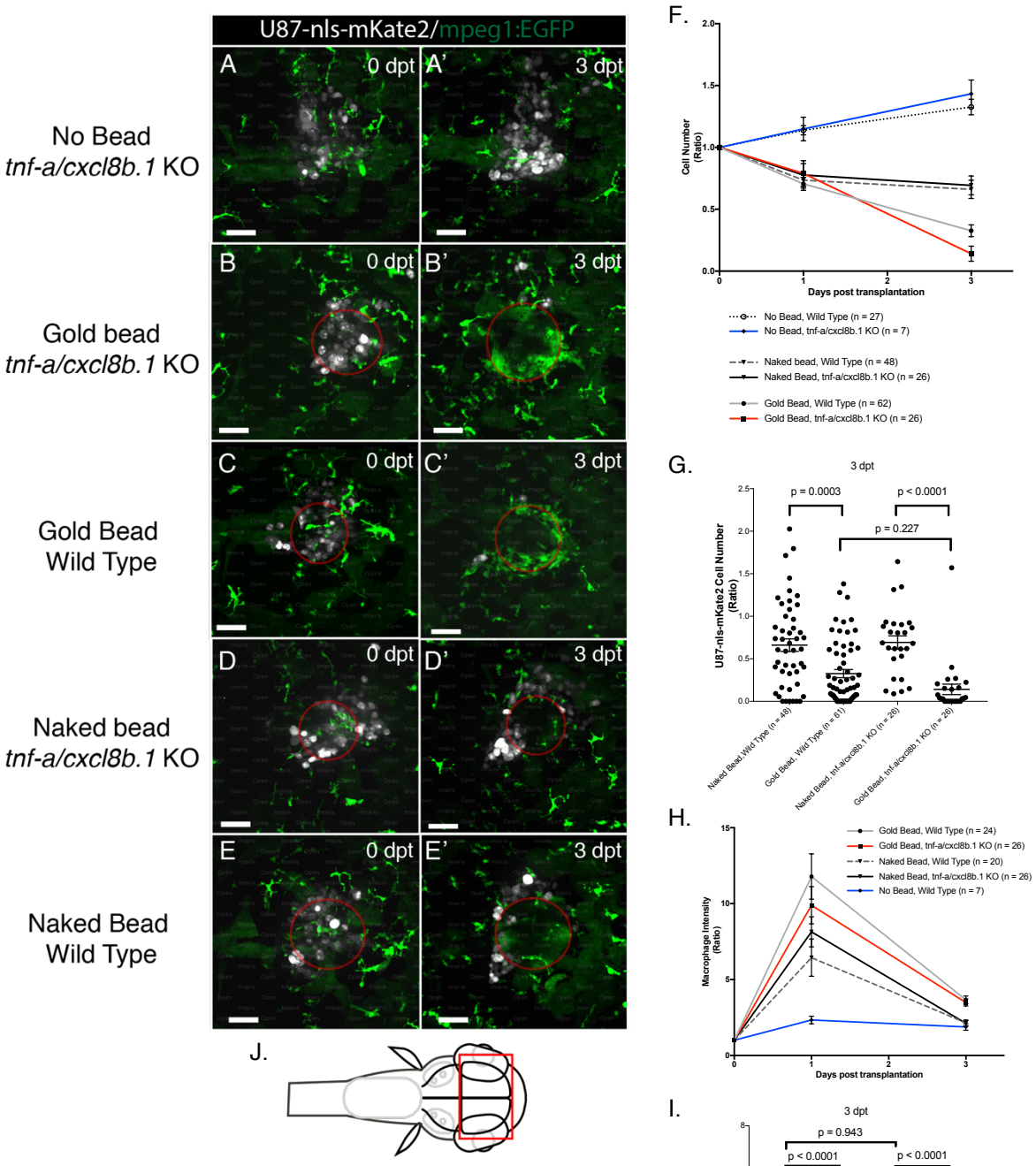

Figure 32. CRISPR knockout of tnf-*a* and cxcl8b.1 had no effect on Gold induced anti-tumour responses of macrophage.

(A-E) tnf-*a* and cxcl8b.1 expression were knocked out using CRISPR in, macrophage labelled (Green), mpeg1:EGFP zebrafish. Human derived Lv-cppt-IRES-nls-mKate2-opre transformed U87-nls-mKate2 cells (White) were xenografted into 3 days post fertilized (dpf) wild type and tnf-*a*/cxcl8b.1 double knockout mpeg1:EGFP zebrafish. Zebrafish embyros (4 dpf) were implanted with Gold or Naked bead and imaged using an Andor spinning disk confocal microscope with a 20X/NA 0.75 objective. Scale bars were set at 50 µm. Images from *left* to *right* are in chronological order showing images from 0 and 3 day post bead transplantation (dpt). (A) The knockout of pro-inflammatory

cytokines tnf-α and cxcl8b.1 expression in bead null zebrafish had no effect on U87-nls-mKate2 proliferation. Tnf-a and cxcl8b.1 expression does not contribute to U87-nls-mKate2 survival. (B) The double knockout of mpeg1:EGFP zebrafish had no effect on Gold induced anti-tumour responses. (C) Gold induced anti-tumour responses in double knock out were identical to wild type conditions. (D) The double knockout of tnf-α and cxcl8b.1 in naked bead zebrafish had no effect on U87-nls-mKate2 survival. U87-nls-mKate2 survived in the brain but did not proliferate. (E) The implantation of Naked bead into wild type zebrafish also had no effect on U87-nls-mKate2. U87-nls-mKate2 also survived in the brain but did not proliferate.

(F) U87-nls-mKate cell numbers were expressed as a ratio calculated by the number of cells at 1 or 3 day post transplantation (dpt) divided by the number of cells at 0 dpt.

(G) At 3 dpt, the implantation of Gold bead elicit a potent anti-tumour effect on both wild type and double knock out zebrafish. tnf-α and cxc8b.1 did not contribute to the anti-tumour phenotype.

(H) Macophage intensity were expressed as a ratio calculated by the sum of intensity at 1 or 3 day post transplantation (dpt) divided by the sum of intensity at 0 dpt. All bead implanted zebrafish elicit a spike in macrophage intensities at 1 dpt.

(I) At 3 dpt, the implantation of Gold bead recruited more macrophages into the brain than Naked bead implanted zerbrafish. Knock out of tnf-α and cxcl8b.1 had no effect on macrophage recruitment into the brain of Gold bead implanted zebrafish.

Brightfield image is representative of the orientation and imaging field of the fluorescent images shown in images A-D and A'-D'.

One way ANOVA statistical analysis and Tukey's multiple comparisons test were conducted to calulate p values. p values were indicated where statistically significant ($p < 0.05$). Error bar indicated standard error.

(J) The imaging field emcompassed both optic tectums of the zebrafish brain. The red box of the schematic image denotes boundary of the imaging region and represented the orientation of all images from A-E.

a recovery of macrophage intensities was observed for all zebrafish genetic conditions including both Gold and Naked bead implanted zebrafish. However, as previously reported (section 3.3.2), the recovery of macrophage intensities to basal levels was not evident in Gold bead implanted zebrafish. At 3 dpt, Gold bead implantation in both wild type and double knockout conditions stimulated a 2 fold increase in macrophage intensities when compared to Naked bead implanted zebrafish and bead null wild type controls (Figure 32H). Thus the implantation of Gold beads recruited macrophages and the knockout of tnf-α and cxcl8b.1 expression had no effect on Gold bead mediated macrophage recruitment in the zebrafish brain.

To understand if tnf-α and cxcl8b.1 knock out had a consequence on neutrophil recruitment, Gold and Naked beads were implanted into wild type and double knock out tnf-a/cxcl8b.1 mutant mpo:EGFP zebrafish. The effects on neutrophil recruitment were closely examined. Previously, we showed that the implantation of Gold bead into the brain of wild type zebrafish stimulated increased neutrophil recruitment into the brain of the zebrafish at 1

dpt (see section 3.5.1). In addition, qPCR results showed that Gold bead implantation increased the expression of cxcl8b.1 and tnf-a. Thus we tested the hypothesis that *tnf-α and cxcl8b.1 expression mediated Gold bead induced recruitment of neutrophil in the zebrafish brain*.

The implantation of Gold bead in double knockout tnf-α/cxcl8b.1 mutant mpo:EGFP zebrafish showed a trend indicating attenuated neutrophil recruitment at 1 dpt (Figure 33F). However, two tailed students t-test revealed that the attenuation of neutrophil recruitment in double knock out mutants mpo:EGFP zebrafish at 1 dpt was statistically insignificant ($p = 0.108$) (Figure 33F). At 1 dpt, Gold bead implantation in wild type and double mutant mpo:EGFP recruited an average of 13.2 ± 1.27 neutrophils and 10.3 ± 1.10 neutrophils respectively (Figure 33F). Likewise, knockout of tnf-α and cxcl8b.1 had no effect on neutrophil recruitment in Naked bead implanted double mutant mpo:EGFP zebrafish when compared to its wild type counterpart (Figure 33G). At 1 dpt, an average of 9.18 ± 1.29 neutrophils and 7.00 ± 1.43 neutrophils were present in Naked bead implanted double knockout mutant and wild type mpo:EGFP zebrafish respectively. Altogether, the knockout of *tnf-α* and *cxcl8b.1* expression had no effect on Gold bead induced neutrophil recruitment in the zebrafish brain.

To investigate if tnf-α and cxcl8b.1 expression mediated Gold bead induced anti-tumour phenotype, the consequences of tnf-α and cxcl8b.1 knockout on U87 survival was evaluated. The knock out of tnf-α and cxcl8b.1 expression had no effect on Gold induced anti-tumour responses. No significant difference in U87-nls-mKate cell number was recorded when comparing Gold bead implanted double knockout zebrafish and Gold bead implanted wild type zebrafish ($p = 0.227$) (Figure 32G). The implantation of Gold bead led to a significant decrease of U87-nls-mKate2 cell count by an average of 86.9 ± 6.10%(($p < 0.0001$) in knockout zebrafish and 66.3 ± 4.76%($p = 0.0003$) in wild type zebrafish (Figure 32F-G). Likewise, when comparing the effects of Naked bead implantation into double knock out mutant zebrafish and wild type zebrafish on U87-nls-mKate survival no significant difference was recorded ($p = 0.990$) (Figure 32F-G). Naked bead implantation attenuated the proliferation of U87-nls-mKate but not its survival in the zebrafish brain. In addition, we confirmed that the

knockout of pro-inflammatory cytokines tnf-a and cxcl8b.1 expression in bead null zebrafish had no effect on U87-nls-mKate2 proliferation. At 3 dpt, U87-nls-mKate2 cell count increased

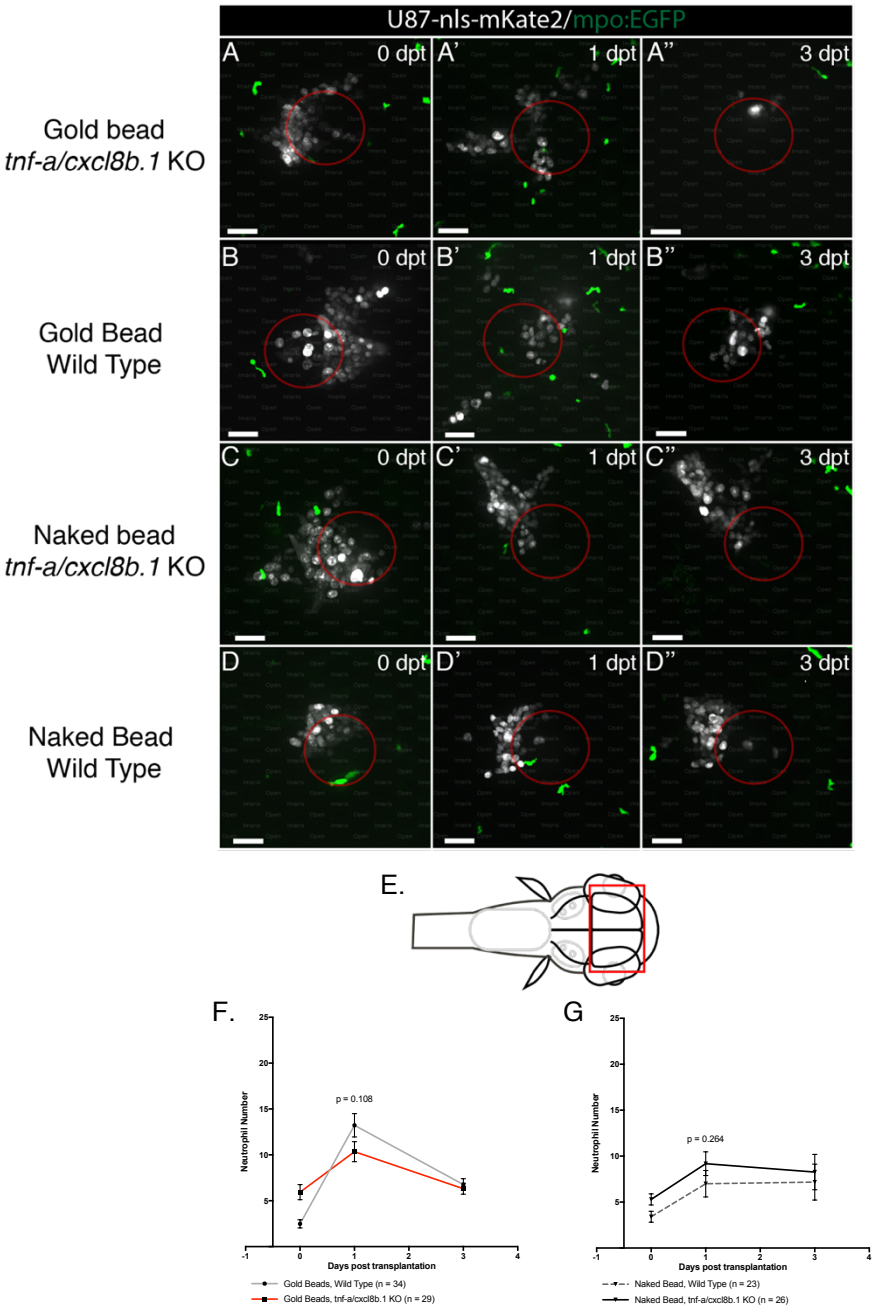

Figure 33. CRISPR knockout of tnf-α and cxcl8b.1 had no effect on Gold induced neutrophil recruitment in the brain of mpo:EGFP zebrafish.

(A-E) tnf-α and cxcl8b.1 expression were knocked out using CRISPR in, neutrophil labelled (Green), mpo:EGFP zebrafish. Human derived Lv-cppt-IRES-nls-mKate2-opre transformed U87-nls-mKate2 cells (White) were xenografted into 3 days post fertilized (dpf) wild type and tnf-α/cxcl8b.1 double knockout mpo:EGFP zebrafish. Xenografted zebrafish embyros (4 dpf) were implanted with Gold or Naked bead and imaged using an Andor spinning disk confocal microscope with a 20X/NA 0.75 objective. Scale bars were set at 50 µm. Images from *left* to *right* are in chronological order showing images from 0 ,1 and 3 day post bead transplantation (dpt). (A) The implantation of Gold bead into double knockout tnf-α/cxcl8b.1 mutant mpo:EGFP zebrafish had no effect on neutrophil recruitment. (B) Implantation of Gold bead recruited neutrophils at 1 dpt and returned to basal

level by 3 dpt. (C) Likewise, knockout of tnf-α and cxcl8b.1 had no effect on neutrophil recruitment in Naked bead implanted double mutant mpo:EGFP zebrafish when compared to (D) wild type counterpart.
(E) The imaging field emcompassed both optic tectums of the zebrafish brain. The red box of the schematic image denotes boundary of the imaging region and represented the orientation of all images from A-D.
(F) The implantation of Gold bead in double knockout tnf-α/cxcl8b.1 mutant mpo:EGFP zebrafish showed a trend to indicated attenuated neutrophil recruitment at 1 dpt. However, two tailed students t-test revealed that the attenuation of neutrophil recruitment in double knock out mutants mpo:EGFP zebrafish at 1 dpt was statically insignificant ($p = 0.108$). At 1 dpt, Gold bead implantation in wild type and double mutant mpo:EGFP recruited an average of 13.2 ± 1.27 neutrophils and 10.3 ± 1.10 neutrophils respectively
(G) The double knockout of tnf-α and cxcl8b.1 had no effect on Naked bead mediated neutrophil recruitment in the zebrafish brain. At 1 dpt, an average of 9.18 ± 1.29 neutrophils and 7.00 ± 1.43 neutrophils were present in Naked bead implanted double knockout mutant and wild type mpo:EGFP zebrafish respectively ($p = 0.264$).

by 1.4 folds in bead null knockout zebrafish. The growth rates mirrored that of bead null wild type control mpeg1:EGFP zebrafish (Figure 32F). Thus, the results here indicated that tnf-α and cxcl8b.1 expression did not contribute to mechanisms that promoted U87-nls-mKate2 survival or Gold induced anti-tumour responses in the zebrafish brain.

This study demonstrated that CRISPR knockout of tnf-α and cxcl8b.1 in Gold bead implanted zebrafish elicited no detectable phenotypic changes of the associated anti-tumour responses when compared to wild type. In support, the knockout of *tnf-α* and *cxcl8b.1* did not alter the responses of either macrophages or neutrophils as a result of Gold bead implantation. Both knockout and wild type zebrafish displayed identical kinetics for macrophages and neutrophils recruitment from 0 dpt to 3 dpt when comparing Gold bead implanted tnf-α/cxcl8b.1 knockout double mutant and Gold bead implanted wild type background. To conclude, *tnf-α* and *cxcl8b.1* were not key mediators of Gold induced anti-tumour responses.

3.5.4. *mpeg1* driven mifepristone-inducible lexPR expression of RFP in macrophages showed weak expression of RFP fluorophore.

In addition to loss of function experiments, gain of function experiments were conducted to further investigate the role of tnf-α and cxcl8b.1 in mediating the anti-tumour phenotype. Ultimately, the overexpression of tnf-α and cxcl8b.1 attempted to replicate the anti-tumour effects observed in the brain of Gold implanted zebrafish. Spatiotemporal control of the expression of *tnf-α* and *cxcl8b.1* was attempted using an inducible genetic expression system. An inducible system conferred the capability to replicate the conditions of bead implantation at 4 dpf instead of a 'traditional' transgenic overexpression of a transgene controlled by a constitutively active cell specific promoter.

The mifepristone-inducible lexPR system was developed to drive and regulate the expression of *tnf-α* and *cxcl8b.1* in transgenic zebrafish to no avail. The Mifepristone inducible LexPR system is a hormone-response transcriptional activator that confers accurate spatiotemporal control of transgene expression (Emelyanov and Parinov, 2008). In order to demonstrate the viability of the LexPR system *in vivo*, transgenic *NBT:lexPR:lexOP:GFP* zebrafish were injected with *lexOP:RFP* at the one cell stage. The neural beta tubulin (NBT) promoter in *NBT:lexPR:lexOP:GFP* is a neuronal lineage marker that drives the expression of *lexPR:lexOP:GFP* transgene in neurons (Peri and Nusslein-Volhard, 2008). Inducible expression of RFP and GFP was achieved at 4 dpf by adding 5 µM Mifepristone into the media and incubated for 24 hours. Indeed, the activation of lexPR by synthetic steroid, mifepristone activated the expression of operator promoter (lexOP) sequence that expressed GFP and RFP proteins in neurons (Figure 34A). The co-expression of RFP and GFP was evident in some

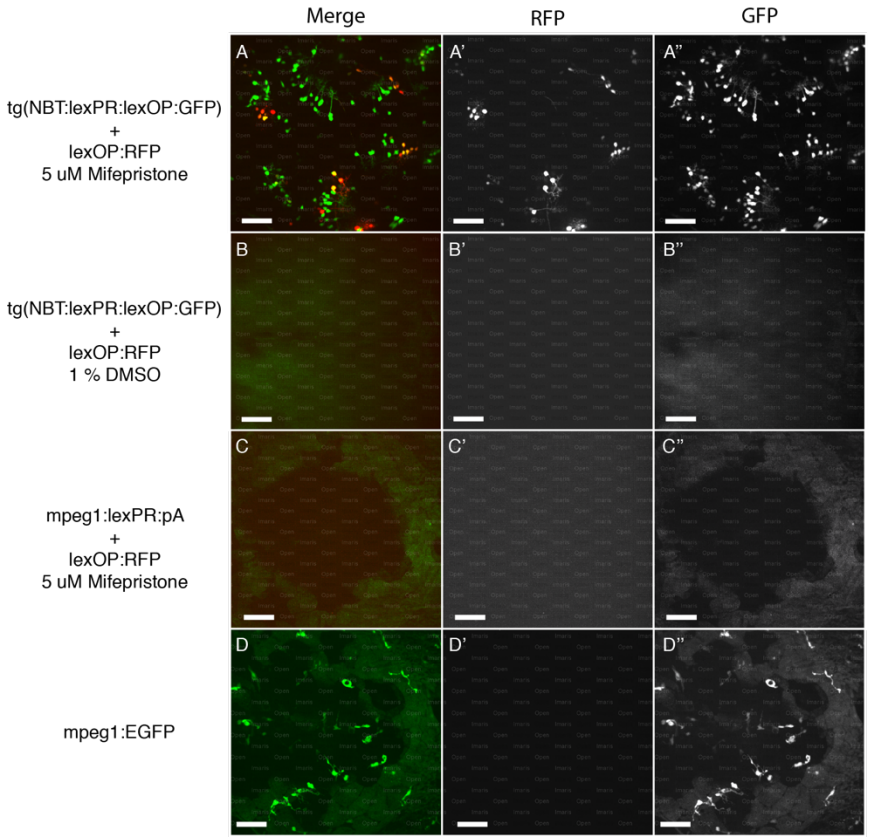

Figure 34. mpeg1 inducible expression of RFP in macrophages showed weak expression of RFP protein.

Inducible expression of RFP was achieved by adding 5 µM Mifepristone into E3 media with 4 dpf zebrafish and incubated for 24 hours. All images were obtained using an Andor spinning disk confocal microscope with a 20X/NA 0.75 objective. Scale bars were set at 50 µm. All zebrafish were at 5 dpf when imaged.

(A) Transgenic *NBT:lexPR:lexOP:GFP* zebrafish were injected with *lexOP:RFP* construct at the one cell stage. The activation of lexPR by synthetic steroid, mifepristone, activated the expression of operator promoter (lexOP) sequence that expressed GFP and RFP fluorophore in neurons. The co-expression of RFP and GFP was evident in cells that morphologically resembled neurons, based on axonal expression of RFP and GFP fluorophore.

(B) 1% DMSO controls showed no expression of RFP or GFP in *NBT:lexPR:lexOP:GFP* zebrafish injected with *lexOP:RFP* construct. This supported the induction capabilities of the mifepristone inducible lexPR system.

(C) Wild type (WIK) zebrafish were co-injected with *mpeg1:lexPR:pA* and *lexOP:RFP* constructs. The application of 5 µM Mifepristone into the embryo media from 4 dpf to 5 dpf failed to induce reliable expression of RFP expression in macrophages. The Mifepristone inducible expression system was not compatible with mpeg1 promoter.

(D) Control injections of mpeg1:EGFP plasmid into wild type (WIK) zebrafish stimulated the expression of GFP fluorophore in macrophages. Thus, the mpeg1 promoter was cloned into mpeg1:tnf-α and mpeg1:cxcl8b.1 plasmids in order to direct tnf-α and cxcl8b.1 overexpression in macrophages.

cells that morphologically resembled neurons, based on axonal expression of RFP and GFP proteins. DMSO controls showed no expression of RFP or GFP (Figure 34B) which supported the induction capabilities of the mifepristone inducible lexPR system.

In order to achieve spatiotemporal control of tnf-α and cxcl8b.1 expression in macrophages, the lexOP operator was cloned into *lexOP:tnf-α* and *lexOP:cxcl8b.1* expression plasmid. In addition, lexPR coding sequence was cloned into *mpeg1:lexPR:pA* plasmid under the control of macrophage lineage *mpeg1* promoter (Ellett et al., 2011). Overexpression of tnf-α and cxcl8b.1 would have been achieved by co-injecting *mpeg1:lexPR:pA, lexOP:tnf-α* and *lexOP:cxcl8b.1* transgenes into mpeg1:EGFP or mpo:EGFP zebrafish and the associated anti-tumour responses, macrophage and neutrophil activities investigated. In order to study the viability of the inducible system under a different promoter (mpeg1) as compared to previous (NBT), wild type (WIK) zebrafish were co-injected with *mpeg1:lexPR:pA* and *lexOP:RFP* constructs and the distribution RFP fluorophore analyzed. The application of 5 μM Mifepristone into the embryo media at 4 dpf failed to induce reliable expression of RFP expression in macrophages (Figure 34C). Faint and weak expression of RFP signal was visible however it was not viable to support robust overexpression studies of *tnf-α* and *cxcl8b.1*. Thus, the Mifepristone inducible expression system was not compatible with mpeg1 promoter and a constitutively active overexpression system was utilised instead.

To achieve the overexpression of tnf-α and cxcl8b.1 in macrophages of the zebrafish brain a constitutively active overexpression system was used under the control of the mpeg1 promoter. Indeed, control injections of *mpeg1:EGFP* plasmid into wild type (WIK) zebrafish stimulated the expression of GFP fluorophore in macrophages (Figure 34D). Therefore, the mpeg1 promoter was cloned into mpeg1:tnf-α and mpeg1:cxcl8b.1 plasmids in order to direct tnf-α and cxcl8b.1 overexpression in macrophages. One of the caveats of a constitutively active promoter driven transgene expression system was the lack of temporally specificity. The overexpression of tnf-α and cxcl8b.1 occurred at birth and thus did not closely replicate the temporal conditions of Gold bead induced tnf-α and cxcl8b.1 overexpression at 5 dpf. Nonetheless, the *mpeg1* promoter driven transgene expression system was the most reliable option to induce *tnf-α* and *cxcl8b.1* overexpression within the timeframe of this study.

3.5.5. *tnf-α* and *cxcl8b.1* overexpression had no effect on U87-nls-mKate2 cell survival or on macrophage and neutrophil number.

To evaluate a possible role for tnf-α and cxcl8b.1 expression in macrophages on the anti-tumour phenotype, transgenic mpeg1:EGFP (tg(mpeg1:EGFP)) and mpo:EGFP (tg(mpo:EGFP)) zebrafish were co-injected with *mpeg1:tnf-α* and *mpeg1:cxcl8b.1* plasmids and transplanted with U87-nls-mKate2 cell. The effect of tnf-α and cxcl8b.1 overexpression in macrophages on U87-nls-mKate2 survival, macrophage intensity and neutrophil infiltration were investigated. Zebrafish embryos (3 dpf) were xenografted with U87-nls-mKate2 cells and imaged at 4, 5 and 7 dpf. The timeline mirrors that of in vivo bead implantation experiments in order to recapitulate the same experimental conditions as Gold bead implanted zebrafish. This study aimed to test the hypothesis that cxcl8b.1 and tnf-a expression in macrophages were important genetic mediators of Gold bead induced anti-tumour effects of macrophages and neutrophils in the zebrafish brain.

To investigate if tnf-α and cxcl8b.1 expression led to increased macrophage number, the effect on macrophage intensity was characterized in tg(mpeg1:EGFP) zebrafish co-injected with mpeg1:tnf-α and mpeg1:cxcl8b.1 (Figure 35A-B). The overexpression of tnf-α and cxcl8b.1 significantly ($p = 0.0318$) increased macrophage intensity by 1.4 fold at 5 dpf when compared to wild type (Figure 35F). However, this initial spike in macrophage intensity was significantly lower than that in Gold bead implanted zebrafish. The implantation of Gold bead at 5 dpf significantly increased macrophage intensity by 13 folds when compared to bead null wild type mpeg1:EGFP zebrafish (Figure 32C,H). The spike in macrophage intensity in tnf-α and cxcl8b.1 overexpressed mpeg1:EGFP zebrafish returned to basal levels by 7 dpf. However, there was a trend ($p = 0.0600$) to indicate that overexpression of tnf-α and cxcl8b.1 of macrophages led to decreased macrophage numbers. Nonetheless, the overexpression of tnf-α and cxcl8b.1 of macrophages in mpeg1:EGFP did not promote increased macrophage number in the zebrafish brain.

To understand if overexpression of tnf-α and cxcl8b.1 in macrophages promoted the recruitment of neutrophils into the zebrafish brain, tg(mpo:EGFP) zebrafish were co-injected

with *mpeg1:tnf-α* and *mpeg1:cxcl8b.1* plasmids (Figure 35C-D). Previous study indicated that Gold bead implantation recruited significantly increased number of neutrophils at 1 dpt when compared to Naked bead implanted tg(mpo:EGFP) zebrafish (Figure 28). However, the over-expression of tnf-α and cxcl8b.1 did not increase the infiltration of neutrophil at all time points (4, 5 and 7 dpf). The number of neutrophils in the zebrafish brains in mpeg1:tnf-α and mpeg1:cxcl8b.1 injected tg(mpo:EGFP) zebrafish were statically similar at 5 dpf ($p = 0.733$) and 7 dpf ($p = 0.323$) (Figure 35G). Thus tnf-α and cxcl8b1 overexpression in macrophages did not increase the recruitment of neutrophils in the zebrafish brain.

The overexpression of tnf-α and cxcl8b.1 in macrophages of the zebrafish brain had no effect on the survival U87-nls-mKate2 cells. A notable absence of anti-tumoural effect was observed in tg(mpeg1:EGFP) and tg(mpo:EGFP) zebrafish co-injected with *mpeg1:tnf-α* and *mpeg1:cxcl8b.1*(Figure 35.. Instead, a significant increase by 27 ± 6.93 % ($p = 0.0387$) in U87-nls-mKate2 cell number was observed at 4 dpf when compared to wild type background (uninjected, tg(*mpeg1:EGFP*)). However, by 7 dpf, only a trend ($p = 0.201$) supported the increase in U87-nls-mKate2 cell number (Figure 35. Nonetheless, tnf-α and cxcl8b.1 overexpression in macrophages of *mpeg1:EGFP* zebrafish did not elicit an anti-tumour phenotype. In agreement with previous CRISPR double mutant knockout studies (See section 3.5.3 for details), the result implied that tnf-α and cxcl8b.1 were not critical genetic effectors of anti-tumour phenotype in the zebrafish brain.

Due to the lack of effect of tnf-α and cxcl8b.1 overexpression in macrophages, we confirmed the overexpression of *tnf-α* and *cxcl8b.1* in tg(*mpeg1:EGFP*) zebrafish by reverse transcription polymerase chain reaction (RT-PCR). tg(mpeg1:EGFP) zebrafish were injected with either *mpeg1:tnf-α* or *mpeg1:cxcl8b.1* plasmid constructs to drive overexpression of either genes. Total RNA content was isolated from whole embryos and first strand cDNA synthesis was performed on extracted RNA. The expression of *β* actin gene of injected and wild type (WIK) zebrafish was used as the reference gene. *β* actin, show no differential expression which indicated that global genetic expression was similar in all zebrafish samples (Figure 36). (GFP). The increase in GFP expression, darker bands, was evident in tg(mpeg1:EGFP)

zebrafish injected with either *mpeg1:tnf-α* or *mpeg1:cxcl8b.1* when compared to wild type zebrafish (WIK) (Figure 36). Therefore, mpeg promoter activity in zebrafish was capable of driving transgene expression.

The injection of *mpeg1:tnf-α* plasmid overexpressed *tnf-α* in the zebrafish. PCR products from tg(mpeg1:EGFP) zebrafish injected with *mpeg1:tnf-α* formed a slightly darker band stain than wild type (WIK) and *mpeg1:cxcl8b.1* injected zebrafish (Figure 36, Black Arrow). In contrast, RT-PCR did not demonstrate the overexpression of *cxcl8b.1* in *mpeg1:cxcl8b.1* injected zebrafish. No significant difference in band staining was observed for *mpeg1:cxcl8b.1* injected zebrafish when compared to wild type (WIK) and *mpeg1:tnf-α* injected zebrafish (Figure 36). It was important to note that the isolation of total RNA content was conducted on whole embryos and not on isolated macrophages. Thus the dilution of the overexpression effect for either *tnf-α* or *cxcl8b.1* transcripts would occur. Nonetheless, RT-PCR validated the overexpression of tnf-α in *mpeg1:tnf-α* injected zebrafish but not for *cxcl8b.1* in *mpeg1:cxcl8b.1* injected zebrafish.

The injection of *mpeg1:tnf-α* and *mpeg1:cxcl8b.1* plasmid into tg(mpeg:EGFP) zebrafish elicited no detectable phenotypic change that indicated an anti-tumour response of macrophages or infiltrating neutrophils. Since only tnf-α overexpression was confirmed, the effects of cxcl8b.1 overexpression remained inconclusive. The overexpression of *tnf-α* in macrophages had no effect on U87-nls-mKate2 cell engraftment and proliferation in the zebrafish brain. In addition, the macrophage and neutrophil response towards genetic overexpression of *tnf-α* was comparable to wild type conditions. Therefore, *tnf-α expression in macrophages was not an important genetic mediator of Gold bead induced anti-tumour responses of macrophages and neutrophils in the zebrafish brain.*

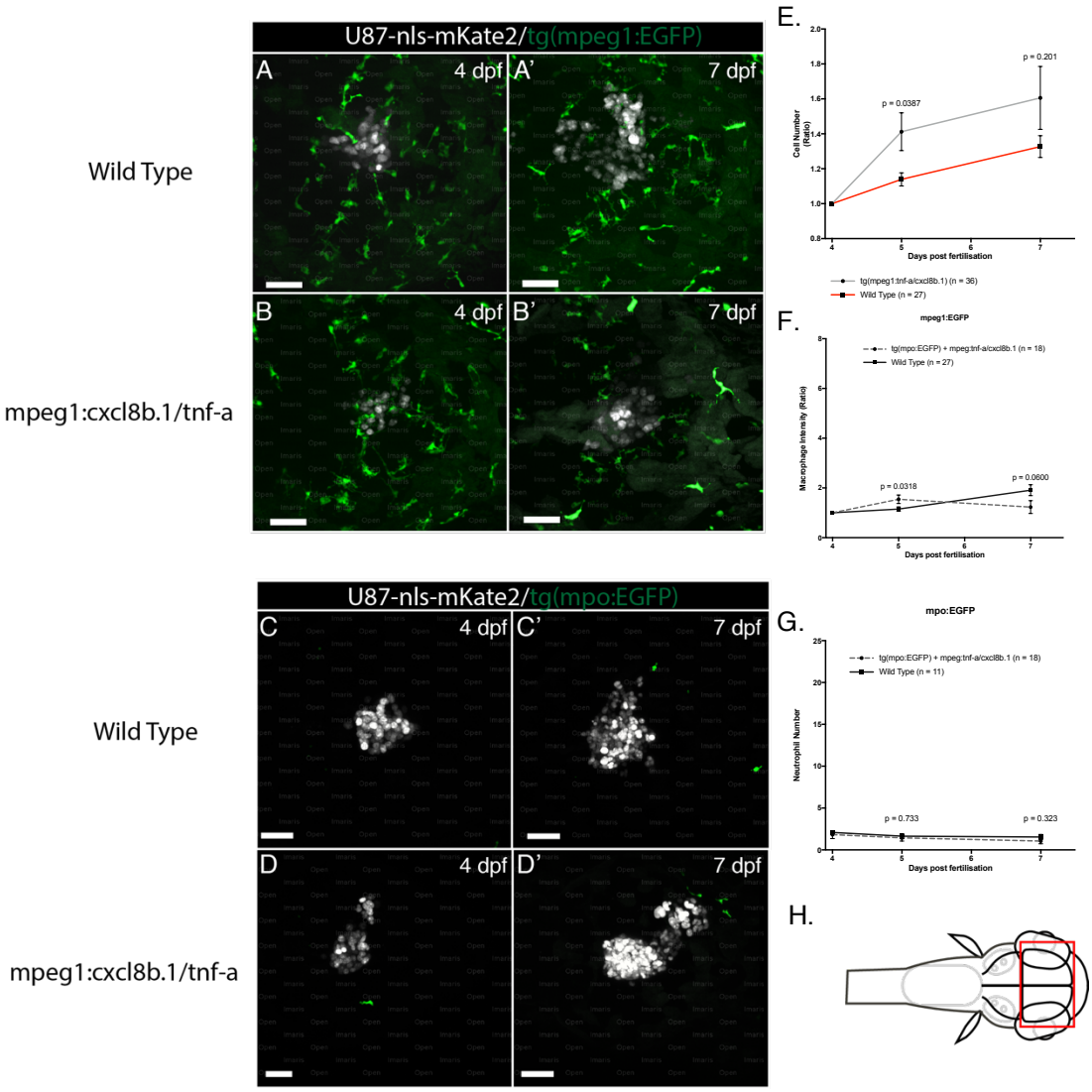

Figure 35. tnf-α and cxcl8b.1 overexpression had no effect on U87-nls-mKate2 cell survival or on macrophage and neutrophil number.

mpo:EGFP and mpeg1:EGFP zebrafish were co-injected with *mpeg1:tnf-α* and *mpeg1:cxcl8b.1* plasmid constructs to overexpress tnf-α and cxcl8b.1 in macrophages. Human derived Lv-cppt-IRES-nls-mKate2-opre transformed U87-nls-mKate2 cells (White) were xenografted into 3 days post post fertilized (dpf) wild type and tnf-α/cxcl8b.1 overexpressed zebrafish. Xenografted zebrafish embyros were imaged using an Andor spinning disk confocal microscope with a 20X/NA 0.75 objective. Scale bars were set at 50 µm. Images from *left* to *right* are in chronological order showing images from 4 and 7 day dpf. (A) The macrophage responses in wild type mpeg1:EGFP zebrafish was comparable to tnf-α and cxcl8b.1 overexpressed zebrafish. (B) The overexpression of *tnf-α* and *cxcl8b.1* in macrophages did not promote increased macrophage number in the zebrafish brain. (C) Low number of neutrophil was present in wild type mpeg1:EGFP zebrafish. (D) *tnf-α* and *cxcl8b.1* overexpression in macrophages had no effect on neutrophil infiltration in the zebrafish brain.

(E) The overexpression of tnf-α and cxcl8b.1 in macrophages of the zebrafish brain had no effect on the survival of U87-nls-mKate2 cells.

(F) The overexpression of tnf-α and cxcl8b.1 significantly (p = 0.0318) increase macrophage intensity by 1.4 folds at 5 dpf when compared to wild type. The spike in macrophage intensity in tnf-α and cxcl8b.1 overexpressed

mpeg1:EGFP zebrafish returned to basal levels by 7 dpf. No significant difference (p = 0.0600) in macrophage intensities was observed by 7 dpf.

(G) The number of neutrophils in the zebrafish brains in mpeg1:tnf-α and mpeg1:cxcl8b.1 injected tg(mpo:EGFP) zebrafish were statically similar at 5 dpf (p = 0.733) and 7 dpf (p = 0.323).

(H) The imaging field emcompassed both optic tectums of the zebrafish brain. The red box of the schematic image denotes boundary of the imaging region and represented the orientation of all images from A-D.

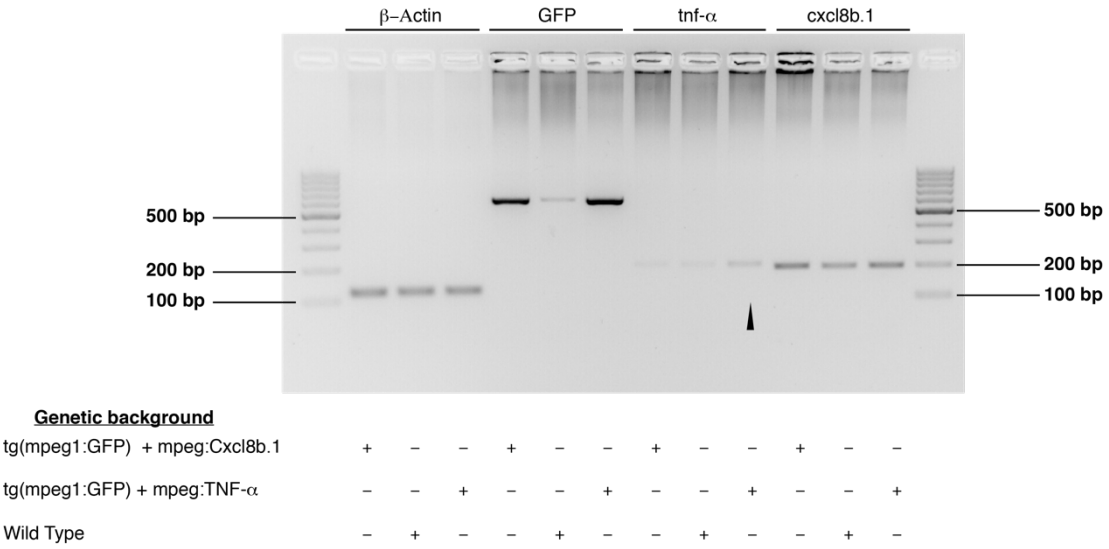

Figure 36. Reverse transcription polymerase chain reaction revealed over-expression of tnf-α in mpeg1:tnf-α injected mpeg1:EGFP zebrafish

tg(mpeg1:EGFP) zebrafish were injected with either *mpeg1:tnf-α* or *mpeg1:cxcl8b.1* plasmid constructs to drive overexpression of either genes. RT-PCR was conducted on total RNA content isolated from whole embryos of wild type (WIK) zebrafish, mpeg1:tnf-α injected tg(mpeg1:EGFP) zebrafish and mpeg1:cxcl8b.1 injected tg(mpeg1:EGFP) zebrafish.

Negative control, β actin, show no differential expression of genes and indicated that global genetic expression was similar in all zebrafish samples.

The increase in GFP expression, darker bands, was evident in tg(mpeg1:EGFP) zebrafish injected with either *mpeg1:tnf-α* or *mpeg1:cxcl8b.1* when compared to wild type.

The injection of *mpeg1:tnf-α* plasmid overexpressed *tnf-α* in the zebrafish. PCR products from tg(mpeg1:EGFP) zebrafish injected with *mpeg1:tnf-α* formed a slightly darker band stain than wild type (WIK) and *mpeg1:cxcl8b.1* injected tg(mpeg1:EGFP) zebrafish.

RT-PCR did not demonstrate the overexpression of *cxcl8b.1* in *mpeg1:cxcl8b.1* injected zebrafish. No significant difference in band staining was observed for *mpeg:cxcl8b.1* injected tg(*mpeg1:EGFP*) zebrafish.

4. Discussion

4.1.1. Palladium metal as a mediator of bioorthogonal drug catalyst *in vivo*

In this study, we attempted to establish an *in vivo* bioorthogonal catalytic drug assay in order to test the efficacy of a novel drug delivery system that had the potential to contribute to the development of novel chemotherapeutics. The idea of utilising nanoparticle mediated drug delivery systems is not entirely novel and has been investigated in many studies (Sangtani et al., 2017, Wang et al., 2019, Clavadetscher et al., 2016, Tonga et al., 2015). Initial medical applications of nanoparticles began as a theranostic (diagnostic imaging) compound used on imaging platform such as MRI, PET and CT (Phillips et al., 2014). Nanoparticles have evolved into multifunctional nanoparticles that can serve as drug carriers and as a theranostic. Here, Palladium nanoparticles, solidly supported within a polystyrene matrix (bead), performed as catalysts that mediated BOOM reactions in the zebrafish brain to convert a pro drug (POB-Vorinostat) to its active form (Vorinostat). However, preliminary experiments indicated that Palladium bead implantation initiated a potent anti-tumour effect in the absence of the chemotherapeutic agent, Vorinostat. Although this was not the first time Palladium nanoparticles had been described to possess anti-tumour properties (Alarifi et al., 2017, Dahal et al., 2015), this study was the first to demonstrate Palladium mediated anti-tumour effects on glioblastoma cells *in vivo* in zebrafish.

4.1.2. Investigating the effects of macrophage polarisation by Palladium beads

The zebrafish model system utilised in this study facilitated the in-depth study of the effects of nanoparticle mediated macrophage polarisation on U87 glioblastoma cells. We first established that macrophage mpeg1:EGFP signal intensity correlated with macrophage number. This allowed for the rapid and robust evaluation of macrophage number, forgoing tedious and time-consuming manual counting of macrophage number. Next, we confirmed that Pal-

ladium bead implantation initiated a potent anti-tumour effect. The anti-tumour effect recruited macrophages and coincided with the decrease in U87 cell survival and an increase in U87 cell fragmentation when compared to the injury model. The anti-tumour effects observed in this study was reminiscent of macrophage polarisation described in previous studies (van Dalen et al., 2018, Vogel et al., 2014, Zanganeh et al., 2016) as a strong macrophage inflammatory response was evident. An increase in macrophage mpeg1:EGFP signal intensity was observed in close proximity with Palladium beads. Indeed, macrophage have been shown to interact with nanoparticles and these interactions have been shown to promote pro-inflammatory responses (Park and Park, 2009, Hutter et al., 2010, Ge et al., 2015, Kusaka et al., 2014). Metallic nanoparticles have been previously shown to polarise macrophages and peripheral blood mononuclear cells. One study investigate the effects of titanium nanoparticles on alveolar macrophages (Scherbart et al., 2011). Scherbart et al,. showed that titanium nanoparticles accumulated in macrophages and caused increased extracellular ROS, heme-oxygenase 1 and tnf-α expression. While in another study, Palladium nanoparticles were demonstrated to enhance Ifn-y release in LPS stimulated peripheral blood mononuclear cells (Boscolo et al., 2010). Macrophage internalisation of nanoparticles has been shown to regulate release of pro-inflammatory cytokines such a il-1β and tnf-α (Kusaka et al., 2014, Leso and Iavicoli, 2018). However, one key difference that sets this study apart is the fact that Palladium nanoparticles were solidly supported upon a polystyrene matrix. As a result, Palladium nanoparticles, in theory, would not be internalised by macrophages. Whether Palladium nanoparticles diffused from the bead surface remains speculatory. However, mechanical manipulation of Palladium bead may dislodge Palladium nanoparticles from the bead surface which may accumulate in macrophages. In addition, Palladium nanoparticles may be released as Palladium ions. One study concluded that Silver ions leaching from the larger fractions of Silver nanoparticles mediates the toxicity of Silver nanoparticles in macrophages (Pratsinis et al., 2013). Therefore, it would be interesting to ascertain if macrophage interacted with Palladium nanoparticles on the bead surface or interacted with internalised free Palladium nano-

particles to initiate macrophage polarisation effects. Nonetheless, there was significant evidence to suggest that the implantation of Palladium bead polarised macrophages to initiate an anti-tumour response.

4.1.3. Identifying the contributions of macrophage function in Palladium mediated anti-tumour effects

The tumour supporting role of macrophage function had been described previously (Noy and Pollard, 2014, Prionisti et al., 2019, van Dalen et al., 2018, Pyonteck et al., 2013). Consequently, we demonstrate in this study that macrophage function supported U87 cell growth in the zebrafish brain. We observed a reduction in U87 cell survival in *irf8*$^{-/-}$, macrophage null, zebrafish when compared to wild type. The inherent disability of U87 to survive in the *irf8*$^{-/-}$ zebrafish was reflected in all xenografted *irf8*$^{-/-}$ zebrafish including Palladium bead implanted *irf8*$^{-/-}$ zebrafish. A trend indicated that the survival rate of U87 cells in Palladium bead implanted *irf8*$^{-/-}$ zebrafish were better than that in Palladium bead implanted mpeg1:EGFP zebrafish. This implied that macrophage function was important in mediating the anti-tumour effects observed in Palladium bead implanted zebrafish. However, due to low n numbers ($n = 4$, $p = 0.109$), the trend was statically insignificant. Several factors contributed to the low n numbers described in Palladium bead implanted *irf8*$^{-/-}$ zebrafish. First, the implantation of Palladium bead was toxic, a 33% survival rate was recorded in Palladium bead implanted mpeg1:EGFP zebrafish. Intriguingly, Weiss et al. report that zebrafish larvae developed normally into the larval stages with no sign of toxicity after Palladium bead implantation (Weiss et al., 2014a). The differences may be attributed to the location of bead implantation as the authors (Weiss et al., 2014a) performed the implantation into the yolk sac of the zebrafish embryo. Secondly, *irf8*$^{-/-}$ zebrafish have reduced survival rates compared to wildtype (Shiau et al., 2015). Thirdly, the absence of macrophage function in *irf8*$^{-/-}$ zebrafish exacerbated defective clearance of apoptotic cells and eliminated neuroprotective effects of macrophages and microglia in the brain following bead implantation procedure (Shiau et al., 2015, Casano

and Peri, 2015, Herzog et al., 2019). When combined, these factors had a detrimental impact on the survival of Palladium bead implanted *irf8*$^{-/-}$ zebrafish reflected as low n numbers (Figure 11). Although the results were statically insignificant, the data support the role of macrophage in mediating the anti-tumour effects of Palladium bead implantation.

4.1.4. ROS mediated anti-tumour effects of macrophages

Next generation RNA sequencing offered the opportunity to investigate key mechanisms underlying macrophage tumoricidal polarisation in Palladium bead implanted zebrafish. Differential analysis of RNA sequencing expression data revealed that the implantation of Palladium bead lead to a stress response of macrophages that increased expression of protein associated with stress tolerance (Hsp70l) and increased reactive oxygen species (ROS) generation. In addition, we also detected the increase in proinflammatory cytokine expression (tnf-a, cxcl8b.1) and the decrease in proangiogenic factors (sema4d and sox7) in Palladium bead implanted zebrafish. Altogether, Palladium bead implantation lead to the polarisation of macrophage genetic profile towards a proinflammatory anti-tumour phenotype.

In agreement, previous works have demonstrated that metallic nanoparticles such as Titanium, Iron oxides, Palladium and Zinc dioxide all increased intracellular ROS generation in macrophages (Yang et al., 2009, Dahal et al., 2015, Scherbart et al., 2011, Reichel et al., 2019, Alarifi et al., 2017). Myeloid cell have been shown to be an important source of ROS in acute and chronic inflammation (Bogdan et al., 2000). ROS are a heterogenous group of highly reactive ions that act as both a signalling molecule and as pro-inflammatory mediators (Mittal et al., 2014, Thannickal and Fanburg, 2000). ROS can combine with nitric oxide to form reactive nitrogen species which contributes to the overall pro-inflammatory signalling axis (Thannickal and Fanburg, 2000, Mittal et al., 2014). The formation of reactive nitrogen species in macrophages have been shown to be a source of highly toxic oxidants capable of microbicidal killing (MacMicking et al., 1995). In addition, ROS secretion has been shown to mediate intracellular signalling pathways that lead to cellular apoptosis (Kamata et al., 2005, Saitoh

et al., 1998). In addition, ROS has been shown to induce apoptosis in U87 cells (Recio Despaigne et al., 2014 , Wang et al., 2013). However, chronic production of ROS has long been hypothesised to be the central driving force leading to inflammatory diseases that contributed to carcinogenesis (Hussain and Harris, 2007, Kawanishi et al., 2017, Canli et al., 2017). ROS have been shown to induce DNA damage that could increase the mutational load leading to genomic instabilities and cancer initiation (Bogdan et al., 2000, Canli et al., 2017). ROS have also been shown to inactivate p53 tumour suppressor genes through the introduction of p53 mutations (Hussain et al., 1994). Therefore, the effects of ROS on cancer have been described as both tumour promoting and tumour suppressing depending on the concentration and duration of exposure (Galadari et al., 2017). However the relatively short duration of this study (3 days) likely initiated ROS mediated acute inflammation that promoted the apoptosis and cytotoxicity of U87 cells. Nonetheless, it would be interesting to investigate the long term chronic consequences of Palladium bead implantation in order to bridge the current knowledge gap. Little is known in regards to the consequences of long term immune responses associated with Palladium nanotherapeutics. These studies have implications in extending our understanding of the chronic effects of nanoparticles in medical technologies.

4.1.5. Differential analysis expression data of U87 versus Control revealed no significant differentially expressed genes

Extensive molecular profiling has been conducted to show that TAMs contribute to the establishment of an immunosuppressive environment through the secretion of anti-inflammatory cytokines (il-10 and TGF-β) and the inhibition of pro-inflammatory cytokines (tnf-α, il-12, il-1*β, NO and Ifn-y)* (Wu et al., 2010, Hussain et al., 2006, Komohara et al., 2008, Rodrigues et al., 2010, Li and Graeber, 2012). In addition, glioma associated macrophages have been shown to display distinct expression profiles when compared to human controls (Szulzewsky et al., 2016). Szulzewsky et al. identified 334 differentially expressed genes in human glioblastoma associated microglia/monocytes compared to human controls (Szulzewsky et al.,

2016). In another study by the same authors, microarray analysis comparing glioma associated macrophages and control macrophages identified approximately 1000 differentially expressed genes (Szulzewsky et al., 2015). Therefore, overwhelming evidence exists to describe TAM as functionally and molecularly distinct from macrophages in the non-diseased setting. Thus, we hypothesised that U87 xenografts would induce genetic expression changes in tumour associated microglia/macrophages. However, differential analysis of RNA seq expression datasets demonstrated that macrophages isolated from U87 xenografted and Control were similar in expression patterns to each other. No significant differentially expressed genes were recorded in comparison to controls. The results here contradicted previous studies which described TAM as being functionally pro-tumoural and genetically distinct when compared to macrophages in the non-diseased setting (Wu et al., 2010, Hussain et al., 2006, Komohara et al., 2008, Rodrigues et al., 2010, Li and Graeber, 2012, Hamilton et al., 2016, Noy and Pollard, 2014). The contributing factors that may have led to this result could have originated from our macrophage isolation and bulk RNA sequencing strategy. In order to isolate macrophages from the zebrafish, the heads of the zebrafish were transacted above the yolk sac and the tissue pooled and homogenised. Therefore, isolated macrophage from mpeg1:EGFP zebrafish would include a pooled macrophage population encompassing those from the telencephalon, olfactory bulb, cerebellum, spinal cord and retina. Tumour associated macrophage would represent a subset of the pooled macrophage population. Consequently, the total RNA content extracted from the pool population of macrophages would not reflect the true population of tumour associated macrophages responsible for the tumour promoting functions in U87 xenografted mpeg1:EGFP zebrafish. Differentially expressed genes in TAMs would be diluted by RNA content from non TAMs resulting in a differential analysis that would be indistinguishable from macrophages in the non-disease setting.

4.1.6. Disadvantages of Bulk RNA seq reveals potential application of single cell RNA sequencing techniques

The combination of bulk RNA sequencing strategy and the utility of a single genetic marker (mpeg1) to isolate macrophages was one of the major pitfalls of this study. Consequently, this led to a lack of genetic sampling resolution required to differentiate infiltrating tumour associated macrophages from resident tumour associated microglia. In order to achieve high genetic sampling resolution using contemporary approaches, researchers have used multi-marker protocols in order to isolate several distinct populations of monocyte/macrophages/microglia from tumours (Poczobutt et al., 2016). However, multi-marker protocols can be technically complex. In addition, the number of monocyte populations that could be isolated is limited by the number of established markers available for flow cytometry, a factor that does not affect scRNA. Therefore, there is significant scope in applying scRNA sequencing techniques to understand the functional and transcriptional dynamics between tumour associated macrophages and microglia in our study.

The advent of single cell RNA (scRNA) sequencing techniques has exposed unique aspects of the cellular and molecular identity of TAMs. In one recent study, single cell profiling of human gliomas revealed distinct macrophage ontogeny that highlighted regional difference in TAMs activation (Muller et al., 2017). By comparing the single cell RNA expression profile of sequenced TAMs to known expression profiles of anatomically defined tumour compartments (Ivy Glioblastoma Atlas Project) the authors were able to infer macrophage localisation within the tumour (Muller et al., 2017). scRNA seq confers greater genetic sampling resolution and higher fidelity than bulk RNA seq (Marinov et al., 2014). One study contrasting scRNA and bulk (cell pooled) RNA seq concluded that the transcriptomes from 30 – 100 cells assessed using scRNA techniques were comparable to those of bulk RNA seq using large amount of genetic material (Marinov et al., 2014). Therefore, the advent of scRNA seq allows researchers to investigate the extensive transcriptional and ontogenetic diversity that exists within macrophage populations in greater depth (Chen et al., 2017, Muller et al., 2017,

Bowman et al., 2016). Extensive studies have been conducted to show that infiltrating tumour associated macrophages have distinct expression profiles and functions when compared to tumour associated microglia (Muller et al., 2017, Chen et al., 2017, Bowman et al., 2016, Szulzewsky et al., 2016). Chen et al., established that the majority of TAMs in GBMs were bone marrow derived (Chen et al., 2017). While in another study, it was demonstrated that blood derived TAMs expressed significantly higher levels of immunosuppressive cytokines il-10 and TGF$\beta 2$ in comparison to microglia (Muller et al., 2017). Therefore, it would be interesting to investigate the level of contribution of distinct populations of polarised tumour associated macrophages or microglia in mediating the anti-tumour effects in Gold or Palladium bead implanted zebrafish. scRNA seq would confer greater transcriptomic fidelity than contemporary methods to identify macrophage genetic signatures associated with anti-tumour efficacy.

4.1.7. Macrophage polarisation by Gold and Palladium beads initiates anti-tumour phenotype.

The anti-tumour effects of Palladium beads excluded the utility of Palladium mediated bioorthogonal drug assays of chemotherapeutics in the zebrafish brain. Therefore in order to achieve our original aim, which was to develop an *in vivo* bioorthogonal catalytic drug assay, Palladium was replaced with Gold beads. Gold nanoparticles have extensive application in biological and medical applications and have been used therapeutically for drug delivery (Niikura et al., 2013, Perez-Lopez et al., 2017, Yeo et al., 2018, Naz et al., 2016). We demonstrated that Gold beads mediated BOOM reactions *in vivo* in the zebrafish brain and converted precursors into fluorescent Rhodamine. Although Gold beads were biocompatible in mediating BOOM reaction in the zebrafish brain, it was immediately evident that Gold bead implantation initiated a potent anti-tumour effect that also recruited macrophages; effects similar to Palladium bead implanted zebrafish. Intriguingly, several studies have demonstrated that Gold nanoparticles initiates anti-inflammatory cytokine production in macrophages. Taratummarat et al., showed that Gold nanoparticles attenuated supernatant tnf-α,

il1-β and enhanced il-10 secretion in bone marrow derived macrophages *in vitro* cultures (Taratummarat et al., 2018). The authors also demonstrated that Gold nanoparticles reduced the percentage of pro-inflammatory macrophages and increased the percentage of anti-inflammatory macrophages (Taratummarat et al., 2018). Likewise, Gold nanoparticles reduced the expression of pro-inflammatory mediators such as prostaglandin E2, il-6 and tnf-α in RAW264.7 macrophages cultures (Ma et al., 2010, Ahn et al., 2017). Consequently the authors conclude that Gold nanoparticles resulted in the suppression of NF-kB pathway, a key transcription factor mediating inflammatory response (Ma et al., 2010, Ahn et al., 2017). The notion that Gold was an anti-inflammatory mediator contradicted our study. In contrast, we observed a significant inflammatory response to Gold bead implantation reflected as an increase in macrophage number in the zebrafish brain. However, it is important to note that the aforementioned studies (Ma et al., 2010, Ahn et al., 2017, Taratummarat et al., 2018) on Gold nanoparticles were conducted *in vitro* and thus would not recapitulate the *in vivo* conditions reflected in Gold bead implanted zebrafish. Nanoparticles exposed to serum proteins have been shown to form a protein corona that has a direct effect on the inflammatory state of macrophages (Cedervall et al., 2007, Ge et al., 2015, Kharazian et al., 2016). Therefore, we speculate that both Gold and Palladium nanoparticles may interact with intracellular proteins to create a protein corona that initiated macrophage polarisation. The adhesion of proteins from the bloodstream to nanoparticles are often inhibited by modifying the surface with PEG to inhibit macrophage uptake (Jokerst et al., 2011, Xie et al., 2007, van Vlerken et al., 2007). Functionalisation of proteins or peptides to nanoparticle surface have been shown to induce pro-inflammatory properties in macrophages (Bastus et al., 2009a, Bastus et al., 2009b, Chen and Gao, 2017). One study compared the inflammatory reactions between PEG and chicken ovalbumin conjugated Gold nanoparticles on RAW246.7 macrophage (Chen and Gao, 2017). Chen et al., reported that Gold nanoparticles conjugated to ovalbumin increased cytokine production of tnf-α, il-6 and il-1β while PEG conjugated Gold nanoparticles significantly attenuated the production of tnf-α and il-6. Furthermore, Bastus et al., demonstrated that the

treatment of macrophages with peptide-conjugated Gold nanoparticles induced pro-inflammatory cytokine production in macrophages mediated by TLR-4 activation (Bastus et al., 2009a). It was interesting to note that although Chen et al. utilised the same *in vitro* RAW264.7 macrophage co-cultures described in previously mentioned studies (Ma et al., 2010, Ahn et al., 2017), the conjugation of albumin to Gold nanoparticles was pro-inflammatory while unconjugated Gold nanoparticles were anti-inflammatory. This further highlighted the significant of nanoparticle surface protein corona in mediating the inflammatory response of macrophages. In addition, the idea that Gold and Palladium nanoparticles may bind intracellular proteins may explain the similarities in pro-inflammatory activation profiles observed between Gold and Palladium implanted zebrafish. Gold and Palladium nanoparticles may recruit similar protein coronas leading to TLR activation. The protein corona have been shown to modulate the functional identity of nanoparticles (Ge et al., 2015, Kharazian et al., 2016). Therefore, intracellular protein-nanoparticle surface interactions may play a key role in conferring the pro-inflammatory tumoricidal response of macrophages to Palladium and Gold beads in the zebrafish brain.

4.1.8. TLR family signalling in Palladium and Gold bead implanted zebrafish mediates anti-tumour potentiation of macrophages

The activation of TLR signalling is well documented to induced a proinflammatory phenotype in macrophages (Beutler, 2009, Cario, 2010, Cook et al., 2004, Hanamsagar et al., 2012, Kawai and Akira, 2010). In this context, solidly supported Gold and Palladium nanoparticles used in this study may represent a novel transition metal based immunotherapeutic that initiates anti-tumour polarisation of TAM. Our findings indicated that the implantation of Gold and Palladium beads into the zebrafish brain led to the pro-inflammatory polarisation of macrophages and the upregulation of key downstream mediators of TLR signalling (tnf-α and cxcl8b.1). In addition, we demonstrated that the inhibition of IRAK4, the downstream activator of TLR signalling, attenuated Gold bead mediated anti-tumour responses *in vivo.* Therefore, TLR signalling played a key role in mediating the anti-tumour responses of macrophages in zebrafish brain. The potential of TLR signalling in mediating anti-tumour polarisation of macrophages has been explored in several studies. In particular, TLR2, TLR7 and TLR8 have shown promise as immunotherapeutic targets in cancer (Singh et al., 2014, Feng et al., 2019, Rodell et al., 2018a). By exploiting the ability of TLR to recognize PAMP structures, one study used specific biomimetic TLR2 agonists (acGM-1.8) to drive polarisation of primary bone marrow-derived macrophages (Feng et al., 2019). Feng et al., demonstrated that TLR2 activation led to the upregulation of anti-tumoural cytokines (tnf-α, il-12 p70 and IFN-γ) and the downregulation of protumoural cytokines (il-10, VEGF-A and tgf-β1) (Feng et al., 2019). Consequently, TLR2 activation mediated polarisation of TAMs and suppressed the growth of tumours in mice in vivo (Feng et al., 2019). Furthermore, TLR7/8 agonist (R848) have been shown to elicit TAM polarisation and demonstrated therapeutic efficacy (Rodell et al., 2018a). Drug loaded nanoparticle delivery of TLR7/8 agonist in TAMs led to a reduction in tumour growth rates and improved survival in *in vivo* mice tumour models (Rodell et al., 2018a). In addition to TLR2, TLR7 and TLR8, TLR4 have also been demonstrated to potentiate macrophage anti-tumour activity *in vitro* and *in vivo* (Lin et al., 2011, Lee et al., 2008). These studies

highlight the diversity of TLR activation pathways that can occur in order to mediate anti-tumour potentiation of TAMs. In that respect, Gold nanoparticles have been shown to activate TLR3 (Rachmawati et al., 2015) and TLR4 (Bastus et al., 2009a) and suggested to activate TLR2 (Ng et al., 2018) while Palladium nanoparticles have been identified to activate TLR4 (Schmidt and Goebeler, 2015, Rachmawati et al., 2013).

The diversification of TAM targeted therapies over the years have grown to include immunotherapies that targets pathways that initiates macrophage polarisation. Tumour associated target therapies have primarily sought to deplete TAM populations, with examples including the delivery of small molecules or antibodies that target macrophage infiltration (CCR2) or survival (CSF-1R) (Yao et al., 2017, Pyonteck et al., 2013, Cannarile et al., 2017). However, harnessing the power of innate immune cells may represent the more effective way to treat cancers (Mantovani and Allavena, 2015, Ruffell and Coussens, 2015, Rodell et al., 2018a, Singh et al., 2014). Our findings highlighted the pivotal role of macrophages in meditating anti-tumour efficacy following macrophage polarisation and thus could be more efficacious when combined with chemotherapeutics that specifically targets tumours. Here we present a potential novel complementary system that combines the potential of Gold/Palladium nanoparticles to polarise macrophage function and to mediate biorthogonal catalytic drug delivery. It offers the possibility to not only eliminate macrophage tumour promoting functions but at the same time capitalise on the potential to mediate local chemotherapeutic drug delivery to maximise therapeutic efficiency.

4.1.9. Nanoparticle composition affects macrophage responses in zebrafish

Intriguingly, we observed distinct differences between the effects of Palladium, Gold and Naked bead implantation on macrophage polarisation in the zebrafish brain. In line with many studies, our assay clearly showed nanoparticle composition to be an important factor that regulated macrophage responses (Reichel et al., 2019, Zanganeh et al., 2016, Kharazian et al., 2016, Ge et al., 2015, Niikura et al., 2013). The implantation of Palladium and Gold beads recruited significantly higher number of macrophages in the brain of the zebrafish when compared to Naked bead implanted zebrafish. Our results showed that Naked bead implantation initiated an injury related macrophage response that returned to basal levels. Thus macrophage recruitment was dependent on the bioavailability of solidly supported Palladium and Gold nanoparticles on the bead surface in the zebrafish brain. The consequences of macrophage polarisation towards the pro-inflammatory phenotype by Palladium and Gold beads initiated a potent anti-tumour effect leading to U87 cellular clearance and fragmentation. In contrast, Naked bead implantation led to the attenuation of U87 cellular proliferation. We speculate that U87 cells may have entered a quiescent state in response to environmental stressors initiated by the bead implantation procedure. By definition, quiescent cells exist in a temporary and reversible state of non-proliferation characterised by the maintenance of G_0 stage of the cell cycle (Cheung and Rando, 2013, Cho et al., 2019). The disruption of tissue integrity in the extracellular matrix has been shown to result in the release of stored growth factors and damage associated molecular patterns capable of regulating the quiescent state of cells (Cho et al., 2019, Mura et al., 2006). Therefore, the Naked bead implantation procedure may contribute to environmental stresses which may drive entry of U87 cells into the quiescent state. In line with this, future experiment should consider the extension of experimental duration of U87 xenografted Naked bead implanted zebrafish to investigate if U87 cells maintain a quiescent state or may be stimulated to exit quiescence.

Further evidence demonstrating the differences between macrophage responses of Palladium, Gold and Naked bead implantation were presented in qPCR analysis. In addition to tnf-α and cxcl8b.1, we detected evidence to suggest increased inflammatory load in Palladium bead implanted zebrafish. The increase in *il-1β* expression in the macrophages of Palladium bead implanted zebrafish may have contributed to Palladium toxicity leading to poor zebrafish survival. *il-1β* is a potent pro-inflammatory cytokine and the transcription, synthesis and secretion of *il-1β* is tightly regulated (Garlanda et al., 2013). Increased *il-1β* expression has been associated with inflammatory diseases, including neuropathic pain and type 2 diabetes, and has been shown to inhibit spinal cord regeneration (Tsarouchas et al., 2018, Anders, 2016, Shao et al., 2015, Donath and Shoelson, 2011). One of the adverse effect of an excessive inflammatory response is the recruitment of plasma proteins and leukocytes into the extravascular tissues (Medzhitov, 2008). The increase in local protein level alters oncotic pressure and thus promotes oedema in the brain leading to local hypoxia and cellular death (Medzhitov, 2008). The combination of increased *il-1β* expression, ROS generation, tnf-α and cxcl8b.1 expression can have a detrimental impact on overall survival of Palladium bead implanted zebrafish.

Our findings demonstrated that Gold, Palladium and Naked bead initiated distinct inflammatory responses that were detected through *in vivo* living imaging and qPCR. This study highlighted the potential of the zebrafish model system as a platform to investigate the short term and potential long term immune consequences of nanoparticle exposure. The zebrafish system offers researchers a standardised, reliable and rapid platform to test associated immune responses as a result of nanoparticle exposure.

4.1.10. Cxcl8b.1 may not mediate anti-tumour efficacy in macrophages

The establishment of TLR signalling in Gold bead implanted zebrafish led us to investigate the functions of tnf-a and cxcl8b.1 in mediating macrophage and neutrophil contribution to the anti-tumour phenotype. Neutrophils are one of the first responders of the immune system and migrate into tissue in response to injury or infection (Kim and Luster, 2015). Consequently, the implantation of Gold and Naked beads into the brain of the zebrafish were observed to recruit neutrophils. Furthermore, the upregulation of cxcl8b.1 is known to be a potent chemoattract for neutrophils, and macrophages are widely accepted to regulate site specific recruitment of neutrophil to facilitate the inflammatory response (Manfroi et al., 2017). We demonstrated that Gold bead implantation led to significantly increased neutrophil recruitment at 1 dpt which coincided with increased macrophage number and an increase in cxcl8b.1 and tnf-alpha expression in macrophages. However, our study was lacking in the assessment of inflammatory cytokine expression at 3 dpt. It would have been interesting to assess if cxcl8b.1 and tnf-a expression in macrophages was maintained or downregulated at 3 dpt and should be addressed in future studies. Based on neutrophil dynamics observed in Gold bead implantation, we speculate that cxcl8b.1 expression in macrophages may be downregulated by 3 dpt as we observed the recovery of neutrophil counts to basal levels by 3 dpt. Nonetheless, our findings demonstrated that the partial mutation of cxcl8b.1 gene did not result in attenuated neutrophil number or anti-tumour response. One of the main reason for the lack of phenotype may have originated from the partial mutation of cxcl8b.1 gene. Although it is unknown if the partial mutation of cxcl8b.1 gene led to impairment of protein function in this study, previous studies have established by western blots that the mutation of gene transcripts using CRISPR Cas9 systems have led to the knockout of protein function (Zabinyakov et al., 2017, Tsarouchas et al., 2018, Wu et al., 2017, Jafari et al., 2017). We speculate that the partial mutation of cxcl8b.1 in this study may not have met the lower expression threshold necessary to attenuate neutrophil responses in the zebrafish brain and may explain the absence of phenotype in this knockout study. Furthermore, we were unable

to confirm cxcl8b.1 overexpression in macrophages in mpeg1 promoter driven transgenesis assays. This was likely attributed to the dilution of RNA content from non-macrophage cells during whole embryo homogenisation Therefore, the function of cxcl8b.1 in mediating anti-tumour efficacy remains inconclusive in this study.

4.1.11. tnf-a does not mediate anti-tumour effects in macrophages

Tnf-a is a key inflammatory cytokine produced by circulating monocytes and tissue resident macrophages in response to infection and inflammation (Locksley et al., 2001). During acute inflammation, tnf-a expression regulates expression of inflammatory genes, apoptosis and the recruitment of immune cells (Locksley et al., 2001, Crisafulli et al., 2009, Szlosarek et al., 2006). In agreement, our findings demonstrated that tnf-a upregulation coincided with a significant increase in macrophage response and the emergence of an anti-tumour phenotype as a result of Palladium and Gold bead implantation. The antitumor actions of tnf-a have been extensively studied with the development of TNFerade, a tnf-a based genetic medicine (Rasmussen et al., 2002, McLoughlin et al., 2005, Kali, 2015, Liu et al., 2004). TNFerade is administered as an intratumoural injection in combination with radiotherapy or chemotherapy and where radiation is used to induce translation of tnf-a (Kali, 2015, Senzer et al., 2004). TNFerade treatment induces a dose dependent potency leading to necrosis tumour models (Rasmussen et al., 2002). In addition, the local administration of tnf-a promotes the destruction of tumour vasculature leading to tumour necrosis (Daniel and Wilson, 2008). The effects of tnf-a are mediated by multiple mechanisms that affect tumour cells directly and indirectly. The binding of tnf-a to its receptor has been identified to activate cellular apoptosis, stimulate T-effector cell activation and promote the polarisation of tumour associated macrophages towards an anti-tumour phenotype (Nie et al., 2013, Lejeune et al., 2006, Qiao et al., 2011, Josephs et al., 2018). Furthermore, tnf-a has been identified to promote neutrophil infiltration (Lejeune et al., 2006, Qiao et al., 2011, Zhang et al., 2018). In agreement, the sig-

nificant upregulation of tnf-a expression and increased neutrophil number in Gold bead implanted zebrafish supported the role of tnf-a in neutrophil recruitment. However, our results indicated that the modulation of tnf-a function had no effect on either Gold bead induced anti-tumour efficacy or on macrophage/neutrophil dynamics. We demonstrated that CRISPR/Cas9 knockout of tnf-a function in Gold bead implanted zebrafish did not promote U87 cell survival or impair Gold bead mediated macrophage recruitment. Furthermore, the overexpression of tnf-a activity in macrophages in bead null zebrafish failed to recapitulate anti-tumour effects of Gold bead implantation. Our findings indicated that tnf-a expression was not vital for anti-tumour efficacy of macrophages in the zebrafish. However, it was important to take into account that CRISPR/Cas9 gRNA injections induced a robust reduction in tnf-a levels but not a complete knockdown (Tsarouchas et al., 2018). Therefore, the transient CRISPR/Cas9 knockdown of tnf-a did not fully recapitulate the genetic background of a stable tnf-a mutant zebrafish. In addition, overexpression transgenesis of tnf-a may not have reached the required threshold to elicit a detectable phenotype. Thus our study did not conclusively exclude the role of tnf-a expression in mediating anti-tumour polarisation in macrophages.

Although tnf-a remain an attractive immunotherapeutic target in cancer, several clinical trials have been conducted and failed to prove therapeutic efficacy (Kimura et al., 1987, Blick et al., 1987). Current clinical trials indicated that tnf-a based treatments may have therapeutic potential as an adjuvant in combination with standard chemotherapy (Ouyang et al., 2018, Li et al., 2012). However, the prolonged exposure of tnf-a may have significant consequences in promoting tumour progression as prolonged tnf-a mediated inflammatory response was well recognised to promote tumour progression (Cruceriu et al., 2020, Mantovani et al., 2008). Therefore, tnf-a may also be considered a pro-tumorigenic molecule (Stathopoulos et al., 2007, Mantovani et al., 2008). Further to the role of tnf-a, it was also identified to play a major role in priming regeneration which adds to the diverse repertoire of functions (Cruceriu et al., 2020, Nguyen-Chi et al., 2018, Tsarouchas et al., 2018). Conse-

quently, the contextual expression of tnf-α both spatially and temporally in the cellular environment guides tnf-α influence and subsequent function in the tumour microenvironment. Therefore further experimentation is required to elucidate tnf-α function in the tumour microenvironment using genetic tools with greater spatial-temporal fidelity.

4.1.12. Final Conclusions

The development of a chemotherapeutic bioorthogonal catalytic drug assay untaken in this study uncovered a novel immunotherapeutic application of Gold and Palladium nanoparticles in cancer treatment. Our findings demonstrated the potent efficacy of Gold and Palladium nanoparticles to induce anti-tumour polarisation of macrophages and emphasised the implications of TLR signalling in immunotherapy. Despite identifying key downstream TLR signalling genes to be upregulated in Gold bead implanted zebrafish, our results concluded that tnf-α was not vital for the induction of macrophage anti-tumour efficacy. It was important to note that RNA sequencing data revealed 1014 differentially expressed genes in Palladium bead implanted zebrafish therefore highlighting a complex web of intracellular signals that initiated the anti-tumour phenotype. Thus tnf-α signalling may only contribute to a small subset of intracellular signalling that conferred anti-tumour efficacy. Furthermore, our findings highlighted the importance for researchers to consider the potential of nanoparticle induced polarisation of macrophages in concert with chemotherapeutics to maximise therapeutic efficacy.

5. List of Abberviations

Abbreviation	Full Name
BOOM	Bioorthogonal Organometallic
CCL2	CC Chemokine Ligand 2
CLRs	C-Type Lectin Receptors
CNS	Central Nervous System
CSF	Colony Stimulating Factor
CT	X-Ray Computed Tomography
DAMP	Damage Associate Molecular Patterns
EGF	Epidermal Growth Factor
GBM	Glioblastoma
GO	Gene Ontology
IFN	Interferon
il	Interleukin
IL	Interleukin
Irf8	Interferon Regulatory Factor 8
MMP	Matrix Metalloproteinase
MPO	Myeloperoxidase
MRI	Magnetic Resonance Imaging
NETs	Neutrophil Extracellular Traps
NK	Natural Killer
NOD	Nucleotide-Binding Oligomerization Domain
OPC	Oligodendrocyte Progenitor Cells
PEG	Poly(Ethyleneglycol)
PET	Positron Emission Tomography
sCSF-1	Soluble Colony-Stimulating Factor
TAMs	Tumour Associated Macrophages
TH1	T Helper 1
TLRs	Toll Like Receptors
TMZ	Temozolomide
TNF	Tumour-Necrosis Factor
VEGF	Vascular Endothelial Growth Factor
WHO	World Health Organisation

6. Supplementary Data

6.1. Biorthogonal catalytic release of Vorinostat by Palladium beads inhibits U87-mCherry cell growth *in vitro*.

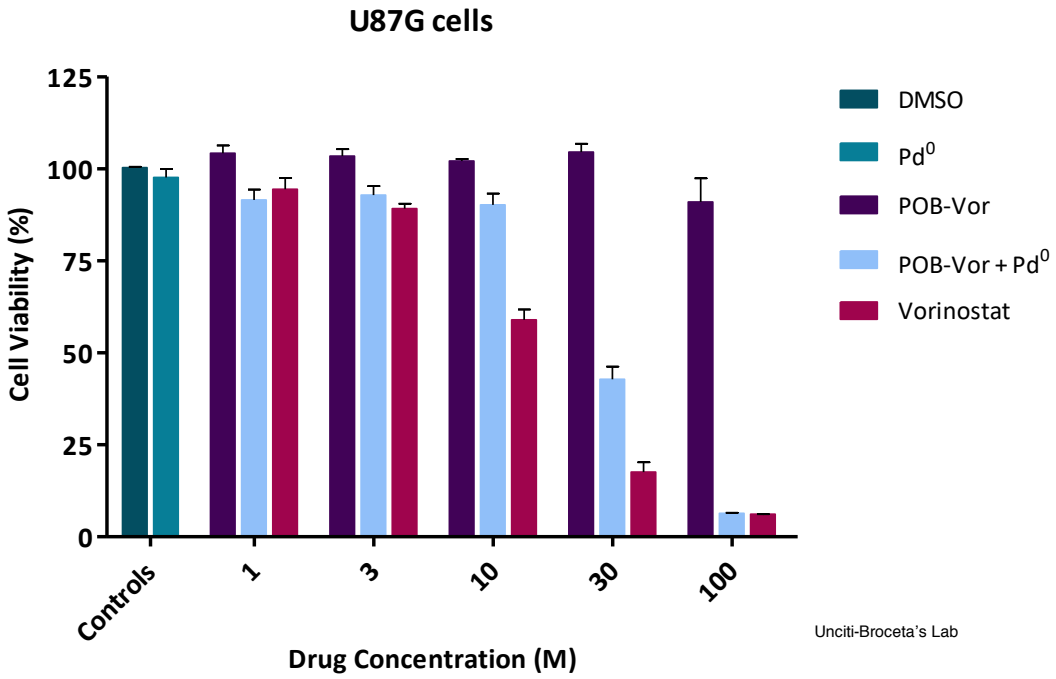

Figure S1. Biorthogonal catalytic release of Vorinostat by Palladium beads inhibits U87-mCherry cell growth *in vitro* in a dose dependent manner.

The incubation of U87-mCherry cells with 1% DMSO and Palladium beads had no effect on U87-mCherry survivial. Caged Vorinostat (POB-Vor) in 1% DMSO had no effect on U87-mCherry cell survival at all concentrations. The incubation of POB-Vor with 1 mg/ml Palladium beads with promoted the biorthogonal catalytic release of Vorinostat leading to a dose dependent inhibiton of U87-mCherry cell viability. As expected, the incubation of Vorinostat alone inhibited U87 cell viability in a dose dependent manner.

Unpublished data was kindly provided by the Unciti-Broceta's Lab (Edinburgh Cancer Center, Edinburgh, UK) with permissions.

Bibliography

ADAM, C., PEREZ-LOPEZ, A. M., HAMILTON, L., RUBIO-RUIZ, B., BRAY, T. L., SIEGER, D., BRENNAN, P. M. & UNCITI-BROCETA, A. 2018. Bioorthogonal Uncaging of the Active Metabolite of Irinotecan by Palladium-Functionalized Microdevices. *Chemistry,* 24**,** 16783-16790.

AHN, S., SINGH, P., CASTRO-ACEITUNO, V., YESMIN SIMU, S., KIM, Y. J., MATHIYALAGAN, R. & YANG, D. C. 2017. Gold nanoparticles synthesized using Panax ginseng leaves suppress inflammatory - mediators production via blockade of NF-kappaB activation in macrophages. *Artif Cells Nanomed Biotechnol,* 45**,** 270-276.

ALARIFI, S., ALI, D., ALKAHTANI, S. & ALMEER, R. S. 2017. ROS-Mediated Apoptosis and Genotoxicity Induced by Palladium Nanoparticles in Human Skin Malignant Melanoma Cells. *Oxid Med Cell Longev,* 2017**,** 8439098.

ALCANTARA LLAGUNO, S., CHEN, J., KWON, C. H., JACKSON, E. L., LI, Y., BURNS, D. K., ALVAREZ-BUYLLA, A. & PARADA, L. F. 2009. Malignant astrocytomas originate from neural stem/progenitor cells in a somatic tumor suppressor mouse model. *Cancer Cell,* 15**,** 45-56.

ALCANTARA LLAGUNO, S. R. & PARADA, L. F. 2016. Cell of origin of glioma: biological and clinical implications. *Br J Cancer,* 115**,** 1445-1450.

ANDERS, H. J. 2016. Of Inflammasomes and Alarmins: IL-1beta and IL-1alpha in Kidney Disease. *J Am Soc Nephrol,* 27**,** 2564-75.

ANDERSON, K. L., SMITH, K. A., CONNERS, K., MCKERCHER, S. R., MAKI, R. A. & TORBETT, B. E. 1998. Myeloid development is selectively disrupted in PU.1 null mice. *Blood,* 91**,** 3702-10.

BACHOO, R. M., MAHER, E. A., LIGON, K. L., SHARPLESS, N. E., CHAN, S. S., YOU, M. J., TANG, Y., DEFRANCES, J., STOVER, E., WEISSLEDER, R., ROWITCH, D. H., LOUIS, D. N. & DEPINHO, R. A. 2002. Epidermal growth factor receptor and Ink4a/Arf: convergent mechanisms governing terminal differentiation and transformation along the neural stem cell to astrocyte axis. *Cancer Cell,* 1**,** 269-77.

BACK, M., RODRIGUEZ, M., JAYAMANNE, D., KHASRAW, M., LEE, A. & WHEELER, H. 2018. Understanding the Revised Fourth Edition of the World Health Organization Classification of Tumours of the Central Nervous System (2016) for Clinical Decision-making: A Guide for Oncologists Managing Patients with Glioma. *Clin Oncol (R Coll Radiol),* 30**,** 556-562.

BADIE, B. & SCHARTNER, J. M. 2000. Flow cytometric characterization of tumor-associated macrophages in experimental gliomas. *Neurosurgery,* 46**,** 957-61; discussion 961-2.

BALKWILL, F. R., CAPASSO, M. & HAGEMANN, T. 2012. The tumor microenvironment at a glance. *J Cell Sci,* 125**,** 5591-6.

BALLIM, R. D., NAGAO, Y. & KELSH, R. N. 2019. Live Imaging of Neural Crest and Pigment Cells and Transient Transgenic Manipulation of Gene Activity. *Methods Mol Biol,* 1976**,** 195-206.

BANERJEE, S., HALDER, K., GHOSH, S., BOSE, A. & MAJUMDAR, S. 2015. The combination of a novel immunomodulator with a regulatory T cell suppressing antibody (DTA-1) regress advanced stage B16F10 solid tumor by repolarizing tumor associated macrophages in situ. *Oncoimmunology,* 4**,** e995559.

BARTON, G. M. & KAGAN, J. C. 2009. A cell biological view of Toll-like receptor function: regulation through compartmentalization. *Nat Rev Immunol,* 9**,** 535-42.

BASTUS, N. G., SANCHEZ-TILLO, E., PUJALS, S., FARRERA, C., KOGAN, M. J., GIRALT, E., CELADA, A., LLOBERAS, J. & PUNTES, V. 2009a. Peptides conjugated to gold nanoparticles induce macrophage activation. *Mol Immunol,* 46**,** 743-8.

BASTUS, N. G., SANCHEZ-TILLO, E., PUJALS, S., FARRERA, C., LOPEZ, C., GIRALT, E., CELADA, A., LLOBERAS, J. & PUNTES, V. 2009b. Homogeneous conjugation of peptides onto gold nanoparticles enhances macrophage response. *ACS Nano,* 3**,** 1335-44.

BECKWITH, L. G., MOORE, J. L., TSAO-WU, G. S., HARSHBARGER, J. C. & CHENG, K. C. 2000. Ethylnitrosourea induces neoplasia in zebrafish (Danio rerio). *Lab Invest,* 80**,** 379-85.

BERGER-ACHITUV, S., BRINKMANN, V., ABED, U. A., KUHN, L. I., BEN-EZRA, J., ELHASID, R. & ZYCHLINSKY, A. 2013. A proposed role for neutrophil extracellular traps in cancer immunoediting. *Front Immunol,* 4**,** 48.

BERGHMANS, S., JETTE, C., LANGENAU, D., HSU, K., STEWART, R., LOOK, T. & KANKI, J. P. 2005. Making waves in cancer research: new models in the zebrafish. *Biotechniques,* 39**,** 227-37.

BERTRAND, J. Y., KIM, A. D., VIOLETTE, E. P., STACHURA, D. L., CISSON, J. L. & TRAVER, D. 2007. Definitive hematopoiesis initiates through a committed erythromyeloid progenitor in the zebrafish embryo. *Development,* 134**,** 4147-56.

BEUTLER, B. A. 2009. TLRs and innate immunity. *Blood,* 113**,** 1399-407.

BHATTACHARJEE, A., YANG, H., DUFFY, M., ROBINSON, E., CONRAD-ANTOVILLE, A., LU, Y. W., CAPPS, T., BRAITERMAN, L., WOLFGANG, M., MURPHY, M. P., YI, L., KALER, S. G., LUTSENKO, S. & RALLE, M. 2016. The Activity of Menkes Disease Protein ATP7A Is Essential for Redox Balance in Mitochondria. *J Biol Chem,* 291**,** 16644-58.

BINGLE, L., BROWN, N. J. & LEWIS, C. E. 2002. The role of tumour-associated macrophages in tumour progression: implications for new anticancer therapies. *J Pathol,* 196**,** 254-65.

BINNEMARS-POSTMA, K., STORM, G. & PRAKASH, J. 2017. Nanomedicine Strategies to Target Tumor-Associated Macrophages. *Int J Mol Sci,* 18.

BISWAS, S. K., ALLAVENA, P. & MANTOVANI, A. 2013. Tumor-associated macrophages: functional diversity, clinical significance, and open questions. *Semin Immunopathol,* 35**,** 585-600.

BLICK, M., SHERWIN, S. A., ROSENBLUM, M. & GUTTERMAN, J. 1987. Phase I study of recombinant tumor necrosis factor in cancer patients. *Cancer Res,* 47**,** 2986-9.

BOGDAN, C., ROLLINGHOFF, M. & DIEFENBACH, A. 2000. Reactive oxygen and reactive nitrogen intermediates in innate and specific immunity. *Curr Opin Immunol,* 12**,** 64-76.

BORGA, C., PARK, G., FOSTER, C., BURROUGHS-GARCIA, J., MARCHESIN, M., SHAH, R., HASAN, A., AHMED, S. T., BRESOLIN, S., BATCHELOR, L., SCORDINO, T., MILES, R. R., TE KRONNIE, G., REGENS, J. L. & FRAZER, J. K. 2019.

Simultaneous B and T cell acute lymphoblastic leukemias in zebrafish driven by transgenic MYC: implications for oncogenesis and lymphopoiesis. *Leukemia,* 33**,** 333-347.

BOSCOLO, P., BELLANTE, V., LEOPOLD, K., MAIER, M., DI GIAMPAOLO, L., ANTONUCCI, A., IAVICOLI, I., TOBIA, L., PAOLETTI, A., MONTALTI, M., PETRARCA, C., QIAO, N., SABBIONI, E. & DI GIOACCHINO, M. 2010. Effects of palladium nanoparticles on the cytokine release from peripheral blood mononuclear cells of non-atopic women. *J Biol Regul Homeost Agents,* 24**,** 207-14.

BOWMAN, R. L., KLEMM, F., AKKARI, L., PYONTECK, S. M., SEVENICH, L., QUAIL, D. F., DHARA, S., SIMPSON, K., GARDNER, E. E., IACOBUZIO-DONAHUE, C. A., BRENNAN, C. W., TABAR, V., GUTIN, P. H. & JOYCE, J. A. 2016. Macrophage Ontogeny Underlies Differences in Tumor-Specific Education in Brain Malignancies. *Cell Rep,* 17**,** 2445-2459.

BRAJER-LUFTMANN, B., NOWICKA, A., KACZMAREK, M., WYRZYKIEWICZ, M., YASAR, S., PIORUNEK, T., SIKORA, J. & BATURA-GABRYEL, H. 2019. Damage-Associated Molecular Patterns and Myeloid-Derived Suppressor Cells in Bronchoalveolar Lavage Fluid in Chronic Obstructive Pulmonary Disease Patients. *J Immunol Res,* 2019**,** 9708769.

BRINKMANN, V. & ZYCHLINSKY, A. 2012. Neutrophil extracellular traps: is immunity the second function of chromatin? *J Cell Biol,* 198**,** 773-83.

BROCHHAUSEN, C., SCHMITT, V. H., MAMILOS, A., SCHMITT, C., PLANCK, C. N., RAJAB, T. K., HIERLEMANN, H. & KIRKPATRICK, C. J. 2017. Expression of CD68 positive macrophages in the use of different barrier materials to prevent peritoneal adhesions-an animal study. *J Mater Sci Mater Med,* 28**,** 15.

BROEKE, T., WUBBOLTS, R. & STOORVOGEL, W. 2013. MHC class II antigen presentation by dendritic cells regulated through endosomal sorting. *Cold Spring Harb Perspect Biol,* 5**,** a016873.

BRUNE, B., DEHNE, N., GROSSMANN, N., JUNG, M., NAMGALADZE, D., SCHMID, T., VON KNETHEN, A. & WEIGERT, A. 2013. Redox control of inflammation in macrophages. *Antioxid Redox Signal,* 19**,** 595-637.

BUTOVSKY, O., JEDRYCHOWSKI, M. P., MOORE, C. S., CIALIC, R., LANSER, A. J., GABRIELY, G., KOEGLSPERGER, T., DAKE, B., WU, P. M., DOYKAN, C. E., FANEK, Z., LIU, L., CHEN, Z., ROTHSTEIN, J. D., RANSOHOFF, R. M., GYGI, S. P., ANTEL, J. P. & WEINER, H. L. 2014. Identification of a unique TGF-beta-dependent molecular and functional signature in microglia. *Nat Neurosci,* 17**,** 131-43.

CANLI, O., NICOLAS, A. M., GUPTA, J., FINKELMEIER, F., GONCHAROVA, O., PESIC, M., NEUMANN, T., HORST, D., LOWER, M., SAHIN, U. & GRETEN, F. R. 2017. Myeloid Cell-Derived Reactive Oxygen Species Induce Epithelial Mutagenesis. *Cancer Cell,* 32**,** 869-883 e5.

CANNARILE, M. A., WEISSER, M., JACOB, W., JEGG, A. M., RIES, C. H. & RUTTINGER, D. 2017. Colony-stimulating factor 1 receptor (CSF1R) inhibitors in cancer therapy. *J Immunother Cancer,* 5**,** 53.

CARIO, E. 2010. Toll-like receptors in inflammatory bowel diseases: a decade later. *Inflamm Bowel Dis,* 16**,** 1583-97.

CASANO, A. M. & PERI, F. 2015. Microglia: multitasking specialists of the brain. *Dev Cell,* 32**,** 469-77.

CEDERVALL, T., LYNCH, I., LINDMAN, S., BERGGARD, T., THULIN, E., NILSSON, H., DAWSON, K. A. & LINSE, S. 2007. Understanding the nanoparticle-protein corona using methods to quantify exchange rates and affinities of proteins for nanoparticles. *Proc Natl Acad Sci U S A,* 104**,** 2050-5.

CHEN, L., ZHOU, Q., XU, B., LIU, J., SHI, L., ZHU, D., WU, C. & JIANG, J. 2014. MT2-MMP expression associates with tumor progression and angiogenesis in human lung cancer. *Int J Clin Exp Pathol,* 7**,** 3469-77.

CHEN, X. & GAO, C. 2017. Influences of size and surface coating of gold nanoparticles on inflammatory activation of macrophages. *Colloids Surf B Biointerfaces,* 160**,** 372-380.

CHEN, Z., FENG, X., HERTING, C. J., GARCIA, V. A., NIE, K., PONG, W. W., RASMUSSEN, R., DWIVEDI, B., SEBY, S., WOLF, S. A., GUTMANN, D. H. & HAMBARDZUMYAN, D. 2017. Cellular and Molecular Identity of Tumor-Associated Macrophages in Glioblastoma. *Cancer Res,* 77**,** 2266-2278.

CHEUNG, T. H. & RANDO, T. A. 2013. Molecular regulation of stem cell quiescence. *Nat Rev Mol Cell Biol,* 14**,** 329-40.

CHIA, K., MAZZOLINI, J., MIONE, M. & SIEGER, D. 2018. Tumor initiating cells induce Cxcr4-mediated infiltration of pro-tumoral macrophages into the brain. *Elife,* 7.

CHO, I. J., LUI, P. P., OBAJDIN, J., RICCIO, F., STROUKOV, W., WILLIS, T. L., SPAGNOLI, F. & WATT, F. M. 2019. Mechanisms, Hallmarks, and Implications of Stem Cell Quiescence. *Stem Cell Reports,* 12**,** 1190-1200.

CHOVATIYA, R. & MEDZHITOV, R. 2014. Stress, inflammation, and defense of homeostasis. *Mol Cell,* 54**,** 281-8.

CIEBIERA, M., WLODARCZYK, M., ZGLICZYNSKA, M., LUKASZUK, K., MECZEKALSKI, B., KOBIERZYCKI, C., LOZINSKI, T. & JAKIEL, G. 2018. The Role of Tumor Necrosis Factor alpha in the Biology of Uterine Fibroids and the Related Symptoms. *Int J Mol Sci,* 19.

CLAVADETSCHER, J., HOFFMANN, S., LILIENKAMPF, A., MACKAY, L., YUSOP, R. M., RIDER, S. A., MULLINS, J. J. & BRADLEY, M. 2016. Copper Catalysis in Living Systems and In Situ Drug Synthesis. *Angew Chem Int Ed Engl,* 55**,** 15662-15666.

CONIGLIO, S. J., EUGENIN, E., DOBRENIS, K., STANLEY, E. R., WEST, B. L., SYMONS, M. H. & SEGALL, J. E. 2012. Microglial stimulation of glioblastoma invasion involves epidermal growth factor receptor (EGFR) and colony stimulating factor 1 receptor (CSF-1R) signaling. *Mol Med,* 18**,** 519-27.

CONTI, I. & ROLLINS, B. J. 2004. CCL2 (monocyte chemoattractant protein-1) and cancer. *Semin Cancer Biol,* 14**,** 149-54.

COOK, D. N., PISETSKY, D. S. & SCHWARTZ, D. A. 2004. Toll-like receptors in the pathogenesis of human disease. *Nat Immunol,* 5**,** 975-9.

CORMA, A. & GARCIA, H. 2008. Supported gold nanoparticles as catalysts for organic reactions. *Chem Soc Rev,* 37**,** 2096-126.

CRISAFULLI, C., GALUPPO, M. & CUZZOCREA, S. 2009. Effects of genetic and pharmacological inhibition of TNF-alpha in the regulation of inflammation in macrophages. *Pharmacol Res,* 60**,** 332-40.

CROCETTI, E., TRAMA, A., STILLER, C., CALDARELLA, A., SOFFIETTI, R., JAAL, J., WEBER, D. C., RICARDI, U., SLOWINSKI, J., BRANDES, A. & GROUP, R. W. 2012. Epidemiology of glial and non-glial brain tumours in Europe. *Eur J Cancer,* 48**,** 1532-42.

CRUCERIU, D., BALDASICI, O., BALACESCU, O. & BERINDAN-NEAGOE, I. 2020. The dual role of tumor necrosis factor-alpha (TNF-alpha) in breast cancer: molecular insights and therapeutic approaches. *Cell Oncol (Dordr)*.

D MEEKER, N., HUTCHINSON, S., HO, L. & TREDE, N. 2007. *Method for isolation of PCR-ready genomic DNA from zebrafish tisues*.

DAHAL, E., CURTISS, J., SUBEDI, D., CHEN, G., HOUSTON, J. P. & SMIRNOV, S. 2015. Evaluation of the catalytic activity and cytotoxicity of palladium nanocubes: the role of oxygen. *ACS Appl Mater Interfaces,* 7**,** 9364-71.

DANIEL, D. & WILSON, N. S. 2008. Tumor necrosis factor: renaissance as a cancer therapeutic? *Curr Cancer Drug Targets,* 8**,** 124-31.

DAVIDSON, A. J. & ZON, L. I. 2004. The 'definitive' (and 'primitive') guide to zebrafish hematopoiesis. *Oncogene,* 23**,** 7233-46.

DEANGELIS, M. M., WANG, D. G. & HAWKINS, T. L. 1995. Solid-phase reversible immobilization for the isolation of PCR products. *Nucleic Acids Res,* 23**,** 4742-3.

DEN HERTOG, J. 2016. Tumor Suppressors in Zebrafish: From TP53 to PTEN and Beyond. *Adv Exp Med Biol,* 916**,** 87-101.

DOBIN, A., DAVIS, C. A., SCHLESINGER, F., DRENKOW, J., ZALESKI, C., JHA, S., BATUT, P., CHAISSON, M. & GINGERAS, T. R. 2013. STAR: ultrafast universal RNA-seq aligner. *Bioinformatics,* 29**,** 15-21.

DONATH, M. Y. & SHOELSON, S. E. 2011. Type 2 diabetes as an inflammatory disease. *Nat Rev Immunol,* 11**,** 98-107.

EDEN, C. J., JU, B., MURUGESAN, M., PHOENIX, T. N., NIMMERVOLL, B., TONG, Y., ELLISON, D. W., FINKELSTEIN, D., WRIGHT, K., BOULOS, N., DAPPER, J., THIRUVENKATAM, R., LESSMAN, C. A., TAYLOR, M. R. & GILBERTSON, R. J. 2015. Orthotopic models of pediatric brain tumors in zebrafish. *Oncogene,* 34**,** 1736-42.

ELLETT, F., PASE, L., HAYMAN, J. W., ANDRIANOPOULOS, A. & LIESCHKE, G. J. 2011. mpeg1 promoter transgenes direct macrophage-lineage expression in zebrafish. *Blood,* 117**,** e49-56.

ELMORE, M. R., NAJAFI, A. R., KOIKE, M. A., DAGHER, N. N., SPANGENBERG, E. E., RICE, R. A., KITAZAWA, M., MATUSOW, B., NGUYEN, H., WEST, B. L. & GREEN, K. N. 2014. Colony-stimulating factor 1 receptor signaling is necessary for microglia viability, unmasking a microglia progenitor cell in the adult brain. *Neuron,* 82**,** 380-97.

EMELYANOV, A. & PARINOV, S. 2008. Mifepristone-inducible LexPR system to drive and control gene expression in transgenic zebrafish. *Dev Biol,* 320**,** 113-21.

EVANS, T. G., YAMAMOTO, Y., JEFFERY, W. R. & KRONE, P. H. 2005. Zebrafish Hsp70 is required for embryonic lens formation. *Cell Stress Chaperones,* 10**,** 66-78.

FENG, Y., MU, R., WANG, Z., XING, P., ZHANG, J., DONG, L. & WANG, C. 2019. A toll-like receptor agonist mimicking microbial signal to generate tumor-suppressive macrophages. *Nat Commun,* 10**,** 2272.

FERRERO, G., MAHONY, C. B., DUPUIS, E., YVERNOGEAU, L., DI RUGGIERO, E., MISEROCCHI, M., CARON, M., ROBIN, C., TRAVER, D., BERTRAND, J. Y. & WITTAMER, V. 2018. Embryonic Microglia Derive from Primitive Macrophages and Are Replaced by cmyb-Dependent Definitive Microglia in Zebrafish. *Cell Rep,* 24**,** 130-141.

FIOR, R., POVOA, V., MENDES, R. V., CARVALHO, T., GOMES, A., FIGUEIREDO, N. & FERREIRA, M. G. 2017. Single-cell functional and chemosensitive profiling of combinatorial colorectal therapy in zebrafish xenografts. *Proc Natl Acad Sci U S A,* 114**,** E8234-E8243.

FLAVELL, R. A., SANJABI, S., WRZESINSKI, S. H. & LICONA-LIMON, P. 2010. The polarization of immune cells in the tumour environment by TGFbeta. *Nat Rev Immunol,* 10**,** 554-67.

FLEURENCE, J., BAHRI, M., FOUGERAY, S., FARAJ, S., VERMEULEN, S., PINAULT, E., GERALDO, F., OLIVER, L., VEZIERS, J., MARQUET, P., RABE, M., GRATAS, C., VALLETTE, F., PECQUEUR, C., PARIS, F. & BIRKLE, S. 2019. Impairing temozolomide resistance driven by glioma stem-like cells with adjuvant immunotherapy targeting O-acetyl GD2 ganglioside. *Int J Cancer*.

FRIDLENDER, Z. G., SUN, J., KIM, S., KAPOOR, V., CHENG, G., LING, L., WORTHEN, G. S. & ALBELDA, S. M. 2009. Polarization of tumor-associated neutrophil phenotype by TGF-beta: "N1" versus "N2" TAN. *Cancer Cell,* 16**,** 183-94.

FU, Y., FODEN, J. A., KHAYTER, C., MAEDER, M. L., REYON, D., JOUNG, J. K. & SANDER, J. D. 2013. High-frequency off-target mutagenesis induced by CRISPR-Cas nucleases in human cells. *Nat Biotechnol,* 31**,** 822-6.

GAJEWSKI, T. F., SCHREIBER, H. & FU, Y. X. 2013. Innate and adaptive immune cells in the tumor microenvironment. *Nat Immunol,* 14**,** 1014-22.

GALADARI, S., RAHMAN, A., PALLICHANKANDY, S. & THAYYULLATHIL, F. 2017. Reactive oxygen species and cancer paradox: To promote or to suppress? *Free Radic Biol Med,* 104**,** 144-164.

GALVAO, R. P., KASINA, A., MCNEILL, R. S., HARBIN, J. E., FOREMAN, O., VERHAAK, R. G., NISHIYAMA, A., MILLER, C. R. & ZONG, H. 2014. Transformation of quiescent adult oligodendrocyte precursor cells into malignant glioma through a multistep reactivation process. *Proc Natl Acad Sci U S A,* 111**,** E4214-23.

GARCIA, G. R., NOYES, P. D. & TANGUAY, R. L. 2016. Advancements in zebrafish applications for 21st century toxicology. *Pharmacol Ther,* 161**,** 11-21.

GARLANDA, C., DINARELLO, C. A. & MANTOVANI, A. 2013. The interleukin-1 family: back to the future. *Immunity,* 39**,** 1003-18.

GARLEY, M., JABLONSKA, E. & DABROWSKA, D. 2016. NETs in cancer. *Tumour Biol,* 37**,** 14355-14361.

GE, C., TIAN, J., ZHAO, Y., CHEN, C., ZHOU, R. & CHAI, Z. 2015. Towards understanding of nanoparticle-protein corona. *Arch Toxicol,* 89**,** 519-39.

GIMENEZ, N., SCHULZ, R., HIGASHI, M., AYMERICH, M., VILLAMOR, N., DELGADO, J., JUAN, M., LOPEZ-GUERRA, M., CAMPO, E., ROSICH, L., SEIFFERT, M. & COLOMER, D. 2019. Targeting IRAK4 disrupts inflammatory pathways and delays tumor development in chronic lymphocytic leukemia. *Leukemia*.

GINHOUX, F., GRETER, M., LEBOEUF, M., NANDI, S., SEE, P., GOKHAN, S., MEHLER, M. F., CONWAY, S. J., NG, L. G., STANLEY, E. R., SAMOKHVALOV, I. M. & MERAD, M. 2010. Fate mapping analysis reveals that adult microglia derive from primitive macrophages. *Science,* 330**,** 841-5.

GORDON, S. & MARTINEZ, F. O. 2010. Alternative activation of macrophages: mechanism and functions. *Immunity,* 32**,** 593-604.

GORE, A. V., PILLAY, L. M., VENERO GALANTERNIK, M. & WEINSTEIN, B. M. 2018. The zebrafish: A fintastic model for hematopoietic development and disease. *Wiley Interdiscip Rev Dev Biol,* 7**,** e312.

GRAEBER, M. B., SCHEITHAUER, B. W. & KREUTZBERG, G. W. 2002. Microglia in brain tumors. *Glia,* 40**,** 252-9.

GRAMATZKI, D., DEHLER, S., RUSHING, E. J., ZAUGG, K., HOFER, S., YONEKAWA, Y., BERTALANFFY, H., VALAVANIS, A., KOROL, D., ROHRMANN, S., PLESS, M., OBERLE, J., ROTH, P., OHGAKI, H. & WELLER, M. 2016. Glioblastoma in the Canton of Zurich, Switzerland revisited: 2005 to 2009. *Cancer,* 122**,** 2206-15.

GRETER, M. & MERAD, M. 2013. Regulation of microglia development and homeostasis. *Glia,* 61**,** 121-7.

GUSYATINER, O. & HEGI, M. E. 2018. Glioma epigenetics: From subclassification to novel treatment options. *Semin Cancer Biol,* 51**,** 50-58.

GUTIERREZ, A., GREBLIUNAITE, R., FENG, H., KOZAKEWICH, E., ZHU, S., GUO, F., PAYNE, E., MANSOUR, M., DAHLBERG, S. E., NEUBERG, D. S., DEN HERTOG, J., PROCHOWNIK, E. V., TESTA, J. R., HARRIS, M., KANKI, J. P. & LOOK, A. T. 2011. Pten mediates Myc oncogene dependence in a conditional zebrafish model of T cell acute lymphoblastic leukemia. *J Exp Med,* 208**,** 1595-603.

HAMBARDZUMYAN, D., GUTMANN, D. H. & KETTENMANN, H. 2016. The role of microglia and macrophages in glioma maintenance and progression. *Nat Neurosci,* 19**,** 20-7.

HAMILTON, L., ASTELL, K. R., VELIKOVA, G. & SIEGER, D. 2016. A Zebrafish Live Imaging Model Reveals Differential Responses of Microglia Toward Glioblastoma Cells In Vivo. *Zebrafish,* 13**,** 523-534.

HANAMSAGAR, R., HANKE, M. L. & KIELIAN, T. 2012. Toll-like receptor (TLR) and inflammasome actions in the central nervous system. *Trends Immunol,* 33**,** 333-42.

HARVIE, E. A. & HUTTENLOCHER, A. 2015. Neutrophils in host defense: new insights from zebrafish. *J Leukoc Biol,* 98**,** 523-37.

HATO, T. & DAGHER, P. C. 2015. How the Innate Immune System Senses Trouble and Causes Trouble. *Clin J Am Soc Nephrol,* 10**,** 1459-69.

HAYNES, S. E., HOLLOPETER, G., YANG, G., KURPIUS, D., DAILEY, M. E., GAN, W. B. & JULIUS, D. 2006. The P2Y12 receptor regulates microglial activation by extracellular nucleotides. *Nat Neurosci,* 9**,** 1512-9.

HEMMATI, H. D., NAKANO, I., LAZAREFF, J. A., MASTERMAN-SMITH, M., GESCHWIND, D. H., BRONNER-FRASER, M. & KORNBLUM, H. I. 2003. Cancerous stem cells can arise from pediatric brain tumors. *Proc Natl Acad Sci U S A,* 100**,** 15178-83.

HENDRICKX, D. A. E., VAN EDEN, C. G., SCHUURMAN, K. G., HAMANN, J. & HUITINGA, I. 2017. Staining of HLA-DR, Iba1 and CD68 in human microglia reveals partially overlapping expression depending on cellular morphology and pathology. *J Neuroimmunol,* 309**,** 12-22.

HERZOG, C., PONS GARCIA, L., KEATINGE, M., GREENALD, D., MORITZ, C., PERI, F. & HERRGEN, L. 2019. Rapid clearance of cellular debris by microglia limits secondary neuronal cell death after brain injury in vivo. *Development,* 146.

HO, V. K., REIJNEVELD, J. C., ENTING, R. H., BIENFAIT, H. P., ROBE, P., BAUMERT, B. G., VISSER, O. & DUTCH SOCIETY FOR, N.-O. 2014. Changing incidence and improved survival of gliomas. *Eur J Cancer,* 50**,** 2309-18.

HOOP, M., RIBEIRO, A. S., RÖSCH, D., WEINAND, P., MENDES, N., MUSHTAQ, F., CHEN, X.-Z., SHEN, Y., PUJANTE, C. F., PUIGMARTÍ-LUIS, J., PAREDES, J., NELSON, B. J., PÊGO, A. P. & PANÉ, S. 2018. Mobile Magnetic Nanocatalysts for Bioorthogonal Targeted Cancer Therapy. *Advanced Functional Materials,* 28**,** 1705920.

HOWE, K., CLARK, M. D., TORROJA, C. F., TORRANCE, J., BERTHELOT, C., MUFFATO, M., COLLINS, J. E., HUMPHRAY, S., MCLAREN, K., MATTHEWS, L., MCLAREN, S., SEALY, I., CACCAMO, M., CHURCHER, C., SCOTT, C., BARRETT, J. C., KOCH, R., RAUCH, G. J., WHITE, S., CHOW, W., KILIAN, B., QUINTAIS, L. T., GUERRA-ASSUNCAO, J. A., ZHOU, Y., GU, Y., YEN, J., VOGEL, J. H., EYRE, T., REDMOND, S., BANERJEE, R., CHI, J., FU, B., LANGLEY, E., MAGUIRE, S. F., LAIRD, G. K., LLOYD, D., KENYON, E., DONALDSON, S., SEHRA, H., ALMEIDA-KING, J., LOVELAND, J., TREVANION, S., JONES, M., QUAIL, M., WILLEY, D., HUNT, A., BURTON, J., SIMS, S., MCLAY, K., PLUMB, B., DAVIS, J., CLEE, C., OLIVER, K., CLARK, R., RIDDLE, C., ELLIOT, D., THREADGOLD, G., HARDEN, G., WARE, D., BEGUM, S., MORTIMORE, B., KERRY, G., HEATH, P., PHILLIMORE, B., TRACEY, A., CORBY, N., DUNN, M., JOHNSON, C., WOOD, J., CLARK, S., PELAN, S., GRIFFITHS, G., SMITH, M., GLITHERO, R., HOWDEN, P., BARKER, N., LLOYD, C., STEVENS, C., HARLEY, J., HOLT, K., PANAGIOTIDIS, G., LOVELL, J., BEASLEY, H., HENDERSON, C., GORDON, D., AUGER, K., WRIGHT, D., COLLINS, J., RAISEN, C., DYER, L., LEUNG, K., ROBERTSON, L., AMBRIDGE, K., LEONGAMORNLERT, D., MCGUIRE, S., GILDERTHORP, R., GRIFFITHS, C., MANTHRAVADI, D., NICHOL, S., BARKER, G., et al. 2013. The zebrafish reference genome sequence and its relationship to the human genome. *Nature,* 496**,** 498-503.

HSU, K., TRAVER, D., KUTOK, J. L., HAGEN, A., LIU, T. X., PAW, B. H., RHODES, J., BERMAN, J. N., ZON, L. I., KANKI, J. P. & LOOK, A. T. 2004. The pu.1 promoter drives myeloid gene expression in zebrafish. *Blood,* 104**,** 1291-7.

HU, J. & NG, P. C. 2012. Predicting the effects of frameshifting indels. *Genome Biol,* 13**,** R9.

HUANG, Z., GAN, J., LONG, Z., GUO, G., SHI, X., WANG, C., ZANG, Y., DING, Z., CHEN, J., ZHANG, J. & DONG, L. 2016. Targeted delivery of let-7b to reprogramme tumor-associated macrophages and tumor infiltrating dendritic cells for tumor rejection. *Biomaterials,* 90**,** 72-84.

HUSSAIN, S. F., YANG, D., SUKI, D., GRIMM, E. & HEIMBERGER, A. B. 2006. Innate immune functions of microglia isolated from human glioma patients. *J Transl Med,* 4**,** 15.

HUSSAIN, S. P., AGUILAR, F., AMSTAD, P. & CERUTTI, P. 1994. Oxy-radical induced mutagenesis of hotspot codons 248 and 249 of the human p53 gene. *Oncogene,* 9**,** 2277-81.

HUSSAIN, S. P. & HARRIS, C. C. 2007. Inflammation and cancer: an ancient link with novel potentials. *Int J Cancer,* 121**,** 2373-80.

HUTTER, E., BORIDY, S., LABRECQUE, S., LALANCETTE-HEBERT, M., KRIZ, J., WINNIK, F. M. & MAYSINGER, D. 2010. Microglial response to gold nanoparticles. *ACS Nano,* 4**,** 2595-606.

HWANG, S. D., KONDO, H., HIRONO, I. & AOKI, T. 2011. Molecular cloning and characterization of Toll-like receptor 14 in Japanese flounder, Paralichthys olivaceus. *Fish Shellfish Immunol,* 30**,** 425-9.

IWASAKI, A. & MEDZHITOV, R. 2015. Control of adaptive immunity by the innate immune system. *Nat Immunol,* 16**,** 343-53.

JACOBS, V. L., LANDRY, R. P., LIU, Y., ROMERO-SANDOVAL, E. A. & DE LEO, J. A. 2012. Propentofylline decreases tumor growth in a rodent model of glioblastoma multiforme by a direct mechanism on microglia. *Neuro Oncol,* 14**,** 119-31.

JAFARI, N., KIM, H., PARK, R., LI, L., JANG, M., MORRIS, A. J., PARK, J. & HUANG, C. 2017. CRISPR-Cas9 Mediated NOX4 Knockout Inhibits Cell Proliferation and Invasion in HeLa Cells. *PLoS One,* 12**,** e0170327.

JANEWAY, C. A., JR. & MEDZHITOV, R. 2002. Innate immune recognition. *Annu Rev Immunol,* 20**,** 197-216.

JAULT, C., PICHON, L. & CHLUBA, J. 2004. Toll-like receptor gene family and TIR-domain adapters in Danio rerio. *Mol Immunol,* 40**,** 759-71.

JIANG, M. C., NI, J. J., CUI, W. Y., WANG, B. Y. & ZHUO, W. 2019. Emerging roles of lncRNA in cancer and therapeutic opportunities. *Am J Cancer Res,* 9**,** 1354-1366.

JIANG, Y. & UHRBOM, L. 2012. On the origin of glioma. *Ups J Med Sci,* 117**,** 113-21.

JOKERST, J. V., LOBOVKINA, T., ZARE, R. N. & GAMBHIR, S. S. 2011. Nanoparticle PEGylation for imaging and therapy. *Nanomedicine (Lond),* 6**,** 715-28.

JONES, T. R., BIGNER, S. H., SCHOLD, S. C., JR., ENG, L. F. & BIGNER, D. D. 1981. Anaplastic human gliomas grown in athymic mice. Morphology and glial fibrillary acidic protein expression. *Am J Pathol,* 105**,** 316-27.

JOSEPHS, S. F., ICHIM, T. E., PRINCE, S. M., KESARI, S., MARINCOLA, F. M., ESCOBEDO, A. R. & JAFRI, A. 2018. Unleashing endogenous TNF-alpha as a cancer immunotherapeutic. *J Transl Med,* 16**,** 242.

JU, B., CHEN, W., SPITSBERGEN, J. M., LU, J., VOGEL, P., PETERS, J. L., WANG, Y. D., ORR, B. A., WU, J., HENSON, H. E., JIA, S., PARUPALLI, C. & TAYLOR, M. R. 2014. Activation of Sonic hedgehog signaling in neural progenitor cells promotes glioma development in the zebrafish optic pathway. *Oncogenesis,* 3**,** e96.

JUNG, I. H., LEEM, G. L., JUNG, D. E., KIM, M. H., KIM, E. Y., KIM, S. H., PARK, H. C. & PARK, S. W. 2013. Glioma is formed by active Akt1 alone and promoted by active Rac1 in transgenic zebrafish. *Neuro Oncol,* 15**,** 290-304.

KAISER, T. & FENG, G. 2019. Tmem119-EGFP and Tmem119-CreERT2 transgenic mice for labeling and manipulating microglia. *eNeuro*.

KALDERON, D., ROBERTS, B. L., RICHARDSON, W. D. & SMITH, A. E. 1984. A short amino acid sequence able to specify nuclear location. *Cell,* 39**,** 499-509.

KALI, A. 2015. TNFerade, an innovative cancer immunotherapeutic. *Indian J Pharmacol,* 47**,** 479-83.

KAMATA, H., HONDA, S., MAEDA, S., CHANG, L., HIRATA, H. & KARIN, M. 2005. Reactive oxygen species promote TNFalpha-induced death and sustained JNK activation by inhibiting MAP kinase phosphatases. *Cell,* 120**,** 649-61.

KAWAGOE, T., TAKEUCHI, O., TAKABATAKE, Y., KATO, H., ISAKA, Y., TSUJIMURA, T. & AKIRA, S. 2009. TANK is a negative regulator of Toll-like receptor signaling and is critical for the prevention of autoimmune nephritis. *Nat Immunol,* 10**,** 965-72.

KAWAI, T. & AKIRA, S. 2010. The role of pattern-recognition receptors in innate immunity: update on Toll-like receptors. *Nat Immunol,* 11**,** 373-84.

KAWANISHI, S., OHNISHI, S., MA, N., HIRAKU, Y. & MURATA, M. 2017. Crosstalk between DNA Damage and Inflammation in the Multiple Steps of Carcinogenesis. *Int J Mol Sci,* 18.

KHARAZIAN, B., HADIPOUR, N. L. & EJTEHADI, M. R. 2016. Understanding the nanoparticle-protein corona complexes using computational and experimental methods. *Int J Biochem Cell Biol,* 75**,** 162-74.

KIENLE, K. & LAMMERMANN, T. 2016. Neutrophil swarming: an essential process of the neutrophil tissue response. *Immunol Rev,* 273**,** 76-93.

KIERDORF, K., ERNY, D., GOLDMANN, T., SANDER, V., SCHULZ, C., PERDIGUERO, E. G., WIEGHOFER, P., HEINRICH, A., RIEMKE, P., HOLSCHER, C., MULLER, D. N., LUCKOW, B., BROCKER, T., DEBOWSKI, K., FRITZ, G., OPDENAKKER, G., DIEFENBACH, A., BIBER, K., HEIKENWALDER, M., GEISSMANN, F., ROSENBAUER, F. & PRINZ, M. 2013. Microglia emerge from erythromyeloid precursors via Pu.1- and Irf8-dependent pathways. *Nat Neurosci,* 16**,** 273-80.

KIM, I. K., KIM, K., LEE, E., OH, D. S., PARK, C. S., PARK, S., YANG, J. M., KIM, J. H., KIM, H. S., SHIMA, D. T., KIM, J. H., HONG, S. H., CHO, Y. H., KIM, Y. H., PARK, J. B., KOH, G. Y., JU, Y. S., LEE, H. K., LEE, S. & KIM, I. 2018. Sox7 promotes high-grade glioma by increasing VEGFR2-mediated vascular abnormality. *J Exp Med,* 215**,** 963-983.

KIM, N. D. & LUSTER, A. D. 2015. The role of tissue resident cells in neutrophil recruitment. *Trends Immunol,* 36**,** 547-55.

KIMURA, K., TAGUCHI, T., URUSHIZAKI, I., OHNO, R., ABE, O., FURUE, H., HATTORI, T., ICHIHASHI, H., INOGUCHI, K., MAJIMA, H. & ET AL. 1987. Phase I study of recombinant human tumor necrosis factor. *Cancer Chemother Pharmacol,* 20**,** 223-9.

KODALI, V., LITTKE, M. H., TILTON, S. C., TEEGUARDEN, J. G., SHI, L., FREVERT, C. W., WANG, W., POUNDS, J. G. & THRALL, B. D. 2013. Dysregulation of macrophage activation profiles by engineered nanoparticles. *ACS Nano,* 7**,** 6997-7010.

KOMOHARA, Y., OHNISHI, K., KURATSU, J. & TAKEYA, M. 2008. Possible involvement of the M2 anti-inflammatory macrophage phenotype in growth of human gliomas. *J Pathol,* 216**,** 15-24.

KUSAKA, T., NAKAYAMA, M., NAKAMURA, K., ISHIMIYA, M., FURUSAWA, E. & OGASAWARA, K. 2014. Effect of silica particle size on macrophage inflammatory responses. *PLoS One,* 9**,** e92634.

LABUSSIERE, M., SANSON, M., IDBAIH, A. & DELATTRE, J. Y. 2010. IDH1 gene mutations: a new paradigm in glioma prognosis and therapy? *Oncologist,* 15**,** 196-9.

LANGENAU, D. M., FENG, H., BERGHMANS, S., KANKI, J. P., KUTOK, J. L. & LOOK, A. T. 2005. Cre/lox-regulated transgenic zebrafish model with conditional myc-induced T cell acute lymphoblastic leukemia. *Proc Natl Acad Sci U S A,* 102**,** 6068-73.

LANGENAU, D. M., FERRANDO, A. A., TRAVER, D., KUTOK, J. L., HEZEL, J. P., KANKI, J. P., ZON, L. I., LOOK, A. T. & TREDE, N. S. 2004. In vivo tracking of T cell development, ablation, and engraftment in transgenic zebrafish. *Proc Natl Acad Sci U S A,* 101**,** 7369-74.

LANGENAU, D. M., TRAVER, D., FERRANDO, A. A., KUTOK, J. L., ASTER, J. C., KANKI, J. P., LIN, S., PROCHOWNIK, E., TREDE, N. S., ZON, L. I. & LOOK, A. T. 2003. Myc-induced T cell leukemia in transgenic zebrafish. *Science,* 299**,** 887-90.

LANGHEINRICH, U., HENNEN, E., STOTT, G. & VACUN, G. 2002. Zebrafish as a model organism for the identification and characterization of drugs and genes affecting p53 signaling. *Curr Biol,* 12**,** 2023-8.

LANZA, F., GIULIANI, A. L., AMELOTTI, F., SPISANI, S., TRANIELLO, S. & CASTOLDI, G. 1988. Depressed neutrophil-mediated tumor cell cytotoxicity in subjects affected by hereditary myeloperoxidase deficiency and secondary neoplasia. *Haematologica,* 73**,** 355-8.

LAVIN, Y., WINTER, D., BLECHER-GONEN, R., DAVID, E., KEREN-SHAUL, H., MERAD, M., JUNG, S. & AMIT, I. 2014. Tissue-resident macrophage enhancer landscapes are shaped by the local microenvironment. *Cell,* 159**,** 1312-26.

LAWRENCE, H., MAWDESLEY, A. E., HOLLAND, J. P., KIRBY, J. A., DEEHAN, D. J. & TYSON-CAPPER, A. J. 2016. Targeting Toll-like receptor 4 prevents cobalt-mediated inflammation. *Oncotarget,* 7**,** 7578-85.

LEE, C. H., WU, C. L. & SHIAU, A. L. 2008. Toll-like receptor 4 mediates an antitumor host response induced by Salmonella choleraesuis. *Clin Cancer Res,* 14**,** 1905-12.

LEJEUNE, F. J., LIENARD, D., MATTER, M. & RUEGG, C. 2006. Efficiency of recombinant human TNF in human cancer therapy. *Cancer Immun,* 6**,** 6.

LESO, V. & IAVICOLI, I. 2018. Palladium Nanoparticles: Toxicological Effects and Potential Implications for Occupational Risk Assessment. *Int J Mol Sci,* 19.

LI, L., DUTRA, A., PAK, E., LABRIE, J. E., 3RD, GERSTEIN, R. M., PANDOLFI, P. P., RECHT, L. D. & ROSS, A. H. 2009. EGFRvIII expression and PTEN loss synergistically induce chromosomal instability and glial tumors. *Neuro Oncol,* 11**,** 9-21.

LI, M., XU, T., ZHANG, Z., XUE, X., ZHANG, C., QIN, X., LI, W., HAO, Q., ZHANG, W. & ZHANG, Y. 2012. Phase II multicenter, randomized, double-blind study of recombinant mutated human tumor necrosis factor-alpha in combination with chemotherapies in cancer patients. *Cancer Sci,* 103**,** 288-95.

LI, W. & GRAEBER, M. B. 2012. The molecular profile of microglia under the influence of glioma. *Neuro Oncol,* 14**,** 958-78.

LI, Y., LI, Y., CAO, X., JIN, X. & JIN, T. 2017. Pattern recognition receptors in zebrafish provide functional and evolutionary insight into innate immune signaling pathways. *Cell Mol Immunol,* 14**,** 80-89.

LIAO, Y., SMYTH, G. K. & SHI, W. 2014. featureCounts: an efficient general purpose program for assigning sequence reads to genomic features. *Bioinformatics,* 30**,** 923-30.

LIESCHKE, G. J. & CURRIE, P. D. 2007. Animal models of human disease: zebrafish swim into view. *Nat Rev Genet,* 8**,** 353-67.

LIN, Y. S., HUANG, L. D., LIN, C. H., HUANG, P. H., CHEN, Y. J., WONG, F. H., LIN, C. C. & FU, S. L. 2011. In vitro and in vivo anticancer activity of a synthetic glycolipid as Toll-like receptor 4 (TLR4) activator. *J Biol Chem,* 286**,** 43782-92.

LIU, X., ZHANG, X. F., ZHENG, Z. W., LU, H., WU, X., HUANG, C., WANG, C. & GUANG, G. 2004. The effect of chemotherapy combined with recombination mutant human tumor necrosis factor on advanced cancer. *J Transl Med,* 2**,** 33.

LIVAK, K. J. & SCHMITTGEN, T. D. 2001. Analysis of relative gene expression data using real-time quantitative PCR and the 2(-Delta Delta C(T)) Method. *Methods,* 25**,** 402-8.

LOCKSLEY, R. M., KILLEEN, N. & LENARDO, M. J. 2001. The TNF and TNF receptor superfamilies: integrating mammalian biology. *Cell,* 104**,** 487-501.

LOKE, P., GALLAGHER, I., NAIR, M. G., ZANG, X., BROMBACHER, F., MOHRS, M., ALLISON, J. P. & ALLEN, J. E. 2007. Alternative activation is an innate response to injury that requires CD4+ T cells to be sustained during chronic infection. *J Immunol,* 179**,** 3926-36.

LONDON, A., ITSKOVICH, E., BENHAR, I., KALCHENKO, V., MACK, M., JUNG, S. & SCHWARTZ, M. 2011. Neuroprotection and progenitor cell renewal in the injured adult murine retina requires healing monocyte-derived macrophages. *J Exp Med,* 208**,** 23-39.

LOUIS, D. N., PERRY, A., BURGER, P., ELLISON, D. W., REIFENBERGER, G., VON DEIMLING, A., ALDAPE, K., BRAT, D., COLLINS, V. P., EBERHART, C., FIGARELLA-BRANGER, D., FULLER, G. N., GIANGASPERO, F., GIANNINI, C., HAWKINS, C., KLEIHUES, P., KORSHUNOV, A., KROS, J. M., BEATRIZ LOPES, M., NG, H. K., OHGAKI, H., PAULUS, W., PIETSCH, T., ROSENBLUM, M., RUSHING, E., SOYLEMEZOGLU, F., WIESTLER, O., WESSELING, P. & INTERNATIONAL SOCIETY OF, N.-H. 2014. International Society Of Neuropathology--Haarlem consensus guidelines for nervous system tumor classification and grading. *Brain Pathol,* 24**,** 429-35.

LOUIS, D. N., PERRY, A., REIFENBERGER, G., VON DEIMLING, A., FIGARELLA-BRANGER, D., CAVENEE, W. K., OHGAKI, H., WIESTLER, O. D., KLEIHUES, P. & ELLISON, D. W. 2016. The 2016 World Health Organization Classification of Tumors of the Central Nervous System: a summary. *Acta Neuropathol,* 131**,** 803-20.

LU, Q. R., QIAN, L. & ZHOU, X. 2019. Developmental origins and oncogenic pathways in malignant brain tumors. *Wiley Interdiscip Rev Dev Biol,* 8**,** e342.

LYONS, A., MCQUILLAN, K., DEIGHAN, B. F., O'REILLY, J. A., DOWNER, E. J., MURPHY, A. C., WATSON, M., PIAZZA, A., O'CONNELL, F., GRIFFIN, R., MILLS, K. H. & LYNCH, M. A. 2009. Decreased neuronal CD200 expression in IL-4-deficient mice results in increased neuroinflammation in response to lipopolysaccharide. *Brain Behav Immun,* 23**,** 1020-7.

MA, J. S., KIM, W. J., KIM, J. J., KIM, T. J., YE, S. K., SONG, M. D., KANG, H., KIM, D. W., MOON, W. K. & LEE, K. H. 2010. Gold nanoparticles attenuate LPS-induced NO production through the inhibition of NF-kappaB and IFN-beta/STAT1 pathways in RAW264.7 cells. *Nitric Oxide,* 23**,** 214-9.

MA, Y., ZHANG, L. & HUANG, X. 2014. Genome modification by CRISPR/Cas9. *FEBS J,* 281**,** 5186-93.

MACMICKING, J. D., NATHAN, C., HOM, G., CHARTRAIN, N., FLETCHER, D. S., TRUMBAUER, M., STEVENS, K., XIE, Q. W., SOKOL, K., HUTCHINSON, N. & ET AL. 1995. Altered responses to bacterial infection and endotoxic shock in mice lacking inducible nitric oxide synthase. *Cell,* 81**,** 641-50.

MADRY, C., KYRARGYRI, V., ARANCIBIA-CARCAMO, I. L., JOLIVET, R., KOHSAKA, S., BRYAN, R. M. & ATTWELL, D. 2018. Microglial Ramification, Surveillance, and Interleukin-1beta Release Are Regulated by the Two-Pore Domain K(+) Channel THIK-1. *Neuron,* 97**,** 299-312 e6.

MANDREKA, P. 2009. *Toll-like Receptor Signaling* [Online]. Cell Signaling Technology. Available: https://www.cellsignal.com/contents/science-cst-pathways-immunology-inflammation/toll-like-receptor-signaling/pathways-tlr [Accessed 05 Aug 2019].

MANFROI, B., MCKEE, T., MAYOL, J. F., TABRUYN, S., MORET, S., VILLIERS, C., RIGHINI, C., DYER, M., CALLANAN, M., SCHNEIDER, P., TZANKOV, A., MATTHES, T., STURM, N. & HUARD, B. 2017. CXCL-8/IL8 Produced by Diffuse Large B-cell Lymphomas Recruits Neutrophils Expressing a Proliferation-Inducing Ligand APRIL. *Cancer Res,* 77**,** 1097-1107.

MANTEGAZZA, A. R., MAGALHAES, J. G., AMIGORENA, S. & MARKS, M. S. 2013. Presentation of phagocytosed antigens by MHC class I and II. *Traffic,* 14**,** 135-52.

MANTHE, R. L., FOY, S. P., KRISHNAMURTHY, N., SHARMA, B. & LABHASETWAR, V. 2010. Tumor ablation and nanotechnology. *Mol Pharm,* 7**,** 1880-98.

MANTOVANI, A. & ALLAVENA, P. 2015. The interaction of anticancer therapies with tumor-associated macrophages. *J Exp Med,* 212**,** 435-45.

MANTOVANI, A., ALLAVENA, P., SICA, A. & BALKWILL, F. 2008. Cancer-related inflammation. *Nature,* 454**,** 436-44.

MARINOV, G. K., WILLIAMS, B. A., MCCUE, K., SCHROTH, G. P., GERTZ, J., MYERS, R. M. & WOLD, B. J. 2014. From single-cell to cell-pool transcriptomes: stochasticity in gene expression and RNA splicing. *Genome Res,* 24**,** 496-510.

MARKOVIC, D. S., VINNAKOTA, K., CHIRASANI, S., SYNOWITZ, M., RAGUET, H., STOCK, K., SLIWA, M., LEHMANN, S., KALIN, R., VAN ROOIJEN, N., HOLMBECK, K., HEPPNER, F. L., KIWIT, J., MATYASH, V., LEHNARDT, S., KAMINSKA, B., GLASS, R. & KETTENMANN, H. 2009. Gliomas induce and exploit microglial MT1-MMP expression for tumor expansion. *Proc Natl Acad Sci U S A,* 106**,** 12530-5.

MARTIN, M. 2011. Cutadapt removes adapter sequences from high-throughput sequencing reads. *2011,* 17**,** 3.

MAYRHOFER, M., GOURAIN, V., REISCHL, M., AFFATICATI, P., JENETT, A., JOLY, J. S., BENELLI, M., DEMICHELIS, F., POLIANI, P. L., SIEGER, D. & MIONE, M. 2017. A novel brain tumour model in zebrafish reveals the role of YAP activation in MAPK- and PI3K-induced malignant growth. *Dis Model Mech,* 10**,** 15-28.

MAZZOLINI, J., CHIA, K. & SIEGER, D. 2018. Isolation and RNA Extraction of Neurons, Macrophages and Microglia from Larval Zebrafish Brains. *JoVE***,** e57431.

MCCURLEY, A. T. & CALLARD, G. V. 2008. Characterization of housekeeping genes in zebrafish: male-female differences and effects of tissue type, developmental stage and chemical treatment. *BMC Mol Biol,* 9**,** 102.

MCKERCHER, S. R., TORBETT, B. E., ANDERSON, K. L., HENKEL, G. W., VESTAL, D. J., BARIBAULT, H., KLEMSZ, M., FEENEY, A. J., WU, G. E., PAIGE, C. J. & MAKI, R. A. 1996. Targeted disruption of the PU.1 gene results in multiple hematopoietic abnormalities. *EMBO J,* 15**,** 5647-58.

MCLOUGHLIN, J. M., MCCARTY, T. M., CUNNINGHAM, C., CLARK, V., SENZER, N., NEMUNAITIS, J. & KUHN, J. A. 2005. TNFerade, an adenovector carrying the transgene for human tumor necrosis factor alpha, for patients with advanced solid tumors: surgical experience and long-term follow-up. *Ann Surg Oncol,* 12**,** 825-30.

MEDZHITOV, R. 2008. Origin and physiological roles of inflammation. *Nature,* 454**,** 428-35.

MEIJER, A. H., GABBY KRENS, S. F., MEDINA RODRIGUEZ, I. A., HE, S., BITTER, W., EWA SNAAR-JAGALSKA, B. & SPAINK, H. P. 2004. Expression analysis of the Toll-like receptor and TIR domain adaptor families of zebrafish. *Mol Immunol,* 40**,** 773-83.

MEIJER, A. H., VAN DER VAART, M. & SPAINK, H. P. 2014. Real-time imaging and genetic dissection of host-microbe interactions in zebrafish. *Cell Microbiol,* 16**,** 39-49.

MIONE, M. C. & TREDE, N. S. 2010. The zebrafish as a model for cancer. *Dis Model Mech,* 3**,** 517-23.

MITTAL, M., SIDDIQUI, M. R., TRAN, K., REDDY, S. P. & MALIK, A. B. 2014. Reactive oxygen species in inflammation and tissue injury. *Antioxid Redox Signal,* 20**,** 1126-67.

MITTENDORF, E. A., ALATRASH, G., QIAO, N., WU, Y., SUKHUMALCHANDRA, P., ST JOHN, L. S., PHILIPS, A. V., XIAO, H., ZHANG, M., RUISAARD, K., CLISE-DWYER, K., LU, S. & MOLLDREM, J. J. 2012. Breast cancer cell uptake of the inflammatory mediator neutrophil elastase triggers an anticancer adaptive immune response. *Cancer Res,* 72**,** 3153-62.

MOSSER, D. M. & EDWARDS, J. P. 2008. Exploring the full spectrum of macrophage activation. *Nat Rev Immunol,* 8**,** 958-69.

MOTT, R. T., AIT-GHEZALA, G., TOWN, T., MORI, T., VENDRAME, M., ZENG, J., EHRHART, J., MULLAN, M. & TAN, J. 2004. Neuronal expression of CD22: novel mechanism for inhibiting microglial proinflammatory cytokine production. *Glia,* 46**,** 369-79.

MUKHERJEE, P., BHATTACHARYA, R., WANG, P., WANG, L., BASU, S., NAGY, J. A., ATALA, A., MUKHOPADHYAY, D. & SOKER, S. 2005. Antiangiogenic properties of gold nanoparticles. *Clin Cancer Res,* 11**,** 3530-4.

MULLER, S., KOHANBASH, G., LIU, S. J., ALVARADO, B., CARRERA, D., BHADURI, A., WATCHMAKER, P. B., YAGNIK, G., DI LULLO, E., MALATESTA, M., AMANKULOR, N. M., KRIEGSTEIN, A. R., LIM, D. A., AGHI, M., OKADA, H. & DIAZ, A. 2017. Single-cell profiling of human gliomas reveals macrophage ontogeny as a basis for regional differences in macrophage activation in the tumor microenvironment. *Genome Biol,* 18**,** 234.

MURA, C. V., DELGADO, R., AGUIRRE, P., BACIGALUPO, J. & NUNEZ, M. T. 2006. Quiescence induced by iron challenge protects neuroblastoma cells from oxidative stress. *J Neurochem,* 98**,** 11-9.

MURPHY, M. E. 2013. The HSP70 family and cancer. *Carcinogenesis,* 34**,** 1181-8.

NAERT, T. & VLEMINCKX, K. 2018. CRISPR/Cas9 disease models in zebrafish and Xenopus: The genetic renaissance of fish and frogs. *Drug Discov Today Technol,* 28**,** 41-52.

NAYAK, D., ROTH, T. L. & MCGAVERN, D. B. 2014. Microglia development and function. *Annu Rev Immunol,* 32**,** 367-402.

NAZ, F., KOUL, V., SRIVASTAVA, A., GUPTA, Y. K. & DINDA, A. K. 2016. Biokinetics of ultrafine gold nanoparticles (AuNPs) relating to redistribution and urinary excretion: a long-term in vivo study. *J Drug Target,* 24**,** 720-9.

NG, C. T., YIP, G. W. C., CHEN, E. S., POH, W. Y. R., BAY, B. H. & YUNG, L. Y. L. 2018. Gold nanoparticles induce serum amyloid A 1-Toll-like receptor 2 mediated NF-kB signaling in lung cells in vitro. *Chem Biol Interact,* 289**,** 81-89.

NGUYEN, A. T., KOH, V., SPITSBERGEN, J. M. & GONG, Z. 2016. Development of a conditional liver tumor model by mifepristone-inducible Cre recombination to control oncogenic kras V12 expression in transgenic zebrafish. *Sci Rep,* 6**,** 19559.

NGUYEN-CHI, M., LAPLACE-BUILHE, B., TRAVNICKOVA, J., LUZ-CRAWFORD, P., TEJEDOR, G., LUTFALLA, G., KISSA, K., JORGENSEN, C. & DJOUAD, F. 2018. Correction to: TNF signaling and macrophages govern fin regeneration in zebrafish larvae. *Cell Death Dis,* 9**,** 709.

NIE, H., ZHENG, Y., LI, R., GUO, T. B., HE, D., FANG, L., LIU, X., XIAO, L., CHEN, X., WAN, B., CHIN, Y. E. & ZHANG, J. Z. 2013. Phosphorylation of FOXP3 controls regulatory T cell function and is inhibited by TNF-alpha in rheumatoid arthritis. *Nat Med,* 19**,** 322-8.

NIIKURA, K., MATSUNAGA, T., SUZUKI, T., KOBAYASHI, S., YAMAGUCHI, H., ORBA, Y., KAWAGUCHI, A., HASEGAWA, H., KAJINO, K., NINOMIYA, T., IJIRO, K. & SAWA, H. 2013. Gold nanoparticles as a vaccine platform: influence of size and shape on immunological responses in vitro and in vivo. *ACS Nano,* 7**,** 3926-38.

NIMMERJAHN, A., KIRCHHOFF, F. & HELMCHEN, F. 2005. Resting microglial cells are highly dynamic surveillants of brain parenchyma in vivo. *Science,* 308**,** 1314-8.

NOVOA, B. & FIGUERAS, A. 2012. Zebrafish: model for the study of inflammation and the innate immune response to infectious diseases. *Adv Exp Med Biol,* 946**,** 253-75.

NOY, R. & POLLARD, J. W. 2014. Tumor-associated macrophages: from mechanisms to therapy. *Immunity,* 41**,** 49-61.

ODAJIMA, T., ONISHI, M., HAYAMA, E., MOTOJI, N., MOMOSE, Y. & SHIGEMATSU, A. 1996. Cytolysis of B-16 melanoma tumor cells mediated by the myeloperoxidase and lactoperoxidase systems. *Biol Chem,* 377**,** 689-93.

OHSAWA, K., IMAI, Y., SASAKI, Y. & KOHSAKA, S. 2004. Microglia/macrophage-specific protein Iba1 binds to fimbrin and enhances its actin-bundling activity. *J Neurochem,* 88**,** 844-56.

OLSON, M. C., SCOTT, E. W., HACK, A. A., SU, G. H., TENEN, D. G., SINGH, H. & SIMON, M. C. 1995. PU. 1 is not essential for early myeloid gene expression but is required for terminal myeloid differentiation. *Immunity,* 3**,** 703-14.

OUYANG, X., SHI, M., JIE, F., BAI, Y., SHEN, P., YU, Z., WANG, X., HUANG, C., TAO, M., WANG, Z., XIE, C., WU, Q., SHU, Y., HAN, B., ZHANG, F., ZHANG, Y., HU, C., MA, X., LIANG, Y., WANG, A., LU, B., SHI, Y., CHEN, J., ZHUANG, Z., WANG, J., HUANG, J., WANG, C., BAI, C., ZHOU, X., LI, Q., CHEN, F., YU, H. & FENG, J. 2018. Phase III study of dulanermin (recombinant human tumor necrosis factor-related apoptosis-inducing ligand/Apo2 ligand) combined with vinorelbine and cisplatin in patients with advanced non-small-cell lung cancer. *Invest New Drugs,* 36**,** 315-322.

PANG, S. H. M., DE GRAAF, C. A., HILTON, D. J., HUNTINGTON, N. D., CAROTTA, S., WU, L. & NUTT, S. L. 2018. PU.1 Is Required for the Developmental Progression of Multipotent Progenitors to Common Lymphoid Progenitors. *Front Immunol,* 9**,** 1264.

PARK, E. J. & PARK, K. 2009. Oxidative stress and pro-inflammatory responses induced by silica nanoparticles in vivo and in vitro. *Toxicol Lett,* 184**,** 18-25.

PENN, C. A., YANG, K., ZONG, H., LIM, J. Y., COLE, A., YANG, D., BAKER, J., GOONEWARDENA, S. N. & BUCKANOVICH, R. J. 2018. Therapeutic Impact of Nanoparticle Therapy Targeting Tumor-Associated Macrophages. *Mol Cancer Ther,* 17**,** 96-106.

PEREZ-LOPEZ, A. M., RUBIO-RUIZ, B., SEBASTIAN, V., HAMILTON, L., ADAM, C., BRAY, T. L., IRUSTA, S., BRENNAN, P. M., LLOYD-JONES, G. C., SIEGER, D., SANTAMARIA, J. & UNCITI-BROCETA, A. 2017. Gold-Triggered Uncaging Chemistry in Living Systems. *Angew Chem Int Ed Engl,* 56**,** 12548-12552.

PERI, F. & NUSSLEIN-VOLHARD, C. 2008. Live imaging of neuronal degradation by microglia reveals a role for v0-ATPase a1 in phagosomal fusion in vivo. *Cell,* 133**,** 916-27.

PHILLIPS, W. T., BAO, A., BRENNER, A. J. & GOINS, B. A. 2014. Image-guided interventional therapy for cancer with radiotherapeutic nanoparticles. *Adv Drug Deliv Rev,* 76**,** 39-59.

POCZOBUTT, J. M., DE, S., YADAV, V. K., NGUYEN, T. T., LI, H., SIPPEL, T. R., WEISER-EVANS, M. C. & NEMENOFF, R. A. 2016. Expression Profiling of Macrophages Reveals Multiple Populations with Distinct Biological Roles in an Immunocompetent Orthotopic Model of Lung Cancer. *J Immunol,* 196**,** 2847-59.

POLLARD, J. W. 2009. Trophic macrophages in development and disease. *Nat Rev Immunol,* 9**,** 259-70.

POLLARD, S. M., YOSHIKAWA, K., CLARKE, I. D., DANOVI, D., STRICKER, S., RUSSELL, R., BAYANI, J., HEAD, R., LEE, M., BERNSTEIN, M., SQUIRE, J. A., SMITH, A. & DIRKS, P. 2009. Glioma stem cell lines expanded in adherent culture have tumor-specific phenotypes and are suitable for chemical and genetic screens. *Cell Stem Cell,* 4**,** 568-80.

POPE, J. E., HONG, P. & KOEHLER, B. E. 2002. Prescribing trends in disease modifying antirheumatic drugs for rheumatoid arthritis: a survey of practicing Canadian rheumatologists. *J Rheumatol,* 29**,** 255-60.

PRATSINIS, A., HERVELLA, P., LEROUX, J. C., PRATSINIS, S. E. & SOTIRIOU, G. A. 2013. Toxicity of silver nanoparticles in macrophages. *Small,* 9**,** 2576-84.

PRIONISTI, I., BUHLER, L. H., WALKER, P. R. & JOLIVET, R. B. 2019. Harnessing Microglia and Macrophages for the Treatment of Glioblastoma. *Front Pharmacol,* 10**,** 506.

PYONTECK, S. M., AKKARI, L., SCHUHMACHER, A. J., BOWMAN, R. L., SEVENICH, L., QUAIL, D. F., OLSON, O. C., QUICK, M. L., HUSE, J. T., TEIJEIRO, V., SETTY, M., LESLIE, C. S., OEI, Y., PEDRAZA, A., ZHANG, J., BRENNAN, C. W., SUTTON, J. C., HOLLAND, E. C., DANIEL, D. & JOYCE, J. A. 2013. CSF-1R inhibition alters macrophage polarization and blocks glioma progression. *Nat Med,* 19**,** 1264-72.

QIAN, B. Z. & POLLARD, J. W. 2010. Macrophage diversity enhances tumor progression and metastasis. *Cell,* 141**,** 39-51.

QIAO, Y., HUANG, X., NIMMAGADDA, S., BAI, R., STAEDTKE, V., FOSS, C. A., CHEONG, I., HOLDHOFF, M., KATO, Y., POMPER, M. G., RIGGINS, G. J., KINZLER, K. W., DIAZ, L. A., JR., VOGELSTEIN, B. & ZHOU, S. 2011. A robust approach to enhance tumor-selective accumulation of nanoparticles. *Oncotarget,* 2**,** 59-68.

QUAIL, D. F. & JOYCE, J. A. 2017. Molecular Pathways: Deciphering Mechanisms of Resistance to Macrophage-Targeted Therapies. *Clin Cancer Res,* 23**,** 876-884.

RACHMAWATI, D., BONTKES, H. J., VERSTEGE, M. I., MURIS, J., VON BLOMBERG, B. M., SCHEPER, R. J. & VAN HOOGSTRATEN, I. M. 2013. Transition metal sensing by Toll-like

receptor-4: next to nickel, cobalt and palladium are potent human dendritic cell stimulators. *Contact Dermatitis,* 68**,** 331-8.

RACHMAWATI, D., BUSKERMOLEN, J. K., SCHEPER, R. J., GIBBS, S., VON BLOMBERG, B. M. & VAN HOOGSTRATEN, I. M. 2015. Dental metal-induced innate reactivity in keratinocytes. *Toxicol In Vitro,* 30**,** 325-30.

RASMUSSEN, H., RASMUSSEN, C., LEMPICKI, M., DURHAM, R., BROUGH, D., KING, C. R. & WEICHSELBAUM, R. 2002. TNFerade Biologic: preclinical toxicology of a novel adenovector with a radiation-inducible promoter, carrying the human tumor necrosis factor alpha gene. *Cancer Gene Ther,* 9**,** 951-7.

RAULET, D. H. 2006. Missing self recognition and self tolerance of natural killer (NK) cells. *Semin Immunol,* 18**,** 145-50.

RECIO DESPAIGNE, A. A., DA SILVA, J. G., DA COSTA, P. R., DOS SANTOS, R. G. & BERALDO, H. 2014. ROS-mediated cytotoxic effect of copper(II) hydrazone complexes against human glioma cells. *Molecules,* 19**,** 17202-20.

REICHEL, D., TRIPATHI, M. & PEREZ, J. M. 2019. Biological Effects of Nanoparticles on Macrophage Polarization in the Tumor Microenvironment. *Nanotheranostics,* 3**,** 66-88.

RENSHAW, S. A., LOYNES, C. A., ELWORTHY, S., INGHAM, P. W. & WHYTE, M. K. 2007. Modeling inflammation in the zebrafish: how a fish can help us understand lung disease. *Exp Lung Res,* 33**,** 549-54.

RENSHAW, S. A., LOYNES, C. A., TRUSHELL, D. M., ELWORTHY, S., INGHAM, P. W. & WHYTE, M. K. 2006. A transgenic zebrafish model of neutrophilic inflammation. *Blood,* 108**,** 3976-8.

RENSHAW, S. A. & TREDE, N. S. 2012. A model 450 million years in the making: zebrafish and vertebrate immunity. *Dis Model Mech,* 5**,** 38-47.

RIERA ROMO, M., PEREZ-MARTINEZ, D. & CASTILLO FERRER, C. 2016. Innate immunity in vertebrates: an overview. *Immunology,* 148**,** 125-39.

RINGNER, M. 2008. What is principal component analysis? *Nat Biotechnol,* 26**,** 303-4.

RODELL, C. B., ARLAUCKAS, S. P., CUCCARESE, M. F., GARRIS, C. S., LI, R., AHMED, M. S., KOHLER, R. H., PITTET, M. J. & WEISSLEDER, R. 2018a. TLR7/8-agonist-loaded nanoparticles promote the polarization of tumour-associated macrophages to enhance cancer immunotherapy. *Nat Biomed Eng,* 2**,** 578-588.

RODELL, C. B., ARLAUCKAS, S. P., CUCCARESE, M. F., GARRIS, C. S., LI, R., AHMED, M. S., KOHLER, R. H., PITTET, M. J. & WEISSLEDER, R. 2018b. TLR7/8-agonist-loaded nanoparticles promote the polarization of tumour-associated macrophages to enhance cancer immunotherapy. *Nat Biomed Eng,* 2**,** 578-588.

RODRIGUES, J. C., GONZALEZ, G. C., ZHANG, L., IBRAHIM, G., KELLY, J. J., GUSTAFSON, M. P., LIN, Y., DIETZ, A. B., FORSYTH, P. A., YONG, V. W. & PARNEY, I. F. 2010. Normal human monocytes exposed to glioma cells acquire myeloid-derived suppressor cell-like properties. *Neuro Oncol,* 12**,** 351-65.

ROSALES, C., DEMAUREX, N., LOWELL, C. A. & URIBE-QUEROL, E. 2016. Neutrophils: Their Role in Innate and Adaptive Immunity. *J Immunol Res,* 2016**,** 1469780.

ROUGEOT, J., TORRACA, V., ZAKRZEWSKA, A., KANWAL, Z., JANSEN, H. J., SOMMER, F., SPAINK, H. P. & MEIJER, A. H. 2019. RNAseq Profiling of Leukocyte Populations in Zebrafish Larvae Reveals a cxcl11 Chemokine Gene as a Marker of Macrophage Polarization During Mycobacterial Infection. *Front Immunol,* 10**,** 832.

ROUSSEAU, A., NUTT, C. L., BETENSKY, R. A., IAFRATE, A. J., HAN, M., LIGON, K. L., ROWITCH, D. H. & LOUIS, D. N. 2006. Expression of oligodendroglial and astrocytic lineage markers in diffuse gliomas: use of YKL-40, ApoE, ASCL1, and NKX2-2. *J Neuropathol Exp Neurol,* 65**,** 1149-56.

RUFFELL, B. & COUSSENS, L. M. 2015. Macrophages and therapeutic resistance in cancer. *Cancer Cell,* 27**,** 462-72.

SAITOH, M., NISHITOH, H., FUJII, M., TAKEDA, K., TOBIUME, K., SAWADA, Y., KAWABATA, M., MIYAZONO, K. & ICHIJO, H. 1998. Mammalian thioredoxin is a direct inhibitor of apoptosis signal-regulating kinase (ASK) 1. *EMBO J,* 17**,** 2596-606.

SANGTANI, A., NAG, O. K., FIELD, L. D., BREGER, J. C. & DELEHANTY, J. B. 2017. Multifunctional nanoparticle composites: progress in the use of soft and hard nanoparticles for drug delivery and imaging. *Wiley Interdiscip Rev Nanomed Nanobiotechnol,* 9.

SATOH, J., KINO, Y., ASAHINA, N., TAKITANI, M., MIYOSHI, J., ISHIDA, T. & SAITO, Y. 2016. TMEM119 marks a subset of microglia in the human brain. *Neuropathology,* 36**,** 39-49.

SAWAI, H. & DOMAE, N. 2011. Discrimination between primary necrosis and apoptosis by necrostatin-1 in Annexin V-positive/propidium iodide-negative cells. *Biochem Biophys Res Commun,* 411**,** 569-73.

SCHERBART, A. M., LANGER, J., BUSHMELEV, A., VAN BERLO, D., HABERZETTL, P., VAN SCHOOTEN, F. J., SCHMIDT, A. M., ROSE, C. R., SCHINS, R. P. & ALBRECHT, C. 2011. Contrasting macrophage activation by fine and ultrafine titanium dioxide particles is associated with different uptake mechanisms. *Part Fibre Toxicol,* 8**,** 31.

SCHMIDT, M. & GOEBELER, M. 2015. Immunology of metal allergies. *J Dtsch Dermatol Ges,* 13**,** 653-60.

SCHMIDT, R., STRAHLE, U. & SCHOLPP, S. 2013. Neurogenesis in zebrafish - from embryo to adult. *Neural Dev,* 8**,** 3.

SCHREIBER-AGUS, N., HORNER, J., TORRES, R., CHIU, F. C. & DEPINHO, R. A. 1993. Zebra fish myc family and max genes: differential expression and oncogenic activity throughout vertebrate evolution. *Mol Cell Biol,* 13**,** 2765-75.

SCHROEDER, A., MUELLER, O., STOCKER, S., SALOWSKY, R., LEIBER, M., GASSMANN, M., LIGHTFOOT, S., MENZEL, W., GRANZOW, M. & RAGG, T. 2006. The RIN: an RNA integrity number for assigning integrity values to RNA measurements. *BMC Mol Biol,* 7**,** 3.

SENZER, N., MANI, S., ROSEMURGY, A., NEMUNAITIS, J., CUNNINGHAM, C., GUHA, C., BAYOL, N., GILLEN, M., CHU, K., RASMUSSEN, C., RASMUSSEN, H., KUFE, D., WEICHSELBAUM, R. & HANNA, N. 2004. TNFerade biologic, an adenovector with a radiation-inducible promoter, carrying the human tumor necrosis factor alpha gene: a phase I study in patients with solid tumors. *J Clin Oncol,* 22**,** 592-601.

SHAKED, I., TCHORESH, D., GERSNER, R., MEIRI, G., MORDECHAI, S., XIAO, X., HART, R. P. & SCHWARTZ, M. 2005. Protective autoimmunity: interferon-gamma enables microglia to remove glutamate without evoking inflammatory mediators. *J Neurochem,* 92**,** 997-1009.

SHAO, Q., LI, Y., WANG, Q. & ZHAO, J. 2015. IL-10 and IL-1beta mediate neuropathic-pain like behavior in the ventrolateral orbital cortex. *Neurochem Res,* 40**,** 733-9.

SHECHTER, R., LONDON, A., VAROL, C., RAPOSO, C., CUSIMANO, M., YOVEL, G., ROLLS, A., MACK, M., PLUCHINO, S., MARTINO, G., JUNG, S. & SCHWARTZ, M. 2009. Infiltrating blood-derived macrophages are vital cells playing an anti-inflammatory role in recovery from spinal cord injury in mice. *PLoS Med,* 6**,** e1000113.

SHIAU, C. E., KAUFMAN, Z., MEIRELES, A. M. & TALBOT, W. S. 2015. Differential requirement for irf8 in formation of embryonic and adult macrophages in zebrafish. *PLoS One,* 10**,** e0117513.

SHOJI, W. & SATO-MAEDA, M. 2008. Application of heat shock promoter in transgenic zebrafish. *Dev Growth Differ,* 50**,** 401-6.

SIEGER, D., MORITZ, C., ZIEGENHALS, T., PRYKHOZHIJ, S. & PERI, F. 2012. Long-range Ca2+ waves transmit brain-damage signals to microglia. *Dev Cell,* 22**,** 1138-48.

SIERRA, J. R., CORSO, S., CAIONE, L., CEPERO, V., CONROTTO, P., CIGNETTI, A., PIACIBELLO, W., KUMANOGOH, A., KIKUTANI, H., COMOGLIO, P. M., TAMAGNONE, L. & GIORDANO, S. 2008. Tumor angiogenesis and progression are enhanced by Sema4D produced by tumor-associated macrophages. *J Exp Med,* 205**,** 1673-85.

SIMARD, A. R. & RIVEST, S. 2004. Bone marrow stem cells have the ability to populate the entire central nervous system into fully differentiated parenchymal microglia. *FASEB J,* 18**,** 998-1000.

SINGH, M., KHONG, H., DAI, Z., HUANG, X. F., WARGO, J. A., COOPER, Z. A., VASILAKOS, J. P., HWU, P. & OVERWIJK, W. W. 2014. Effective innate and adaptive antimelanoma immunity through localized TLR7/8 activation. *J Immunol,* 193**,** 4722-31.

SMITH, G. F., ALTMAN, M. D., ANDRESEN, B., BAKER, J., BRUBAKER, J. D., CHEN, H., CHEN, Y., CHILDERS, M., DONOFRIO, A., FERGUSON, H., FISCHER, C., FISCHMANN, T. O., GIBEAU, C., HICKS, A., JIN, S., KATTAR, S., KLEINSCHEK, M. A., LECCESE, E., LESBURG, C., LI, C., LIM, J., LIU, D., MACLEAN, J. K. F., MANSOOR, F., MOY, L. Y., MULROONEY, E. F., NECHEVA, A. S., PRESLAND, J., RAKHILINA, L., YANG, R., TORRES, L., ZHANG-HOOVER, J. & NORTHRUP, A. 2017. Identification of quinazoline based inhibitors of IRAK4 for the treatment of inflammation. *Bioorg Med Chem Lett,* 27**,** 2721-2726.

SPITSBERGEN, J. M., TSAI, H. W., REDDY, A., MILLER, T., ARBOGAST, D., HENDRICKS, J. D. & BAILEY, G. S. 2000a. Neoplasia in zebrafish (Danio rerio) treated with 7,12-dimethylbenz[a]anthracene by two exposure routes at different developmental stages. *Toxicol Pathol,* 28**,** 705-15.

SPITSBERGEN, J. M., TSAI, H. W., REDDY, A., MILLER, T., ARBOGAST, D., HENDRICKS, J. D. & BAILEY, G. S. 2000b. Neoplasia in zebrafish (Danio rerio) treated with N-methyl-N'-nitro-N-nitrosoguanidine by three exposure routes at different developmental stages. *Toxicol Pathol,* 28**,** 716-25.

STATHOPOULOS, G. T., KOLLINTZA, A., MOSCHOS, C., PSALLIDAS, I., SHERRILL, T. P., PITSINOS, E. N., VASSILIOU, S., KARATZA, M., PAPIRIS, S. A., GRAF, D., ORPHANIDOU, D., LIGHT, R. W., ROUSSOS, C., BLACKWELL, T. S. & KALOMENIDIS, I. 2007. Tumor necrosis factor-alpha promotes malignant pleural effusion. *Cancer Res,* 67**,** 9825-34.

STOHRER, M., BOUCHER, Y., STANGASSINGER, M. & JAIN, R. K. 2000. Oncotic pressure in solid tumors is elevated. *Cancer Res,* 60**,** 4251-5.

STRATAKIS, M. & GARCIA, H. 2012. Catalysis by supported gold nanoparticles: beyond aerobic oxidative processes. *Chem Rev,* 112**,** 4469-506.

STUPP, R., TAILLIBERT, S., KANNER, A., READ, W., STEINBERG, D., LHERMITTE, B., TOMS, S., IDBAIH, A., AHLUWALIA, M. S., FINK, K., DI MECO, F., LIEBERMAN, F., ZHU, J. J., STRAGLIOTTO, G., TRAN, D., BREM, S., HOTTINGER, A., KIRSON, E. D., LAVY-SHAHAF, G., WEINBERG, U., KIM, C. Y., PAEK, S. H., NICHOLAS, G., BRUNA, J., HIRTE, H., WELLER, M., PALTI, Y., HEGI, M. E. & RAM, Z. 2017. Effect of Tumor-Treating Fields Plus Maintenance Temozolomide vs Maintenance Temozolomide Alone on Survival in Patients With Glioblastoma: A Randomized Clinical Trial. *JAMA,* 318**,** 2306-2316.

SZLOSAREK, P., CHARLES, K. A. & BALKWILL, F. R. 2006. Tumour necrosis factor-alpha as a tumour promoter. *Eur J Cancer,* 42**,** 745-50.

SZULZEWSKY, F., ARORA, S., DE WITTE, L., ULAS, T., MARKOVIC, D., SCHULTZE, J. L., HOLLAND, E. C., SYNOWITZ, M., WOLF, S. A. & KETTENMANN, H. 2016. Human glioblastoma-associated microglia/monocytes express a distinct RNA profile compared to human control and murine samples. *Glia,* 64**,** 1416-36.

SZULZEWSKY, F., PELZ, A., FENG, X., SYNOWITZ, M., MARKOVIC, D., LANGMANN, T., HOLTMAN, I. R., WANG, X., EGGEN, B. J., BODDEKE, H. W., HAMBARDZUMYAN, D., WOLF, S. A. & KETTENMANN, H. 2015. Glioma-associated microglia/macrophages display an expression profile different from M1 and M2 polarization and highly express Gpnmb and Spp1. *PLoS One,* 10**,** e0116644.

TAKALE, B. S., BAO, M. & YAMAMOTO, Y. 2014. Gold nanoparticle (AuNPs) and gold nanopore (AuNPore) catalysts in organic synthesis. *Org Biomol Chem,* 12**,** 2005-27.

TARATUMMARAT, S., SANGPHECH, N., VU, C. T. B., PALAGA, T., ONDEE, T., SURAWUT, S., SEREEMASPUN, A., RITPRAJAK, P. & LEELAHAVANICHKUL, A. 2018. Gold nanoparticles attenuates bacterial sepsis in cecal ligation and puncture mouse model through the induction of M2 macrophage polarization. *BMC Microbiol,* 18**,** 85.

THANNICKAL, V. J. & FANBURG, B. L. 2000. Reactive oxygen species in cell signaling. *Am J Physiol Lung Cell Mol Physiol,* 279**,** L1005-28.

TIAN, Y., XU, J., FENG, S., HE, S., ZHAO, S., ZHU, L., JIN, W., DAI, Y., LUO, L., QU, J. Y. & WEN, Z. 2017. The first wave of T lymphopoiesis in zebrafish arises from aorta endothelium independent of hematopoietic stem cells. *The Journal of Experimental Medicine,* 214**,** 3347-3360.

TONGA, G. Y., JEONG, Y., DUNCAN, B., MIZUHARA, T., MOUT, R., DAS, R., KIM, S. T., YEH, Y. C., YAN, B., HOU, S. & ROTELLO, V. M. 2015. Supramolecular regulation of bioorthogonal catalysis in cells using nanoparticle-embedded transition metal catalysts. *Nat Chem,* 7**,** 597-603.

TOTH, G. B., VARALLYAY, C. G., HORVATH, A., BASHIR, M. R., CHOYKE, P. L., DALDRUP-LINK, H. E., DOSA, E., FINN, J. P., GAHRAMANOV, S., HARISINGHANI, M., MACDOUGALL, I., NEUWELT, A., VASANAWALA, S. S., AMBADY, P., BARAJAS, R., CETAS, J. S., CIPOREN, J., DELOUGHERY, T. J., DOOLITTLE, N. D., FU, R., GRINSTEAD, J., GUIMARAES, A. R., HAMILTON, B. E., LI, X., MCCONNELL, H. L., MULDOON, L. L., NESBIT, G., NETTO, J. P., PETTERSON, D., ROONEY, W. D., SCHWARTZ, D., SZIDONYA, L. & NEUWELT, E. A. 2017. Current and potential imaging applications of ferumoxytol for magnetic resonance imaging. *Kidney Int,* 92**,** 47-66.

TRUBIROHA, A., GILLOTAY, P., GIUSTI, N., GACQUER, D., LIBERT, F., LEFORT, A., HAERLINGEN, B., DE DEKEN, X., OPITZ, R. & COSTAGLIOLA, S. 2018. A Rapid CRISPR/Cas-based Mutagenesis Assay in Zebrafish for Identification of Genes Involved in Thyroid Morphogenesis and Function. *Sci Rep,* 8**,** 5647.

TSAROUCHAS, T. M., WEHNER, D., CAVONE, L., MUNIR, T., KEATINGE, M., LAMBERTUS, M., UNDERHILL, A., BARRETT, T., KASSAPIS, E., OGRYZKO, N., FENG, Y., VAN HAM, T. J., BECKER, T. & BECKER, C. G. 2018. Dynamic control of proinflammatory cytokines Il-1beta and Tnf-alpha by macrophages in zebrafish spinal cord regeneration. *Nat Commun,* 9**,** 4670.

UNAL CEVIK, I. & DALKARA, T. 2003. Intravenously administered propidium iodide labels necrotic cells in the intact mouse brain after injury. *Cell Death Differ,* 10**,** 928-9.

VAN DALEN, F. J., VAN STEVENDAAL, M., FENNEMANN, F. L., VERDOES, M. & ILINA, O. 2018. Molecular Repolarisation of Tumour-Associated Macrophages. *Molecules,* 24.

VAN VLERKEN, L. E., VYAS, T. K. & AMIJI, M. M. 2007. Poly(ethylene glycol)-modified nanocarriers for tumor-targeted and intracellular delivery. *Pharm Res,* 24**,** 1405-14.

VATNER, R. E. & FORMENTI, S. C. 2015. Myeloid-derived cells in tumors: effects of radiation. *Semin Radiat Oncol,* 25**,** 18-27.

VENERO GALANTERNIK, M., NIKAIDO, M., YU, Z., MCKINNEY, S. A. & PIOTROWSKI, T. 2016. Localized Gene Induction by Infrared-Mediated Heat Shock. *Zebrafish,* 13**,** 537-540.

VERHAAK, R. G., HOADLEY, K. A., PURDOM, E., WANG, V., QI, Y., WILKERSON, M. D., MILLER, C. R., DING, L., GOLUB, T., MESIROV, J. P., ALEXE, G., LAWRENCE, M., O'KELLY, M., TAMAYO, P., WEIR, B. A., GABRIEL, S., WINCKLER, W., GUPTA, S., JAKKULA, L., FEILER, H. S., HODGSON, J. G., JAMES, C. D., SARKARIA, J. N., BRENNAN, C., KAHN, A., SPELLMAN, P. T., WILSON, R. K., SPEED, T. P., GRAY, J. W., MEYERSON, M., GETZ, G., PEROU, C. M., HAYES, D. N. & CANCER GENOME ATLAS RESEARCH, N. 2010. Integrated genomic analysis identifies clinically relevant subtypes of glioblastoma characterized by abnormalities in PDGFRA, IDH1, EGFR, and NF1. *Cancer Cell,* 17**,** 98-110.

VIDYARTHI, A., KHAN, N., AGNIHOTRI, T., NEGI, S., DAS, D. K., AQDAS, M., CHATTERJEE, D., COLEGIO, O. R., TEWARI, M. K. & AGREWALA, J. N. 2018. TLR-3 Stimulation Skews M2 Macrophages to M1 Through IFN-alphabeta Signaling and Restricts Tumor Progression. *Front Immunol,* 9**,** 1650.

VOGEL, D. Y., GLIM, J. E., STAVENUITER, A. W., BREUR, M., HEIJNEN, P., AMOR, S., DIJKSTRA, C. D. & BEELEN, R. H. 2014. Human macrophage polarization in vitro: maturation and activation methods compared. *Immunobiology,* 219**,** 695-703.

VOISIN, P., BOUCHAUD, V., MERLE, M., DIOLEZ, P., DUFFY, L., FLINT, K., FRANCONI, J. M. & BOUZIER-SORE, A. K. 2010. Microglia in close vicinity of glioma cells: correlation between phenotype and metabolic alterations. *Front Neuroenergetics,* 2**,** 131.

WALKEY, C. D., OLSEN, J. B., GUO, H., EMILI, A. & CHAN, W. C. 2012. Nanoparticle size and surface chemistry determine serum protein adsorption and macrophage uptake. *J Am Chem Soc,* 134**,** 2139-47.

WALTON, M. R., GIBBONS, H., MACGIBBON, G. A., SIRIMANNE, E., SAURA, J., GLUCKMAN, P. D. & DRAGUNOW, M. 2000. PU.1 expression in microglia. *J Neuroimmunol,* 104**,** 109-15.

WANG, T., ZHANG, J., HOU, T., YIN, X. & ZHANG, N. 2019. Selective targeting of tumor cells and tumor associated macrophages separately by twin-like core-shell nanoparticles for enhanced tumor-localized chemoimmunotherapy. *Nanoscale,* 11**,** 13934-13946.

WANG, Z. S., LUO, P., DAI, S. H., LIU, Z. B., ZHENG, X. R. & CHEN, T. 2013. Salvianolic acid B induces apoptosis in human glioma U87 cells through p38-mediated ROS generation. *Cell Mol Neurobiol,* 33**,** 921-8.

WATANABE, T., SAITO, D., TANABE, K., SUETSUGU, R., NAKAYA, Y., NAKAGAWA, S. & TAKAHASHI, Y. 2007. Tet-on inducible system combined with in ovo electroporation dissects multiple roles of genes in somitogenesis of chicken embryos. *Dev Biol,* 305**,** 625-36.

WATKINS, S. K., EGILMEZ, N. K., SUTTLES, J. & STOUT, R. D. 2007. IL-12 rapidly alters the functional profile of tumor-associated and tumor-infiltrating macrophages in vitro and in vivo. *J Immunol,* 178**,** 1357-62.

WEISS, J. T., DAWSON, J. C., MACLEOD, K. G., RYBSKI, W., FRASER, C., TORRES-SANCHEZ, C., PATTON, E. E., BRADLEY, M., CARRAGHER, N. O. & UNCITI-BROCETA, A. 2014a. Extracellular palladium-catalysed dealkylation of 5-fluoro-1-propargyl-uracil as a bioorthogonally activated prodrug approach. *Nat Commun,* 5**,** 3277.

WEISS, J. T., FRASER, C., RUBIO-RUIZ, B., MYERS, S. H., CRISPIN, R., DAWSON, J. C., BRUNTON, V. G., PATTON, E. E., CARRAGHER, N. O. & UNCITI-BROCETA, A. 2014b. N-alkynyl derivatives of 5-fluorouracil: susceptibility to palladium-mediated dealkylation and toxigenicity in cancer cell culture. *Front Chem,* 2**,** 56.

WELKER, A. M., JAROS, B. D., PUDUVALLI, V. K., IMITOLA, J., KAUR, B. & BEATTIE, C. E. 2016. Standardized orthotopic xenografts in zebrafish reveal glioma cell-line-specific characteristics and tumor cell heterogeneity. *Dis Model Mech,* 9**,** 199-210.

WELLER, M., VAN DEN BENT, M., HOPKINS, K., TONN, J. C., STUPP, R., FALINI, A., COHEN-JONATHAN-MOYAL, E., FRAPPAZ, D., HENRIKSSON, R., BALANA, C., CHINOT, O., RAM, Z., REIFENBERGER, G., SOFFIETTI, R., WICK, W. & EUROPEAN ASSOCIATION FOR NEURO-ONCOLOGY TASK FORCE ON MALIGNANT, G. 2014. EANO guideline for the diagnosis and treatment of anaplastic gliomas and glioblastoma. *Lancet Oncol,* 15**,** e395-403.

WHITE, R., ROSE, K. & ZON, L. 2013. Zebrafish cancer: the state of the art and the path forward. *Nat Rev Cancer,* 13**,** 624-36.

WU, A., WEI, J., KONG, L. Y., WANG, Y., PRIEBE, W., QIAO, W., SAWAYA, R. & HEIMBERGER, A. B. 2010. Glioma cancer stem cells induce immunosuppressive macrophages/microglia. *Neuro Oncol,* 12**,** 1113-25.

WU, M., LI, J., GAO, Q. & YE, F. 2016. The role of Sema4D/CD100 as a therapeutic target for tumor microenvironments and for autoimmune, neuroimmune and bone diseases. *Expert Opin Ther Targets,* 20**,** 885-901.

WU, N., LIU, B., DU, H., ZHAO, S., LI, Y., CHENG, X., WANG, S., LIN, J., ZHOU, J., DECIPHERING DISORDERS INVOLVING, S., STUDY, C. O., QIU, G., WU, Z. & ZHANG, J. 2019. The Progress of CRISPR/Cas9-Mediated Gene Editing in Generating Mouse/Zebrafish Models of Human Skeletal Diseases. *Comput Struct Biotechnol J,* 17**,** 954-962.

WU, W., DUAN, Y., MA, G., ZHOU, G., PARK-WINDHOL, C., D'AMORE, P. A. & LEI, H. 2017. AAV-CRISPR/Cas9-Mediated

Depletion of VEGFR2 Blocks Angiogenesis In Vitro. *Invest Ophthalmol Vis Sci,* 58**,** 6082-6090.

WU, Y., ZHOU, H., FAN, X., ZHANG, Y., ZHANG, M., WANG, Y., XIE, Z., BAI, M., YIN, Q., LIANG, D., TANG, W., LIAO, J., ZHOU, C., LIU, W., ZHU, P., GUO, H., PAN, H., WU, C., SHI, H., WU, L., TANG, F. & LI, J. 2015. Correction of a genetic disease by CRISPR-Cas9-mediated gene editing in mouse spermatogonial stem cells. *Cell Res,* 25**,** 67-79.

XIE, J., XU, C., KOHLER, N., HOU, Y. & SUN, S. 2007. Controlled PEGylation of Monodisperse Fe3O4 Nanoparticles for Reduced Non-Specific Uptake by Macrophage Cells. *Advanced Materials,* 19**,** 3163-3166.

XU, J., DU, L. & WEN, Z. 2012. Myelopoiesis during zebrafish early development. *J Genet Genomics,* 39**,** 435-42.

XU, J., ZHU, L., HE, S., WU, Y., JIN, W., YU, T., QU, J. Y. & WEN, Z. 2015. Temporal-Spatial Resolution Fate Mapping Reveals Distinct Origins for Embryonic and Adult Microglia in Zebrafish. *Dev Cell,* 34**,** 632-41.

YAN, C., BRUNSON, D. C., TANG, Q., DO, D., IFTIMIA, N. A., MOORE, J. C., HAYES, M. N., WELKER, A. M., GARCIA, E. G., DUBASH, T. D., HONG, X., DRAPKIN, B. J., MYERS, D. T., PHAT, S., VOLORIO, A., MARVIN, D. L., LIGORIO, M., DERSHOWITZ, L., MCCARTHY, K. M., KARABACAK, M. N., FLETCHER, J. A., SGROI, D. C., IAFRATE, J. A., MAHESWARAN, S., DYSON, N. J., HABER, D. A., RAWLS, J. F. & LANGENAU, D. M. 2019. Visualizing Engrafted Human Cancer and Therapy Responses in Immunodeficient Zebrafish. *Cell,* 177**,** 1903-1914 e14.

YANG, H., LIU, C., YANG, D., ZHANG, H. & XI, Z. 2009. Comparative study of cytotoxicity, oxidative stress and genotoxicity induced by four typical nanomaterials: the role of particle size, shape and composition. *J Appl Toxicol,* 29**,** 69-78.

YANG, L., WANG, F., WANG, L., HUANG, L., WANG, J., ZHANG, B. & ZHANG, Y. 2015. CD163+ tumor-associated macrophage is a prognostic biomarker and is associated with therapeutic effect on malignant pleural effusion of lung cancer patients. *Oncotarget,* 6**,** 10592-603.

YAO, W., BA, Q., LI, X., LI, H., ZHANG, S., YUAN, Y., WANG, F., DUAN, X., LI, J., ZHANG, W. & WANG, H. 2017. A Natural CCR2 Antagonist Relieves Tumor-associated Macrophage-mediated Immunosuppression to Produce a Therapeutic Effect for Liver Cancer. *EBioMedicine,* 22**,** 58-67.

YEO, C. I., OOI, K. K. & TIEKINK, E. R. T. 2018. Gold-Based Medicine: A Paradigm Shift in Anti-Cancer Therapy? *Molecules,* 23.

YI, G. Z., HUANG, G., GUO, M., ZHANG, X., WANG, H., DENG, S., LI, Y., XIANG, W., CHEN, Z., PAN, J., LI, Z., YU, L., LEI, B., LIU, Y. & QI, S. 2019. Acquired temozolomide resistance in MGMT-deficient glioblastoma cells is associated with regulation of DNA repair by DHC2. *Brain,* 142**,** 2352-2366.

ZABINYAKOV, N., BULLIVANT, G., CAO, F., FERNANDEZ OJEDA, M., JIA, Z. P., WEN, X. Y., DOWLING, J. J., SALOMONS, G. S. & MERCIMEK-ANDREWS, S. 2017. Characterization of the first knock-out aldh7a1 zebrafish model for pyridoxine-dependent epilepsy using CRISPR-Cas9 technology. *PLoS One,* 12**,** e0186645.

ZADEH, G., BHAT, K. P. & ALDAPE, K. 2013. EGFR and EGFRvIII in glioblastoma: partners in crime. *Cancer Cell,* 24**,** 403-4.

ZANGANEH, S., HUTTER, G., SPITLER, R., LENKOV, O., MAHMOUDI, M., SHAW, A., PAJARINEN, J. S., NEJADNIK, H., GOODMAN, S., MOSELEY, M., COUSSENS, L. M. & DALDRUP-LINK, H. E. 2016. Iron oxide nanoparticles inhibit tumour growth by inducing pro-inflammatory macrophage polarization in tumour tissues. *Nat Nanotechnol,* 11**,** 986-994.

ZAZO, H., COLINO, C. I., WARZECHA, K. T., HOSS, M., GBURECK, U., TRAUTWEIN, C., TACKE, F., LANAO, J. M. & BARTNECK, M. 2017. Gold Nanocarriers for Macrophage-Targeted Therapy of Human Immunodeficiency Virus. *Macromol Biosci,* 17.

ZFIN. 2013. *zgc:198419 data for this paper were retrieved from the Zebrafish Information Network (ZFIN)* [Online]. Available: http://zfin.org/ [Accessed 05 July 2019].

ZHAI, H., HEPPNER, F. L. & TSIRKA, S. E. 2011. Microglia/macrophages promote glioma progression. *Glia,* 59**,** 472-85.

ZHANG, C., SHU, W., ZHOU, G., LIN, J., CHU, F., WU, H. & LIU, Z. 2018. Anti-TNF-alpha Therapy Suppresses Proinflammatory Activities of Mucosal Neutrophils in Inflammatory Bowel Disease. *Mediators Inflamm,* 2018**,** 3021863.

ZHANG, F., WANG, H., WANG, X., JIANG, G., LIU, H., ZHANG, G., WANG, H., FANG, R., BU, X., CAI, S. & DU, J. 2016. TGF-beta induces M2-like macrophage polarization via SNAIL-mediated suppression of a pro-inflammatory phenotype. *Oncotarget,* 7**,** 52294-52306.

ZHANG, Y., LI, Q., ZHUANG, R., GAO, Z., LIU, J., LI, J., YANG, A., CHENG, G. & JIN, B. 2012. Plexin-B1: a potential diagnostic biomarker for glioma and a future target for glioma immunotherapy. *J Neuroimmunol,* 252**,** 113-7.

ZHOU, J., SHEN, B., ZHANG, W., WANG, J., YANG, J., CHEN, L., ZHANG, N., ZHU, K., XU, J., HU, B., LENG, Q. & HUANG, X. 2014. One-step generation of different immunodeficient mice with multiple gene modifications by CRISPR/Cas9 mediated genome engineering. *Int J Biochem Cell Biol,* 46**,** 49-55.

ZHU, C., KROS, J. M., VAN DER WEIDEN, M., ZHENG, P., CHENG, C. & MUSTAFA, D. A. 2017. Expression site of P2RY12 in residential microglial cells in astrocytomas correlates with M1 and M2 marker expression and tumor grade. *Acta Neuropathol Commun,* 5**,** 4.

ZHU, Y., GUIGNARD, F., ZHAO, D., LIU, L., BURNS, D. K., MASON, R. P., MESSING, A. & PARADA, L. F. 2005. Early inactivation of p53 tumor suppressor gene cooperating with NF1 loss induces malignant astrocytoma. *Cancer Cell,* 8**,** 119-30.

ZONG, H., VERHAAK, R. G. & CANOLL, P. 2012. The cellular origin for malignant glioma and prospects for clinical advancements. *Expert Rev Mol Diagn,* 12**,** 383-94.